The University of Nottingham

School of Civil Engineering

Discrete Element Modelling of Idealised Asphalt Mixture

by

York Wei Lee

Thesis submitted to the University of Nottingham
for the degree of Doctor of Philosophy

June 2006

To my parents

Declaration

The research described in this thesis was conducted at the University of Nottingham, School of Civil Engineering between October 2002 and December 2005. I declare that the work is my own and has not been submitted for a degree of another university.

<div align="right">

York Lee
Nottingham
June 2006

</div>

Abstract

This thesis investigates the use of Discrete Element Modelling (DEM) to simulate the behaviour of a highly idealised bituminous mixture under uniaxial and triaxial compressive creep tests. The idealised mixture comprises single-sized spherical (sand-sized) particles mixed with bitumen and was chosen so that the packing characteristics are known (dense random packing) and the behaviour of the mixture will be dominated by the bitumen and complex aggregate interlock effects will be minimised. In this type of approach the effect of the bitumen is represented as shear and normal contact stiffnesses. A numerical sample preparation procedure has been developed to ensure that the final specimen is isotropic and has the correct volumetrics. Elastic contact properties have been used to investigate the effect of the shear and normal contact stiffnesses on bulk material properties. The bulk modulus was found to be linearly dependent on the normal contact stiffness and independent of the shear contact stiffness. Poisson's ratio was found to be dependent on only the ratio of the shear contact stiffness to the normal contact stiffness. An elastic contact has been assumed for the compressive normal contact stiffness and a viscoelastic contact for shear and tensile normal contact stiffness to represent the contact behaviour in idealised mixture. The idealised mixture is found to dilate when the ratio of compressive to tensile contact stiffness increases as a function of loading time. Uniaxial and triaxial viscoelastic simulations have been performed to investigate the effect of stress ratio on the rate of dilation with shear strain for the sand asphalt. The numerical results have been validated with experimental data. The geometric factors that influence asphalt dilation are investigated. The level of dilation was found to be dominated by the proportion of frictional contacts in the sample. Simulations have been performed to investigate the effect of particle shape on asphalt dilation. Greater dilation was found in the sample with clumps under loading.

Acknowledgements

Table of Contents

Chapter Three

Chapter Four

Chapter Five

Chapter Six

Chapter Seven

Chapter Eight

Chapter Nine

1 Introduction

1.1 Problem Definition

Asphalt is a complex multi-phase material that comprises 3 phases: bitumen, aggregate and air. A range of asphalt mixtures can be produced depending on the proportions of these components and the grading of aggregate. A typical continuously graded mixture (e.g. bitumen macadam) relies on an interlocking aggregate skeleton for its strength with the binder primarily acting as a lubricant to aid compaction and "glue" the mixture together. At the other extreme, a typical gap-graded mixture (e.g. stone mastic asphalt) will have a discontinuous aggregate grading (i.e. some stone sizes will not be present) and relies on a coarse aggregate skeleton bound by a bitumen/filler "mortar" for its strength. For both these mixture types the micromechanical behaviour, at the scale of an aggregate particle (e.g. particle size distribution, angularity), will be an important factor in terms of overall material performance.

The traditional approach to modelling asphaltic materials is to treat them at the macro-scale using continuum-based models. This usually involves undertaking careful experiments over a range of conditions (e.g. stress levels, loading rates, temperatures etc), measuring the macroscopic response of the material and fitting continuum-based constitutive models to the measured behaviour. The continuum approach implemented into a Finite Element (FE) program can incorporate nonlinear constitutive equations that include anisotropic, dynamic, viscous and plastic effects. The micromechanical behaviour of the mixture is typically not explicitly included in

this approach, which means that it is not easy to relate observed behaviour to the micromechanics of the material.

In reality, the deformation of asphalt takes place mainly in the bitumen. The contact properties between aggregates in the asphalt mixture depend strongly on the thickness of bitumen film separating aggregates. It should be emphasised that an understanding of the physical mechanism of deformation is crucial in understanding and modelling the deformation behaviour of asphalt mixtures. With the Discrete Element Method (DEM), it is possible to model materials that consist of individual particles where a particle may roll or slide relative to other particles.

The DEM offers a means of gaining an insight into the micromechanics of the deformation process. The program used in this thesis models a particle as a ball or a number of balls bonded together. The balls are non-deformable, but can overlap at the contact points and a contact law is used to calculate contact forces from the relative displacements. The aim of this project is to use the DEM program PFC3D (Particle Flow Code in Three Dimensions) to model the deformation behaviour of idealised asphalt mixtures. Previously gathered experimental data will be used for comparison with the modelling. An idealised asphalt mixture comprising relatively single-sized sand and bitumen has been chosen because of the relatively simple internal geometry compared to a more realistic asphalt mixture. This can be considered as a necessary first step towards understanding the micromechanics of the deformation behaviour in a real asphalt.

1.2 Thesis Structure

Chapter 2 provides an introduction to typical asphalt mixtures that are used in UK road construction. The major causes and the mechanics of permanent deformation are described. This is then followed by the review of recent research into permanent deformation of bitumen, idealised mixtures and realistic mixtures. Several continuum models for asphalt are described in this chapter. This chapter concludes with the review of micromechanical models for asphalt.

Chapter 3 describes the DEM and the software package PFC3D (Particle Flow Code in Three Dimensions) used in the modelling. This is then followed by the review of the development and application of the DEM in soil and rock mechanics. This chapter also reviews the theory and background of modelling using PFC3D. The Burger's time-dependent contact model is described.

Chapter 4 introduces the numerical sample preparation procedure used to create a sample that replicates the packing characteristics of an idealised asphalt mixture. A measurement method is established to quantify the deformation quantities of the asphalt specimens used in numerical simulations.

Chapter 5 presents simulations used to model the elastic response of the idealised mixtures. The effects of sample size, loading rate and normal and shear contact stiffness on bulk elastic properties are examined. A mean field approach is presented to theoretically investigate the dependence of bulk modulus on normal contact stiffness. The effect of non-equal tensile and compressive normal contact stiffnesses on dilation is investigated.

Chapter 6 presents uniaxial viscoelastic simulations. The Burger's contact model is used to simulate the time dependent shear and tensile normal contact behaviour of an idealised asphalt mixture and the normal compressive contact is taken to be elastic. The effects of the ratio of the various contact stiffnesses, sample density, deviator stress and bitumen film geometry factor on asphalt dilation are investigated.

Chapter 7 presents triaxial viscoelastic simulations. The first part of this chapter reviews experimental work by previous researchers in describing the effect of stress ratio on asphalt dilation. A modelling procedure to simulate the triaxial test in the laboratory is developed. The effect of deviator stress on dilation is investigated.

Chapter 8 describes the geometric factors that influence asphalt dilation. Two main effects are investigated. The effect of introducing a proportion of frictional contacts is investigated. Both the proportion of frictional contacts and the magnitude of the friction coefficient are investigated. The second part of this chapter simulates the

effect of particle shape on asphalt dilation. A sample preparation procedure is developed to prepare a numerical sample with non-spherical particles.

Chapter 9 summarises conclusions from this research and presents recommendations for further work.

2 *Reviewing the Deformation Behaviour of Bitumen and Asphalt*

2.1 Introduction

The first part of this chapter presents a brief review of the deformation behaviour of pure bitumen and asphalt mixtures. The second part presents a review of literature related to continuum and micromechanical modelling of asphalt mixtures.

2.2 Permanent Deformation of Asphalt Mixtures

Permanent deformation occurs when material from under the wheel path of a truck flows and compacts to form a groove or rut [112]. To describe pavement performance under various loading conditions, experiments in the field and under controlled conditions in the laboratory have been undertaken by many researchers [19, 56, 92]. However, the methodologies for rutting prediction and its elimination are far from perfect.

Pure bitumen behaves as an elastic solid at low temperatures and/or high loading rates, and a viscous fluid at high temperatures and/or low loading rates. It exhibits viscoelastic behaviour in the intermediate range. When a load is applied to an asphalt mixture, it deforms with an instantaneous elastic response after which the strain gradually increases with time. Upon removal of load, the initial elastic strain is recovered as is a further delayed elastic strain component leaving an irrecoverable small residual strain. This residual strain will be accumulated under many load

applications and will lead to pavement rutting. The phenomenon of permanent strain accumulation is illustrated in Figures 2.1 and 2.2.

The two major mechanisms in asphalt materials that contribute to rutting are densification and shear displacement. Densification occurs when the aggregate skeleton becomes more closely packed and tends to occur relatively early in the life of the pavement due to poor compaction during construction. Eisenmann and Hilmer [44] reported that if a pavement has been well compacted during construction, further densification is unlikely. Shear displacement is the process of lateral material flow, which can result in the development of shoulders on either side of a rut. Hofstra and Klomp [55] indicated that the shear displacement was the primary factor responsible for rutting. They emphasised that the material should be well compacted to a high density in order to minimise shear deformation. They concluded that rutting could be controlled by a good compaction in the field.

2.2.1 Permanent Deformation of Pure Bitumen

Early experiments indicated that the mechanical behaviour of asphalt mixtures is strongly dependent on the bituminous binder even though the mixture contains typically less than 10% by volume of bitumen. Research into the mechanical behaviour of pure bitumen started around 1960's when van der Poel reported that the stiffness of bitumen at low strains could be correlated with the *penetration*[1] and *softening point*[2] of the bitumen [118, 120]. He summarised the mechanical behaviour of bitumen as a function of temperature and loading time in the well known van der Poel Nomograph [119]. Following this, several researchers have attempted to characterise bitumen as a linear viscoelastic material using rheological models based on combinations of springs and dashpots [63, 118, 122]. However, these approaches are only applicable for small strains and stresses.

---

[1] Penetration is the distance travelled into a bitumen sample by a standard needle under a standard load (100g) for a standard period of time (5s) measured in decimillimetres.

[2] The softening point is the temperature at which a bitumen sample contained in a brass ring under the loading of a steel ball will touch a base plate 25mm below the ring when the bath temperature is raised at 5 °C per minute.

Previous researchers have shown that pure bitumen exhibits very complex stress-strain behaviour [22-25]. Cheung and Cebon [24] developed a deformation mechanism map (Figure 2.3) for bitumen over a wide range of temperatures, stresses and strain rates. They found that at temperatures above the *glass transition*[3], the deformation behaviour of the 50 pen grade of bitumen tested was linear viscous at low stress levels and power law creep at high stress levels with a creep exponent of approximately 2.3. The transition stress at which there is a change from linear to power law behaviour was found to be approximately 115kPa [22]. Early research also demonstrated that the steady state behaviour of bitumen is linear viscous at low stresses [14, 69, 97]. At higher stresses (0.1MPa to 1MPa), several experimental studies [47, 76, 102, 123] demonstrated that the bitumen behaves as a nonlinear viscous solid.

Cheung and Cebon [24] suggested that the transition from linear viscous behaviour at low stresses to nonlinear viscous behaviour at high stresses could be captured by the Modified Cross Model (MCM) [30]. They described the steady-state uniaxial behaviour of pure bitumen for temperatures well above the glass transition temperature by a MCM [22] which relates steady-state stress (σ_{ss}), steady-state strain rate ($\dot{\varepsilon}_{ss}$), reference stress (σ_o), reference strain rate ($\dot{\varepsilon}_p$) and material constant (*m*):

$$\frac{\sigma_{ss}}{\dot{\varepsilon}_{ss}} = \frac{\sigma_o}{\dot{\varepsilon}_p}\left(\frac{1}{1+\left(\dfrac{\dot{\varepsilon}_{ss}}{\dot{\varepsilon}_P}\right)^m}\right) \tag{2.1}$$

Figure 2.3 shows the steady state stress/strain rate relationship of the 50 pen grade of bitumen at temperatures ranging from $-10°C$ to $30°C$.

Ossa et al. [82] performed an extensive experimental study of the monotonic, recovery and cyclic behaviour of 50 and 100 pen grades of bitumen over a wide range of strain rates, stresses and temperatures. Based on these experiments, they

---

[3] The glass transition temperature, T_g, is defined as the temperature range at which bitumens change from a glassy to a fluid condition. The usual range of T_g for bitumens is between $-40°C$ and $0°C$.

proposed a phenomenological model which could be calibrated by a minimum of four uniaxial tensile experiments. A comparison between results from a constant stress creep test and their model is shown in Figure 2.4. It can be concluded that the phenomenological model can be used to predict the behaviour of pure bitumen.

2.2.2 Permanent Deformation of Idealised Mixtures

Deshpande [40] performed uniaxial and triaxial compression tests on various types of idealised mixtures under various stresses, strain rates and temperatures. Five types of mixture with different volume fractions of rigid inclusions (ranging from 40% to 85%) and a 50 pen grade of bitumen were used. Different sand sized particle were used in different mixtures to examine the effect of particle size. A series of tests (creep and constant strain rate at various temperatures and strain rates) were performed on the mixture with 64% by volume inclusions (denoted mixture A). Tests on the other mixes were performed only at a single temperature to study the effects of volume fraction of aggregate.

The steady state axial creep behaviour observed from the tests on mixture A for temperatures ranging from 0°C to 40°C is shown in Figure 2.5. It can be seen from Figure 2.5 that the curve at 20°C has the same shape as the curve for pure bitumen at 20°C obtained by Cheung [22] plotted using the Modified Cross Model (Equation 2.1). Consequently, the model proposed by Cheung [22] was modified to describe the uniaxial steady state creep behaviour of the asphalt mixture by simply replacing $\dot{\varepsilon}/\dot{\varepsilon}_o$ in Equation 2.1 with $S\dot{\varepsilon}/\dot{\varepsilon}_o$:

$$\frac{\sigma_{ss}}{\sigma_o} = \frac{S\dot{\varepsilon}_{ss}}{\dot{\varepsilon}_p}\left(\frac{1}{1+\left(\dfrac{S\dot{\varepsilon}_{ss}}{\dot{\varepsilon}_P}\right)^m}\right) \qquad (2.2)$$

where S is the stiffening factor due to the presence of aggregate. From Figure 2.5, it can be seen that the stiffening factor for the mixture at 20°C is approximately 1000.

This indicates that at the same stress level, the mixture at 20°C has a steady-state strain rate about 1000 times lower than that of the pure bitumen at 20°C. Deshpande [40] reported that the stiffening effect is only dependent on the volume fraction of aggregate and is independent of the size and shape of aggregate used. The stiffening factor was found to increase with the volume fraction of the aggregate in the mixture. He also found that the idealised mixtures with a high volume fraction of aggregate dilated under uniaxial compressive loading.

Khanzada [65] also investigated the deformation behaviour of idealised mixtures using simple laboratory deformation tests. Two types of idealised mixtures were used: Mixture A comprising single sized sand and Mixture A/D comprising double sized sand. A 50 pen grade of bitumen was used as the binder. A typical plot of axial strain versus time for Mixture A from a creep test is shown in Figure 2.6. It can be seen from this figure that the creep curve can be divided into three regions: primary creep where the strain rate decreases, secondary creep where the strain rate is approximately constant and tertiary creep where the strain rate increases. The deformation in the secondary creep region is defined as 'steady-state' [65]. The relationship between radial strain and axial strain for mixture A is plotted in Figure 2.7. It can be seen from this figure that the slope is approximately 1 in the region where steady state conditions are achieved. Consequently, Khanzada [65] concluded that the idealised mixtures dilate under uniaxial and triaxial compressive loading.

Collop and Khanzada [26] performed wheel tracking tests on the idealised mixtures A and A/D at three temperatures (20, 30 and 40°C) and three stress levels (500, 750 and 1000kPa). The experimental results are shown in Figure 2.8. It can be seen from this figure that after an initial period where the rutting rate decreases, the rut depth increases approximately in proportion to the number of cumulative passes. They explained that the initial behaviour was thought to be associated with densification where the density of the material increases. The second part of the curve was characterised by a steady state rutting rate (gradient) which they used to characterise the permanent deformation behaviour of the idealised mixtures.

2.2.3 Permanent Deformation of Realistic Mixtures

Khanzada [65] performed uniaxial tests, triaxial tests, Repeated Load Axial (RLA) tests and wheel tracking tests on an HRA mortar, a 30/10 HRA and a 10mm DBM mixture over a range of temperatures (20 to 40°C) and applied stress levels (200 to 2000kPa). They were all found to have the same form as the steady-state deformation behaviour of the pure bitumen and idealised mixtures. Figure 2.9 shows the plot of the steady state deformation behaviour of the HRA mixture, HRA mortar and pure bitumen. It can be seen from this figure that the stiffening factor (S) of the HRA mortar has a lower value compared to the HRA mixture. Figure 2.10 shows the stiffening factor of all the mixtures that contained 50 pen grade of bitumen tested by Khanzada [65]. The stiffening factor was found to increase with the volume fraction of aggregate. Consequently, he concluded that increasing the volume of aggregate in the mixture results in stiffening of the mixture.

Khanzada [65] further investigated the dilation for different idealised and realistic asphalt mixtures. Figure 2.11 shows the dilation gradients (defined as ratio of volumetric strain to distortional strain) measured for the various mixtures plotted as a function of volume fraction of the aggregates in the mixtures. It can be seen from this figure that the dilation gradients increase with increasing volume fraction of aggregate (aggregate proportion in the mixture). A higher dilation gradient was found to result in a higher stiffening factor for a mixture with the same volume fraction of aggregates subjected to the same stress ratio.

2.3 Continuum Models for Asphalt Mixtures

Constitutive modelling of the deformation behaviour of asphalt materials using continuum mechanics has been accepted for over fifty years (see Cheung [22]). Because of the complexity of the problem and limited understanding of the behaviour of heterogeneous materials, most of the current approaches are of a qualitative or empirical nature. The following sub-sections review the main types of continuum models that have been used for asphalt mixtures.

2.3.1 Stiffness Representation

The use of 'stiffness' for asphalt was first introduced by van der Poel [118] to describe the behaviour of pure bitumen as a function of loading time and temperature. This research resulted in the well known van der Poel Nomograph [118]. Van der Poel [120] extended the stiffness concept to describe the dynamic behaviour of asphalt mixtures under small strains where linear behaviour dominates. Subsequently, the use of stiffness for describing both the dynamic and quasi-static behaviour of asphalt mixtures became widely accepted.

Van der Poel [120] assumed that the stiffness of an asphalt mixture was a function only of the stiffness of the bitumen and the volume fraction of the aggregate. Similar findings were reported by Heukelom and Klomp [52]. They stated that for a particular mix, there is a relationship between the stiffness of mixture, S_{mix} and the stiffness of the binder, S_{bit} irrespective of the combination of loading time and temperature. Consequently, Heukelom and Klomp [52] proposed the following relationship for predicting the stiffness of an asphalt mixture:

$$\frac{S_{mix}}{S_{bit}} = \left[1 + \frac{2.5}{n}\frac{C_V}{1-C_V}\right]^n \tag{2.3}$$

where C_v is the volume of concentration of the aggregate defined by:

$$C_v = \frac{\text{Volume of aggregates}}{\text{Volume of (aggregates + bitumen + air)}} \tag{2.4}$$

and

$$n = 0.83\log\left[\frac{4 \times 10^{10}}{S_{bit}(Pa)}\right] \tag{2.5}$$

The above equations were derived from empirical fits to test data obtained from static and dynamic tests on well-compacted mixes having about 3% of air voids and C_v values ranging from 0.7 to 0.9.

Brown et al. [18] modified this approach by defining the mix stiffness as a function of bitumen stiffness and the percentage of voids in mixed aggregate (VMA). They proposed that:

$$\frac{S_{mix}}{S_{bit}} = \left[1 + \frac{275.5 - 2.5VMA}{n(VMA - 3)}\right]^n \qquad (2.6)$$

where n is the same function of S_{bit} as in Equation 2.5.

Figure 2.12 shows a plot of mix stiffness versus bitumen stiffness for different values of VMA based on Equation 2.6. It should be noted that Equation 2.6 is valid for VMA values between 12% to 30% and $S_{bit} \geq$ 5MPa. This is because the transition to a well-ordered, predictable relationship occurs at a bitumen stiffness of 5MPa [18] where the bitumen behaves as an elastic solid, whereas for lower values of S_{bit}, the stiffness ratio becomes a function of the elastic, viscoelastic and viscous response of the material [22].

2.3.2 Elastic Model

The simplest constitutive model for an asphalt mixture is based on the theory of linear elasticity. A material is described as elastic, where the loading curve is identical to the unloading curve, and all the strains are recovered upon the removal of the applied load. According o Hooke's law, the stress and strain relationship for an elastic material in three-dimensions is expressed as:

$$\{\sigma\} = [D] \times \{\varepsilon\} \qquad (2.7)$$

where [D] is the stiffness matrix of elasticity including two material constants (Young's modulus, E and Poisson's ratio, v) expressed as:

$$[D] = \frac{E}{(1+v)(1-2v)}\begin{bmatrix} 1-v & v & v & 0 & 0 & 0 \\ & 1-v & v & 0 & 0 & 0 \\ & & 1-v & 0 & 0 & 0 \\ & & & 0.5-v & 0 & 0 \\ & SYM & & & 0.5-v & 0 \\ & & & & & 0.5-v \end{bmatrix} \quad (2.8)$$

For an asphaltic material, Young's modulus is replaced by a "stiffness modulus" [118] since the stiffness varies with loading time and temperature. It is well known that at low temperatures and short loading times, the prediction of asphalt pavement behaviour by using linear elastic method is accurate enough for engineering purposes. At present, elastic models are extensively used in computer design program such as BISAR[4] for pavement structural analysis. A few researchers, such as Eisenmann et al. [45], Ulliditz [114] and Peutz et al. [87] have applied linear elastic models in flexible pavement design and performance evaluation in the past. Non-linear elastic models are also employed to solve the problem of non-linear behaviour of asphalt mixtures [53, 108].

2.3.3 Linear Viscoelastic Models

Materials that exhibit time-dependant behaviour in the relationship between stress and strain can be described as viscoelastic. The behaviour of asphalt materials subjected to loading can be described as linear viscoelastic at low stress and strain levels [75]. The viscoelastic description of the behaviour of bitumen became popular in 1950's when van der Poel modified Young's modulus for an elastic solid to define the stiffness modulus of bitumen as a function of loading time and temperature [118]. Thereafter, linear viscoelastic models have been widely applied to describe the behaviour of asphalt. However, to fully describe the actual behaviour of the asphalt mixtures, research has been undertaken to develop more complicated models which consist of elastic, plastic, viscoelastic and viscoplastic components [5, 86, 116]. Recent research has also focused on constitutive models that reflect the complex non-linear behaviour of asphalt materials [98, 106, 107, 115]. For

---

[4] BISAR (Bitumen Stress Analysis in Roads): A computer program developed by Shell which calculates stresses, strains and displacements in an elastic multi-layer system.

simplicity, the viscoelastic relationship described in this section is assumed to be linear.

Johnson [62] suggested that the relationship for an incompressible viscoelastic material could be written in terms of the deviatoric stress (σ) and the deviatoric strain (ε):

$$\sigma(t) = \int_0^t Y(t - t') \frac{\partial \varepsilon(t')}{\partial t'} dt' \qquad (2.9)$$

$$\varepsilon(t) = \int_0^t J(t - t') \frac{\partial \sigma(t')}{\partial t'} dt' \qquad (2.10)$$

where $Y(t)$ is the relaxation modulus which expresses the stress response to a step change in strain and $J(t)$ is the creep compliance which expresses the strain response to a step change of stress.

The deformation behaviour of asphaltic materials exhibits initial elastic, delayed elastic and steady creep behaviour under constant loading. Johnson [62] showed two examples to demonstrate separately the effects of delayed elasticity and steady creep by using two idealised viscoelastic materials. The first material is represented by two springs of modulus k_1 and k_2 together with a dashpot of viscosity C connected as shown in Figure 2.13(a). The creep response to a step change in stress σ_o is given by:

$$\varepsilon(t) = J(t)\sigma_o = \left\{ \frac{1}{k_1} + \frac{1}{k_2} \left[1 - e^{(-t/\tau_1)} \right] \right\} \sigma_o \qquad (2.11)$$

where $\tau_1 = C / k_2$.

The second material, which is known as a Maxwell model is illustrated in Figure 2.13(b) and is represented by a spring of modulus k in series with a dashpot of viscosity C. The creep response is given by:

$$\varepsilon(t) = J(t)\sigma_o = \left[\frac{1}{k} + \frac{1}{C}t\right]\sigma_o \qquad (2.12)$$

The first material exhibits delayed elasticity but the ultimate strain is limited to a finite value whereas the second material exhibits steady-state creep under constant stress, hence the strains increase continuously with time.

A Burger's model exhibits both delayed elasticity and steady creep behaviour for an asphalt material. It is a combination of four elements with a spring and dashpot in parallel (Voigt model) connected in series to a spring and dashpot in series (Maxwell model) as shown in Figure 2.14. The uniaxial creep response to a step change in stress σ_o is given by:

$$\varepsilon(t) = J(t)\sigma_o = \left\{\frac{1}{k_1} + \frac{t}{C_\infty} + \frac{1}{k_2}\left[1 - e^{(-t/\tau_1)}\right]\right\}\sigma_o \qquad (2.13)$$

where $\tau_1 = C_2 / k_2$.

The features of the viscoelastic behaviour represented by a Burger's model subjected to a square pulse application of stress are illustrated in Figure 2.15. It can be seen that there is an instantaneous elastic response (strain OA) when the stress is applied. A further delayed elastic strain AB is acquired in time as is a steadily increasing creep strain component BC. When the stress is removed, there is an instantaneous elastic recovery (same in magnitude as OA) and a delayed elastic recovery DE leaving a permanent strain at E.

Pagen [84] analysed the viscoelastic behaviour of asphalt mixtures using rheological concepts [7, 85]. A phenomenological treatment of linear viscoelastic behaviour of asphalt mixtures was performed and a creep compliance function J_c (t) was proposed to describe the creep behaviour of the asphalt (see Pagen [84] for details). Pagen [83] extended his work to perform testing on dense asphalt mixtures prepared in the laboratory by gyratory compaction and field core test specimens. He reported that

the data obtained from these specimens indicated that linear viscoelastic theory can be applied to studies of asphalt mixtures to evaluate their engineering properties on a fundamental level. Consequently, it was concluded that linear viscoelastic models were applicable to the asphalt mixtures for low levels of applied stress.

Monismith et al. [77, 78] evaluated the suitability of a simple four-element linear viscoelastic model (see Figure 2.16) to describe the behaviour of an asphalt by performing four types of triaxial compression tests (creep, stress relaxation, constant strain rate, repeated axial load) on one asphalt mixture. Monismith and Secor [78] demonstrated the ability of the model to express the rheological characteristics of an asphalt mixture. They reported that the use of a four-element model could provide a general approximation of the properties of the material under study over a wide range of load types and ambient conditions. It was concluded that the asphalt mixtures could be considered as linear viscoelastic for small amounts of deformation (0.1% strain or less) [77]. However, the simple linear viscoelastic models have a limited applicability in predicting the real behaviour of asphalt mixtures.

2.3.4 Nonlinear Viscoelastic Models

It was noted in the last section that at high stress and strain levels, the response of asphalt mixtures cannot adequately be modelled by a linear viscoelastic approximation. Fitzgerald and Vakili [46] emphasised that linear viscoelasticity is not applicable for characterising asphalt materials under repeated loading. They performed experimental and theoretical investigations to demonstrate that extended nonlinear, homogeneous constitutive equations are readily applicable to defining the mechanical behaviour of a sand-asphalt mixture.

Lai and Anderson [67] suggested that the nonlinear viscoelastic behaviour of asphalt mixtures can be represented by a non linear generalised Kelvin model that consists of a nonlinear dashpot connected in series with a nonlinear Kelvin chain, where the nonlinear dashpot accounts for the time dependent irrecoverable strain (viscous flow) and the nonlinear Kelvin chain accounts for the power law time dependent recoverable strain (see Lai and Anderson [67] for the constitutive equations). They

claimed that the accuracy in predicting the creep behaviour of an asphalt mixture under multiple-step loading and repeated loading using the proposed constitutive equation was very satisfactory.

Judycki [64] applied nonlinear viscoelastic theories to model the nonlinear behaviour of asphalt mixtures under 3-point bending tests and he reported that the nonlinear effects increased with the stress level and loading time for test results at 10°C.

2.3.5 Elasto-visco-plastic Models

Various research has been undertaken [5, 43, 86, 101, 124] to propose a model that accounts for elastic, plastic, viscoelastic and viscoplastic responses of the asphalt material.

Perl et al [86] presented a constitutive model for an asphalt mixture subjected to repeated loading incorporating elastic, plastic, viscoelastic and viscoplastic strain components. They performed a series of repeated uniaxial creep and creep recovery tests under constant stresses of various magnitudes at a constant temperature of 25°C. From the tests results, they reported that the total strain has recoverable and irrecoverable elements, some of which are time-dependent and some are time-independent. The total strain ε_t was resolved in four components:

$$\varepsilon_t = \varepsilon_e + \varepsilon_p + \varepsilon_{ve} + \varepsilon_{vp} \tag{2.14}$$

where,

ε_e = elastic strain (recoverable and time independent)

ε_p = plastic strain (irrecoverable and time independent)

ε_{ve} = viscoelastic strain (recoverable and time dependent)

ε_{vp} = viscoplastic strain (irrecoverable and time dependent)

A typical schematic cycle is shown in Figure 2.17. It can be seen from this figure that at $t = t_o$ (when load is applied), the strain ε_o comprises elastic ε_e and plastic strain ε_p components instantaneously. As the specimen undergoes creep ($t_o \leq t \leq t_1$), viscoelastic ε_{ve} and viscoplastic ε_{vp} strains are built up. Once the load is removed ($t = t_1$), the elastic strain ε_e is recovered. The viscoelastic strain is then recovered in the period ($t_1 \leq t \leq t_2$). At the end of the cycle, the residual strain consists of the irrecoverable plastic and viscoplastic strain components. The elastic and plastic strains are time independent and the viscoelastic and viscoplastic strains are time dependent.

Drescher et al [43] stated that the strains due to viscosity depend on the load duration and the loading/unloading rate whilst the plastic strains are independent of the loading/unloading rate. They performed a series of uniaxial compressive creep/recovery tests on one asphalt mixture and concluded that the plastic strains are proportional to the applied stress level, the elastic strains are a linear function of stress and the viscoelastic strains are slightly nonlinear with respect to stress level.

2.4 Micromechanical Models of Asphalt Mixtures

The traditional approach to modelling asphalt materials is to treat them at the macro-scale using continuum based approaches [29]. This usually involves the undertaking of careful experiments over a range of conditions (e.g. stress levels, loading rates, temperatures etc), measuring the macroscopic response of the material and fitting continuum-based constitutive models to the measured behaviour. However, it is not easy to relate the observed behaviour of asphalt mixtures to the micromechanics of the material. A micromechanical model can predict fundamental material properties of a composite based upon the properties of the individual constituents and it allows a thorough examination of micro structure material behaviour. This section reviews the applications of micromechanical models in modelling asphalt.

2.4.1 Thin Film Bitumen Creep Model

Hills [54] developed a model for creep behaviour of asphalt mixtures. He assumed that any deformations in the mixture are the result of relative sliding displacements between adjacent mineral particles separated by a thin film of bitumen (see Figure 2.18). Thus, this model takes account only of the shear strains in the bitumen. In this approach, the internal structure of asphalt mixtures is described in terms of the bitumen film thickness and the evolution of this state variable as a function of the macroscopic straining of material. The rate of strain was dependent on the magnitude of stresses, the thickness of bitumen (changes as a function of time) and the bitumen properties.

The creep behaviour of asphalt mixes indicates that their internal structure changes during the course of a test. Hence, Hills [54] proposed a theoretical model considering bitumen as forming the binder layer between a pair of adjacent particles and taking account of the thinning of the binder films and the gradation of the aggregate. He also proposed another theoretical model for frictional or boundary lubrication conditions. Further details on derivation of constitutive equations for these models are described in Hills [54]. He found that the models give good agreement with experimental results and are applicable to the linear, shear and volumetric strains in uniaxial compression tests.

2.4.2 Microstructural Model

Sadd et al [71] indicated that the load carrying behaviour in an asphalt mixture is strongly related to the local load transfer between aggregate particles, and this is taken as the microstructural response. They developed a microstructural model and simulated the microstructural response of the load carrying behaviour of the aggregate/binder system. An elliptical aggregate model as shown in Figure 2.19(b) was presented to represent the typical asphalt material (Figure 2.19(a)). Two models were developed. The first model incorporates a network of frame elements with a special stiffness matrix to predict load transfer between cemented particles, as shown in Figure 2.19(c). A 6×6 stiffness matrix is derived as a function of the

micromechanical material variables including particle size and shape and cementation geometry and moduli (see Sadd et al [71] for details). The second model incorporates the commercial ABAQUS finite element code using user-defined continuum elements for the binder and rigid elements for aggregate, as shown in Figure 2.19(d). This model employed four-noded quadrilateral elements to simulate the binder and two-noded rigid element to model the aggregate.

An Indirect Tensile Test (IDT) was simulated using these models and the elastic compressive modulus and Poisson's ratio were predicted. An experimental verification was performed by conducting an IDT on a specially prepared cemented particulate system, which allowed measurement of aggregate displacement and rotations using video imaging and computer analysis. As a result, they stated that the differences between model prediction and experimental data are generally within 5%, thus indicating a good agreement. However, the modelling has been limited to two-dimensional behaviour.

2.4.3 Discrete Element Model

The Discrete Element Method (DEM) is an approach capable of modelling the micromechanical behaviour of an asphalt mixture. This method has been widely applied in modelling of soil and rock material and is reviewed in detail in Chapter 3. This sub-section describes the few applications that have used DEM to simulate asphalt behaviour.

Buttlar and You [20] used DEM to develop a two-dimensional model of an indirect tensile (IDT) test comprising 130 cylindrical stones (12.5mm in diameter) arranged in a hexagonal packing structure glued together with asphalt mastic (see Figure 2.20). They validated predictions with experimental data (for the same idealised mixture) obtaining good agreement. Buttlar and You [20] extended this approach to develop a two-dimensional IDT model of Stone Mastic Asphalt (SMA) using a microfabric approach whereby the various material phases are modelled as clusters of discrete elements. The aggregate structure was captured using a high-resolution optical scanner. Predicted horizontal displacements were approximately 40% greater than

measurements which were attributed to the two-dimensional microstructural representation underestimating the actual amount of aggregate interlock.

Rothenburg et al [95] presented a micromechanical model of asphalt in which the material is represented as a set of discrete elastic particles bounded by viscoelastic bitumen as shown in Figure 2.21. In this model, the binder is treated as an incompressible Newtonian fluid. A binder-aggregate interaction model was developed to account for the behaviour of asphalt concrete. The simulations were carried out by numerically solving Newton's equations of motion for individual particles incrementally in time. They performed a few creep test simulations and concluded that when the number of frictional contacts is below a certain minimum, asphalt can exhibit steady state creep which would lead to rutting in a pavement. However, the simulations were two-dimensional and no calibration with laboratory data was given.

Chang and Meegoda [21] presented a microscopic model, ASBAL by modifying the microscopic model TRUBAL by Cundall [32] to include the bitumen binder between particles. The rheological analog of the viscoelastic bitumen binder is presented as a linear spring and a dashpot (Voigt element) as shown in Figure 2.22. They performed a few uniaxial simulations consisting of 152 spherical particles subjected to monotonic, constant strain rate and cyclic loading. However, the simulations were undertaken just to perform a study on important factors that can influence the simulation results by using ASBAL. Meegoda and Chang [74] extended the ASBAL model by replacing the Voigt element with a Burgers element to simulate the viscoelastic behaviour of bitumen binder. They then developed a microscopic model for Hot Mix Asphalt (HMA) using ASBAL. A few simulations were performed with different microscopic parameters under varied types of loadings such as monotonic and cyclic loading. They showed that under monotonic loading, a typical HMA test exhibits non-linear behaviours and under cyclic loading, permanent deformation was modelled.

The few micromechanics approaches that have been undertaken to model the asphalt using DEM have been limited to two-dimensional behaviour. Hence, there is a need

to extend this to three dimensions so that the effect of sample volumetric strain and aggregate interlocking can be modelled more accurately.

2.5 Thin Film Behaviour of Bitumen

To simulate asphalt using the Discrete Element Method, it is important to understand the behaviour of bitumen in the form of a thin film. This section reviews the thin film behaviour of bitumen in compression, shear and tension. For elastic contact behaviour in compression, Nadai [79] suggested that the effective Young's modulus for an incompressible material subject to axisymmetric deformation is:

$$E_n^{ai} = \frac{E_m}{8} A^2 \qquad (2.15)$$

where A is the aspect ratio, which is defined as the ratio of particle diameter to film thickness. Cheung [22] suggested that for compressible material subject to axisymmetric deformation:

$$\frac{E_n^{ac}}{E_n^{ai}} = 1 - \left[1 + \frac{3}{8} \frac{K/E_m}{(5/8)A^2}\right]^{-1} \qquad (2.16)$$

where K is the bulk modulus of film material. However, these approaches are only applicable for an elastic material that is subject to compression. For a viscous contact in compression, Cheung [22] proposed a "thin film stiffening factor (T_F)" subjected to axisymmetric deformation:

$$T_F = \left[\left(\frac{n}{3n+1}\right)\left(\frac{n+2}{2}\right)^{\frac{1}{n}}\left(\frac{A_R}{\sqrt{3}}\right)^{\frac{n+1}{n}}\right] \qquad (2.17)$$

where n is the power-law creep exponent and A_R is the aspect ratio. The relationship between the thin film stiffening factor and the aspect ratio reproduced from Equation

2.17 is plotted in Figure 2.23. Harvey [50] further modified the "thin film stiffening factor" by introducing the thick film adjustment with following equation:

$$T_{TF} = \left(\frac{A}{A_o}\right)^{\left(\frac{n+1}{n}\right)} + 1 \tag{2.18}$$

where A_o is a reference aspect ratio with a constant of 3.1. This is also shown in Figure 2.23. It can be seen from this figure that the bitumen film stiffness increases at a higher aspect ratio. Therefore, it can be concluded that the normal stiffness of bitumen film is dependent on the aspect ratio of bitumen film.

Cheung and Cebon [24] performed an experimental study on pure bitumens tested in uniaxial tension, compression and shear over a wide range of temperatures, stresses and strain rates. They found that for isothermal conditions constitutive behaviour of pure bitumen in uniaxial tension is given by:

$$\left(\frac{\dot{\varepsilon}}{\dot{\varepsilon}_0}\right) = \left(\frac{\sigma}{\sigma_0}\right)^n \tag{2.19}$$

In general, the power-law constitutive behaviour in three dimensions can be expressed as:

$$\left(\frac{\dot{\varepsilon}_{ij}}{\dot{\varepsilon}_0}\right) = \frac{3}{2}\left(\frac{\sigma_e}{\sigma_0}\right)^n \frac{\sigma'_{ij}}{\sigma_e} \tag{2.20}$$

where $\sigma'_{ij} = \sigma_{ij} - \frac{1}{3}\delta_{ij}\sigma_{kk}$ is the deviator stress, δ_{ij} is the Kronecker delta, and $\sigma_e = \left(\frac{3}{2}\sigma'_{ij}\sigma'_{ij}\right)^{1/2}$ is the von Mises effective stress. Equation 2.19 approximates the steady-state creep behaviour shown by many metals, polymers and ceramics (Bower et al. [13]). Cheung and Cebon [24] studied its applicability to bitumens by examining the measured behaviour of bitumen in pure shear. They indicated that the generalised power-law equation predicts that under pure shear, the steady strain rate is given by:

$$\left(\frac{\dot{\gamma}}{\dot{\varepsilon}_0}\right) = \sqrt{3}^{-n+1}\left(\frac{\tau}{\sigma_0}\right)^n \tag{2.21}$$

It can be seen from Equation 2.21 that the bitumen behaviour in tension and in shear are expected to be related by the factor of $\sqrt{3}^{-n+1}$. This indicates that for bitumen behaviour in linear region ($n = 1$), the shear strain rate is three times the tensile strain rate for a given applied stress throughout the stress range. Lethersich [69] performed a numerical analysis to investigate the mechanical behaviour of bitumen. He indicated that bitumen viscosities are associated with a shear stress which is equal to one third of the tensile stress in a plane where the shear and tensile strains are equal. Consequently, it can be concluded that in the linear region the tensile stiffness of pure bitumen is approximately three times the shear stiffness of pure bitumen.

2.6 Summary

The literature review presented in this chapter indicates that the deformation behaviour of asphalt mixtures at the marco-scale is reasonably well understood. It is time, loading rate and temperature dependent and during deformation, dilation can occur. Asphalt materials are usually assumed to be linear viscoelastic at small strains. However they are generally nonlinear materials and visco-elasto-plastic constitutive relationships are capable of fully describing the behaviour of an asphalt mixture.

A number of empirical continuum models are available to predict the behaviour of asphalt materials. These models have been reasonably successful although large calibration factors are needed in a quantitative analysis of pavement structures. No developed models at present are capable of describing comprehensively the behaviour of asphalt mixtures.

Micromechanical models of asphalt mixture deformation behaviour are poorly developed at present. The physical mechanisms of deformation are not well understood. It should be emphasised that an understanding of the deformation mechanism is crucial in modelling the deformation behaviour of asphalt mixtures.

Further development should emphasise more specific descriptions of the microstructure of the asphalt mixtures.

The review also showed that the mechanical behaviour of pure bitumen in compression, shear and tension is well understood. This understanding will be applied to model contact behaviour in DEM simulation of asphalt.

Figures:
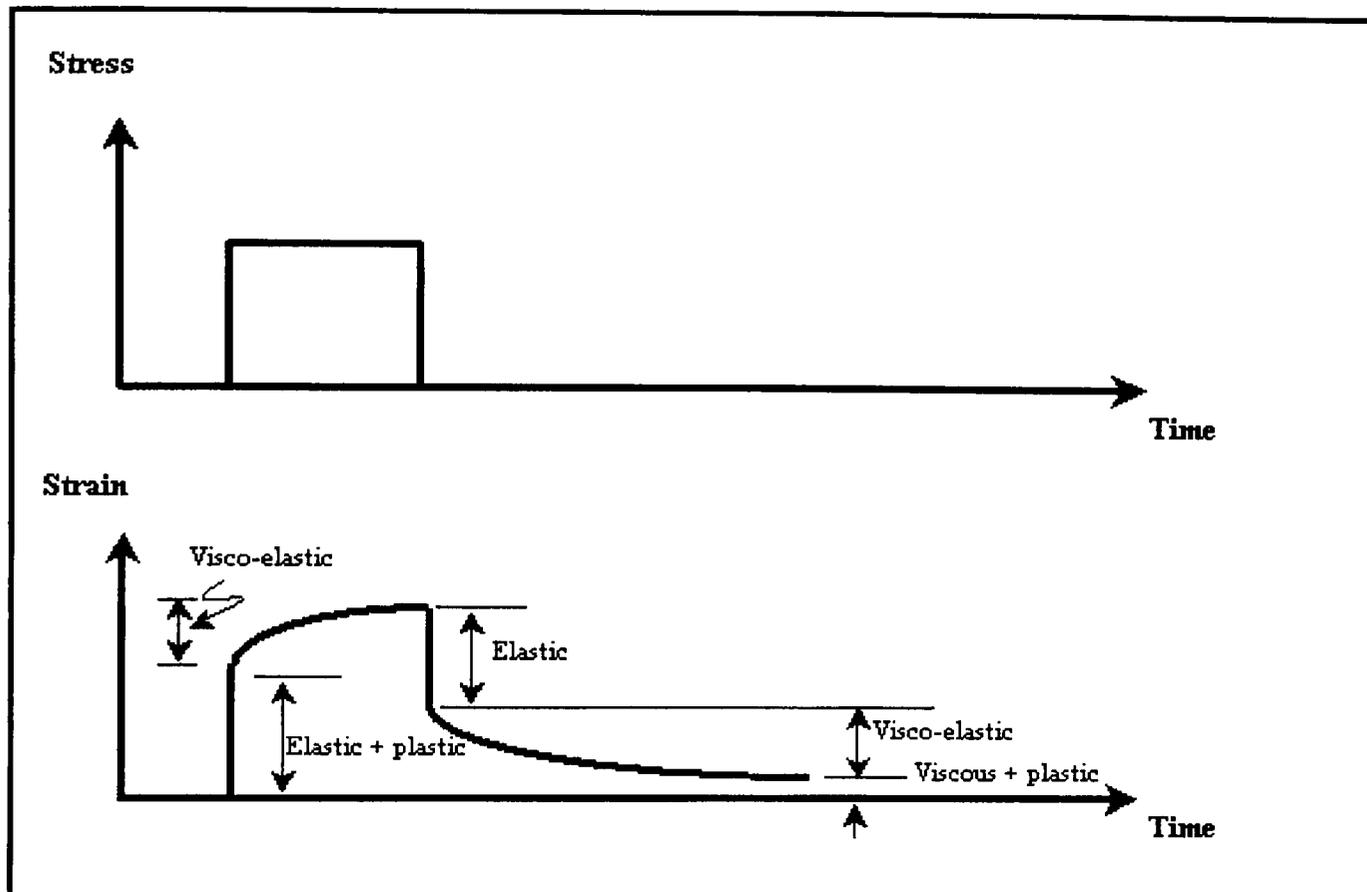
Figure 2.1: Strain response of asphalt mixtures under single load [65].
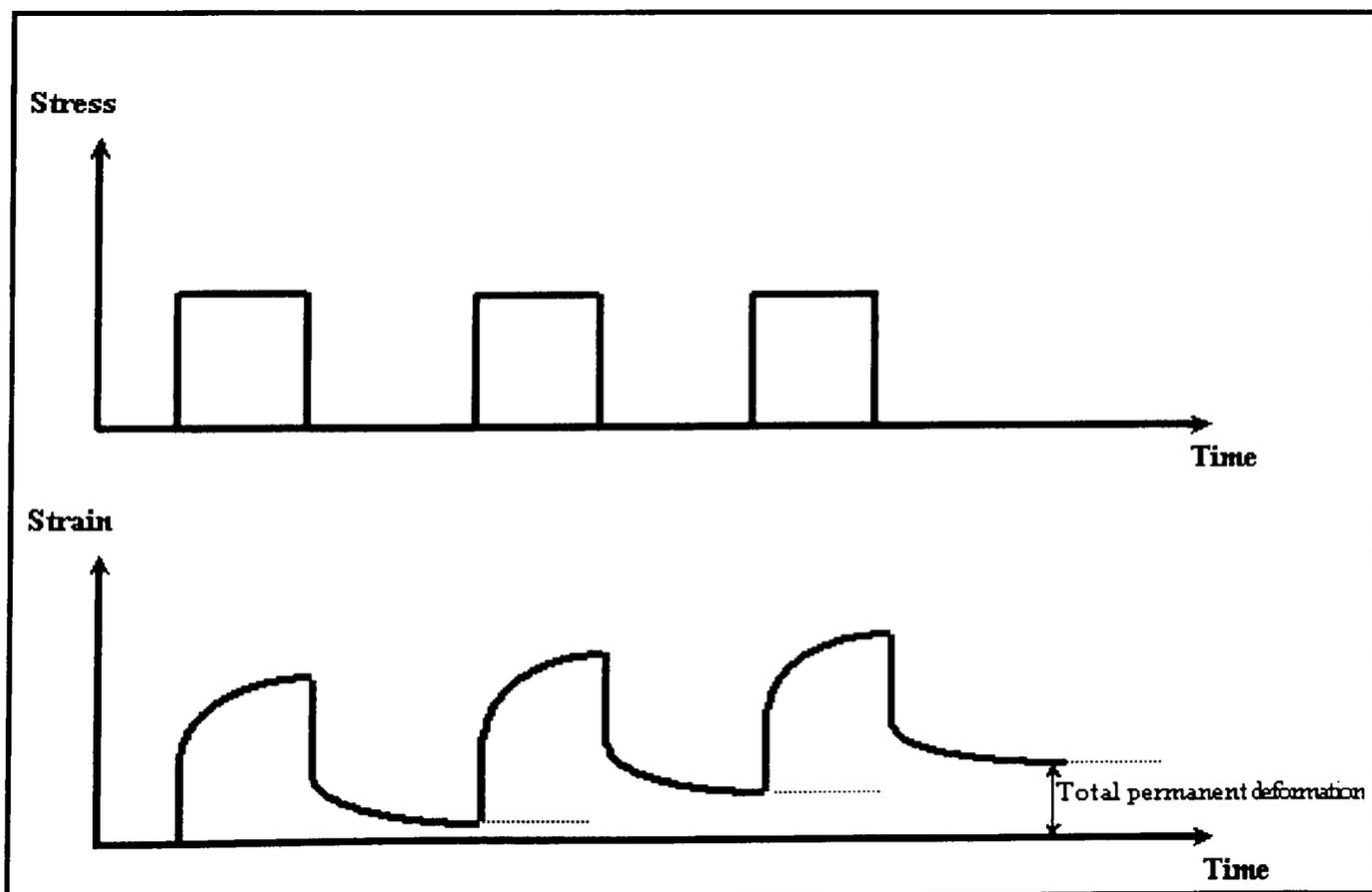
Figure 2.2: Accumulation of residual strain of asphalt mixtures under repeated load [65].
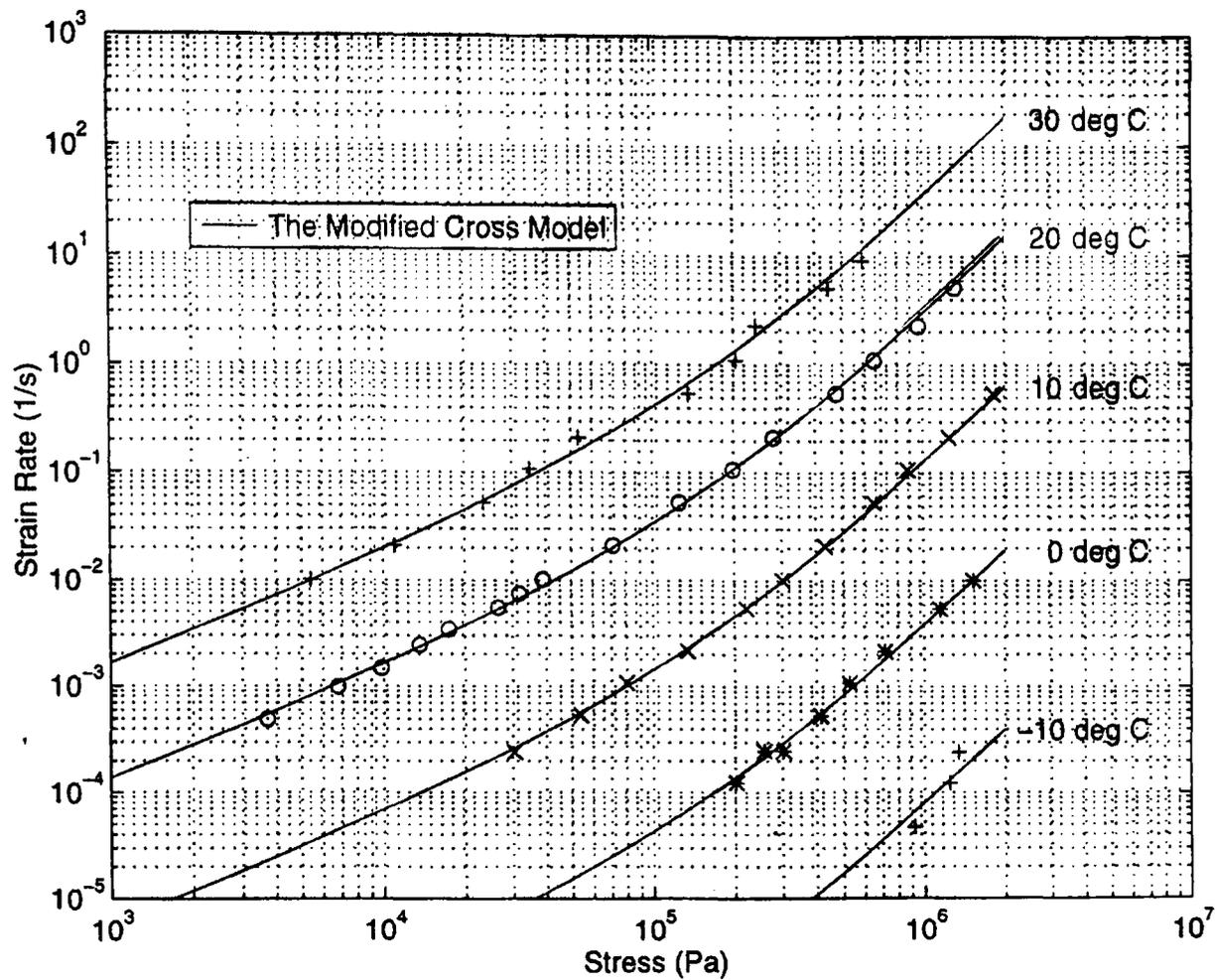
Figure 2.3: Deformation map of the 50 pen grade of bitumen at various temperatures, after Cheung [22].
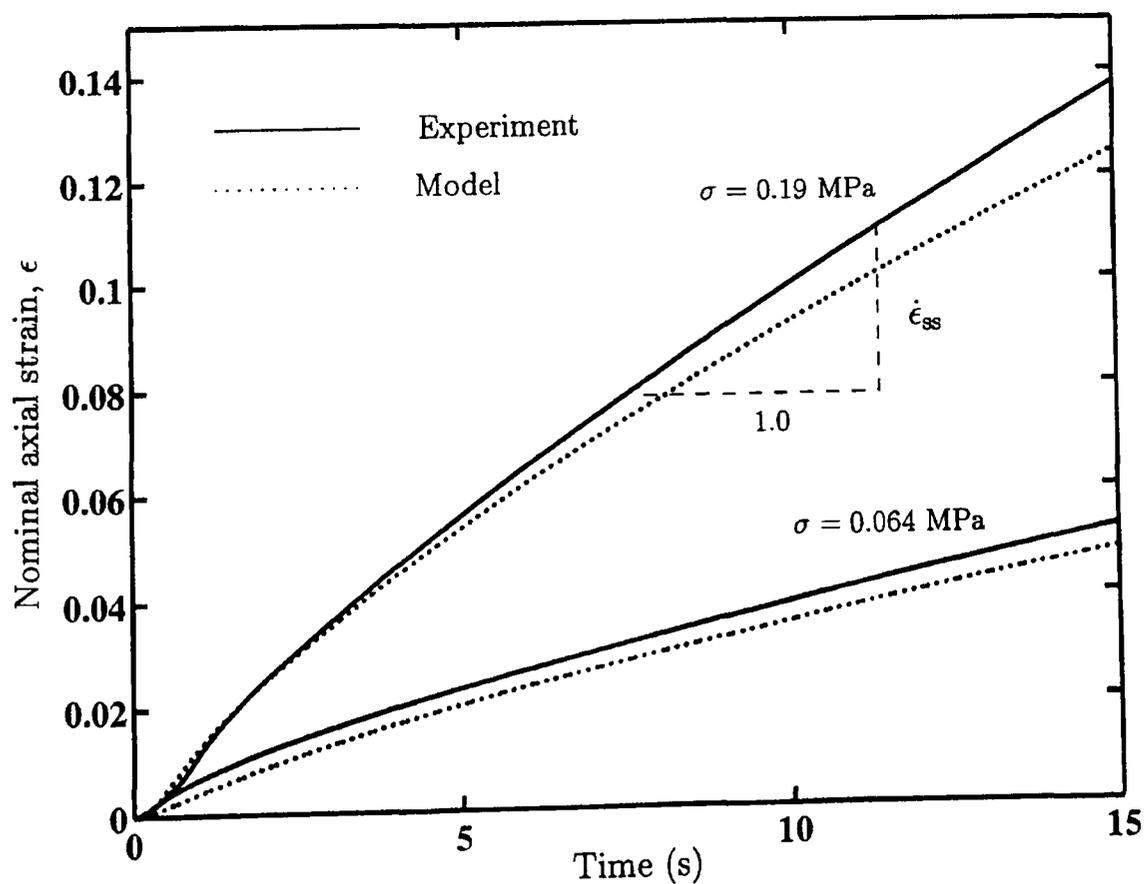
Figure 2.4: Constant stress creep tests at two selected creep stresses on the 50 pen bitumen at 10°C, after Ossa [82].
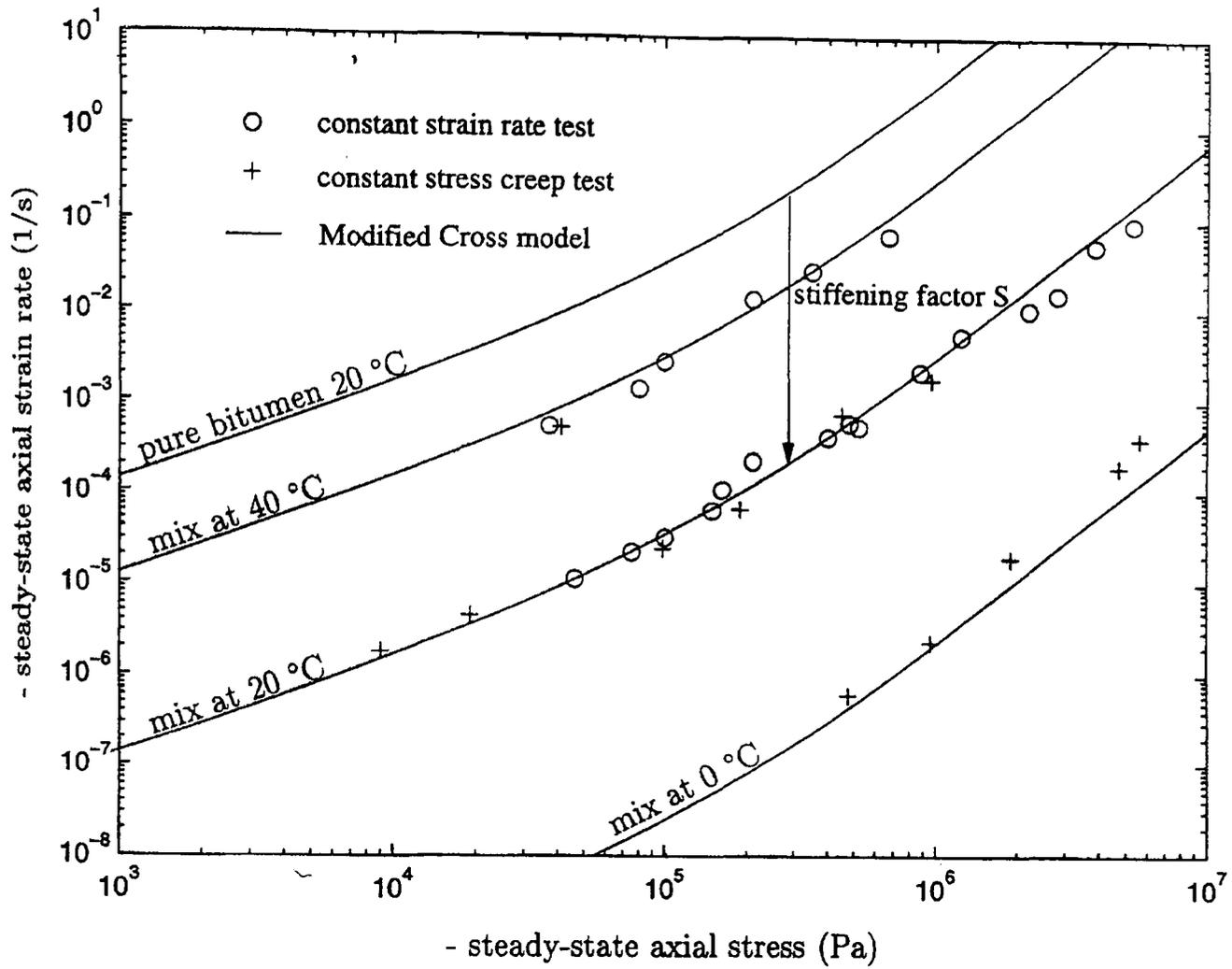
Figure 2.5: Deformation map of idealised mixture A, after Deshpande [40].
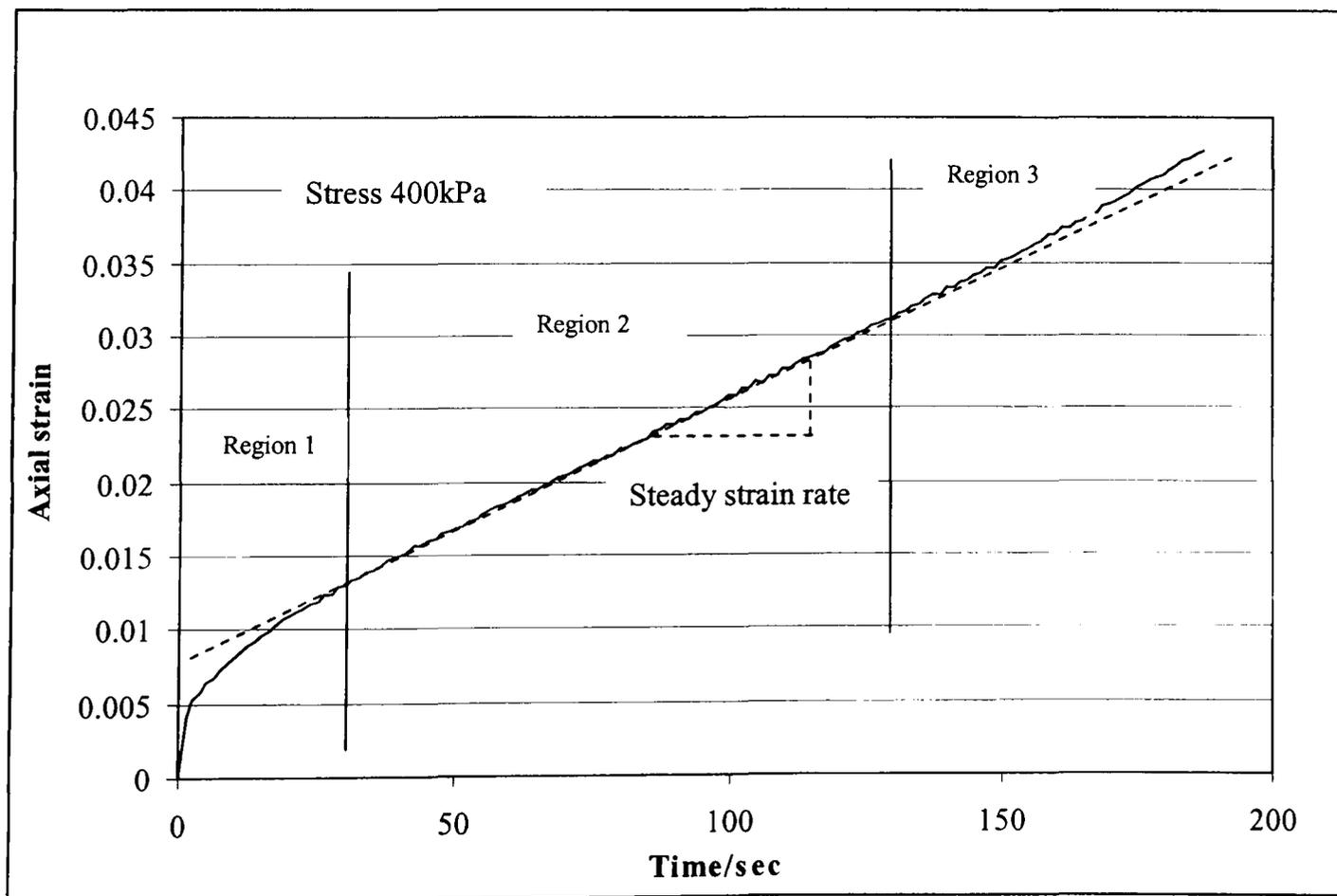
Figure 2.6: Creep test result of mixture A at 20°C, after Khanzada [65].
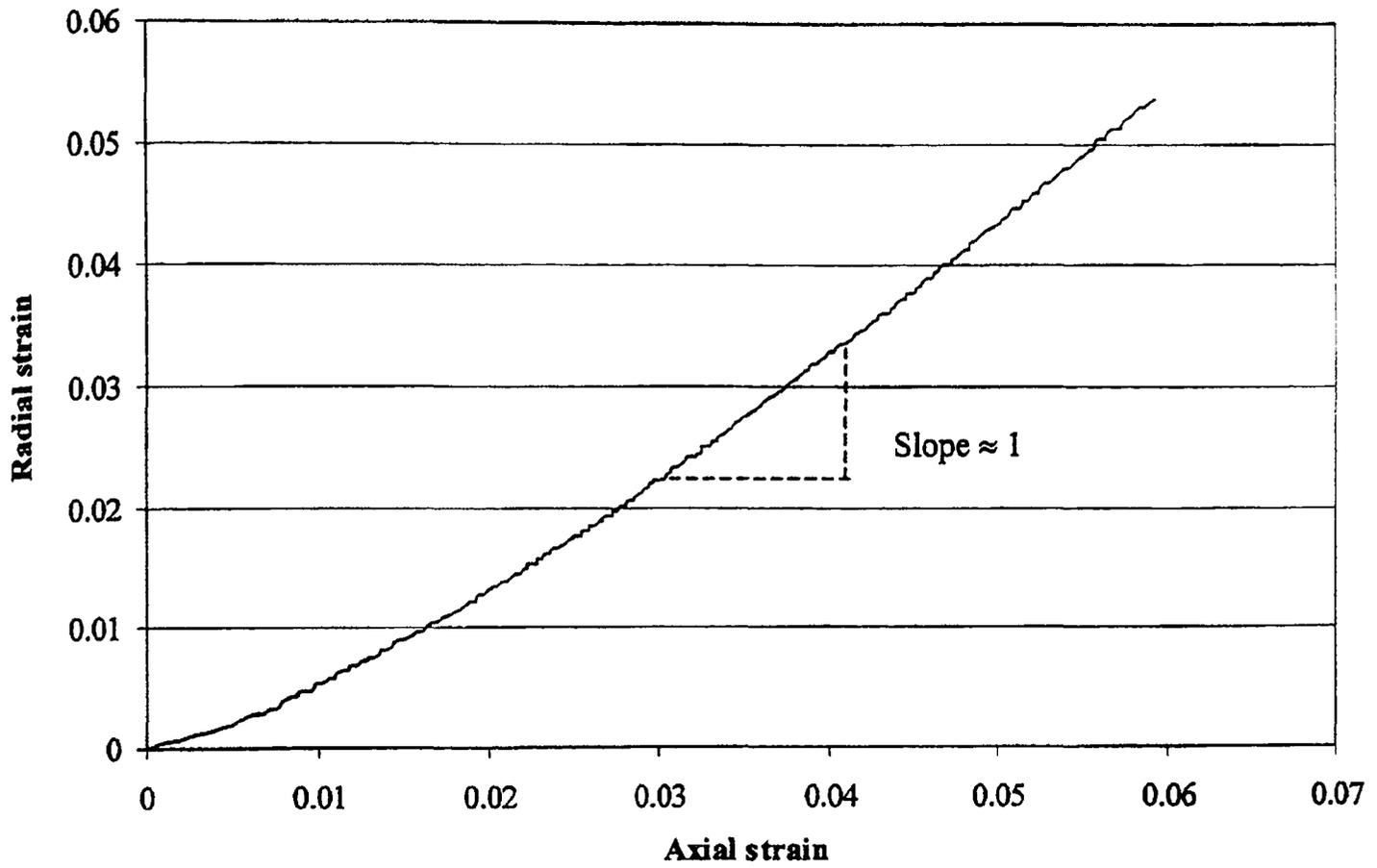
Figure 2.7: Radial strain versus axial strain for creep test at 20°C (mixture A), after Khanzada [65].
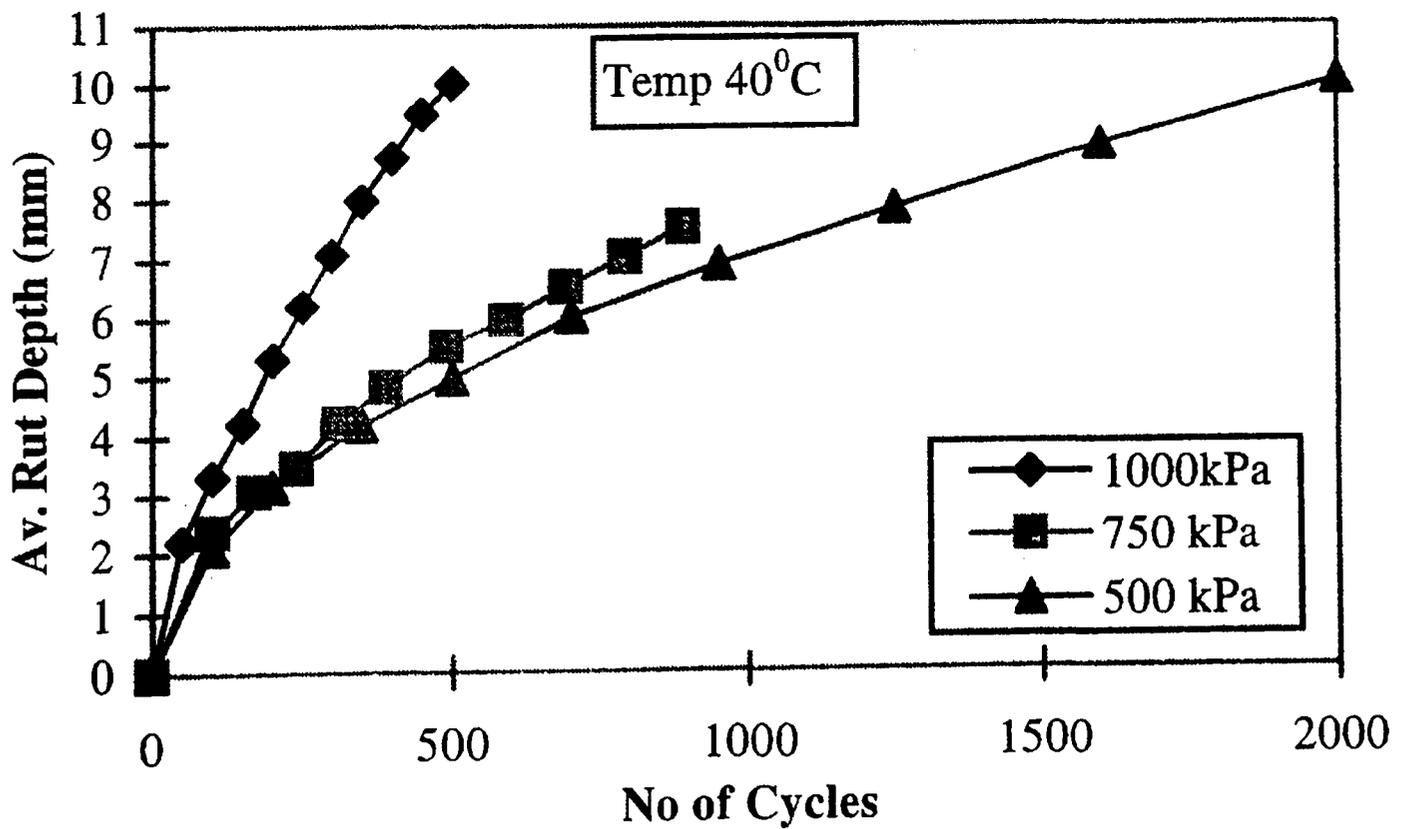
Figure 2.8: Wheel tracking test results for mixture A/D at 20°C, after Collop [26].
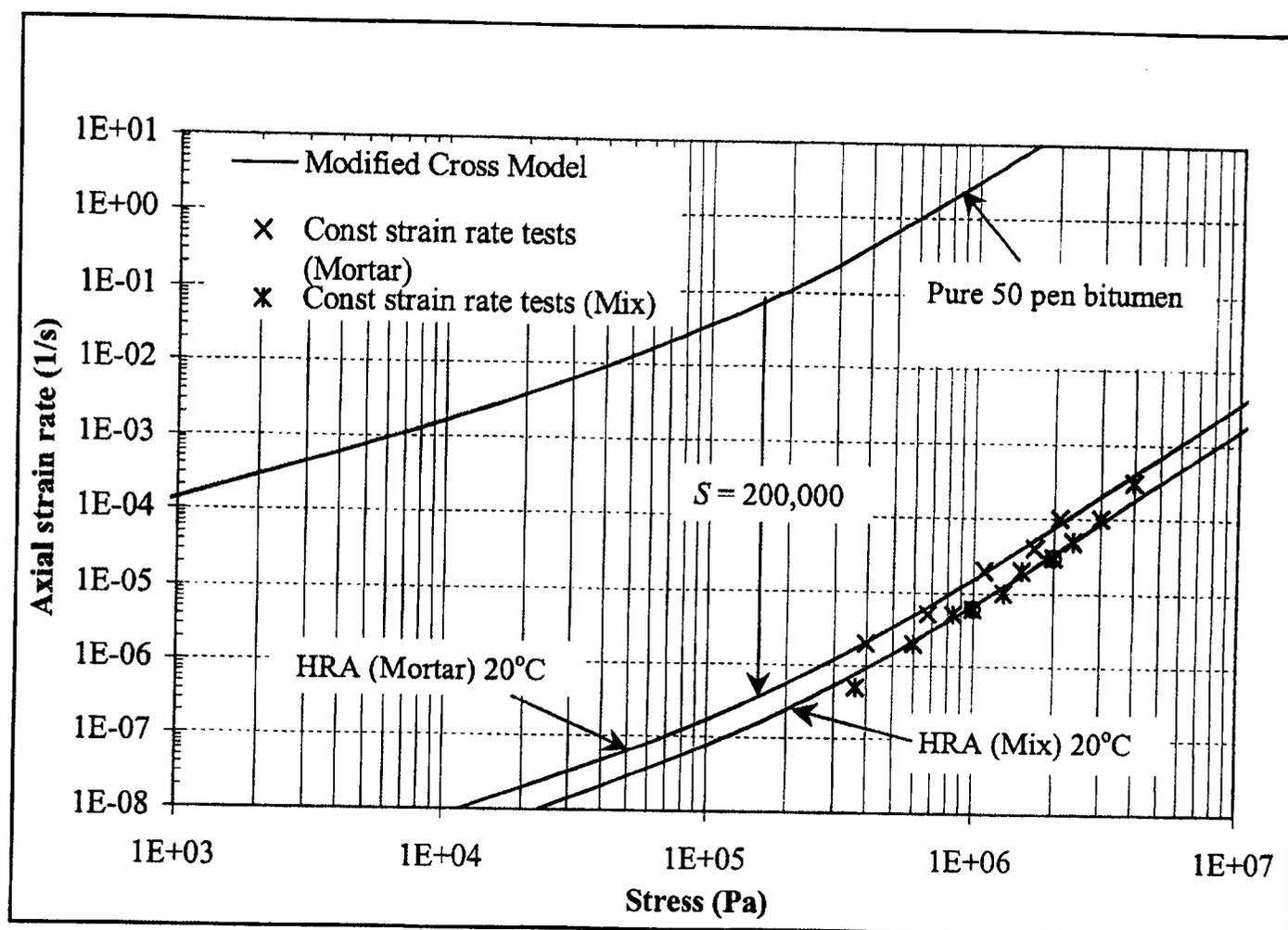
Figure 2.9: Steady state deformation behaviour of HRA mortar and mixture at 20°C, after Khanzada [65].
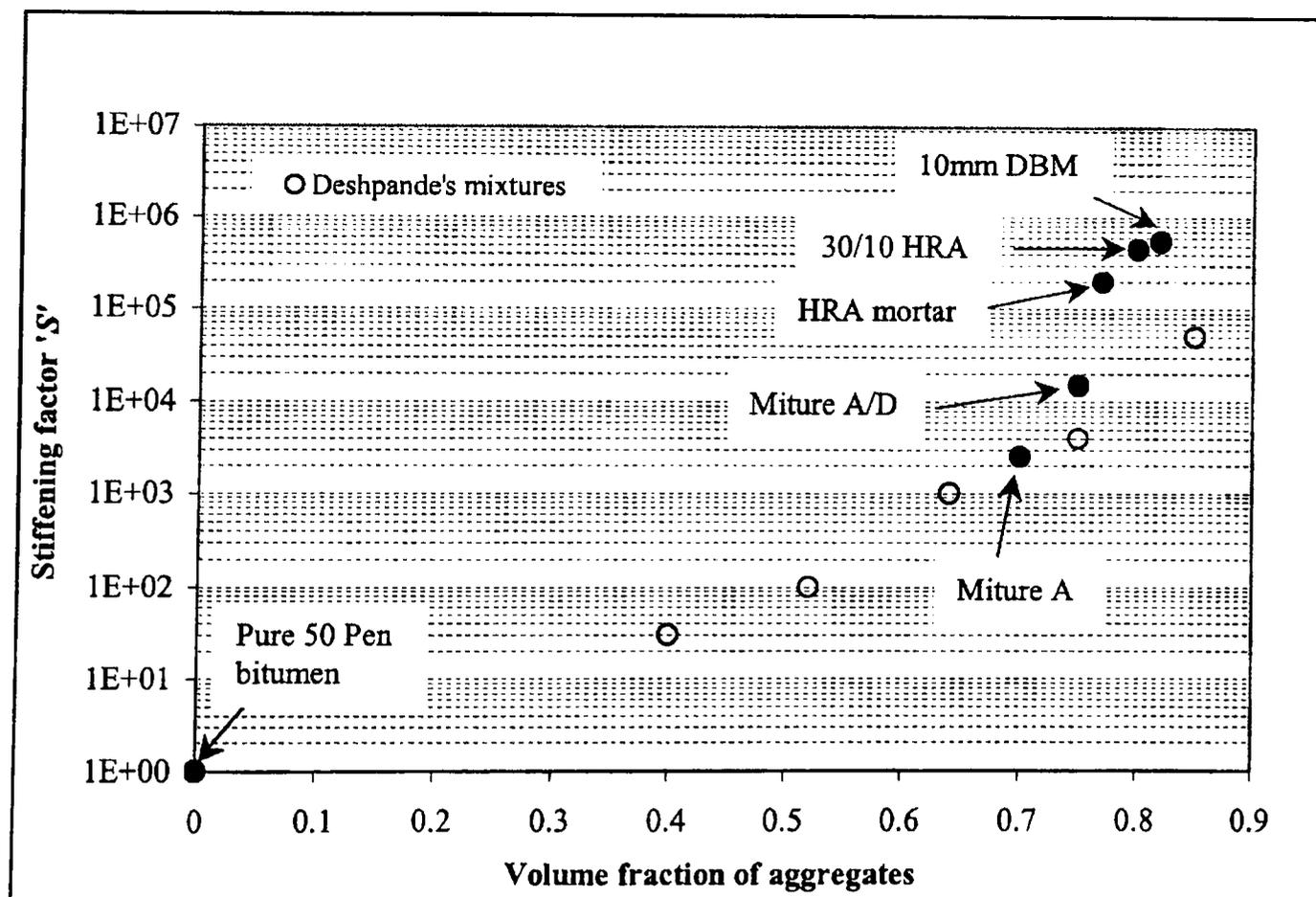
Figure 2.10: Variation of stiffening factor (*S*) with volume fraction of aggregate, after Khanzada [65].
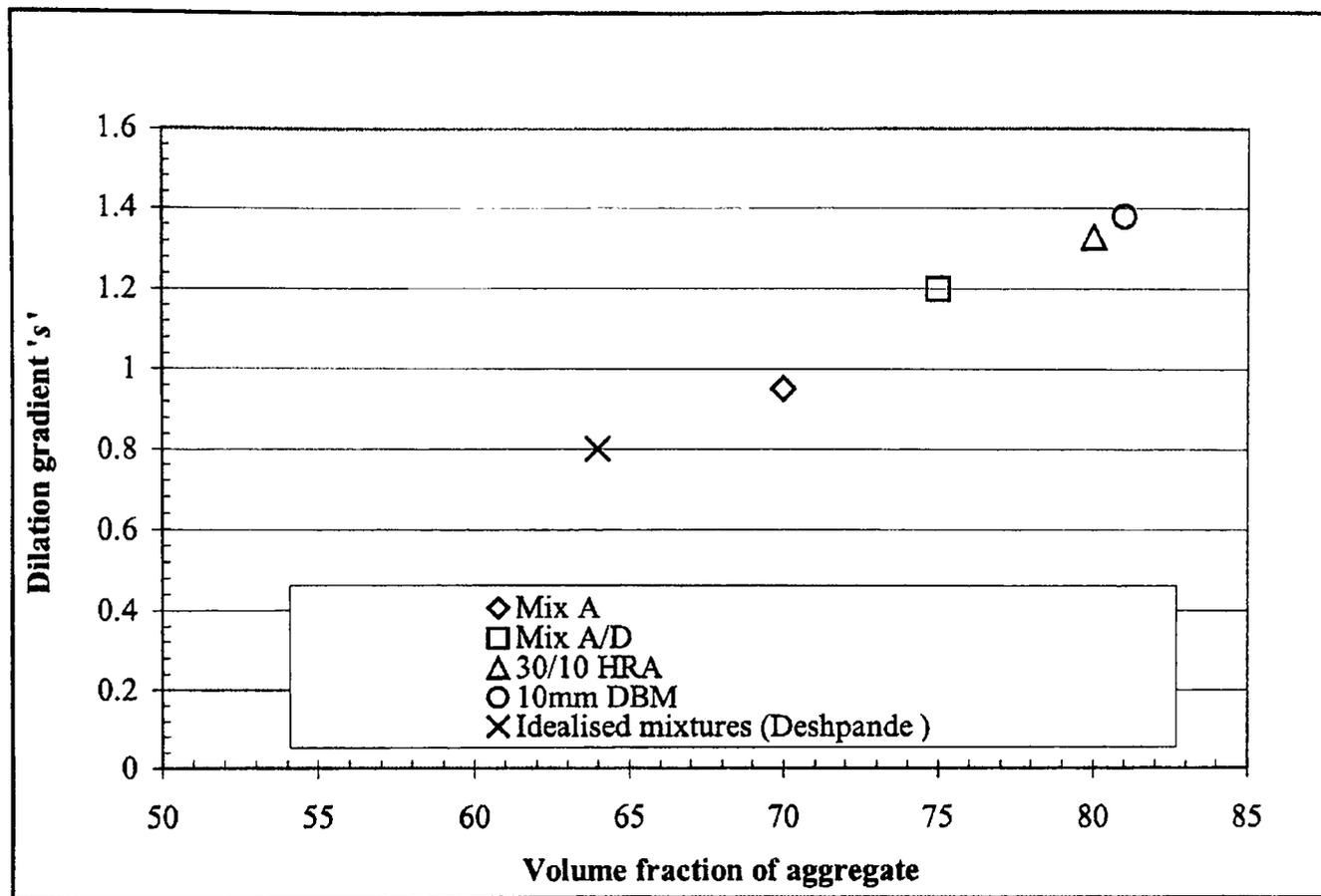
Figure 2.11: Variation of dilation gradient with volume fraction of aggregate, after Khanzada [65].
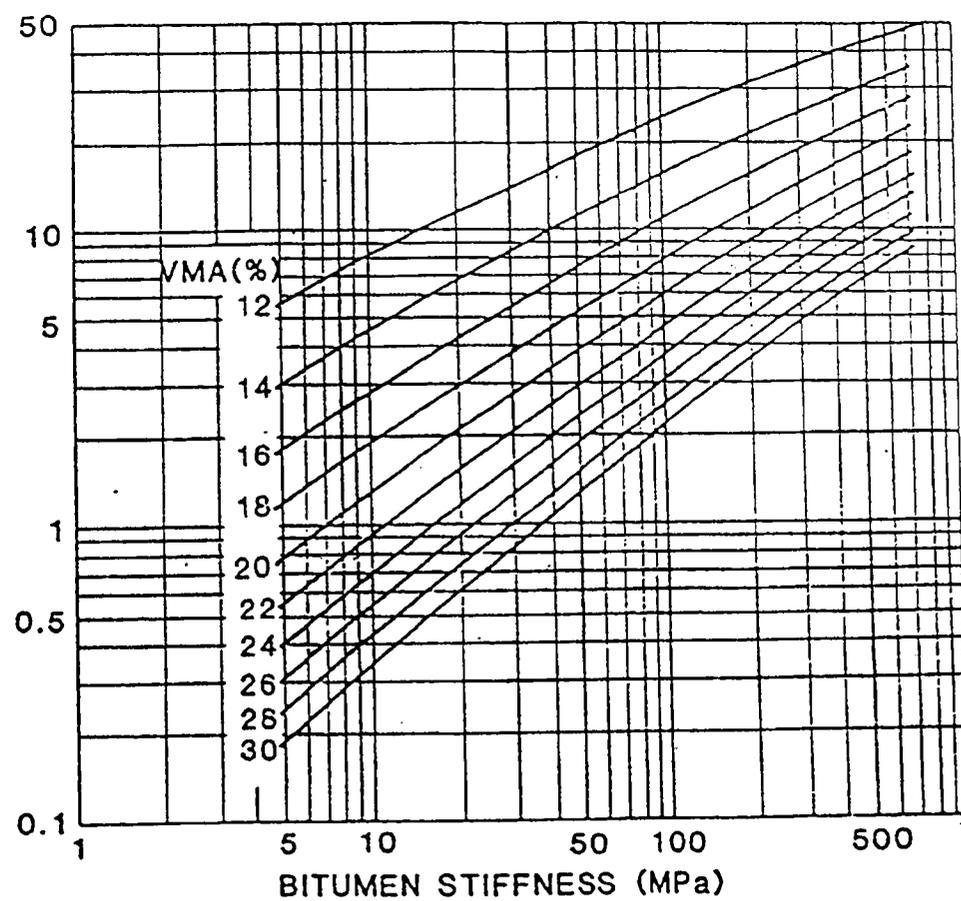
Figure 2.12: Nottingham nomograph for the prediction of mix stiffness, after Brown [18].
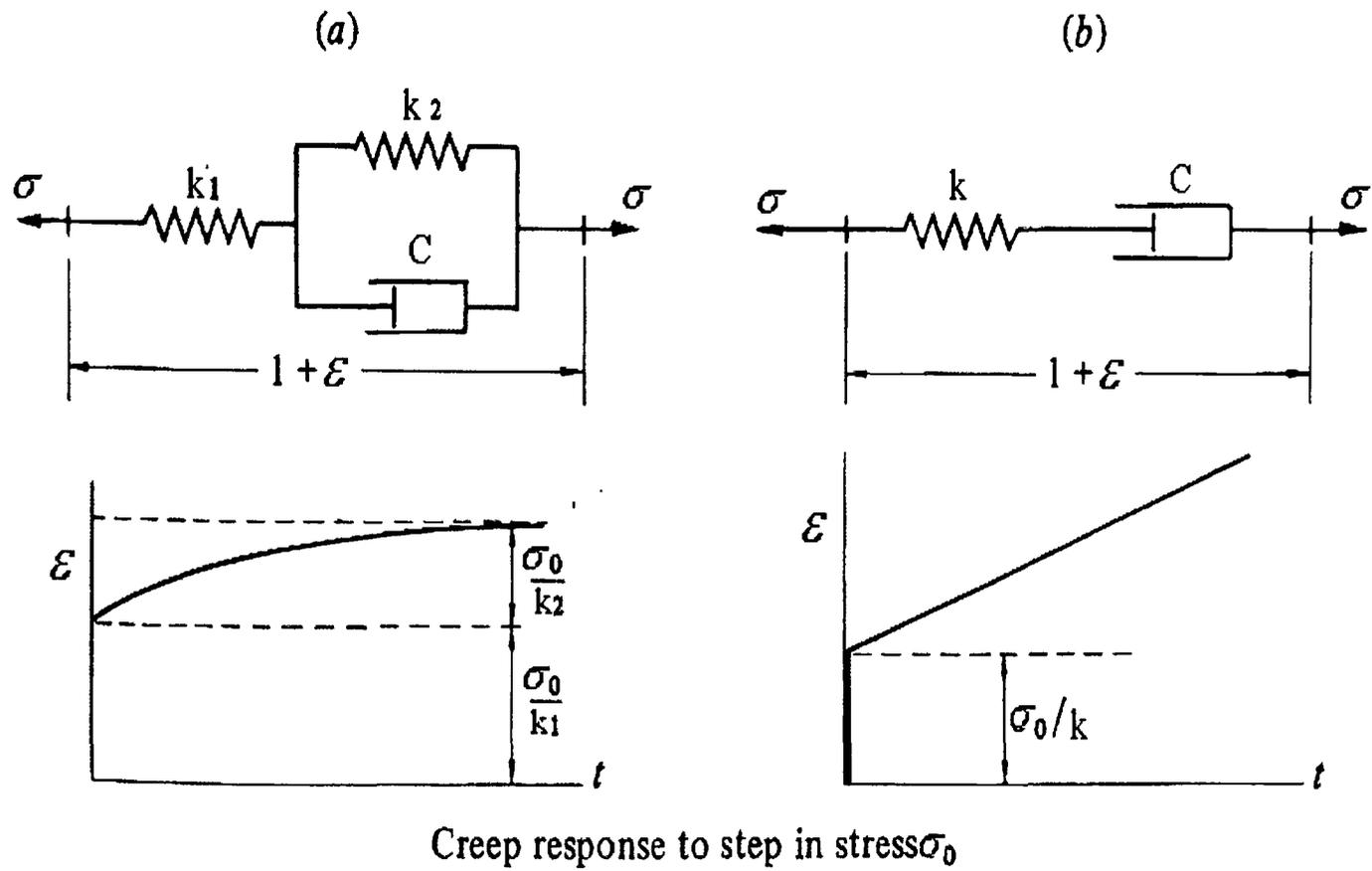
Figure 2.13: Simple viscoelastic materials which display (a) delayed elasticity, (b) steady creep (Maxwell), after Johnson [62].
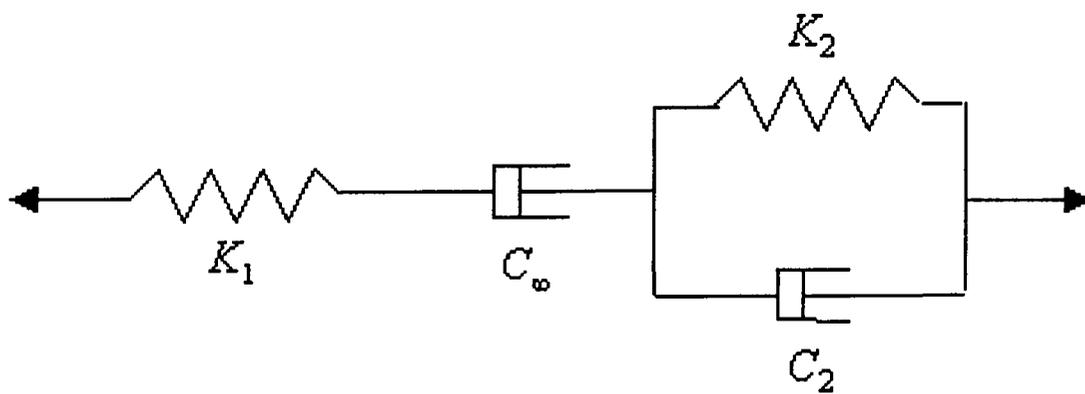
Figure 2.14: Burger's Model.
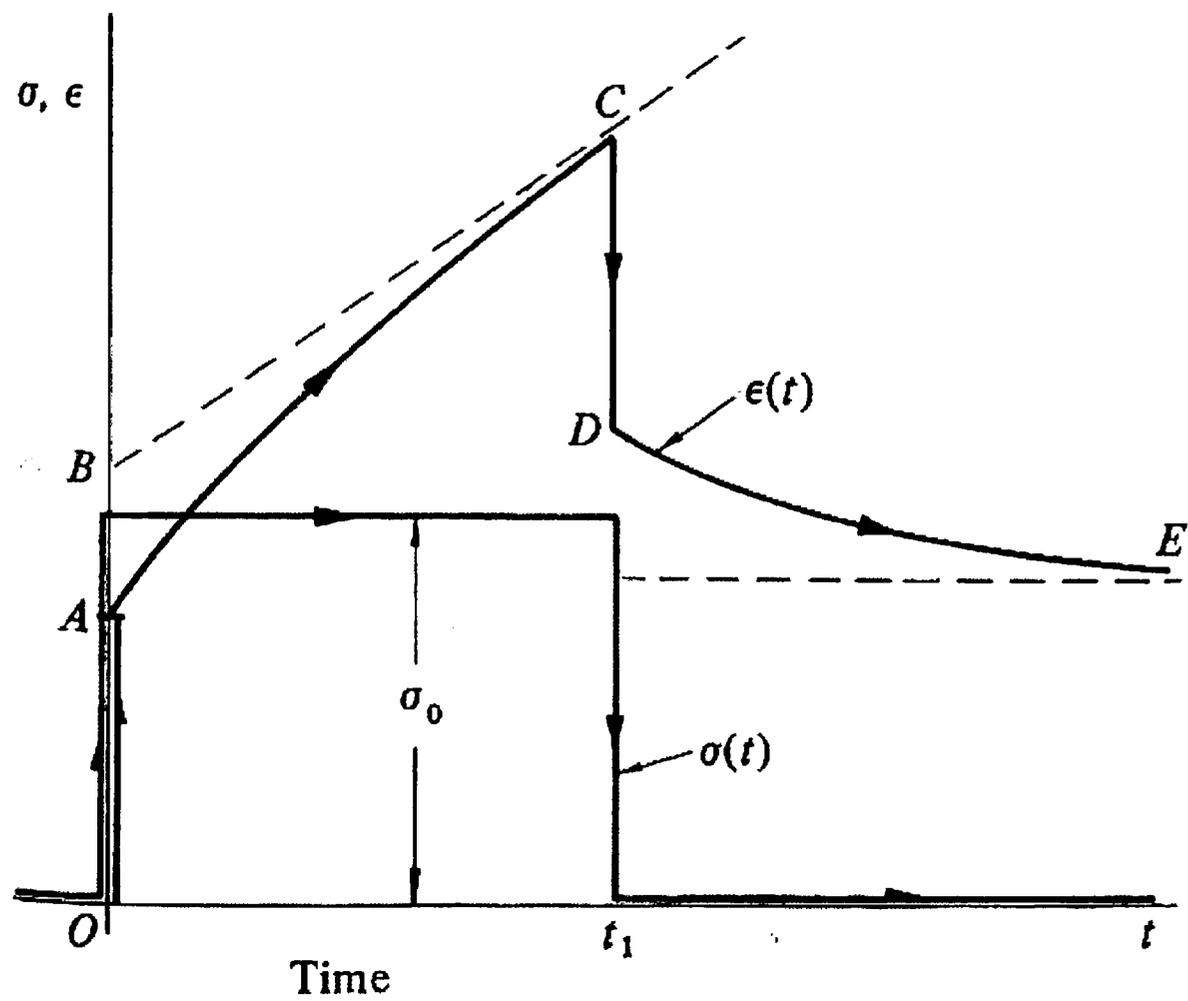
Figure 2.15: Viscoelastic response of stress and strain, after Johnson [62].
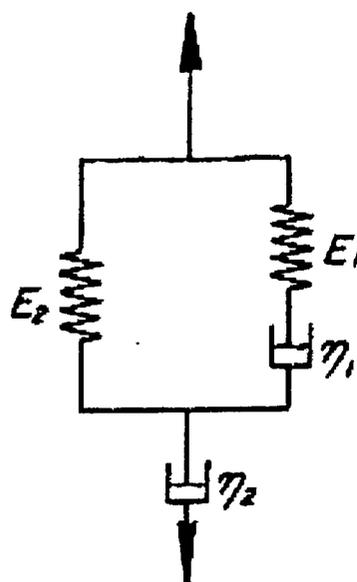
Figure 2.16: Four-element Model, after Monismith [78].
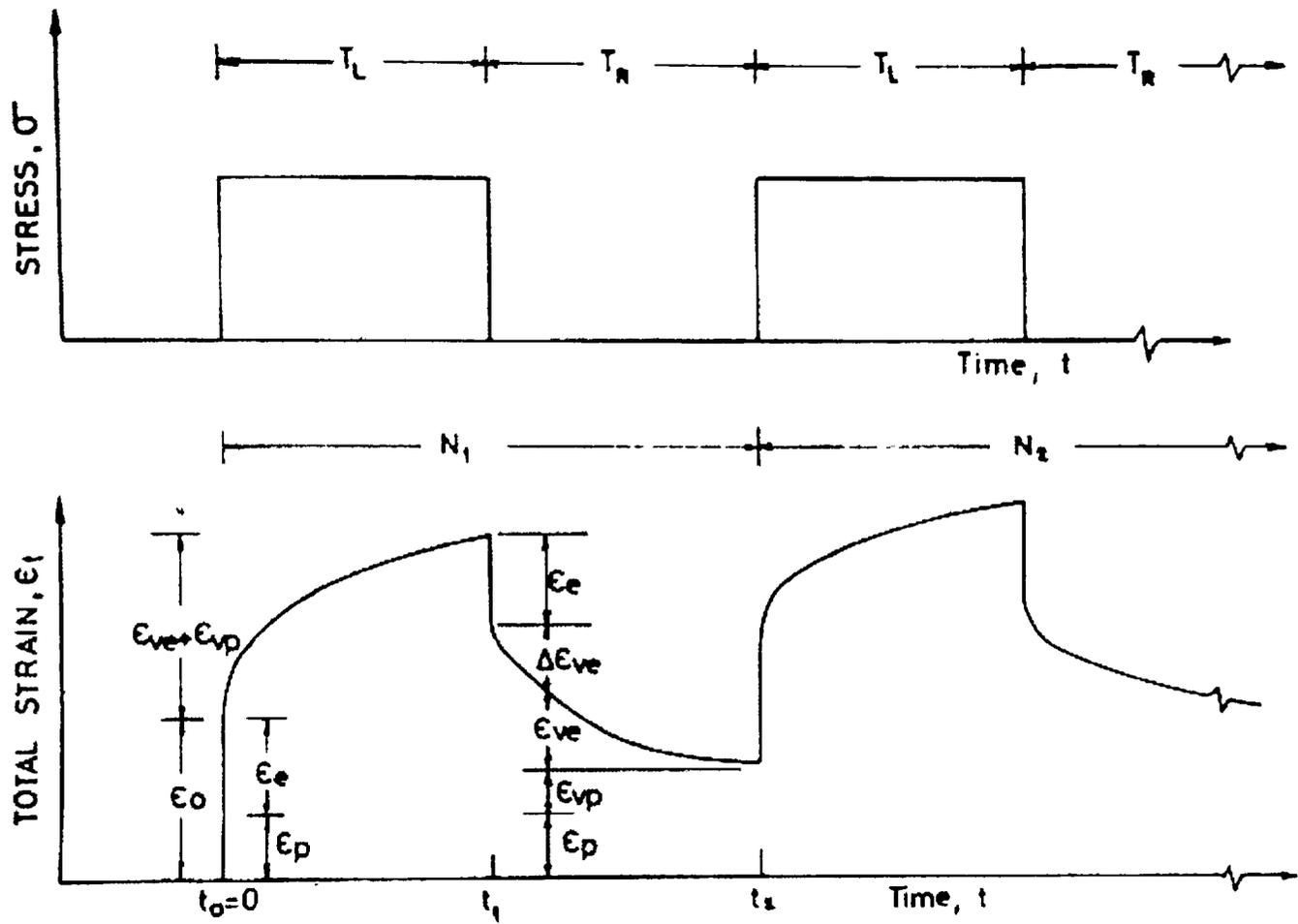
Figure 2.17: Schematic representation of strain components, after Perl [86].
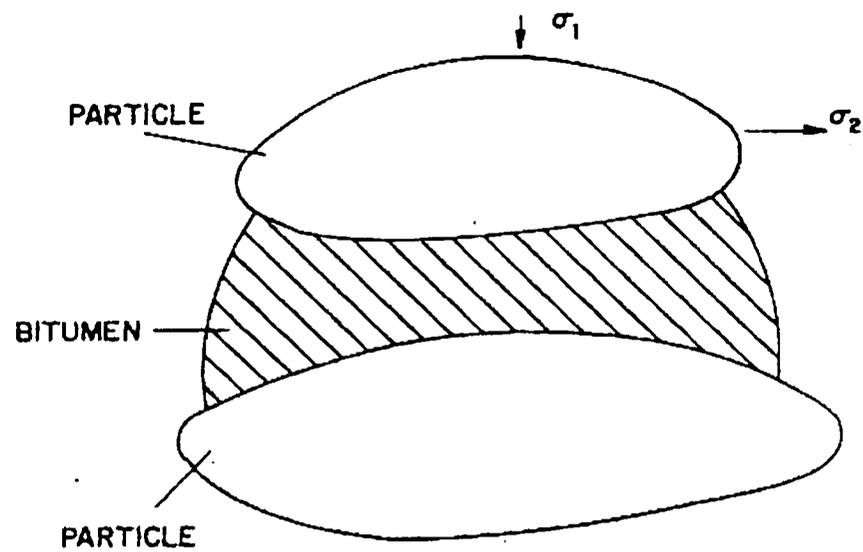
Figure 2.18: Two particles separated by a film of bitumen, after Hill [117].

(a) Typical Asphalt Material   (b) Model Asphalt System

(c) Network Finite Element Model   (d) ABAQUS Finite Element Model
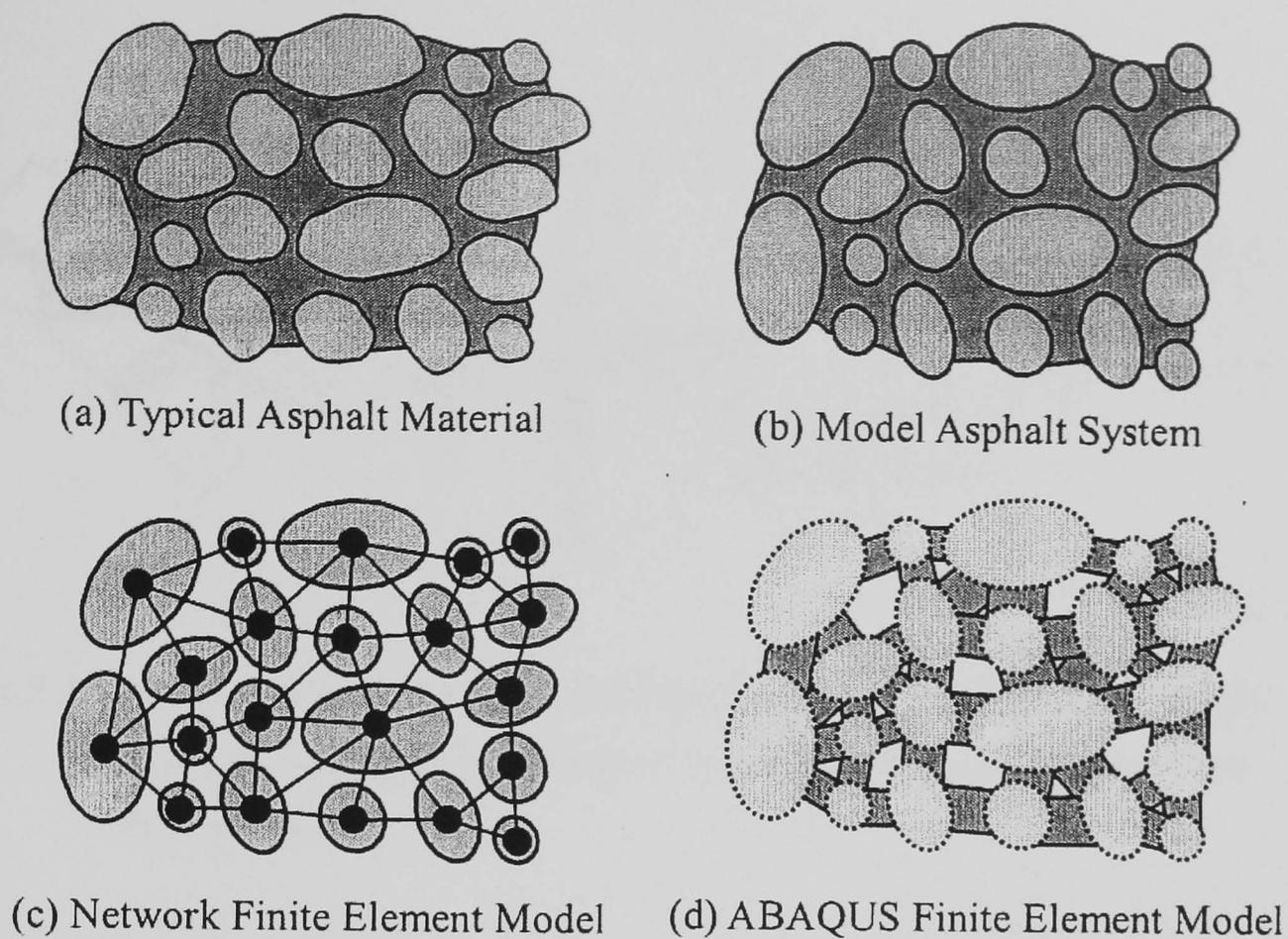
Figure 2.19: Asphalt modelling concept, after Sadd [71].
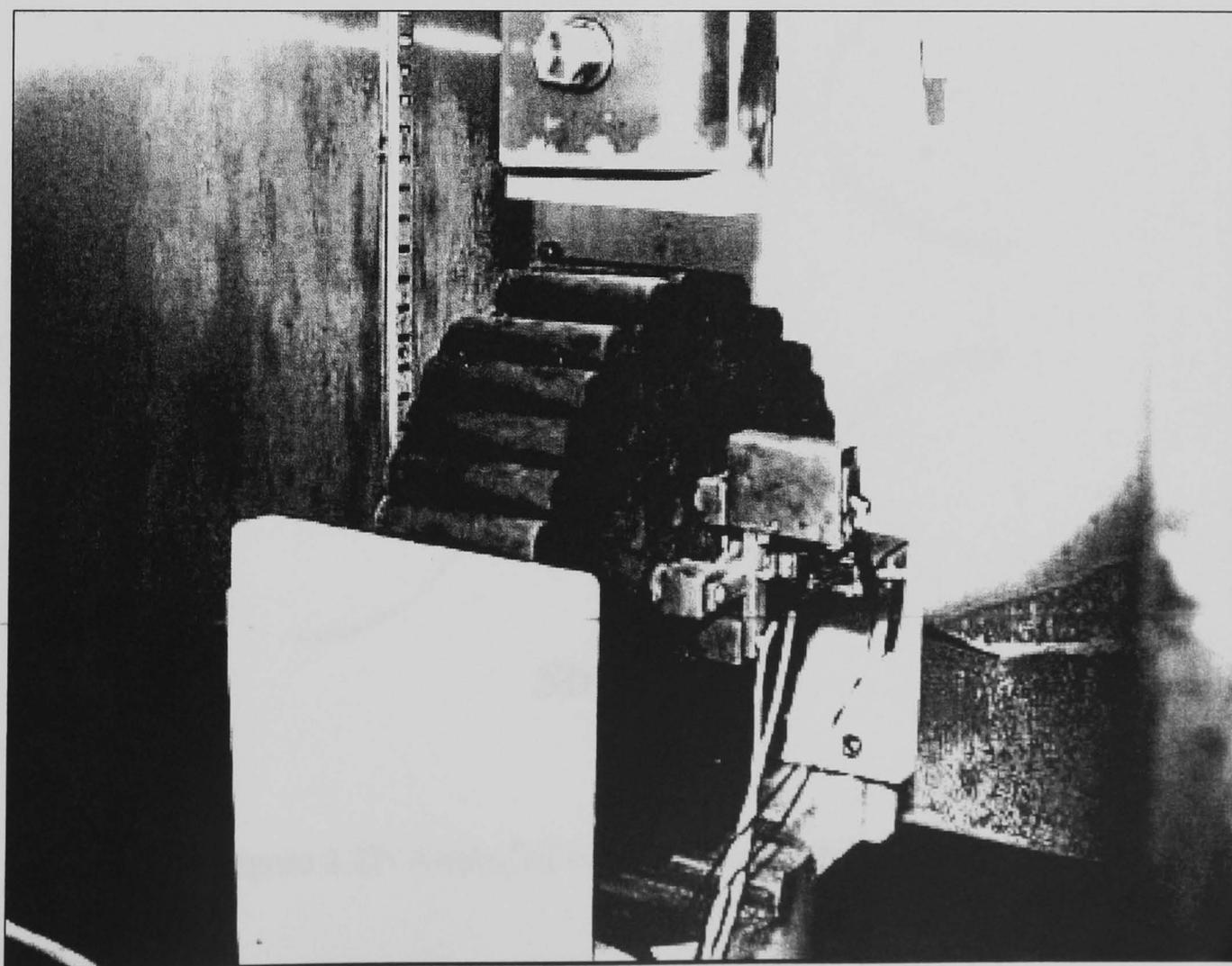
Figure 2.20: Testing of synthetic specimen using IDT, after Buttlar [20].
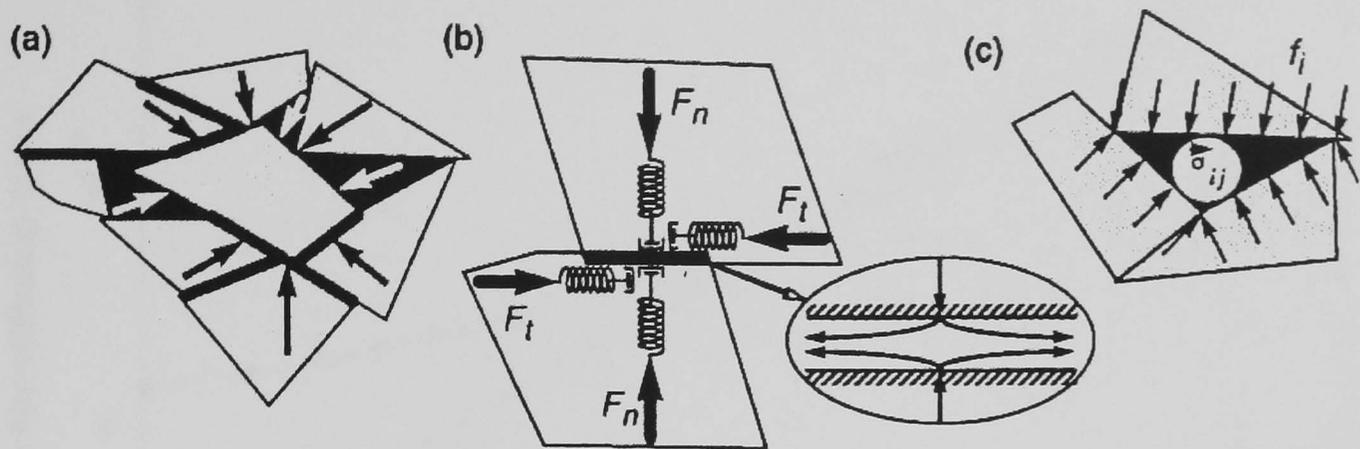
Figure 2.21: Forces acting on aggregate and binder. (a) forces acting on particles (b) aggregate-aggregate interaction. (c) aggregate-binder interaction, after Rothenburg [95].
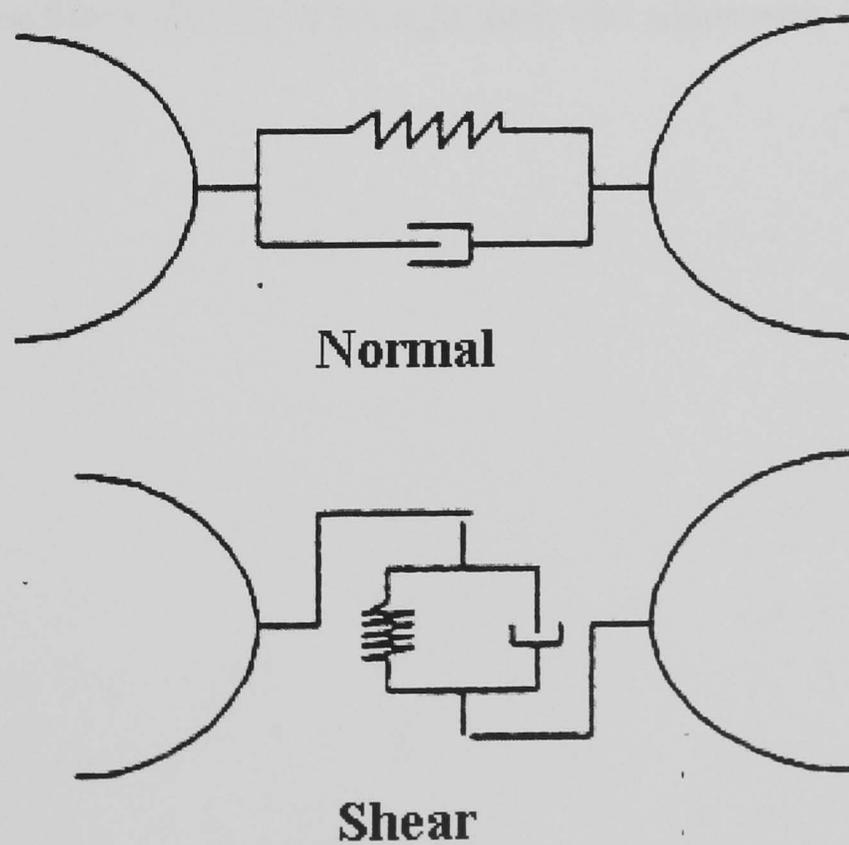
Figure 2.22: Analog of viscoelasticity, after Chang [21]
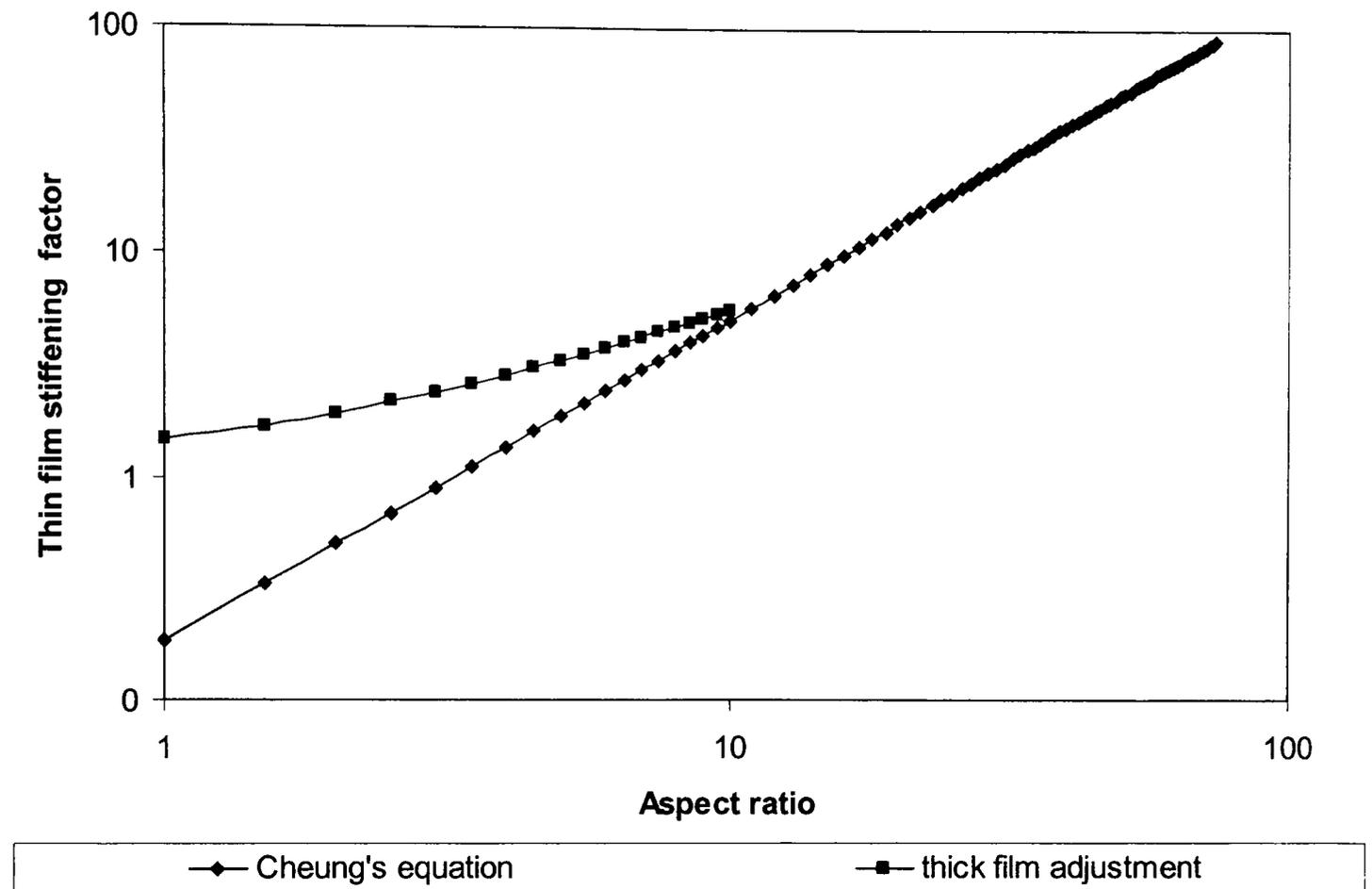
Figure 2.23: Thin film stiffening factor with think film adjustment, after Harvey [49].

3 | *Introduction to Discrete Element Modelling*

3.1 Introduction

The previous chapter reviewed different types of continuum and micromechanical models for the asphalt. It was concluded that DEM represents a promising method for modelling asphalt at the particle scale although previous research has focussed on 2-dimensional behaviour. This chapter describes DEM in more detail.

The Discrete Element Method (DEM) was first introduced by Cundall [31] for the analysis of rock mechanics problems. A thorough description of DEM can be found in Cundall and Hart [33, 35, 48]. DEM is a numerical procedure capable of describing the mechanical behaviour of assemblies of discs and spheres. It is implemented in a computer program that allows finite displacement and rotation of discrete bodies including complete detachment, and recognises new contacts automatically as the calculation progresses. This method refers to the particular discrete element scheme that uses deformable contacts and explicit, time-domain solution of the equations of motion. The simulation of non-linear particle interaction can be performed without excessive memory requirements or the need for an interactive procedure. By tracing the movements of the individual particles, contact forces and displacement of a stressed assembly of particles can be determined. These movements are caused by the propagation of disturbance from wall and particle motion throughout the particle system.

Dynamic behaviour in DEM is represented by the timestep algorithm where velocities and accelerations are assumed to be constant in each timestep. The timestep is chosen to be so small that disturbance can only propagate to its immediate neighbours during a single timestep. Then, at all times, the forces acting on any particle are determined exclusively by its interaction with the particles with which it is in contact. The calculations performed in DEM alternate between application of Newton's second law and the force-displacement law. The calculation cycle is described in Section 3.3.1.

3.2 Development and Application of DEM

The Discrete Element Method has been widely applied in soil and rock mechanics. In the early 70's, Cundall [31] introduced a computer program to model the progressive failure of a discrete block system where interaction between blocks is governed by friction and stiffness. There is no limit to the amount of displacement or rotation in each block and any block is permitted to touch any other block. In his paper [31], the basic DEM theory such as force displacement law, law of motion and calculation cycle are introduced.

In the late 70's, Cundall and Strack [37] developed a computer program, BALL in two dimensions by incorporating the DEM theory as described in [31]. BALL was used to model granular assemblies comprised of distinct particles that displace independently from one another and interact only at contact points. The effects of damping and speed of loading were included in this model. This model was then validated by comparing force vector plots with the corresponding plots obtained from the photoelastic analysis undertaken by de Josselin de Jong and Verruijt [38]; good agreement was found. The program BALL was further developed by Cundall and Strack [36] to model the behaviour of assemblies of discs under loading and unloading. 100 and 1000 disc tests were performed with computer interactive graphics to study the internal mechanism within a granular mass and the response to stress probes. The 100-disc test is shown in Figure 3.1. As a result, Cundall and Strack concluded that the DEM and BALL were valid tools for research into the behaviour of granular assemblies. In the early 80's, Cundall, Drescher and Strack

[34] further improved BALL by introducing methodologies for measurements of granular assemblies in simulation. Various forms of boundary conditions and definitions of average stresses and strains were described. A catalogue of observed mechanisms such as force chains, spins and locked-in-forces were presented. However, the program BALL was limited to model the behaviour of granular assemblies in two dimensions.

In the late 80's, Cundall developed a DEM program called TRUBAL [32] to simulate three dimensional assemblies. TRUBAL was used to generate a dense random packed assembly of spheres to the desired porosity. A numerical "servo-control" algorithm was introduced to bring the sample to equilibrium under the desired isotropic stress. Biaxial tests were performed and the numerical results agreed with physical results described by Ishibashi and Chen [59], except for the volume strain observed in triaxial extension tests. Cundall suggested that this discrepancy might indicate the presence of an initial fabric in the physical sample. However, this work extended DEM into three dimensional modelling.

Thornton et al. [109] described a modified version of TRUBAL which they called GRANULE. This program is capable of modelling the fracture of an agglomerate of spherical balls bonded together. In their model, they attributed a surface energy to the balls in the agglomerates so that tensile forces between balls are auto-adhesive. The general methodology is described in Thornton et al. [111] and the theoretical basis of the algorithms can be found in Thornton and Yin [110].

The first version of Particle Flow Code in Three Dimensions (PFC3D) for DEM simulations was released in 1995 by Itasca Consulting Group Inc. [1-4]. Hazzard et al. [51] used PFC to analyse crack nucleation and propagation in brittle rock. Their paper outlines how the mechanical behaviour of different rock types can be reproduced by considering the micromechanical structure of different rocks. The cracking of rock models is examined and they concluded that the cracking pattern in their granite model agreed with the laboratory result.

McDowell and Harireche [72] used PFC3D to model the fracture of soil grains. They modelled a soil particle as an agglomerate of balls bonded together with

contact bonds. Realistic particle parameters were used and gravity was applied to stabilise the agglomerate prior to loading in order to replicate a real soil particle crushing experiment. They demonstrated the possibility of obtaining the correct size effect on strength. McDowell and Harireche [73] further used PFC3D to model one dimensional normal compression of a sand. Each sand particle is modelled as an agglomerate of balls bonded together as shown in Figure 3.2. Oedometer tests were performed on small and large agglomerates and the yield stress found to be reduced by increasing the agglomerate size. The yield stress predicted by the model is lower than the experimental results probably due to the different shape of the agglomerate compared to real sand. As a result, they concluded that DEM with PFC3D is a powerful tool in modelling the behaviour of crushable soils and it is capable of providing a micromechanical insight into soil behaviour.

Powrie et al. [89] demonstrated the ability of DEM using PFC3D to capture the essential macro-features of soil behaviour as observed from laboratory tests. Each soil particle was modelled as two spheres bonded together with a high strength bond so that each pair of spheres behaves as a single rigid particle, as shown in Figure 3.3. A sample, as shown in Figure 3.4, was prepared for biaxial simulations. The effects of loading platen friction, initial sample porosity and inter-particle friction angle were investigated. The peak effective angle of friction and volumetric dilation of the sample were found to be increased with the particle shape factor (defined as (R+ r)/R in Figure 3.3). They concluded that a numerical sample with 10,000 particles comprising pairs of bonded spheres of shape factor 1.5 and inter-particle friction angle of 26° have demonstrated the ability to model the behaviour of soil as observed in the laboratory. More details can be found from Ni [80].

Dolezalova et al. [42] used PFC3D to model medium dense Zbraslav sand. They calibrated the micro properties of a synthetic sand model to match the macro scale response of the physical sand. The comparison between the sand model and the laboratory result is shown in Figure 3.5. They showed that the predicted influence of stress path direction changes on the deformational response of synthetic sand was in good agreement with the laboratory test results. Furthermore, PFC3D has been used by many researches in a wide range of applications. For example, Wanne [121] modelled compressive strength testing of anisotropic hard rock, Konietzky et al. [66]

modelled cyclic fatigue under tension and Zhou and Chi [125] performed shear band simulations on synthetic sand based on the biaxial simulation.

Although DEM has been applied to model the behaviour of soils and granular materials, it has not been widely used to investigate the mechanical behaviour of asphalt materials. It can be concluded that PFC3D is the best developed tool available for DEM; hence it will be used in this research for modelling the deformation behaviour of idealised asphalt material. A more detailed description of PFC3D follows.

3.3 Particle Flow Code in Three Dimensions (PFC3D)

PFC3D has been developed by ITASCA Consulting Group Inc. to model the movement and interaction of stresses in assemblies of rigid spherical particles using DEM. It is classified as a Discrete Element Code by Cundall and Hart [35] since it allows finite displacements and rotations of discrete bodies, including complete detachment and recognises new contacts automatically as calculation progresses.

The PFC3D particle flow model simulates the mechanical behaviour of a system comprising of a collection of particles. A particle denotes a body that occupies a finite amount of space. In this model, distinct particles displace independently of one another and interact only at contacts between them. The particles are assumed to be rigid but can deform locally at contact points using a soft contact approach, in which finite normal and shear stiffnesses are taken to represent measurable contact stiffnesses. The contact force between two contacting particles is calculated based on the overlapping magnitude and the contact stiffnesses of two contacting particles at the contact. The PFC3D model refers to spherical particles as 'balls' and boundaries as 'walls'. Walls allow confinement and compaction by applying a boundary velocity. The balls and walls interact with each other via the contact forces between them.

Softening behaviour of a bonded material can be modelled by introducing bonds at the contact points such that, the bond is broken when inter-particle forces at any contact exceed the specified bond strength. This allows tensile forces to be

developed between particles and enables the formation of micro-cracks in the system to be modelled. Bonded assemblies exhibit complex macroscopic behaviour such as strain softening, dilation, and fracture. PFC3D can be applied to the analysis of solids subjected to prescribed boundary and initial conditions. Continuum behaviour can be modelled by treating a solid as an assembly of many small particles and stresses and strains can be measured by averaging their quantities over a representative measurement volume in such a system.

3.3.1 Basic Calculation Procedure

The PFC3D calculation cycle is shown in Figure 3.6. It is based around a timestepping algorithm that requires the repeated application of the law of motion to each particle, a force-displacement law to each contact, and a constant updating of wall positions. The contacts (ball to ball and ball to wall) are traced during the simulation and they can be formed or removed automatically. At the start of the timestep, a set of contacts is updated from known particle and wall positions. The force-displacement law is then applied to update contact forces based on the relative motions between two particles in contact via a contact constitutive law. Next, the law of motion is applied to update the velocity and position at each particle based on the resulting force and moment arising from contact and body forces acting on the particle. Wall positions are also updated based on specified wall velocity. The force-displacement law and the law of motion are described in the following sub-sections.

Force-Displacement Law

The force-displacement law is described for both ball to ball and ball to wall contacts. This law is applied at the start of each cycle to contacts to obtain new contact force. The contact forces vector F_i is resolved into normal and shear components with respect to the contact plane:

$$F_i = F_i^n + F_i^s \qquad (3.1)$$

where F_i^n and F_i^s denote normal and shear component vectors respectively. The normal contact force vector is given by:

$$F_i^n = K^n U^n n_i \tag{3.2}$$

where K^n is the normal stiffness at contact, U^n is the overlapping magnitude of two contacting entities and n_i is the unit normal vector. For ball-to-ball contact, the normal vector is directed along the line between ball centres. For ball-to-wall contact, the normal vector is directed along the line defining the shortest distance between the ball centre and the wall.

It should be noted that the normal stiffness is a secant modulus which relates total displacement and force, whilst the shear stiffness is a tangent stiffness which relates incremental displacement and force. When the contact is formed, the total shear force is initialised to zero. Each subsequent relative shear displacement will cause an incremental shear force to be developed and added to its current value. The incremental shear force is calculated using:

$$\Delta F_i^s = -K^s V_i^s \Delta t \tag{3.3}$$

where K_s is the shear contact stiffness, V_i^s is the shear component of contact velocity and Δt is the timestep. The new shear force is then calculated by summing the shear force vector existing at start of timestep with the incremental shear force vector.

$$F_i^s = \left\{ F_i^s \right\}^{current} + \Delta F_i^s \tag{3.4}$$

The current shear force $\left\{ F_i^s \right\}^{current}$ is updated in each timestep by taking account of the motion of contact. These updated contact forces (and moment) will be used in the following timestep to calculate the acceleration using Newton's second law and then integrated to give velocity and displacement and hence the updated position. This is described in the law of motion in the next sub-section.

Law of Motion

The motion of a rigid particle is determined by the resultant force and moment vectors acting upon it. The Equations of motion are expressed as two vector quantities, one relates the resultant force to translational motion and the other relates the resultant moment to rotational motion of the particle. The equation for translational motion is written in vector form as:

$$F_i = m(\ddot{x}_i - g_i) \tag{3.5}$$

where F_i is the sum of all externally applied forces acting on the particle, m is the total mass of the particle, $\ddot{x}_i$ is the acceleration of particle and g_i is the body force acceleration vector (e.g., gravity loading).

The equation for rotational motion is written in the vector form as:

$$M_i = I\dot{\omega}_i = \left(\frac{2}{5} mR^2 \right) \dot{\omega}_i \tag{3.6}$$

where M_i is the resultant moment acting on particle, I is the moment of inertia of a particle, $\dot{\omega}_i$ is the angular acceleration of a particle and R is the radius of a spherical particle whose mass is distributed uniformly throughout its volume.

The equations of motion, given by Equation (3.5) and (3.6) are integrated using a centred finite difference procedure involving a timestep Δt. The quantities $\dot{x}_i$ and ω_i are computed at the mid-intervals of $t \pm \Delta t/2$, while the quantities $x_i, \ddot{x}_i, \dot{\omega}_i$, F_i, and M_i are computed at the primary intervals of $t \pm \Delta t$. The translational and rotational accelerations at time t are calculated as:

$$\ddot{x}_i^{(t)} = \frac{1}{\Delta t}\left(\dot{x}_i^{(t+\Delta t/2)} - \dot{x}_i^{(t-\Delta t/2)}\right)$$

$$\dot{\omega}_i^{(t)} = \frac{1}{\Delta t}\left(\omega_i^{(t+\Delta t/2)} - \omega_i^{(t-\Delta t/2)}\right) \tag{3.7}$$

The translational and rotational velocities at time $t+\Delta t/2$ can be solved by substituting Equation (3.7) into Equations (3.5) and (3.6) giving:

$$\dot{x}_i^{(t+\Delta t/2)} = \dot{x}_i^{(t-\Delta t/2)} + \left(\frac{F_i^{(t)}}{m} + g_i\right)\Delta t$$

$$\omega_i^{(t+\Delta t/2)} = \omega_i^{(t-\Delta t/2)} + \left(\frac{M_i^{(t)}}{I}\right)\Delta t \tag{3.8}$$

Finally, the position of the particle centre is updated by integrating velocities in Equation (3.8) giving:

$$x_i^{(t+\Delta t)} = x_i^{(t)} + \dot{x}_i^{(t+\Delta t/2)}\Delta t \tag{3.9}$$

In conclusion, given the values of $\dot{x}_i^{(t-\Delta t/2)}$, $\omega_i^{(t-\Delta t/2)}$, $x_i^{(t)}$, $F_i^{(t)}$ and $M_i^{(t)}$, Equation (3.8) is used to obtain $\dot{x}_i^{(t+\Delta t/2)}$, $\omega_i^{(t+\Delta t/2)}$. Then, Equation (3.9) is used to obtain $x_i^{(t+\Delta t)}$. The values of $F_i^{(t+\Delta t)}$ and $M_i^{(t+\Delta t)}$, to be used in the next cycle, are obtained by application of the Force-displacement law.

3.3.2 Mechanical Timestep

The PFC3D timestepping algorithm assumes that velocities and accelerations are constant within each timestep. Therefore, the timestep chosen in the PFC3D calculation cycle must be small enough so that the disturbance cannot propagate from any particle further that its immediate neighbour during a single timestep. The computed solution produced by Equations (3.8) and (3.9) will remain stable if the

timestep does not exceed a critical value. PFC3D has the ability to estimate the critical timestep at the start of each calculation cycle. The actual timestep is then taken as a fraction of this estimated critical value.

The estimation of the critical timestep is determined firstly by considering a one dimensional mass spring system described by a point mass (m) and spring stiffness (k). The critical timestep is given by [9]:

$$t_{crit} = \frac{T}{\pi}$$

$$T = 2\pi\sqrt{m/k} \tag{3.10}$$

where T is the period of the system. Now, consider the infinite series of point masses and springs in Figure 3.7, which illustrate the contacts in the system. The smallest period of this system will occur when the masses are moving in synchronised opposing motion such that there is no motion at the centre of each spring. The motion in a single point mass is described by two equivalent systems shown in Figure 3.7(b) and 3.7(c). Hence the critical timestep in this system is found by using Equation (3.10) to be:

$$t_{crit} = 2\sqrt{m/(4k)} = \sqrt{m/k} \tag{3.11}$$

3.3.3 Elastic Contact Model

This section describes the elastic contact model for two particles in contact subjected to compression and/or shear. It should be noted that alternate contact models are also available to simulate more complex behaviour. The contact stiffness relates the contact force and relative displacement in the normal and shear directions by the Force-Displacement Law described in Section 3.3.1. The normal contact stiffness is described in Equation (3.12) and the shear contact stiffness is described in Equation (3.13). The contact stiffnesses for the contact model are calculated assuming that the stiffnesses of two contacting entities act in series giving:

$$K^n = \frac{k_n^{[A]} k_n^{[B]}}{k_n^{[A]} + k_n^{[B]}}$$

(3.12)

$$K^s = \frac{k_s^{[A]} k_s^{[B]}}{k_s^{[A]} + k_s^{[B]}}$$

(3.13)

where superscript [A] and [B] denote the two entities in contact. The parameters of normal stiffness (k_n) and shear stiffness (k_s) of two contacting entities are specified in PFC3D, the contact stiffnesses of two contacting entities are then computed using Equation (3.12) and (3.13). This contact stiffness is multiplied by the magnitude of the overlap to obtain the contact force.

3.3.4 Contact Bond

This section describes the contact bond used to model a bonded material in PFC3D. The contact bonds have a specified tensile strength in the normal and shear directions. The particles bonded together with a contact bond cannot slip but they can roll over each other. Figure 3.8 shows the rolling of ball at a contact bond. It can be seen from this figure that two identical balls (A and B) are joined by a single contact bond. Ball A has rotated about ball B (fixed) without slipping and without breaking the contact bond. The contact bond will remain (as shown in Figure 3.8) at the new position of ball A.

In the normal direction, contact bonds allow tensile forces to develop at a contact when the overlapping magnitude between a pair of contacting balls is less than zero. The contact bond binds the balls together and the magnitude of tensile normal contact force is limited by the normal contact bond strength. If the magnitude of the tensile normal contact force equals or exceeds the normal contact bond strength, the bond breaks and both normal and shear contact forces are set to zero.

In the shear direction, if the magnitude of the shear contact force is equal to or exceeds the shear contact bond strength, the bond breaks, but the contact forces are not altered providing that the shear force does not exceed the friction limit. A

coefficient of friction is set so that the slip model will activate when the bond breaks, the shear force is resisted if it does not exceed the friction limit.

3.3.5 Burger's Viscoelastic Contact Model

A Burger's contact model is a user defined contact model implemented in PFC3D to simulate the time dependent behaviour of a material. This contact model is written in the C++ programming language. The Burger's contact model is shown in Figure 3.9. This model contains a Kelvin element and Maxwell element connected in series in the normal and shear direction respectively at a contact point. The properties of the Burger's model are shown in Table 3.1.

The total displacement of a Burgers' model u (sum of the displacement of the Kelvin element and the Maxwell element) and its first derivative are given by:

$$u = u_k + u_{mk} + u_{mc}$$
$$\dot{u} = \dot{u}_k + \dot{u}_{mk} + \dot{u}_{mc} \tag{3.14}$$

where u_k is the displacement of the viscoelastic component in the Kelvin element, u_{mk} is the displacement of the elastic component in the Maxwell element and u_{mc} is the displacement of the viscoplastic component in the Maxwell element.

The contact force using stiffness (K_k) and viscosity (C_k) of the Kelvin element is given by:

$$f = K_k u_k + C_k \dot{u}_k \tag{3.15}$$

The contact forces using stiffness (K_m) and viscosity (C_m) of the Maxwell element are given by:

$$f = K_m u_{mk} \tag{3.16}$$
$$\dot{f} = K_m \dot{u}_{mk} \tag{3.17}$$
$$f = C_m \dot{u}_{mc} \tag{3.18}$$

From Equation (3.15) the velocity of the Kelvin element is given by:

$$\dot{u}_k = \frac{-K_k u_k + f}{C_k} \qquad (3.19)$$

Using a central difference approximation of the finite difference scheme for the time derivative and taking average values for u_k and f gives:

$$\frac{u_k^{t+1} - u_k^t}{\Delta t} = \frac{1}{C_k}\left[-\frac{K_k(u_k^{t+1} + u_k^t)}{2} + \frac{f^{t+1} + f^t}{2} \right] \qquad (3.20)$$

therefore:

$$u_k^{t+1} = \frac{1}{A}\left[Bu_k^t + \frac{\Delta t}{2C_k}\left(f^{t+1} + f^t\right) \right] \qquad (3.21)$$

where

$$A = 1 + \frac{K_k \Delta t}{2C_k}$$

$$B = 1 - \frac{K_k \Delta t}{2C_k} \qquad (3.22)$$

For the Maxwell element, the displacement and velocity are given by:

$$u_m = u_{mk} + u_{mc}$$

$$\dot{u}_m = \dot{u}_{mk} + \dot{u}_{mc} \qquad (3.23)$$

Substituting Equations (3.17) and (3.18) into Equation (3.23) gives:

$$\dot{u}_m = \frac{\dot{f}}{K_m} + \frac{f}{C_m} \qquad (3.24)$$

Using central difference approximation of the finite difference scheme and taking the average value for f gives:

$$\frac{u_m^{t+1} - u_m^t}{\Delta t} = \frac{f^{t+1} - f^t}{K_m \Delta t} + \frac{f^{t+1} + f^t}{2C_m} \tag{3.25}$$

therefore:

$$u_m^{t+1} = \frac{f^{t+1} - f^t}{K_m} + \frac{\Delta t (f^{t+1} + f^t)}{2C_m} + u_m^t \tag{3.26}$$

The total displacement and velocity of the Burger's model are given by:

$$u = u_k + u_m$$
$$\dot{u} = \dot{u}_k + \dot{u}_m \tag{3.27}$$

Using finite difference scheme for time derivative gives:

$$u^{t+1} - u^t = u_k^{t+1} - u_k^t + u_m^{t+1} - u_m^t \tag{3.28}$$

Substituting Equations (3.21) and (3.26) into (3.28), the contact force, f^{t+1}, is given by:

$$f^{t+1} = \frac{1}{C}\left[u^{t+1} - u^t + \left(1 - \frac{B}{A}\right)u_k^t - Df^t \right] \tag{3.29}$$

where

$$C = \frac{\Delta t}{2C_k A} + \frac{1}{K_m} + \frac{\Delta t}{2C_m}$$

$$D = \frac{\Delta t}{2C_k A} - \frac{1}{K_m} + \frac{\Delta t}{2C_m} \tag{3.30}$$

In conclusion, the contact force f^{t+1} can be calculated from known values for u^{t+1}, u^t, u_k^t and f^t. Verification of the Burger's contact model in PFC3D was performed by

ITASCA [1]. A relaxation test was performed and the result was found to coincide with the analytical solution (see [1] for more details).

3.3.6 Servo-Control Mechanism

The compressive stress (or load) on a numerical sample in PFC3D is applied by moving the wall (or loading platen) with a specified velocity. For simulations that require constant loading throughout the test (e.g. constant stress creep test), the servo-control mechanism is implemented which is a function that is integrated in PFC3D to maintain a constant stress (axial and confining) throughout the simulation. This function is called in every calculation cycle to determine the current wall stresses and it then adjusts the wall velocities in such a way to reduce the difference between measured stress and required stress. The calculation algorithm for the servo-control mechanism is given by:

$$\dot{u}^{(w)} = G(\sigma^{measured} - \sigma^{required}) = G\Delta\sigma \qquad (3.31)$$

where G is the 'gain' parameter estimated using the following reasoning. The maximum increment in wall force arising from wall movement in one timestep is given by:

$$\Delta F^{(w)} = k_n^{(w)} N_c \dot{u}^{(w)} \Delta t \qquad (3.32)$$

where, N_c is the number of contacts on the wall and k_n is the average stiffness of these contacts. Hence the change in mean wall stress is given by:

$$\Delta\sigma^{(w)} = \frac{k_n^{(w)} N_c \dot{u}^{(w)} \Delta t}{A} \qquad (3.33)$$

where A is the wall area. For stability reasons, the change in wall stress must be less than the difference between the measured and required wall stress. To fulfil this stability requirement, a relaxation factor α is introduced such that:

$$\left| \Delta \alpha^{(w)} \right| < \alpha \left| \Delta \sigma \right| \tag{3.34}$$

Substituting Equations (3.31) and (3.33) into Equation (3.34) gives:

$$\frac{k_n^{(w)} N_c G \left| \Delta \sigma \right| \Delta t}{A} < \alpha \left| \Delta \sigma \right|$$

$$G = \frac{\alpha A}{k_n^{(w)} N_c \Delta t} \tag{3.35}$$

where G is the 'gain' parameter to be substituted in Equation (3.31) for adjusting the wall velocity to achieve the required wall stress in numerical servo-control.

3.4 Summary

The traditional approach in modelling is insufficient to simulate the micromechanical behaviour of asphalt. Recent developments in computer technology have allowed the behaviour of asphalt as a heterogeneous material to be investigated using DEM. DEM has been widely applied in soil and rock mechanics. Many DEM programming codes have been developed since the 1970's. PFC3D has been applied in a wide range of applications by many researchers.

The PFC3D particle flow model and its calculation algorithms were described in Section 3.3. The calculation cycle in PFC3D is a timestepping algorithm involving the repeated application of the law of motion and a force displacement law. The determination of the mechanical timestep and the elastic contact model were described. To model asphalt as a bound material, a contact bond is introduced. The Burger's contact model is implemented to simulate the time dependent behaviour of asphalt. The servo control mechanism was introduced for constant stress control in numerical simulations. In conclusion, PFC3D appeared to be most powerful DEM programming code available to model asphalt materials.

Tables:

Table 3.1: Properties of Burger's Model

Properties	Notation
Normal stiffness for Kelvin element	K_{kn}
Normal viscosity for Kelvin element	C_{kn}
Normal stiffness for Maxwell element	K_{mn}
Normal viscosity for Maxwell element	C_{mn}
Shear stiffness for Kelvin element	K_{ks}
Shear viscosity for Kelvin element	C_{ks}
Shear stiffness for Maxwell element	K_{ms}
Shear viscosity for Maxwell element	C_{ms}
Friction coefficient	f_s

Figures:

Maximum force:
━━━ 0.1379E+09

B. STRESS:
(1,1) -1.500E+06
(1,2)   0.000E+00
(2,1)   0.000E+00
(2,2) -1.500E+06

components of applied
stress tensor

boundary particles
identified by dashed line
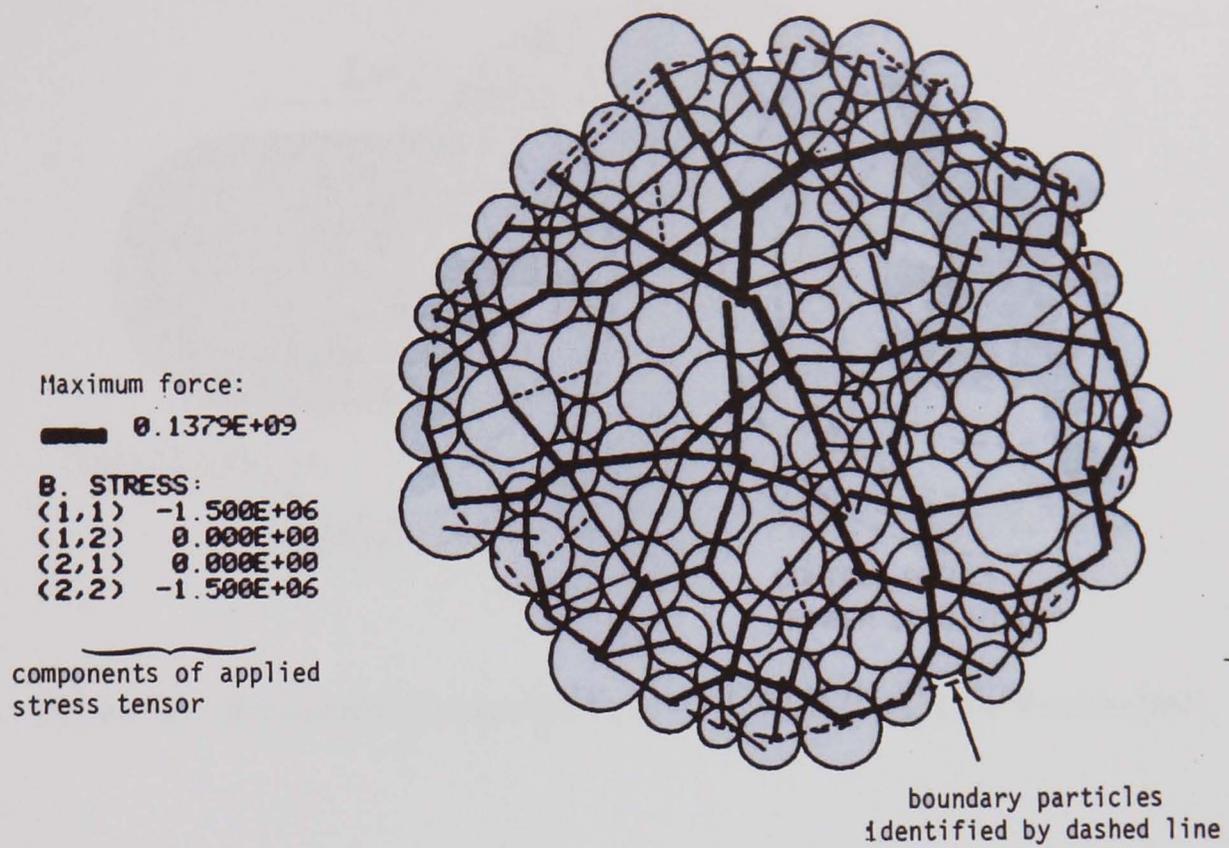
Figure 3.1: Initial state of 100-disc test, after Cundall [36]
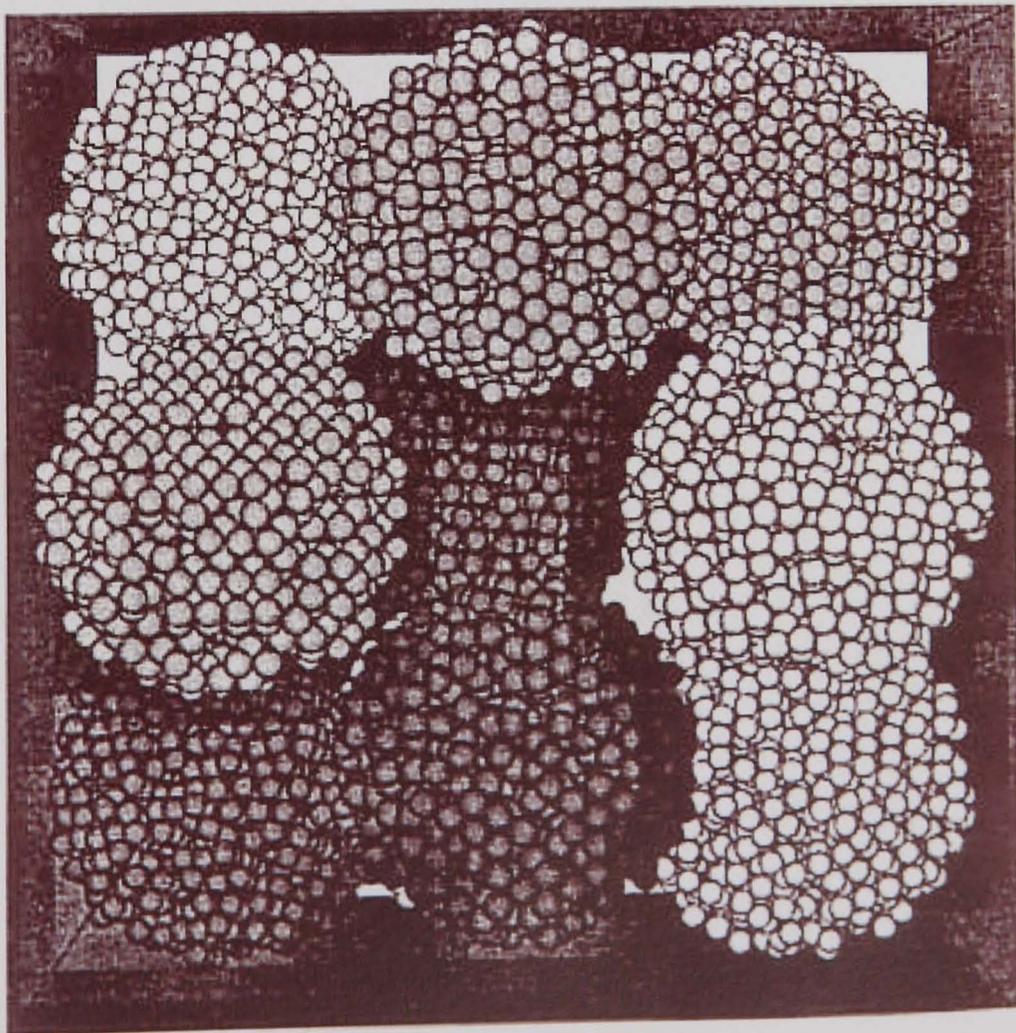
Figure 3.2: Aggregate of 13 agglomerates in a cubic Oedometer, after McDowell [73]
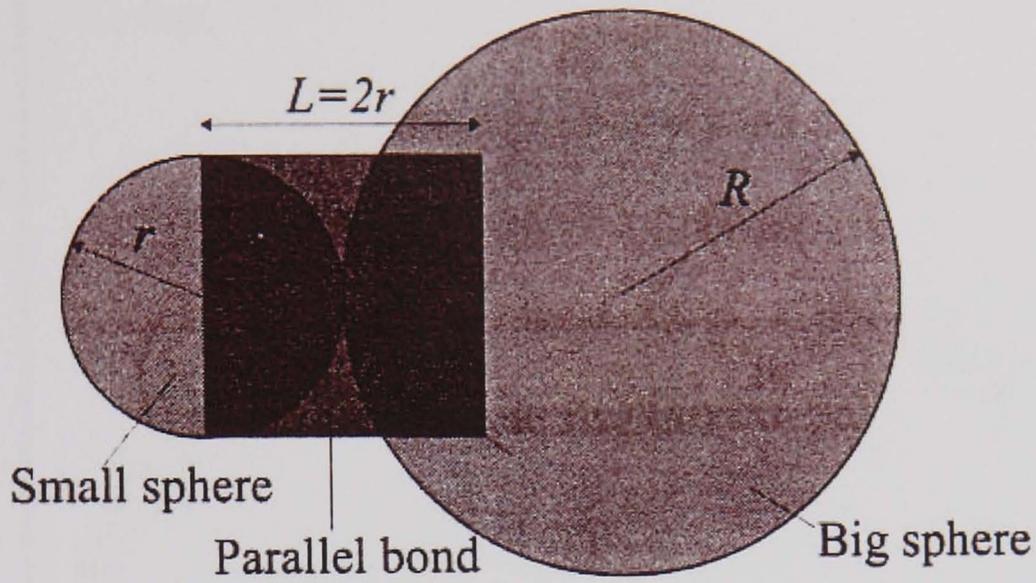
Figure 3.3: Schematic illustration of a bonded particle, after Powrie [89].
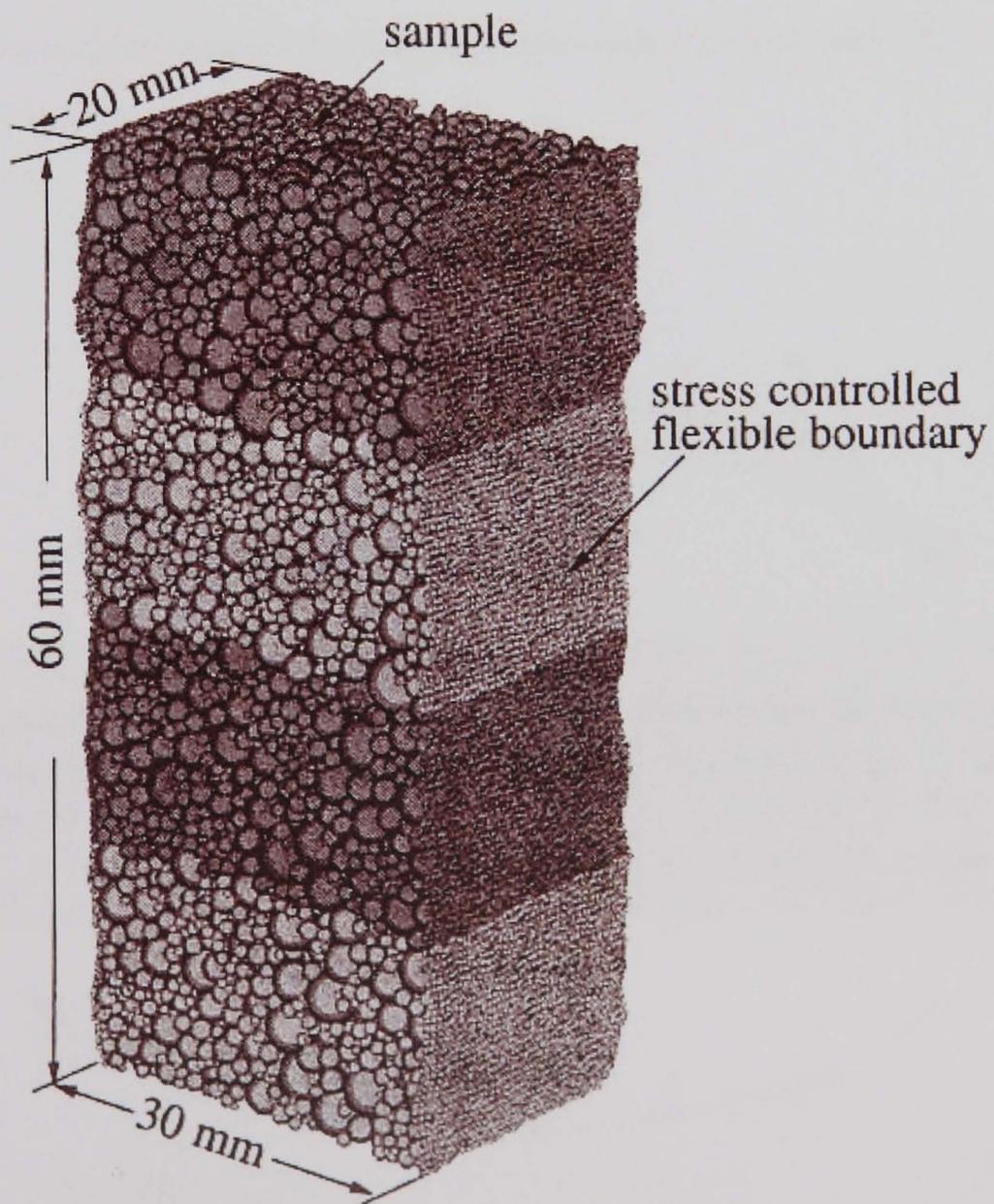
Figure 3.4: Typical sample with 10,000 particles, after Powrie [89].
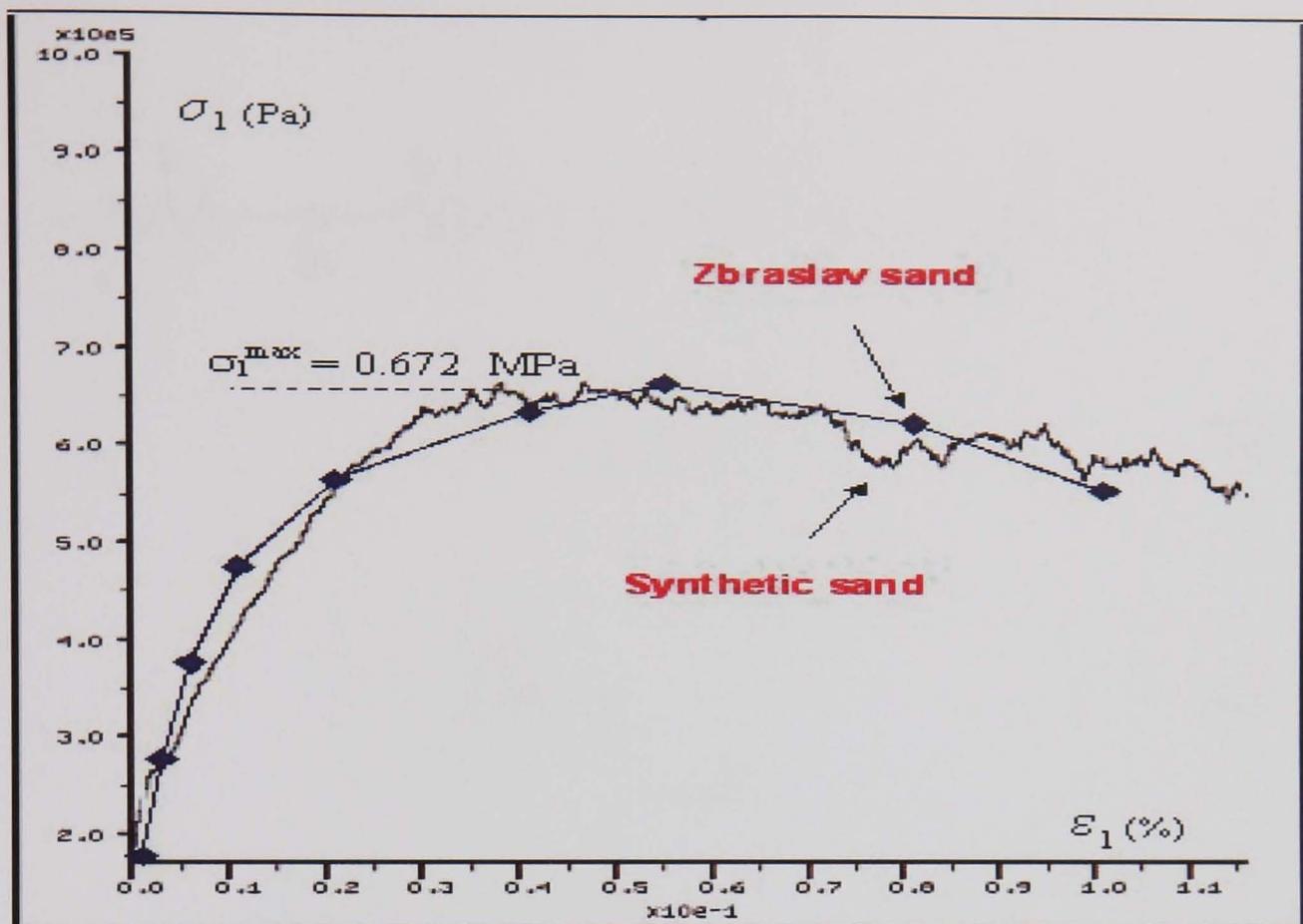
Figure 3.5: Stress-strain response of Zbraslav sand and Synthetic sand, after Dolezalova [42].
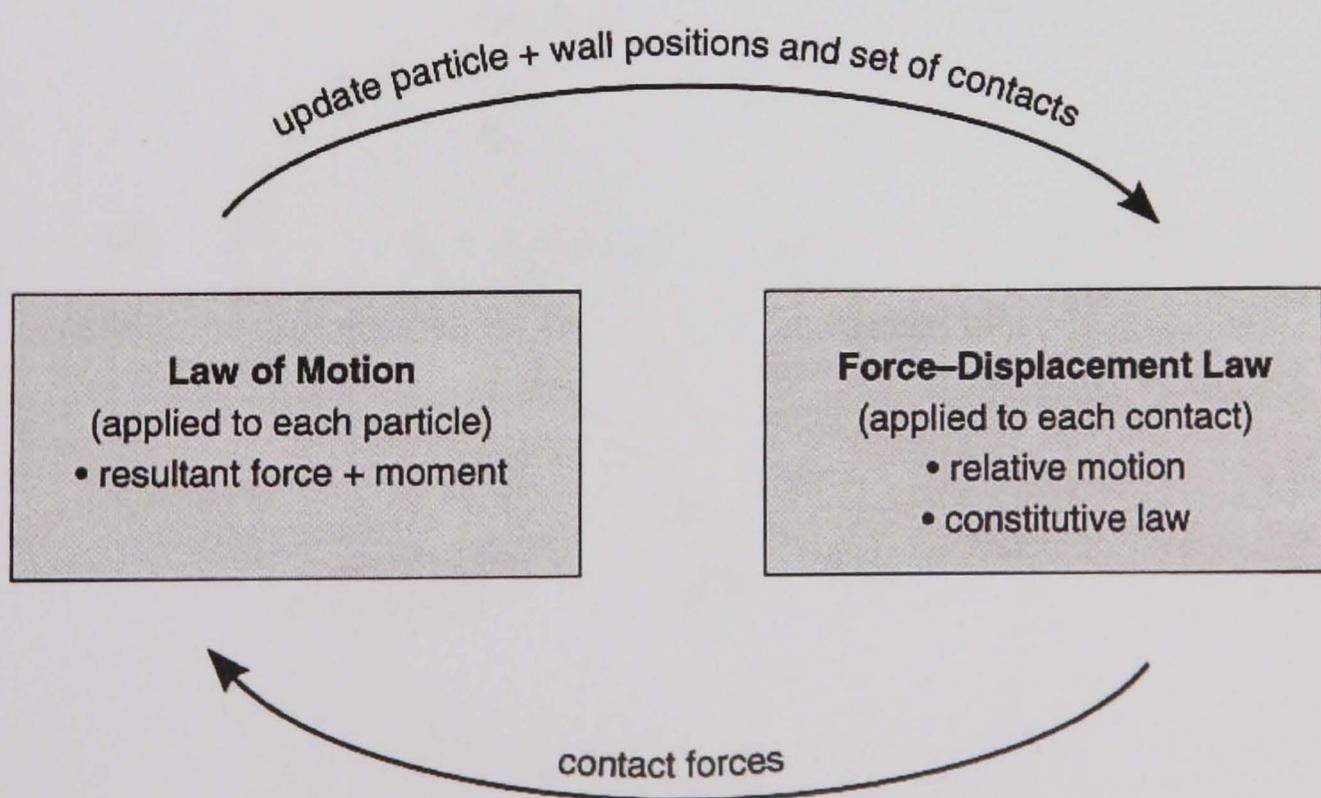
Figure 3.6: Calculation cycle in PFC3D [3].
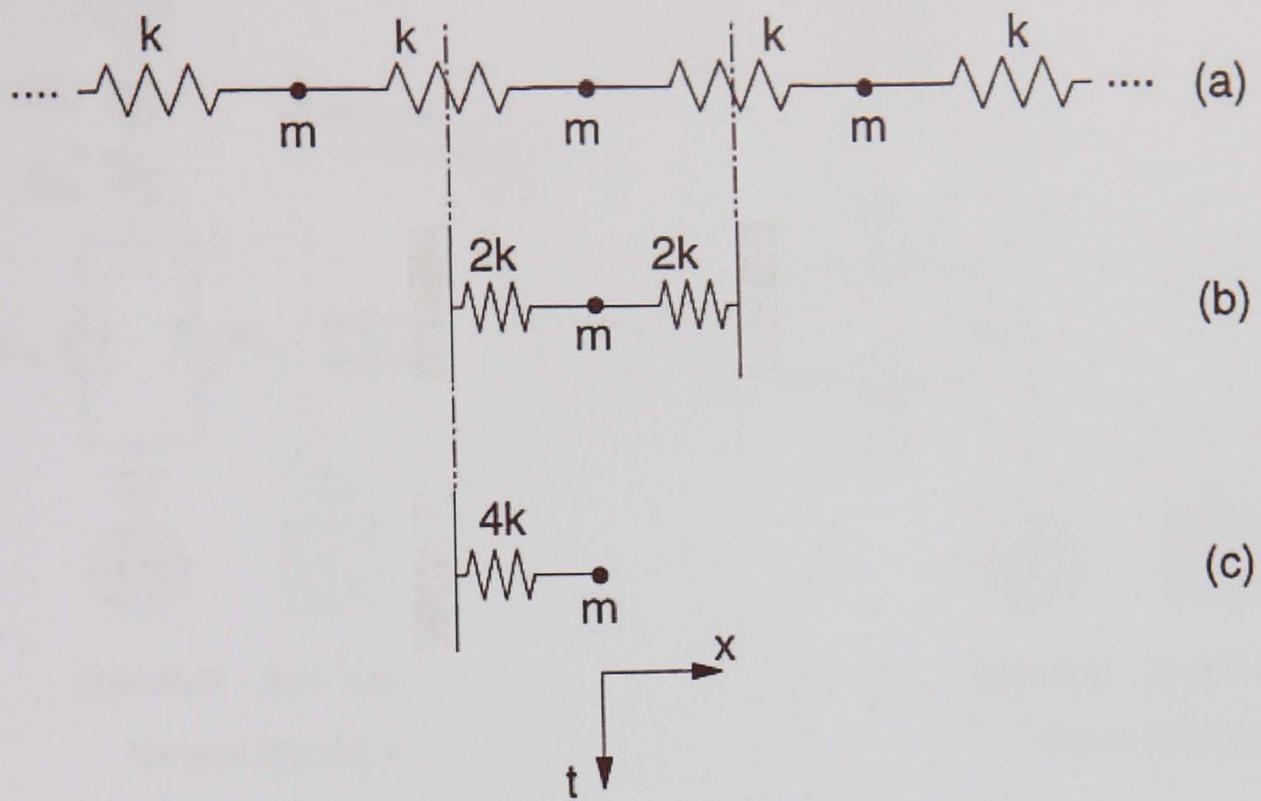
Figure 3.7: Multiple mass spring system [3].
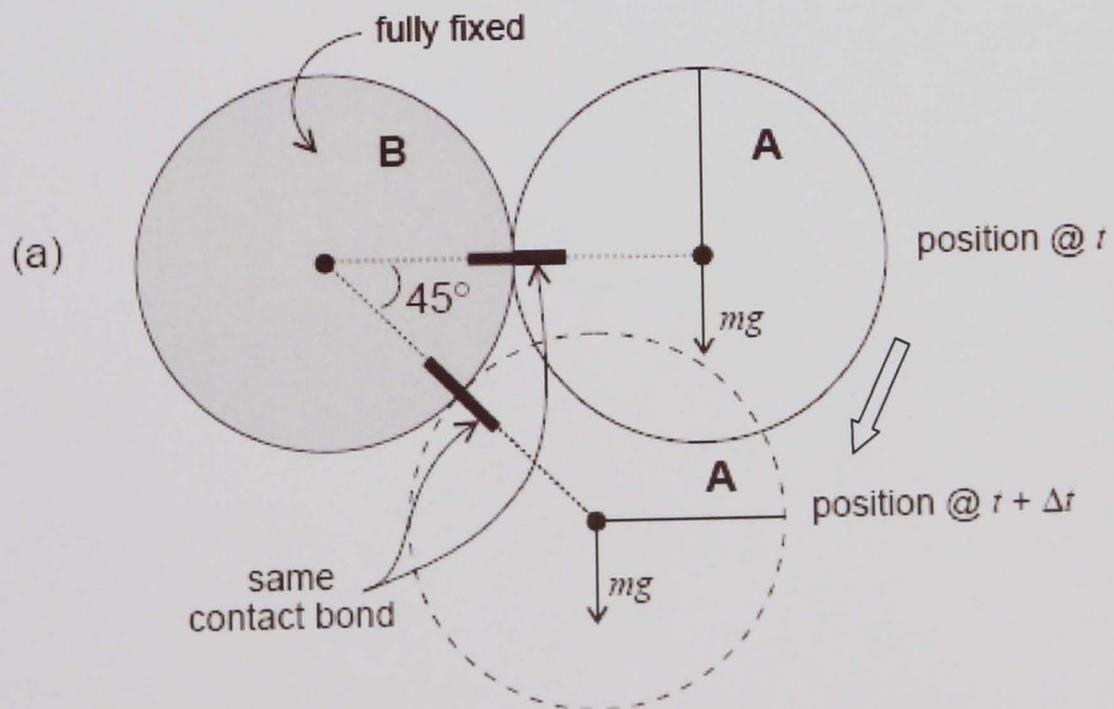
Figure 3.8: Rolling at a contact bond [3].
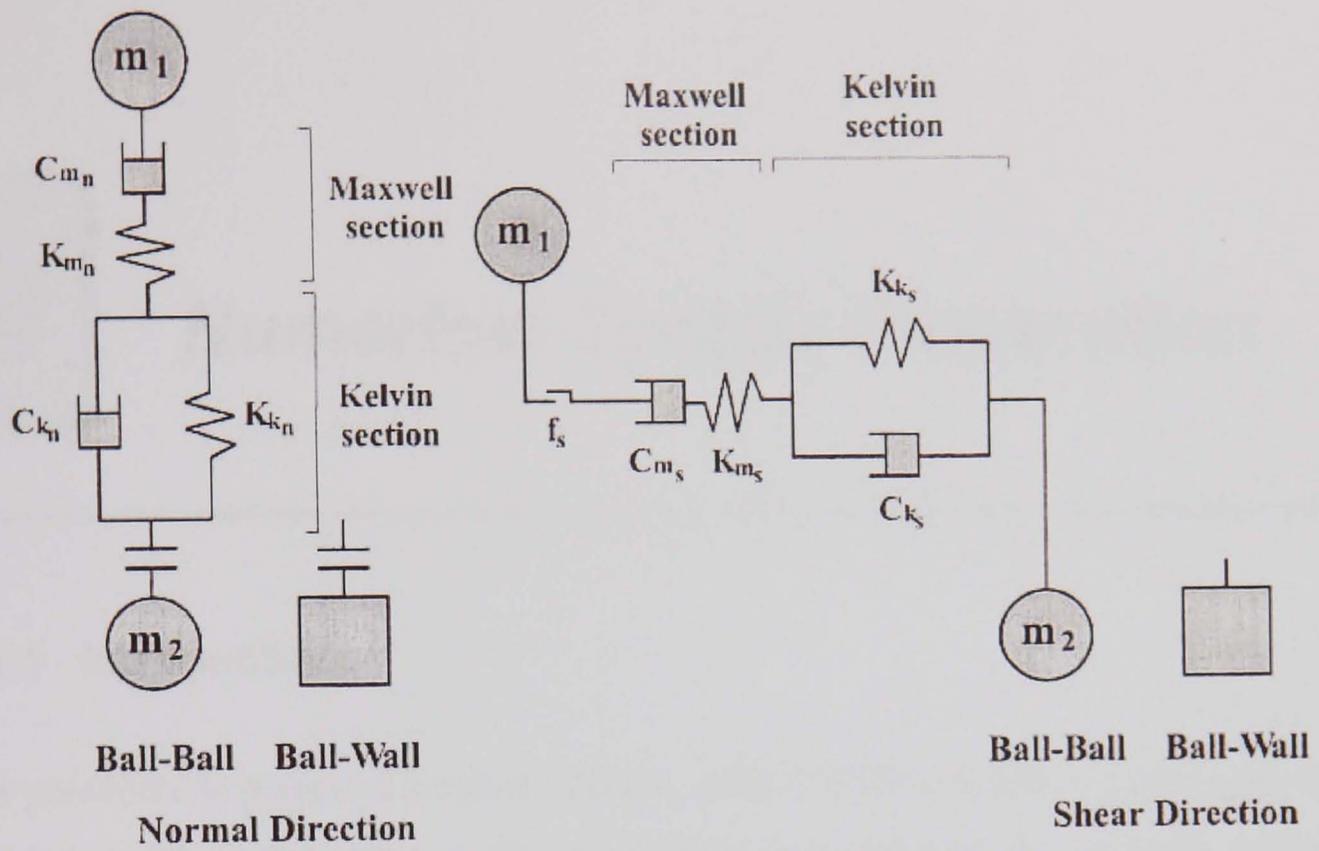
Figure 3.9: Burger's contact model in PFC3D [2]

4 | *Numerical Sample Preparation*

4.1 Introduction

A procedure to prepare a synthetic sample using PFC3D to simulate a laboratory test is presented in this chapter. The mechanical behaviour of the synthetic material depends on physical parameters such as porosity, particle size distribution, stiffness and the strength of contacts. It is important to generate a synthetic sample that mimics the test specimen in the laboratory. This chapter also describes the measurement methods for strains, porosity and number of contacts used in the numerical sample.

It should be noted that the objective of this chapter is to develop a procedure that results in specimens that replicate the single-sized sand asphalt specimens tested in the laboratory. As noted in Chapter 1, this idealised mixture has been chosen because of the relatively simple internal geometry. Previous experimental work undertaken using this material demonstrated that the approximate volumetric proportions are as follows:

- Sand (1.18 – 2.36mm) = 65%
- Bitumen = 25%
- Air voids = 10%

The sand is approximately single-sized. The following section presents a review of the packing characteristic of spheres.

4.2 Review on Packing Characteristic of Spheres

Packing of the particles is an important issue for sample preparation in DEM simulations. The basic parameter related to an array of spheres is the packing density, which is the ratio of the volume of the spheres to the total volume they occupy. Scott [100] defined dense random packing as the upper limit of packing density when spherical balls of equal size are poured into rigid containers. He claimed that it is unlikely that the packing of balls was significantly influenced by the friction. His experimental work showed that the packing density is 0.63 for dense random packed spheres. The same result was found by Sohn and Moreland [105] when they conducted a series of experiments using sands to investigate the effect of particle size distribution on packing density. Computational work by Adam and Matheson [6] showed a similar result. Therefore, it can be concluded that a dense random packing sample has a packing density of 0.63.

The number of contacts between spheres is another important issue in packing of spheres. Bezrukov et al. [11] emphasised that contacts between spheres determine the topological connectivity of the system of spheres and the transfer of forces. They observed an average contact number of 6 for dense random packing spheres using a spatial statistic approach. For real packing of equal spheres, Bernal and Mason [10] observed an average contact number of 6.4 for a "random close" packing with a packing density of 0.62.

In conclusion, to simulate asphalt comprising of single-sized sand using DEM, the sample generated should have a packing density of 0.63 and an average number of contacts of approximately six per particle.

4.3 Numerical Sample Preparation Procedure

To model the behaviour of a highly idealised asphalt mixture, it is necessary to artificially generate a numerical specimen that replicates the material. The idealised mixture comprises approximately single-sized spherical (sand-sized) particles mixed with bitumen. The principal reasons that this form of idealised asphalt was chosen are that the packing characteristics are known (dense random packing) and the

behaviour of the mixture will be dominated by the bitumen and complex aggregate interlock effects will be minimised. In this type of approach the effect of the bitumen is represented by shear and normal contact stiffnesses. It is important to generate an initially isotropic sample that exhibits approximately the same packing characteristics as the dense material being modelled. The following sub-sections describe the preparation of an isotropic cylindrical sample to simulate the triaxial and uniaxial tests.

4.3.1 Boundary and Particle Generation

To prepare a numerical sample, the particle assembly will be generated and compacted within a set of confining boundaries. Therefore, the first step in the sample preparation procedure is to generate a set of confining boundaries for the sample. The boundary (wall in PFC3D) is a plane that has arbitrarily defined contact properties for interaction with particles (balls in PFC3D). These finite walls act as boundary constraint for the assembly and restrict the movement of particles through the boundaries. Contact forces for the particle to boundary contacts are calculated via the force-displacement law as for particle to particle contact. For uniaxial and triaxial simulations, the top and bottom boundaries are used to simulate the loading platens of the sample. In triaxial simulations, the lateral cylindrical wall (nearly circular) is used to provide the lateral confinement to the sample, whilst in uniaxial simulation the lateral wall is removed after sample preparation. The typical boundaries generated for a cylindrical sample are shown in Figure 4.1.

After preparation of boundaries, a dense random packing sample with an approximate volume fraction of solids equal to 64% is generated. The particle (or spherical ball) is the fundamental geometric entity for the discrete element calculation. The desired number of particles required to occupy the available space is calculated using the following equation:

$$N = \frac{3V(1-n)}{4\pi \overline{R}^3}$$

(4.1)

where N is the number of particles to be generated, V is the total volume of given space, n is the desired porosity and $\bar{R}$ is the mean radius.

Particles are generated with random centroid coordinates to give an irregular packing type with no discernible pattern in the arrangement of particles. It should be noted that all particles are generated with the same radius. The particles are first generated to half of their final size randomly distributed such that no two particles overlap, as shown in Figure 4.2. Then, the particle radii are increased to their final values, as shown in Figure 4.3.

It should be noted that the desired porosity in Equation 4.1 is not the true porosity of the sample. This is because overlapping particles at contacts under compression result in a "lost" volume of solids in the overlapping region. Consequently, the procedure above only serves as a guideline to generate the sample to a final porosity that is close to the required porosity. The true porosity of the sample is measured by using the 'Measurement Sphere' described in Section 4.4.1.

4.3.2 Isotropic Equilibrium State

To generate a numerical sample that replicates an idealised asphalt mixture, it is important that the sample is initially isotropic and essentially free from internal stresses. In the particle generation procedure (described above), the particles are expanded to their final radii and overlap as shown in Figure 4.3 which results in internal forces between overlapping particles. It should be noted that the magnitude of overlap varies at every contact causing a non-uniform distribution of contact forces within the sample.

To achieve an isotropic equilibrium condition, particles are allowed to re-orient themselves until the stresses on the sample are approximately isotropic. This is achieved by applying pre-load cycling where the particles are allowed to settle to equilibrium so that the contact forces of particles in the sample will be uniformly distributed, as shown in Figure 4.4. It should be noted that during pre-load cycling,

the wall and particle friction are set to zero temporarily to facilitate the re-orientation process.

However, the sample prepared under these conditions has a high level of isotropic stress (typically $\approx 10MPa$). It should be noted that the sample must have a low (or negligible) internal stress prior to testing. To prepare a "stress free" sample, the radius of all particles is reduced uniformly and the sample is cycled to equilibrium. Reducing the particle radii causes a reduction in overlapping magnitude between particles, hence reduces the contact forces and isotropic stresses in the sample. During this process, the particles are again allowed to re-orient themselves so that the sample can be maintained at isotropic equilibrium state. Figure 4.5 shows the effect of reduction in particle radii on isotropic stress in the sample. It can be seen from this figure that if the particle radii are reduced by approximately 0.3% of their original size the isotropic stress reduces from $10MPa$ to $0.1kPa$. It is suggested [1] that the specified isotropic stress in the sample needs to be reduced to less than one percent of the uniaxial compressive strength. Therefore, an initial isotropic stress of $0.1kPa$ is used in the simulations.

The contact force distribution under the isotropic equilibrium state is shown in Figure 4.6. The lines represent compressive forces and the thickness of the lines corresponds to the magnitude of contact force generated. It can be seen from this figure that the contact forces are distributed uniformly which is expected under an isotropic equilibrium state.

4.3.3 Preparation of a Bonded Sample

The previous section described the preparation of "stress free" numerical sample. To represent asphalt as a bonded material, this section develops the procedure of preparing a bonded numerical sample. In DEM, the particles must have a real contact with a non-zero overlap so that a contact bond can be created. Therefore, a high coordination number (defined as the average number of contacts per particle) is required to create a good contact bond network in the dense bonded sample so that its behaviour can be fully represented in modelling. Rothenburg et al [95] suggested

that the particle assembly needs at least four contacts per particle on average to carry the load.

To create a sample with good contact bond network, it is necessary to make sure that every particle in the sample has a minimum of four contacts with neighbour particles. This is done by first scanning every contact in the sample to detect the particles with less than four contacts. These particles are then expanded slightly (typically by 1%) to create additional contacts with neighbouring particles. During this process, the particles are allowed to re-orient themselves so that the sample can be maintained in isotropic equilibrium. It should be noted that particles with less than four contacts are typically 5 to 8% of total particles in the sample. The location of these particles in a typical sample is shown in Figure 4.7.

By adopting the procedures above, a sample is prepared in a dense randomly packed state with low isotropic internal stresses and a minimum of four contacts per particle. To prepare a bonded sample, normal and shear contact bonds are then added to all the contacts in the sample as shown in Figure 4.8. It should be noted that a new contact bond will be created automatically at new contact formed in the sample during the simulation.

4.3.4 Preparation for Uniaxial and Triaxial Simulations

This section develops a procedure to prepare the sample for the uniaxial and triaxial simulations. In the process of preparing the numerical sample, the particle assembly is confined by the top, bottom and lateral walls. The top and bottom walls simulate the loading platens while the lateral wall simulates any confinement (for example in a triaxial test). To prepare the bonded sample for a uniaxial simulation, the lateral wall must be removed (deleted in PFC3D) to give zero confinement to the sample. It should be noted that, as described in previous sections, the sample was prepared to a low isotropic internal stress condition before removing the lateral wall. Consequently, removing of the lateral wall causes some unloading resulting in a self-equilibrating set of compressive and tensile locked-in forces. The locked-in force distribution (tension and compression) in the sample is shown in Figure 4.9. It

should be noted that the typical locked-in forces are less than 0.01% of the average contact force in the sample at peak strength. Hence, the locked-in forces can be considered to be negligible in the numerical simulations.

4.4 Method of Measurement

The method of measurement (e.g. for bulk stress, bulk strain and porosity) on a test sample is an important issue in the numerical simulation. This section describes a few measurement methodologies investigated.

4.4.1 Measurement Sphere

A measurement sphere is defined as a specified measurement volume in PFC3D and is capable of measuring properties such as the coordination number, porosity, stress and strain rate. This specified measurement volume is a sphere, so referred as "a measurement sphere". A measurement sphere with a specified radius can be installed at any point in the sample. In later simulations, two measurement spheres are used in the upper and lower parts of the sample to measure the air void content and average number of contacts during the simulation, as shown in Figure 4.10.

Porosity

This sub-section describes how a measurement sphere can be used to measure the porosity (void content) of a numerical sample. The porosity n is defined as the ratio of total void volume within the measurement sphere to measurement sphere volume.

$$n = \frac{V_{void}}{V_{sphere}} = \frac{V_{sphere} - V_{ball}}{V_{sphere}} = 1 - \frac{V_{ball}}{V_{sphere}} \tag{4.2}$$

where V_{sphere} is the volume of the measurement sphere, V_{void} is the volume of voids within the measurement sphere and V_{ball} is determined by:

$$V_{\text{ball}} = \sum_{N_p} (V_p) - V_{\text{overlap}} \tag{4.3}$$

where V_{ball} is the volume of the measurement sphere occupied by balls, N_p is the number of balls that intersect the measurement sphere and $V_{overlap}$ is the volume of particles overlapping contained within the measurement sphere.

As seen from Equation 4.3, the volume of particles overlapping is accounted in the computation of porosity. Therefore, it can be concluded that the measurement sphere is able to measure the porosity of a synthetic material in a numerical simulation with great accuracy. This measurement method will be utilised in the later simulations to measure the porosity of the numerical sample.

Coordination number

The coordination number C_n is defined as the average number of contacts per particle. It is one of the important parameters that can be obtained from the measurement spheres. The coordination number will be calculated for particles with their centroids contained within the measurement sphere using:

$$C_n = \frac{\sum_{N_b} n_c^{(b)}}{N_b} \tag{4.4}$$

where N_b is the number of particles with centroids contained within the measurement sphere and $n_c^{(b)}$ is the number of contacts between balls.

The tracking of coordination number is important in the sample preparation procedure to ensure that the sample has a certain minimum number of contacts per particle (refer to section 4.3.3). The coordination number is also updated and plotted graphically during the simulation to track the number of new contacts formed.

4.4.2 Measurement of Bulk Strains

Typically, in laboratory experiments the deformation of the sample is measured at the sample boundary using a Linear Variable Differential Transformer (LVDT) or a dial gauge. Those measurements are then used to calculate strain values. The objective of this section is to develop a method to measure the bulk strains in the numerical sample that mimics the measurement method used in the laboratory experiment. It should be noted that in PFC3D, the history of particle movement is tracked. The measurement methodologies are described in the following subsections.

Bulk Radial Strain

To measure the bulk radial strain in a numerical sample, artificial "measuring gauges" (replicating the function of the LVDT in the laboratory) are constructed from specified particles at the boundary of a numerical sample. The following measurement procedure has been adopted to measure the radial strain of a numerical sample:

1. Particles located at the cylindrical boundary are assigned as measuring gauges.

2. Original (or initial) coordinates of these particles are recorded in computer memory prior to loading.

3. Updated coordinates of the particles are tracked during the simulation.

4. The radial strain for each particle is calculated based on the difference between the updated coordinate and original coordinate.

5. The bulk radial strain of the sample is determined by averaging the radial strains from all the particles.

Initially all the particles on the circumference of the sample were used to measure the bulk radial strain in the numerical sample. However, this approach is computationally expensive because of the large number of particles to be monitored during the simulation. Consequently, to reduce the computation time, fewer measuring particles are used. This is achieved by specifying the height of the gauges on the circumference with respect to the sample height, defined as "gauge thickness".

Two samples with gauge thicknesses of 0.4 and 0.8 to are illustrated in Figures 4.11 and 4.12.

A number of simulations were performed to investigate the effect of gauge thickness on the sensitivity in measurement values. Two samples with elastic contact stiffness and contact bonds containing 6,000 and 12,000 particles were used. The radial strains were measured using different gauge thickness for the different samples. The percentage error with respect to the value calculated using all the particles on the perimeter was then calculated for different gauge thickness and is plotted in Figure 4.13. It can be seen from Figure 4.13 that the percentage mean error reduces from 4% to 1% when the gauge thickness increases from 0.1 to 0.8. It can be concluded that a gauge thickness of at least 0.8 is needed to ensure that the radial strain is within 1% of the value calculated using all the particles on the perimeter.

Axial Strain

The method of measurement for axial strain in a numerical sample is much more simple and direct compared to the method used for radial strain. The original coordinates of the top and bottom loading platens are first recorded in computer memory prior to testing. The platen coordinates are then updated regularly during the simulation. The axial strain of a numerical sample is calculated based on the relative displacement of the loading platens. It should be noted that the overlapping magnitude (under compression) of the wall and adjacent balls is small compared with the axial displacement of the sample and hence it is negligible.

4.5 Conclusions

The following conclusions can be drawn from this chapter:

- A cylindrical sample can be generated replicating the testing specimen in the laboratory.

- The packing characteristic of the sample generated is dense random packing with volume fraction of solids equal to 64% which is approximately the same packing characteristics as an idealised mixture.

- The numerical sample is prepared to an equilibrium state with low internal isotropic stresses.

- A procedure has been adopted to confirm that every particle in the sample has a minimum of four contacts with neighbouring particles.

- Normal and shear contact bonds are applied at each contact point to represent asphalt as bonded material.

- The cylindrical boundary of the sample is removed for uniaxial simulation.

- Measurement spheres are used to measure the porosity and coordination number of the sample.

- Radial strain is measured by tracking the displacement of particles on the circumference of the sample (measuring gauges).

- Axial strain is measured based on the relative displacement of the loading platens.

Figures:
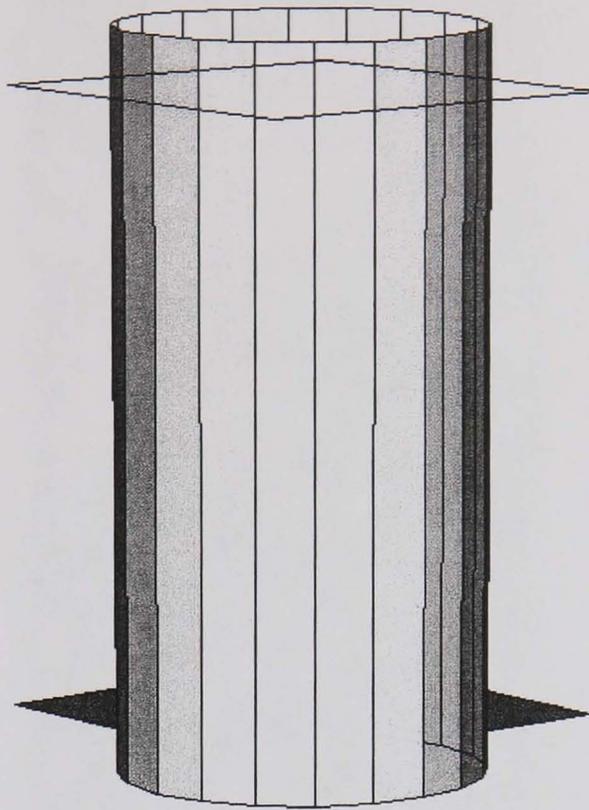
Figure 4.1: Boundaries generated in PFC3D.
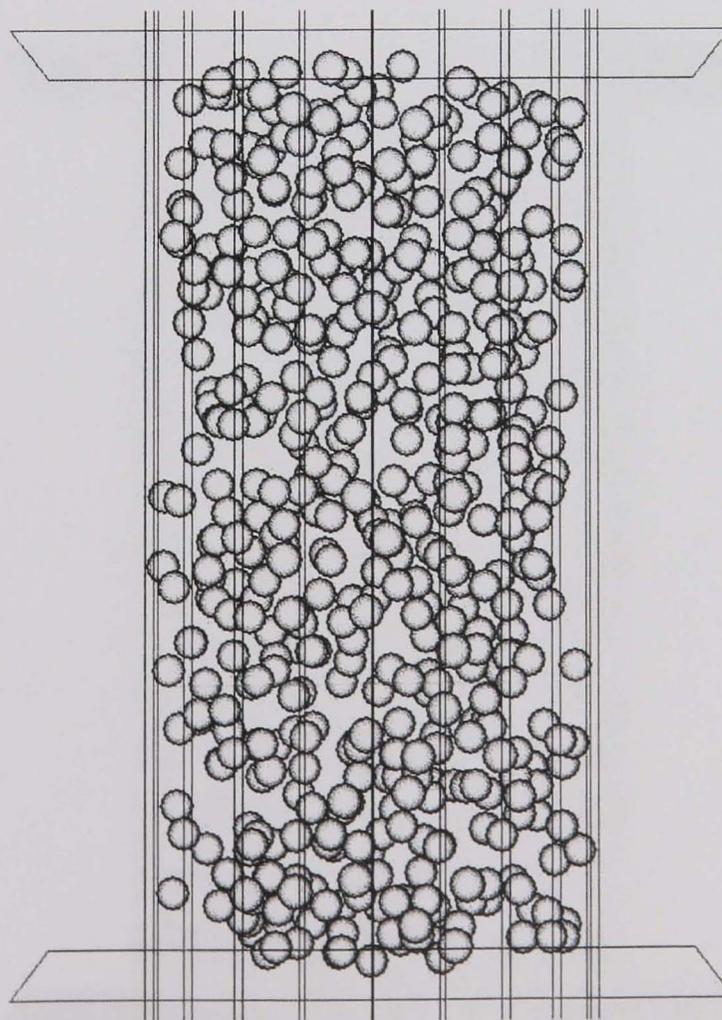
Figure 4.2: Particles generated randomly in space to half of final size.
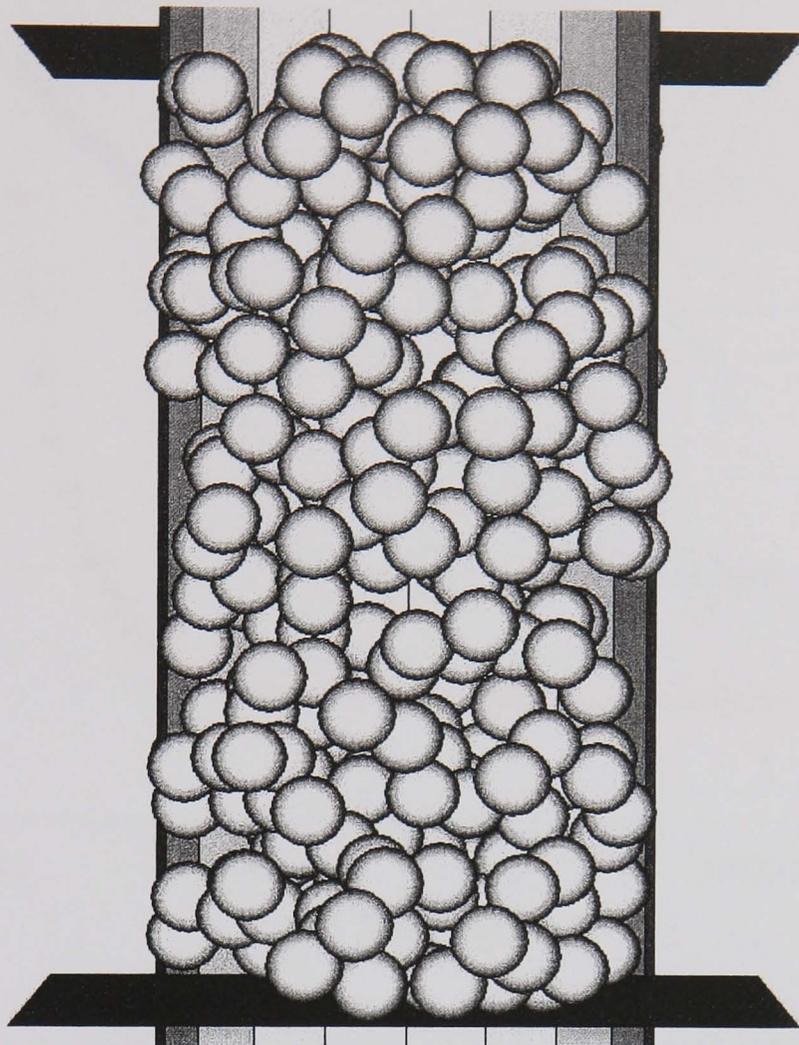
Figure 4.3: Particles expanded to final radii.
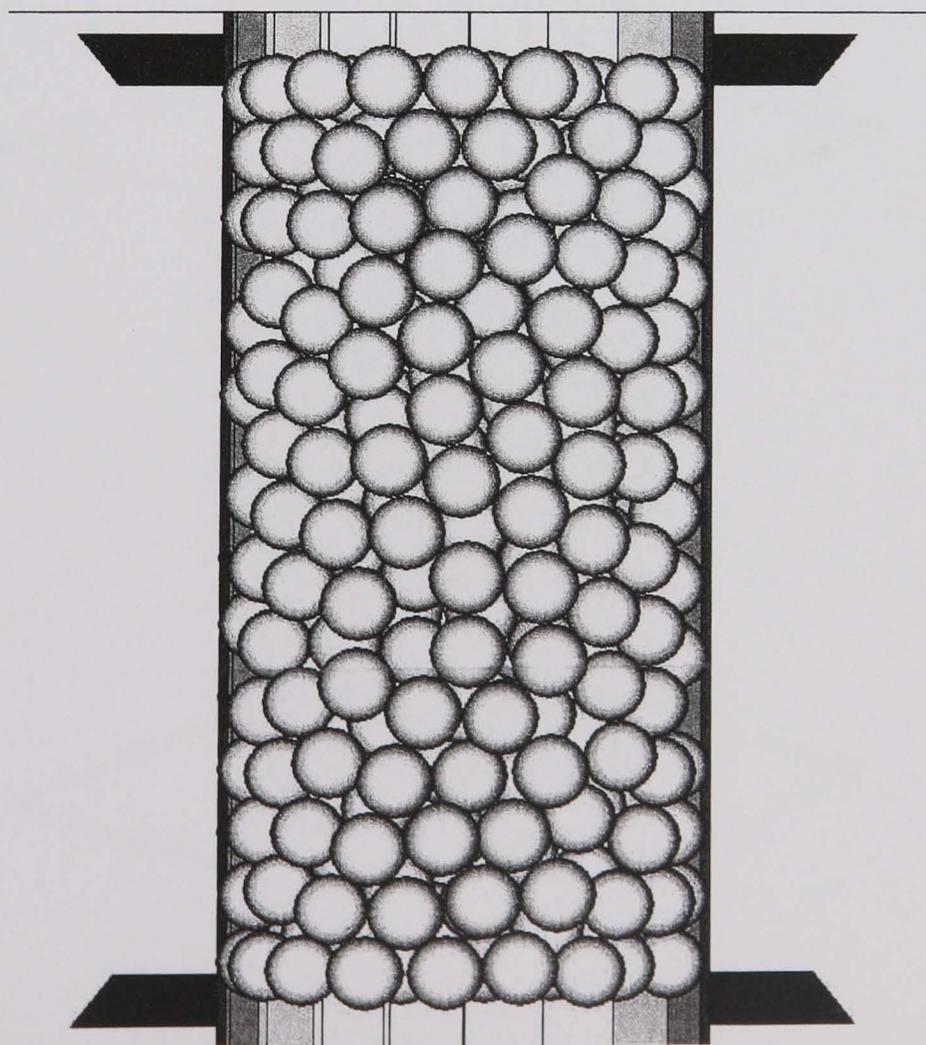
Figure 4.4: Particle re-oriented to isotropic equilibrium state.
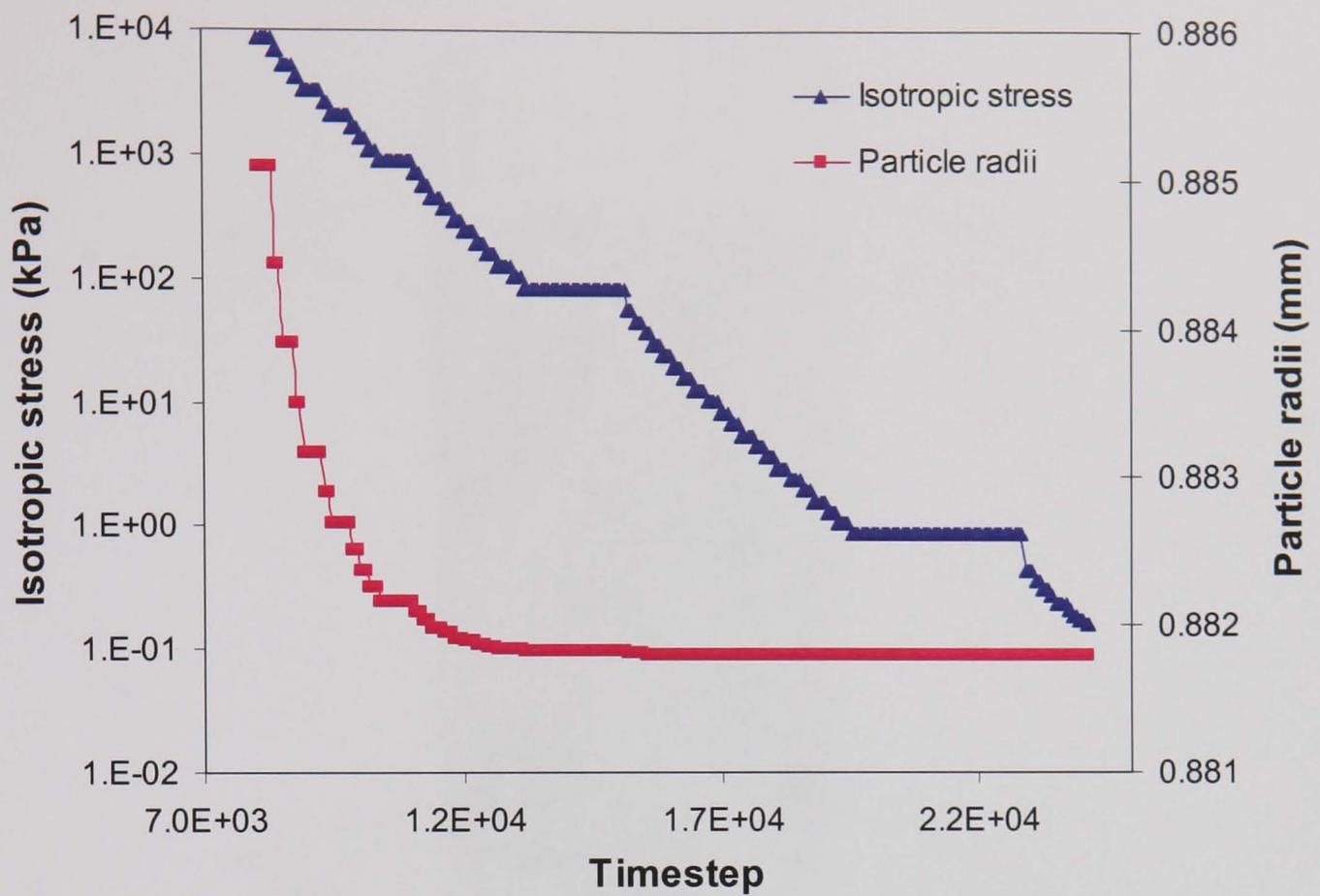
Figure 4.5: Effect of reduction of particle radii on isotropic stress.
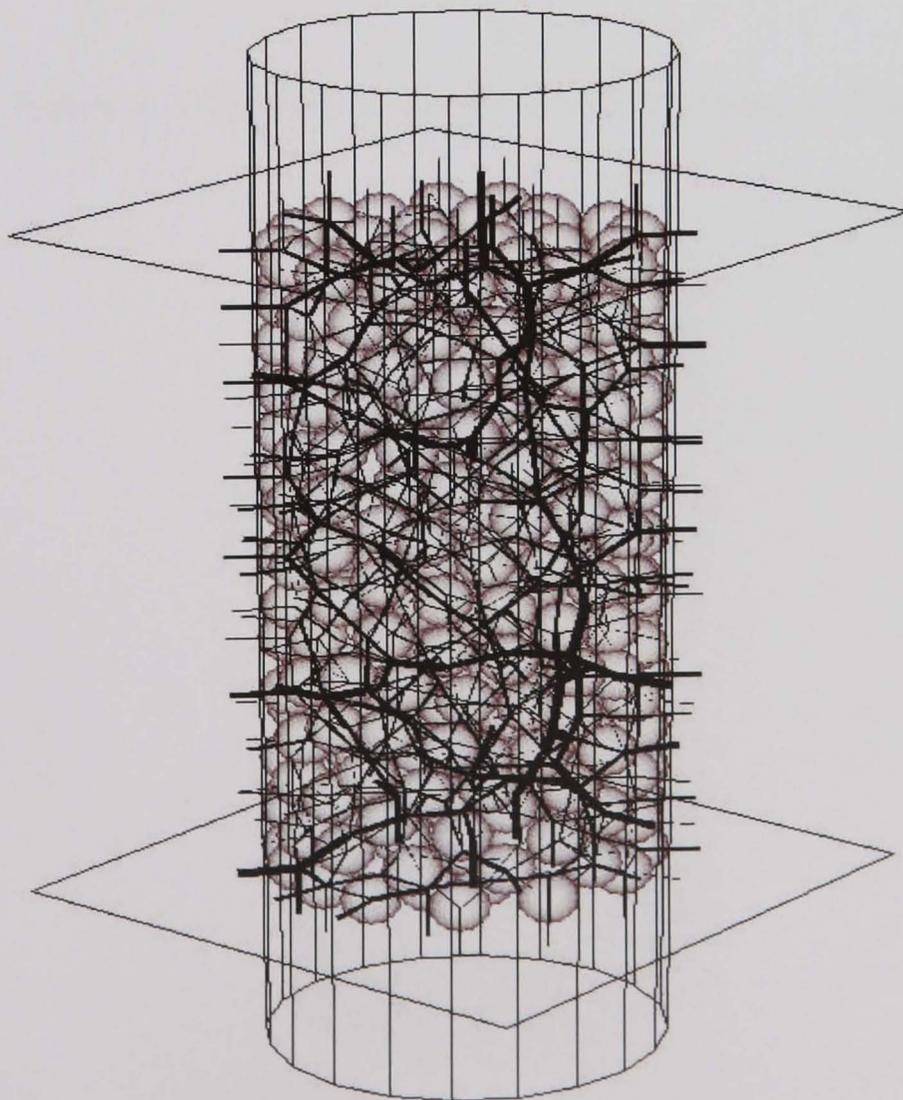
Figure 4.6: Contact force distribution under isotropic stress.
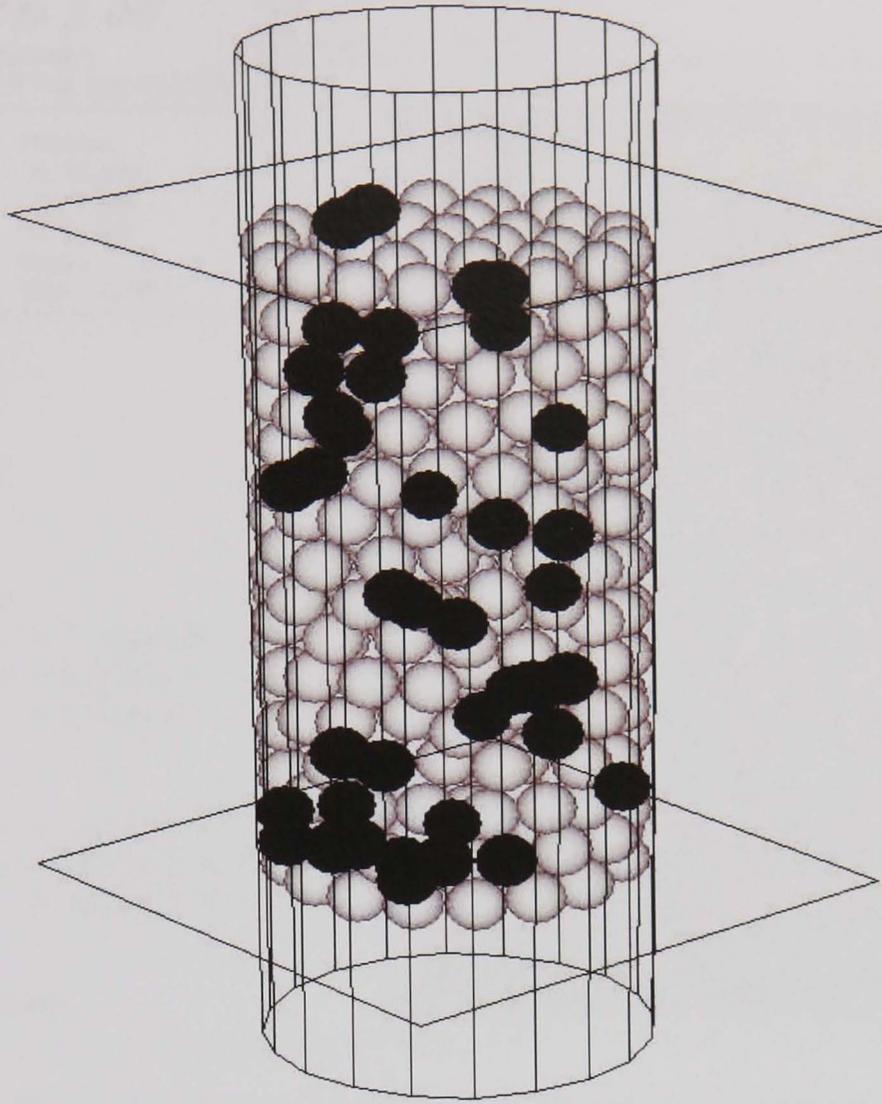
Figure 4.7: Location of particles with less than four contacts.
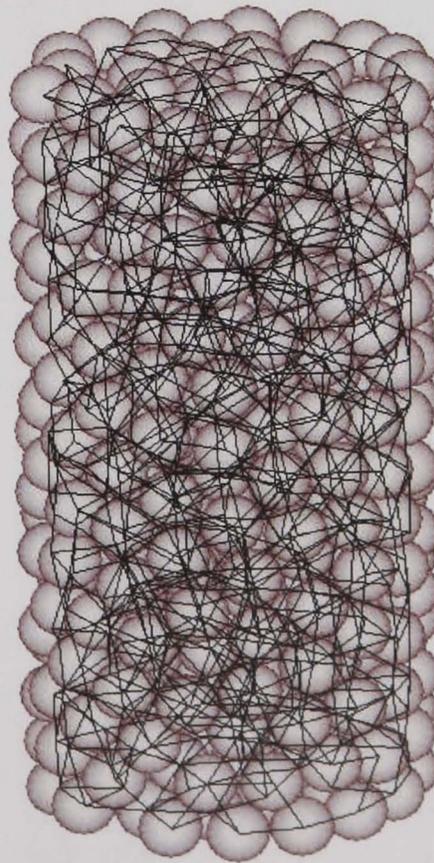
Figure 4.8: Contact bond network.

PFC3D 3.00
Settings: ModelPerspective
Step 34231 14:40:09 Tue Sep 09 2003

Center: Rotation
 X: 0.000e+000   X: 90.000
 Y: 0.000e+000   Y: 0.000
 Z: 0.000e+000   Z: 0.000
 Dist: 8.013e-002   Mag.:   1
                            Ang.: 22.500

Ball

CForce Chains
 ■ Compression
 ■ Tension

 Compression:
      Minimum = 1.14e-6 N
      Maximum = 5.20e-2 N
      Average   = 2.53e-3 N

 Tension:
      Minimum = -2.14e-8 N
      Maximum = -8.17e-2 N
      Average   = -5.95e-3 N

University of Nottingham
NCPE & NCG

Job Title: sample size effects
View Title: Contact force distibution

Figure 4.9: Locked-in forces in tension and compression.
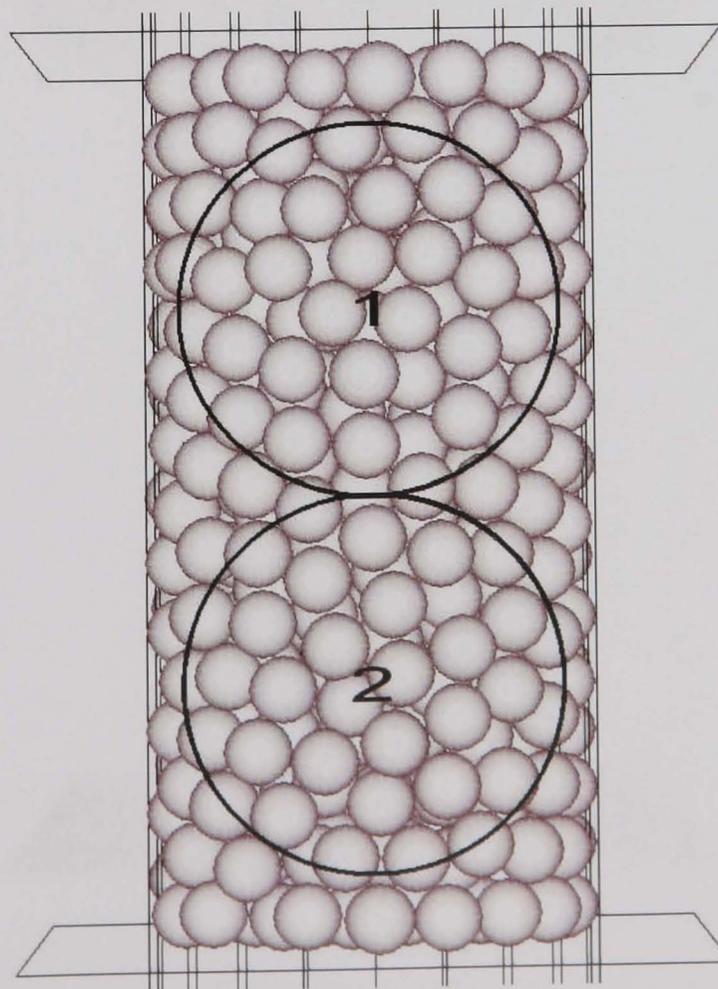
Figure 4.10: Measurement spheres in the sample.
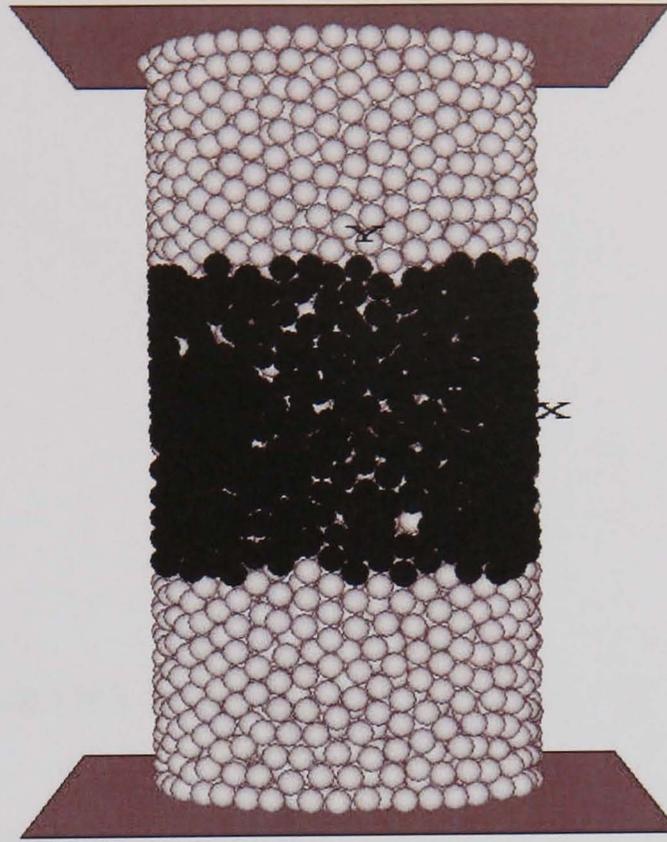
Figure 4.11: Gauge thickness of 40% to sample height.
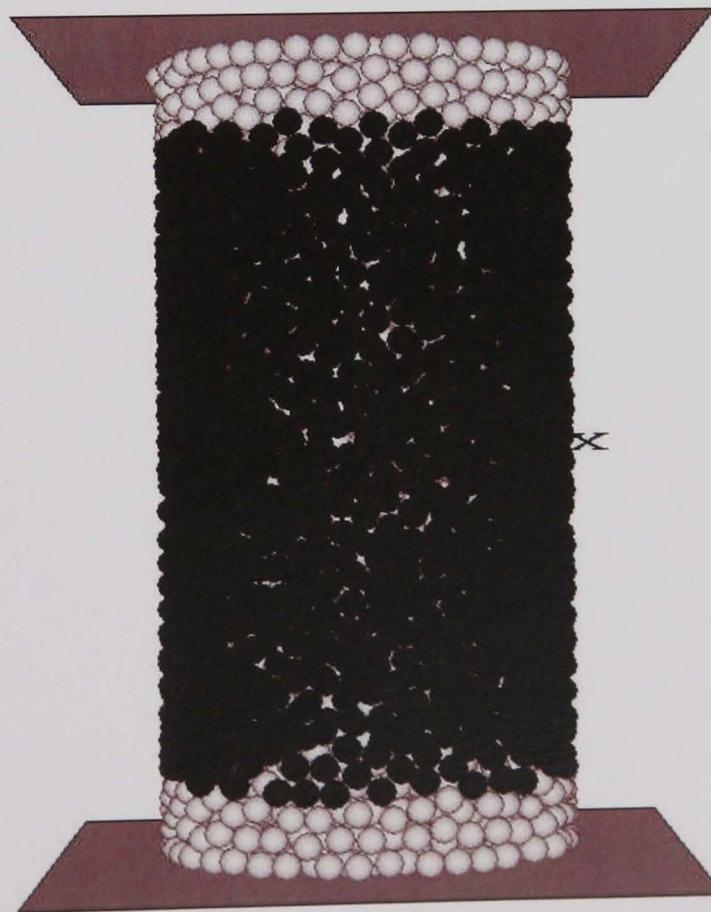
Figure 4.12: Gauge thickness of 80% to sample height.
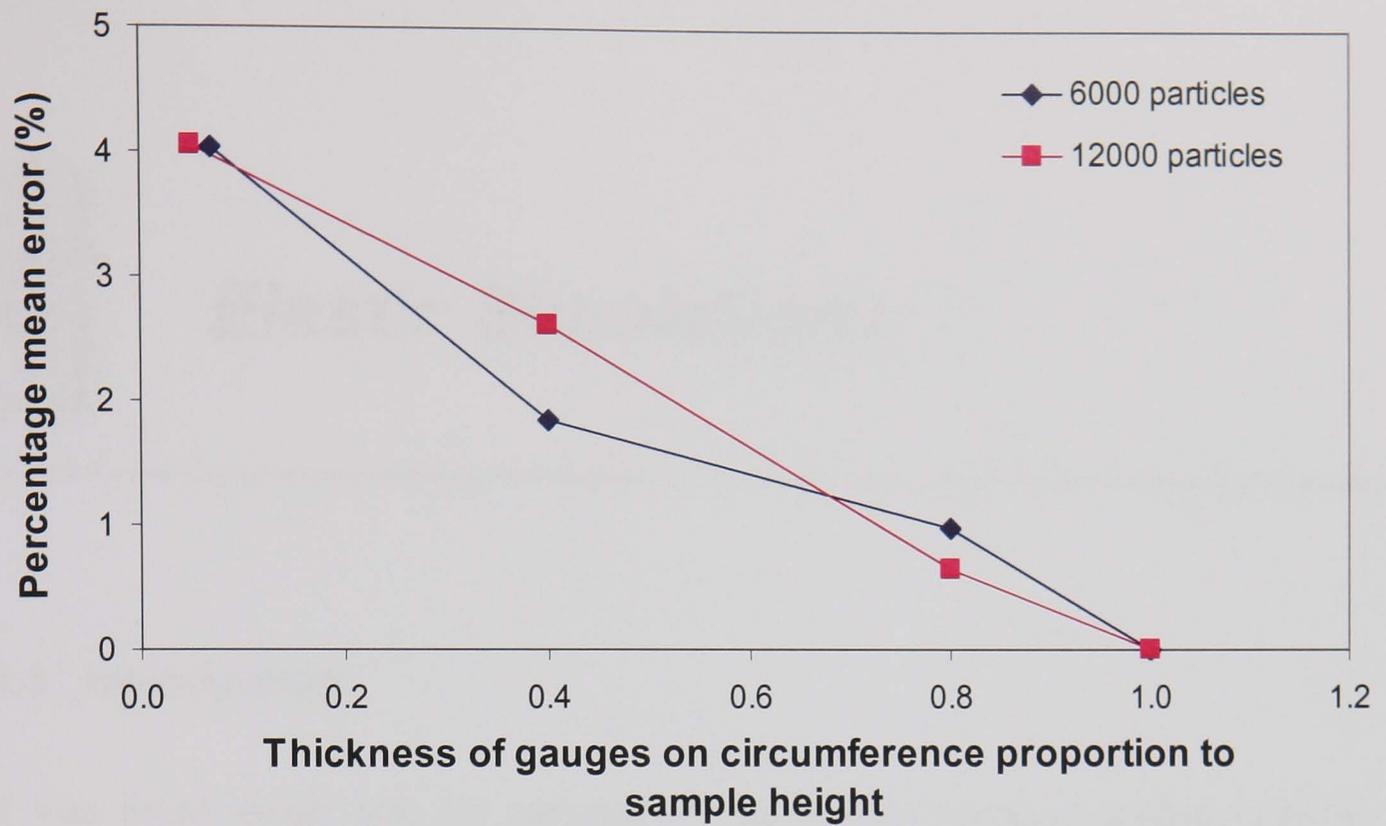
Figure 4.13: Percentage mean error of two samples at different thicknesses of gauges.

5 | Elastic Simulations

5.1 Introduction

It was noted earlier that the response of the type of idealised asphalt mixture simulated in this thesis will be dominated by the bitumen. It is well known that bitumen is a viscoelastic material whose response depends on loading time and temperature. This section investigates the elastic part of the response by using linear elastic normal and shear contact stiffnesses. As noted earlier, in this type of approach the effect of the bitumen is represented as shear and normal contact stiffnesses and so other more complex theories for contact between elastic bodies (ie Hertzian contact) are not appropriate. Time dependent effects will be introduced in a later chapter.

The following sections investigate the effects of sample size and the shear and normal contact stiffnesses on elastic bulk material properties (Young's modulus, Poisson's ratio, shear modulus, bulk modulus). The second part of this chapter investigates the effect of non-equal tensile and compressive normal contact stiffness on the dilation behaviour.

5.2 Material Properties

In a DEM elastic simulation, the effect of the bitumen is represented as elastic shear and normal contact stiffnesses and the aggregates are represented as spherical particles. All particles are bonded together with elastic normal and shear contact bonds to resist the tensile stresses between the particles. It should be noted that the

normal and shear contact stiffnesses are calculated relating the stiffnesses of two particles in contact as described in Equations 3.12 and 3.13.

A contact bond breaks when the tensile stress it is carrying exceeds the particle strength, σ_c or τ_c. The contact-bond normal and shear strengths, ϕ_n and ϕ_s, are expressed in units of force: thus the desired strength criterion relating contact-bond strengths and particle strengths is described in PFC3D manual [1] as:

$$\phi_n = 4\sigma_c R^2$$

$$\phi_s = 4\tau_c R^2 \tag{5.1}$$

All samples are prepared according to the sample preparation procedure described in Chapter 4. The material properties that are used for the elastic simulation are summarised in Table 5.1. Single sized particles were used in the simulations and the friction coefficient between particles was set to zero. The shear stiffnesses and friction coefficients between the loading platens and the particles were also set to zero to avoid sample barrelling and hence ensure a uniform deformation of the sample when subjected to loading. To simulate the behaviour of asphalt as a bonded material, the particle normal and shear bond strengths were taken to be large to avoid bond breakage during the simulation.

5.3 Effects of Number of Particles

Since the DEM method is based on simulating individual particles, it is necessary to determine the effect of the sample size on bulk material properties. A series of uniaxial simulations was performed on six samples generated with different numbers of particles. The samples were generated according to the developed sample preparation procedure described in Chapter 4. The material properties are shown in Table 5.1. Figure 5.1 shows the example of three samples size. The dimensions of all samples are shown in Table 5.2. The ratio of sample height to sample diameter was kept constant at 2:1 for all samples. In these simulations the absolute values of the shear and normal contact stiffnesses were taken to be $1.8MN/m$ and $20MN/m$,

respectively. The ratio of the normal contact to the shear contact stiffness was chosen to give a reasonably realistic value of Young's modulus and Poisson's ratio.

To simulate a uniaxial compressive creep test it is necessary to apply an axial load (stress) to the sample and measure the axial displacement (strain) and radial displacement (strain) during the test. The load was applied at a maximum velocity of 0.1m/s to ensure that dynamic wave propagation effects within the sample are avoided (see section 5.4). The samples were loaded numerically and the simulation was terminated at an axial strain of 0.5%. No bond breakage was detected during the simulations.

The compressive and tensile forces are approximately uniformly distributed in the sample under loading as shown in Figure 5.2. It should be noted that the thickness of the lines corresponds to the magnitude of contact force generated. In this figure, the red chains indicate the compressive forces, which transmit between the top loading platen and the bottom platen (fixed) in the sample under compression. The black chains indicate tensile forces, which developed almost laterally between the particles. This is because as the particles compress vertically they move laterally and hence tensile forces develop.

During the simulation, the axial strain was calculated using the displacement of the top loading platen (the bottom loading platen was fixed) and the radial strain was taken to be the average radial strain for all particles on the circumference of the specimen. In all simulations, the relationships between axial stress and axial strain are found to be linear as plotted in Figure 5.3. Linear relationships are also found from the plot of radial strain against axial strain (Figure 5.4) for all samples.

Young's modulus and Poisson's ratio for all samples are determined from the gradients of the curves shown in Figures 5.3 and 5.4 and are plotted in Figure 5.5. It can be seen from Figure 5.5 that the general trend is for Poisson's ratio to decrease and Young's modulus to increase as the sample size (number of particles) is increased, tending towards constant values of 0.34 and 3.6*GPa* respectively. It can also be seen from this figure that Young's modulus and Poisson's ratio calculated

from the sample containing only 300 particles are approximately 30% lower and 28% higher than those calculated from the sample containing 6,000 particles.

The main purpose of performing the sample size effect analysis was to choose a sample size which is large enough to fully represent the material behaviour but small enough to reduce the computation time. Therefore, it can be concluded from Figure 5.5 that at least 4,500 particles are required for the results to be with 2% of those obtained using 12,000 particles. It should be noted that in later chapters, samples containing fewer particles have been used to speed up the computation. In these cases, Figure 5.5 can be used to give an indication of the likely error in prediction due to a smaller sample.

5.4 Effects of Loading Rate

In DEM, the contact forces and displacements of a stressed assembly of particles are found by tracing movements of the individual particles. Movements result from the propagation through the particle system of disturbances caused by specified wall and particle motion and/or body forces [3]. A higher wall velocity imposed on the sample can cause the dynamic stress wave to propagates within the sample. Hazzard et al [51] indicated that the loading velocity has little effect on the mechanical behaviour of the modelled sample as long as it is slow enough to ensure that no transient waves are being produced.

The loading rate in the numerical simulation must be low enough to avoid dynamic effects but high enough to reduce the computation time. Therefore, an optimum loading rate is required to maintain the accuracy of simulation. To examine the effects of loading rate, a series of uniaxial simulations was performed by using 4,500 particle samples with different loading rates. The loading rates were chosen arbitrarily range from 0.05 *m/s* to 5 *m/s*. It is should be noted that only the top loading platen was allowed to move and the bottom loading platen was fixed. The reaction stresses on top and bottom loading platens were recorded at 5% axial strain in the simulations.

Figure 5.6 shows a plot of reaction stresses on the top and bottom platens at the different loading rates. It can be seen from this figure that the difference between the reaction stresses on top and bottom platens increases at the higher loading rates. The difference in stresses between platens was recorded as 12% at a loading rate of 1.2 *m/s* and 0.8% at a loading rate of 0.1 *m/s*. This indicates that by applying a lower loading rate (0.1 *m/s*) dynamic effects could be avoided. This effect can be further explained in Figure 5.7 and 5.8. It can be seen from Figure 5.7 that at a loading rate of 1.2 *m/s*, the reaction stresses on both loading platens fluctuate. This clearly indicates the effect of transient or dynamic stress wave propagation within the sample at the higher loading rate. However, it can be seen from Figure 5.8 that the loading rate of 0.1 *m/s* resulted in a virtually identical reaction stresses on the platens.

Consequently, a loading rate of 0.1 *m/s* was chosen as the optimum loading rate.

5.5 Effects of Normal and Shear Contact Stiffness on Bulk Properties

As noted earlier, the bulk properties (macro-response) of the sample depend on the micro-properties (contact stiffness etc.) of the particles in the sample. This section investigates how the bulk material properties depend on the shear and normal contact stiffnesses of the particles. To investigate this effect, a series of uniaxial simulations were performed over a range of contact stiffnesses and ratio of shear to normal contact stiffnesses of the particles in the sample.

A sample containing 6,000 particles was used. Its micro-properties are shown in Table 5.1. Figure 5.9 shows a plot of Young's modulus corresponding to shear contact stiffnesses of $0.5MN/m$, $5MN/m$ and $50MN/m$. The normal contact stiffnesses were varied so that the ratios of shear to normal contact stiffnesses (K_S / K_N) range from 0.2 to 1.0. It can be seen from this figure that the Young's modulus varies at different ratios of (K_S / K_N). This indicates that the value of Young's modulus depends on both shear and normal contact stiffnesses. It can also be seen from Figure 5.9 that at the same ratio of shear to normal contact stiffness (e.g. 0.6),

increasing the ratio of shear contact stiffnesses by a factor of ten results in an increment of Young's modulus by a factor of ten.

Figure 5.10 shows the relationship between Poisson's ratio and the ratio of shear to normal contact stiffnesses for a range of shear contact stiffnesses. Poisson's ratio (defined as ratio of radial to axial strain) was found to increase as the ratio of (K_S / K_N) is reduced. This indicates that the material is more incompressible at the smaller ratio of (K_S / K_N). It can be seen from Figure 5.10 that Poisson's ratio is only dependent on the ratio of shear to normal contact stiffness. This is the expected result since, by dimensional analysis, Poisson's ratio can only depend on the ratio of contact stiffnesses and not their absolute values. It can be concluded from Figure 5.10 that a (K_S / K_N) ratio of 0.1 gives a reasonably realistic Poisson's ratio of approximately 0.35 for the idealised mixtures. However, no experimental data is available for justification.

The relationships between shear and normal contact stiffnesses and bulk material properties (Young's modulus and Poisson's ratio) have been established. There is also a possibility to establish a relationship between the shear and normal contact stiffnesses and the bulk modulus of the material. It should be noted that the bulk modulus is defined as the ratio of mean stress increment to volumetric strain increment. The standard elastic equation for relating bulk modulus K to Young's modulus E and Poisson's ratio v is:

$$K = \frac{E}{3(1-2v)} \qquad (5.2)$$

Figure 5.11 shows a plot of bulk modulus versus normal contact stiffness for a range of shear contact stiffnesses. It can be seen from this figure that the bulk modulus is linearly related to the normal contact stiffness and is approximately independent of the shear contact stiffness.

To explain this, a mean field approach has been adopted to theoretically investigate the dependence of bulk modulus on normal contact stiffness [27]. The response in

isotropic compression of a triaxial sample containing a random array of identical spheres has been considered. General details relating to the mean field approach can be found in Jenkins and Strack [60].

For a general pair of spherical particles of radius R in contact, α is taken to be the unit vector from the centre of a particle to the contact point. Assuming that particle centres move in accordance with a uniform displacement field, the displacement u of a contact relative to the centre of a sphere can be calculated from the average strain ε of the aggregate (taking compressive strain as positive):

$$u_i = -R\varepsilon_{ij}\alpha_j \qquad (5.3)$$

where ε_{ij} is the strain tensor. The underlying assumption in this statement is that the average particle spin is equal to the rigid body rotation of the particle [60]. The force $F(\alpha)$ exerted on a sphere at a contact with orientation α is given in terms of its components parallel and perpendicular to α:

$$F_i = -P\alpha_i + T_i \qquad (5.4)$$

with $\mathbf{T}\cdot\mathbf{\alpha} = 0$. P and T are the normal and tangential components of forces. The key step in the mean field approach is the application of the principle of virtual work, with an arbitrary set of compatible strains and displacements:

$$\sigma_{ij}\varepsilon_{ij} = N_s \iint F_i u_i A(\alpha)\, d\omega \qquad (5.5)$$

where σ_{ij} is the stress tensor, N_s is the number of spheres per unit volume and $d\omega = \sin\theta\, d\theta\, d\phi$ is the element of solid angle centred at α. $A(\alpha)$ is the orientational distribution of contacts defined such that $A(\alpha)d\omega$ is the probable number of contacts in an element of solid angle $d\omega$ centred at α. For an isotropic distribution of contacts,

$$A(\alpha) = \frac{C}{4\pi} \tag{5.6}$$

where C is average number of contacts per particle (co-ordination number). Substituting Equation 5.3 and 5.6 into Equation 5.5 gives:

$$\sigma_{ij} = -\frac{N_s CR}{4\pi} \iint F_i \alpha_j \, d\omega \tag{5.7}$$

For isotropic conditions, the mean field approach predicts no tangential displacements at particle contacts, and no tangential contact forces. In this case, substituting Equation 5.4 into Equation 5.7 gives:

$$\sigma_{ij} = \frac{N_s CR}{4\pi} \iint P\alpha_i \alpha_j \, d\omega \tag{5.8}$$

The mean stress p is then given by:

$$p = \sigma_{ii}/3 = \frac{N_s CR}{12\pi} \iint P \, d\omega \tag{5.9}$$

The normal contact force in the PFC3D aggregate is related to the contact overlap δ and the normal contact stiffness k_n by the equation:

$$P = k_n \delta \tag{5.10}$$

and the mean field approach gives the normal displacement $\delta/2$ as a function of volumetric strain as:

$$\delta = R\frac{\varepsilon_v}{3} \tag{5.11}$$

Substituting Equation 5.10 and 5.11 into Equation 5.9, and integrating over all contacts gives:

$$p = \frac{2N_s CR^2 k_n}{9} \varepsilon_v \qquad (5.12)$$

so that the bulk modulus K is related to normal contact stiffness according to the equation:

$$K = \frac{2N_s CR^2}{9} k_n \qquad (5.13)$$

The number of spheres per unit volume N_s is related to the percentage volume of air voids in the sample *(Vv)* and the radius of a sphere R by the equation:

$$N_s = \frac{3(100 - V_V)}{400\pi R^3} \qquad (5.14)$$

so that for an isotropic sample, the bulk modulus is related to the percentage volume of air voids in the sample and particle radius according to the following equation:

$$K = \frac{(100 - V_V)C}{600\pi R} k_n \qquad (5.15)$$

The predicted relationship using Equation 5.15 is also shown in Figure 5.11 (solid line) using the following parameters $V_V = 36\%$, $C = 6$, $R = 0.9$mm. It can be seen that agreement is generally very good with the predicted bulk modulus using Equation 5.15 (for a given normal contact stiffness) being slightly greater than the predicted bulk modulus using PFC3D [28] .

It should be noted that Young's modulus and the shear modulus could be calculated from the bulk modulus and Poisson's ratio using the standard elastic equations (Equation 5.2 and 5.16).

$$G = \frac{3K(1 - 2v)}{2(1 + v)} \qquad (5.16)$$

It can be seen from Equations 5.2 and 5.16 that, since Young's modulus and the shear modulus depend on both the bulk modulus and Poisson's ratio, they will be functions of the ratio of the shear to normal contact stiffness as well as their absolute values.

5.6 Modelling Dilation of an Asphalt Mixture

The mechanism of dilation in asphalt is not well understood. Deshpande and Cebon [41] stated that an important factor in modelling the deformation behaviour of a particulate granular material such as asphalt is the phenomenon of "dilatancy", which causes an increase of volumetric strain with distortional strain. This phenomenon was first revealed by Reynold [91] where he stated that for a granular material in a state of maximum density, any contraction in one direction is accompanied by equal extensions in mutual perpendicular directions. It was later adopted in Rowe's "stresss-dilatancy" theory [96]. Previous researchers [40, 65] indicated that the dilation gradient of an asphalt material is dependent on the volume fraction of aggregate in the mixture. Deshpande [40] and Khanzada [65] performed experimental work on single sized sand asphalt with 64% volume fraction of aggregate under uniaxial and triaxial constant stress compression creep tests. They concluded that the single sized sand asphalt dilates significantly under loading.

As noted above, in previous simulations the normal contact stiffnesses in tension and compression are assumed to be equal. This results in high overlapping magnitude at every contact in compression because the identical normal contact stiffnesses (in compression and tension) are forcing the particles to overlap in compression rather than roll past each other giving no volumetric dilation of the sample. This can be seen in Figure 5.10 where the Poisson's ratio values are less than 0.5.

Cheung [22] and Harvey [49] suggested that a thin film bitumen exhibits a different "effective" stiffness in tension and compression as a function of the geometry of the thin film. For mechanical modelling of the asphalt mixture, there are two sets of normal contact stiffnesses to be considered. The first set are the compression contact

stiffnesses, which are defined as the stiffnesses at contacts where pairs of particles are subjected to compressive forces. The second set are the tension contact stiffnesses, which are defined as the stiffnesses at contacts where pairs of particles are subjected to tensile forces. In the default PFC3D modelling code, these two contact stiffnesses are assumed to be the same. Therefore, for micromechanical modelling of the asphalt mixture, the normal contact stiffnesses are given by:

$$F_C = [K_C] \times U_C \quad \text{(compression)}$$

$$F_T = [K_T] \times U_T \quad \text{(tension)} \tag{5.17}$$

where,

F_C = Magnitude of contact force in compression

F_T = Magnitude of contact force in tension

U_C = Magnitude of overlapping at contact point

U_T = Distance of particle separation at contact point

$[K_C]$ = Compressive contact stiffness

$[K_T]$ = Tensile contact stiffness

The default PFC3D code was modified to enable the definition of different sets of contact stiffnesses in tension and compression. The in-built algorithms have been designed to recognise contacts in compression and tension, and then use the force-displacement law to calculate the particle displacement. For compressive contact, the particle overlapping magnitude is calculated based compressive contact stiffness. Whilst for tensile contact, the separation distance between two particles is calculated based on tensile contact stiffness. This modified code is then introduced to simulate the sample with elastic contacts to investigate the effect on bulk properties.

5.7 Effect of non-equal tensile and compressive normal contact stiffnesses

The previous sections investigated the effect of normal and shear contact stiffness on bulk properties where the tensile and compressive normal contact stiffnesses were

taken to be equal. The objective of this section is to investigate the effect of non-equal tensile and compressive normal contact stiffnesses on bulk material properties.

5.7.1 Effect of the ratio of compressive to tensile contact stiffness (K_C/ K_T) where K_S = K_C

This sub-section investigates the effect of the ratio of compressive to tensile contact stiffnesses on dilation where the shear contact stiffness is taken to be equal to the compressive contact stiffness. A dense random packing sample of 1000 particles was generated according to previously developed sample preparation procedures. A very high contact bond strength is applied to all contacts to prevent bond breakage. The compressive and shear contact stiffnesses are taken to be equal to 0.6 *MN/m* (chosen arbitrarily) and the tensile contact stiffnesses have been reduced so that the ratio of compressive to tensile contact stiffness ranges from 1 to 200. Five elastic simulations were performed. From the observations of contact force distribution in PFC3D, most of the compressive contact forces were found to be vertical due to the applied compressive loading, whereas most of the tensile contact forces were found to be horizontal.

Figure 5.12 shows the dilation gradient plotted as a function of the ratio of compressive to tensile contact stiffness for the case where the shear contact stiffness has been taken to be equal to the compressive contact stiffness (diamond symbols). The dilation gradient (*s*) is defined as the ratio of the volumetric strain (*H*) divided by the distortional strain (*E*) and has been used to quantify dilation. The volumetric strain (*H*) and distortional strain (*E*) are defined for a cylindrical specimen as:

$$H = 2\varepsilon_{11} + \varepsilon_{33}$$

$$E = \varepsilon_{33} - \frac{H}{3} = \frac{2}{3}(\varepsilon_{33} - \varepsilon_{11})$$

(5.18)

where ε_{11} is defined as the radial strain and ε_{33} is defined as the axial strain. It should be noted that, using this sign convention for a compression test, the radial strain is tensile and positive and hence the distortional strain is negative since the

axial strain is compressive and negative. In all the figures presented in this thesis, the magnitude of the distortional strain has been plotted.

A negative value of dilation gradient implies that the material is reducing in volume (contracting) whereas a positive dilation gradient means that the material is increasing in volume (dilating). It can be seen from Figure 5.12 that the dilation gradient increases as the ratio of compressive (and shear) to tensile contact stiffness is increased. It can also be seen from this figure that the general trend is for the dilation gradient to increase tending towards an approximately constant value of 0.7 at high stiffness ratios indicating a significant amount of dilation which was not found when the tensile and compressive contact stiffnesses were taken to be equal. This is because the relatively high compressive contact stiffnesses (compared to the tensile contact stiffness) are forcing the particles to roll past each other rather than simply overlap in compression resulting in dilation. Skinner [104] stated that rolling must be accompanied by a volume change and, if the aggregate is in its most dense arrangement, this volume change would be a dilation.

When the ratio of compressive (and shear) to tensile contact stiffness is reduced to one, a dilation gradient of -1.0 is observed indicating contraction in the sample. In a compressive test, the average contact forces in compression are much higher than the average contact forces in shear and tension. By defining an identical value for all contact stiffnesses in compression, shear and tension on a bonded material, the overlapping magnitude (displacement in compression) is much larger compared to the particle displacement in shear and tension. Hence, the particles tend to overlap instead of moving in shear and tension directions.

5.7.2 Effect of the ratio of compressive to shear and tensile contact stiffnesses, (K_C/ K_T) where K_S = K_T

This sub-section investigates the effect of the ratio of compressive to tensile contact stiffnesses on dilation where the shear contact stiffness is taken to be equal to the tensile contact stiffness. For all simulations in this section, the value of compressive

contact stiffness is taken to be 0.6 *MN/m* and the ratio of compressive to shear (and tensile) contact stiffness was varied between 1 and 200.

Figure 5.12 (rectangular symbols) shows the dilation gradients from these simulations plotted against the ratio of compressive to the shear (and tensile) contact stiffness. It can be seen from this figure that, above the stiffness ratio of approximately 10, the values of dilation gradients are positive indicating dilation. The dilation gradient increases as the ratio of compressive to shear (and tensile) contact stiffness increased, tending towards a constant value of approximately 0.8. It should be noted that the general shape of the curve is the same as shown previously (diamond symbols) although, for the same stiffness ratio, the value of dilation gradient is greater. This is because for a given ratio of compressive to tensile contact stiffness, the shear contact stiffness is lower than in the previous case resulting in higher levels of shear deformation giving greater dilation.

5.7.3 Effect of the ratio of compressive to shear contact stiffness (K_C / K_S) where $K_T = K_C$

This sub-section investigates the effect of the ratio of compressive to shear contact stiffness on dilation where the tensile contact stiffnesses are taken to be equal to the compressive contact stiffnesses. For all simulations in this section, the contact stiffnesses in compression and tension were taken to be equal to 0.6 *MN/m* and the ratio of compressive (and tensile) to shear contact stiffness was varied between 1 and 200.

Figure 5.12 (triangular symbols) shows the dilation gradients plotted against the ratio of compressive (and tensile) to shear contact stiffness. It can be seen from this graph that the dilation gradient tends to increase as the ratio of compressive (and tensile) to shear contact stiffness is increased. However, it can also be seen from this figure that above a stiffness ratio of approximately 20, the dilation gradient is approximately constant at a value of -0.20 indicating that the material is contracting.

It can also seen from Figure 5.12 (triangular symbols) that the dilation gradient increases from -1.0 to -0.4 when the ratio of compressive (and tensile) to shear contact stiffness increases from 0 to 10. This indicates that the material is less compressible when the ratio of compressive (and tensile) to shear contact stiffness is higher. However, increasing this ratio can only reduce the compressibility of the material but not the dilation level. No experimental verification is available to justify this effect hence further experimental work is needed.

5.8 Conclusions

The following conclusions can be drawn from this chapter:

- Elastic contact properties have been used to investigate the effect of sample size (number of particles) and the effect of the values of shear and normal contact stiffnesses on bulk material properties (Young's modulus, bulk modulus and Poisson's ratio).

- A sample containing at least 4,500 particles is required for Young's modulus of Poisson's ratio to be within 2% of the values calculated using a much larger number of particles.

- Poisson's ratio was found to be dependent on only the ratio of shear contact stiffness to the normal contact stiffness.

- The bulk modulus was found to be linearly dependent on the normal contact stiffness and independent of the shear contact stiffness. A mean field approach was used to develop a theoretical model that predicted this behaviour.

- The sample was found to dilate under non-equal normal compressive and tensile contact stiffnesses.

- The level of dilation was found to be dominated by the ratio of normal compressive to normal tensile contact stiffnesses.

• The dilation gradient was found to increase when the ratio of normal compressive to normal tensile contact stiffnesses increases.

Tables:

Table 5.1 Micro-properties of material used for elastic simulation

Symbol	Description	Magnitude
R	Particle radius	0.885 *mm*
ρ	Particle density	2630 *kg/m³*
μ	Particle friction coefficient	0
σ_c	Particle normal strength	200 *MPa*
τ_c	Particle shear strength	200 *MPa*
k_{nw}	Platen normal stiffness	200 *MPa*
k_{sw}	Platen shear stiffness	0
μ_w	Platen friction coefficient	0

Table 5.2: Dimensions of the samples with different numbers of particles.

Number of particles	Sample height (*mm*)	Sample width (*mm*)
300	19.6	9.8
1,000	29.2	14.6
3,000	42.0	21.0
4,500	48.0	24.0
6,000	52.0	26.0
12,000	66.0	33.0

Figures:
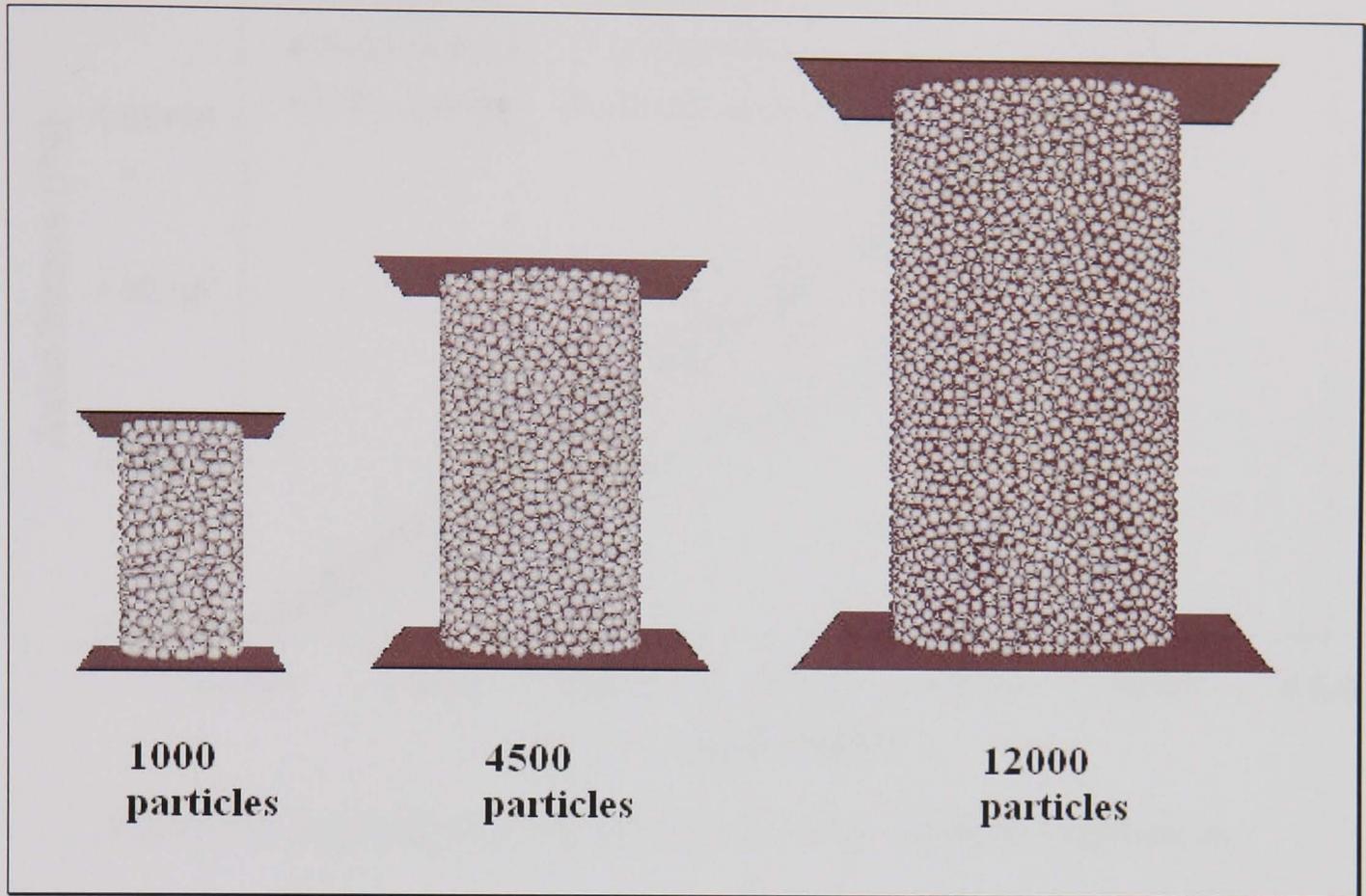
Figure 5.1: Three samples of different sizes.
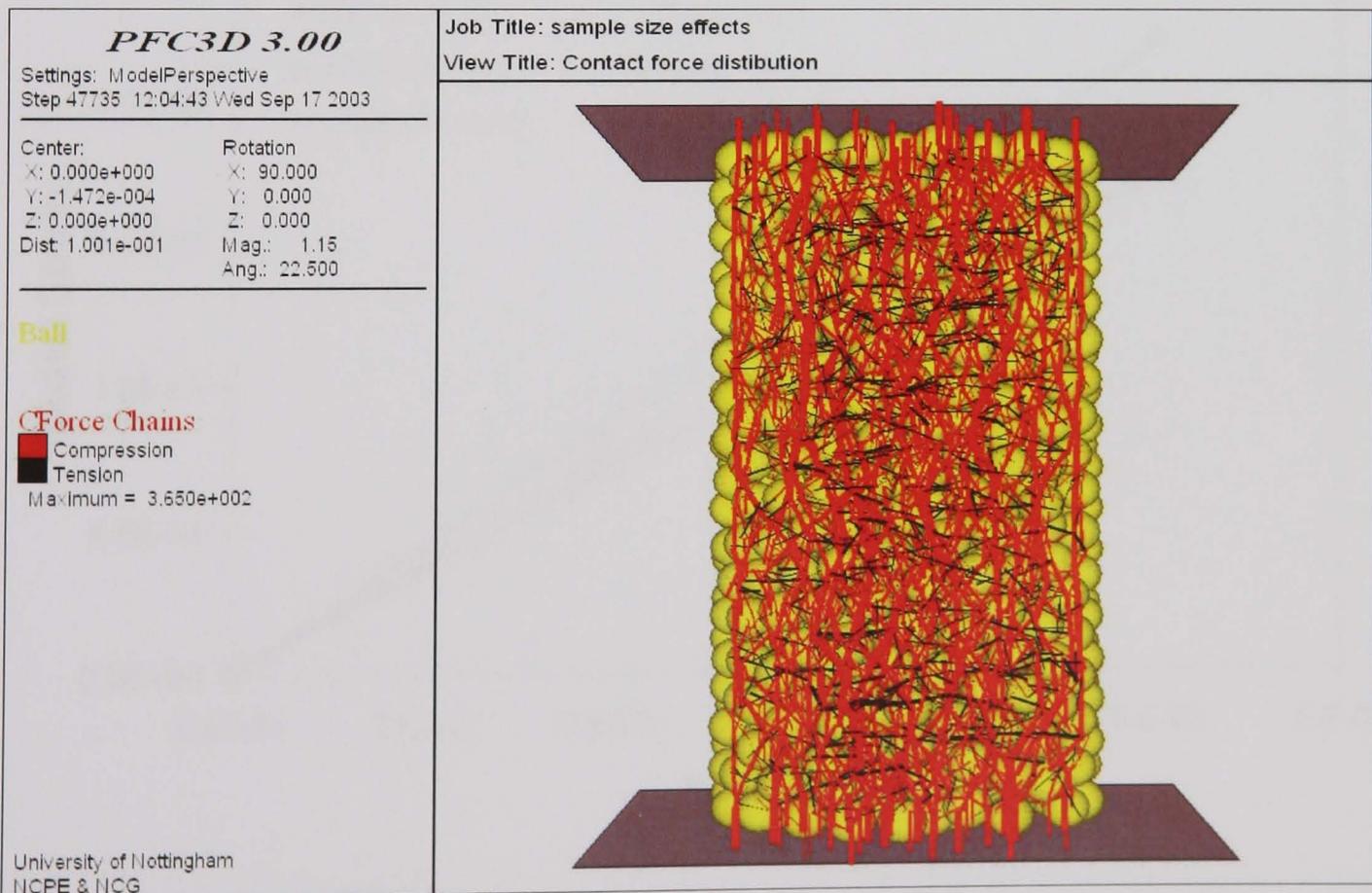
Figure 5.2: Contact forces distribution in a 4,500 particle sample.
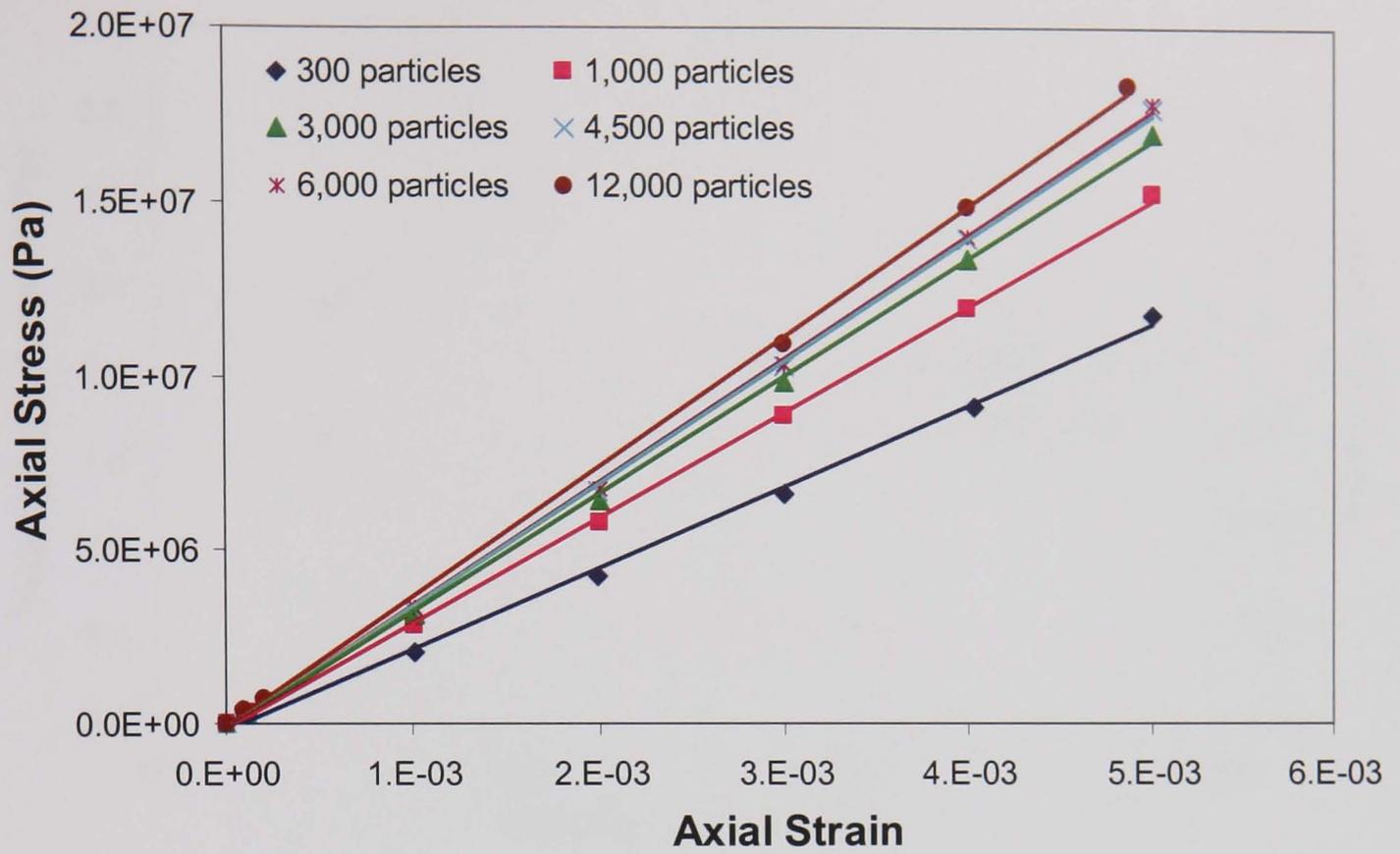
Figure 5.3: Axial stress versus axial strain for the different sample sizes.
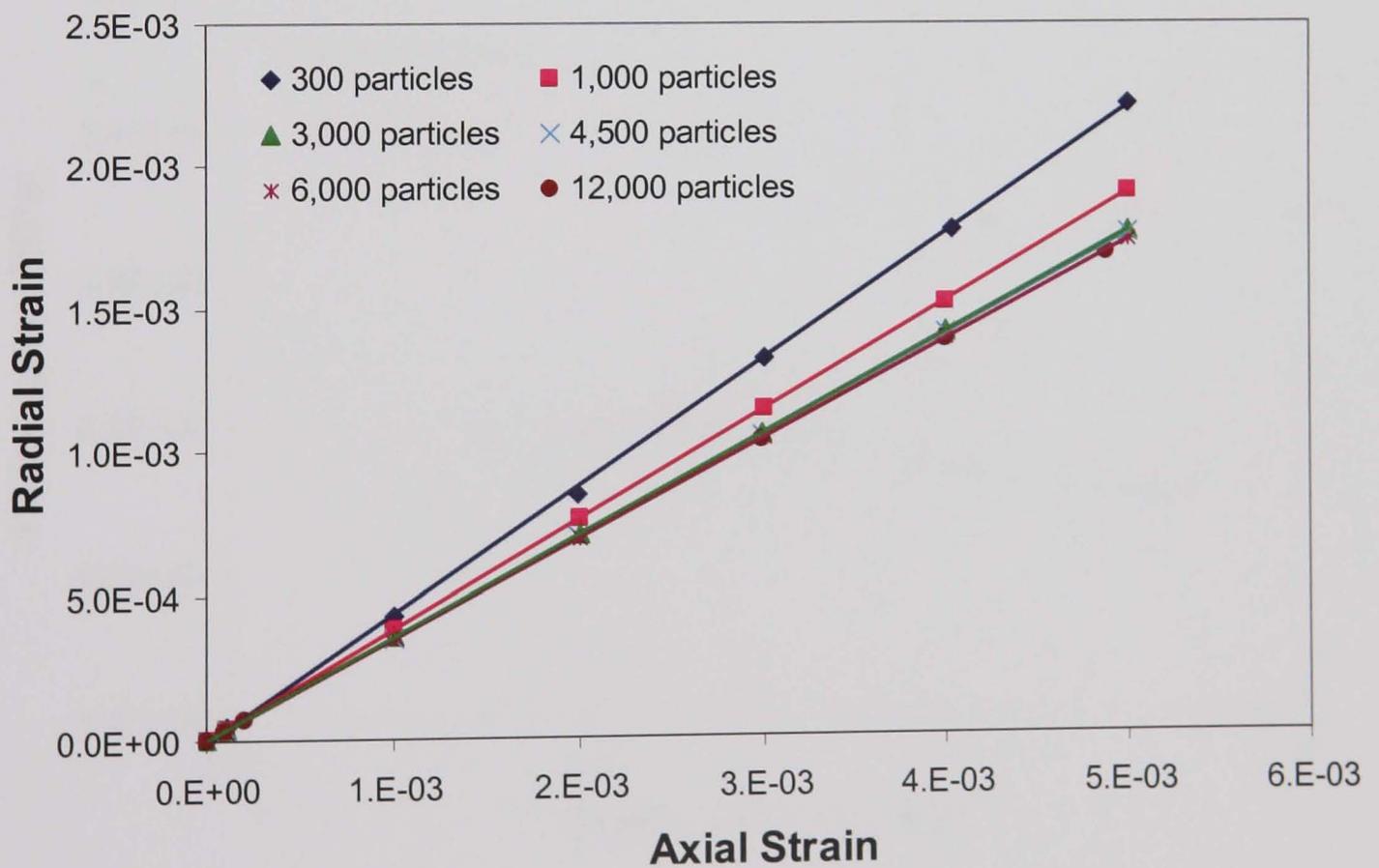
Figure 5.4: Radial strain versus axial strain for the different sample sizes.
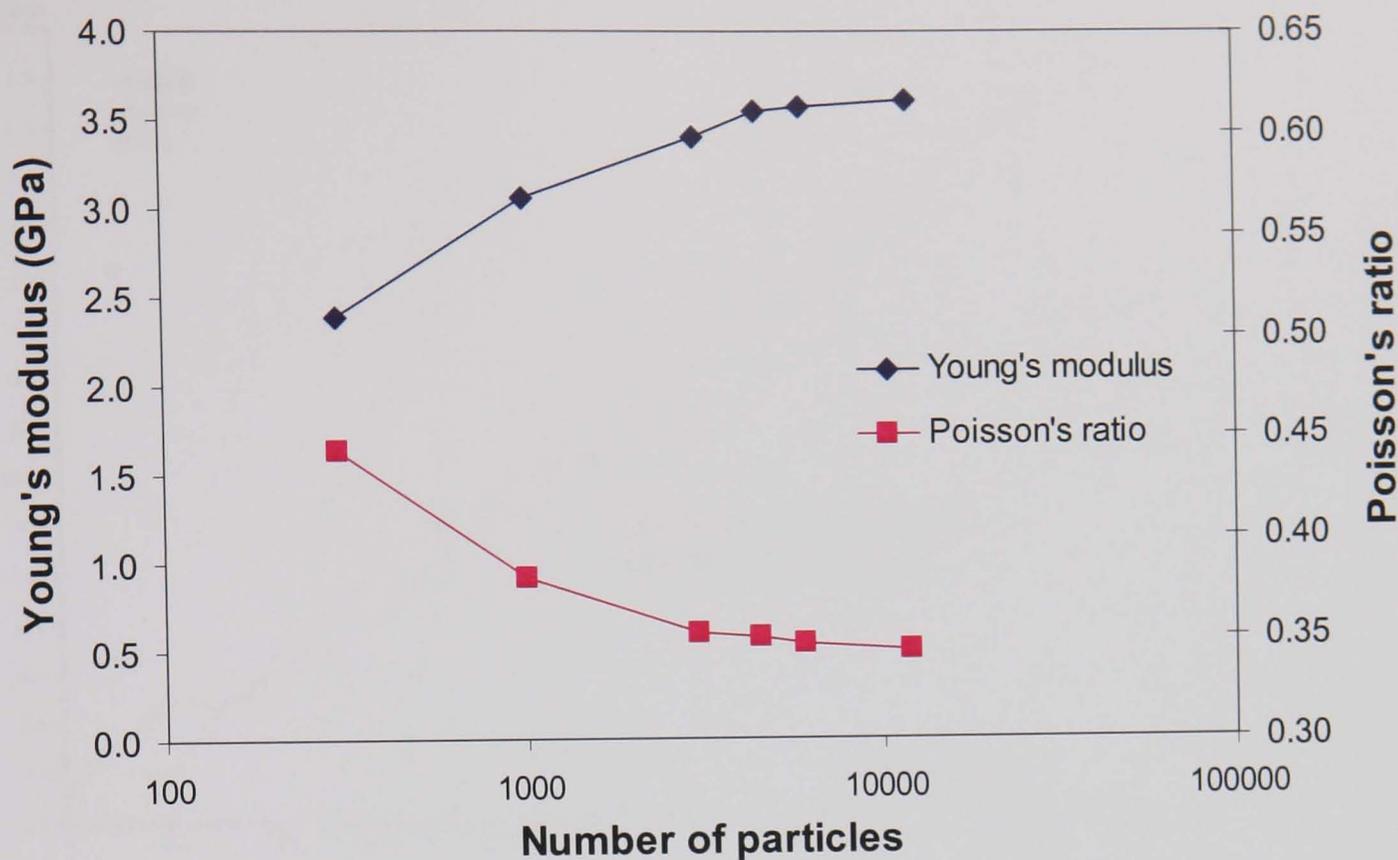
Figure 5.5: Effects of the number of particles on bulk elastic properties.
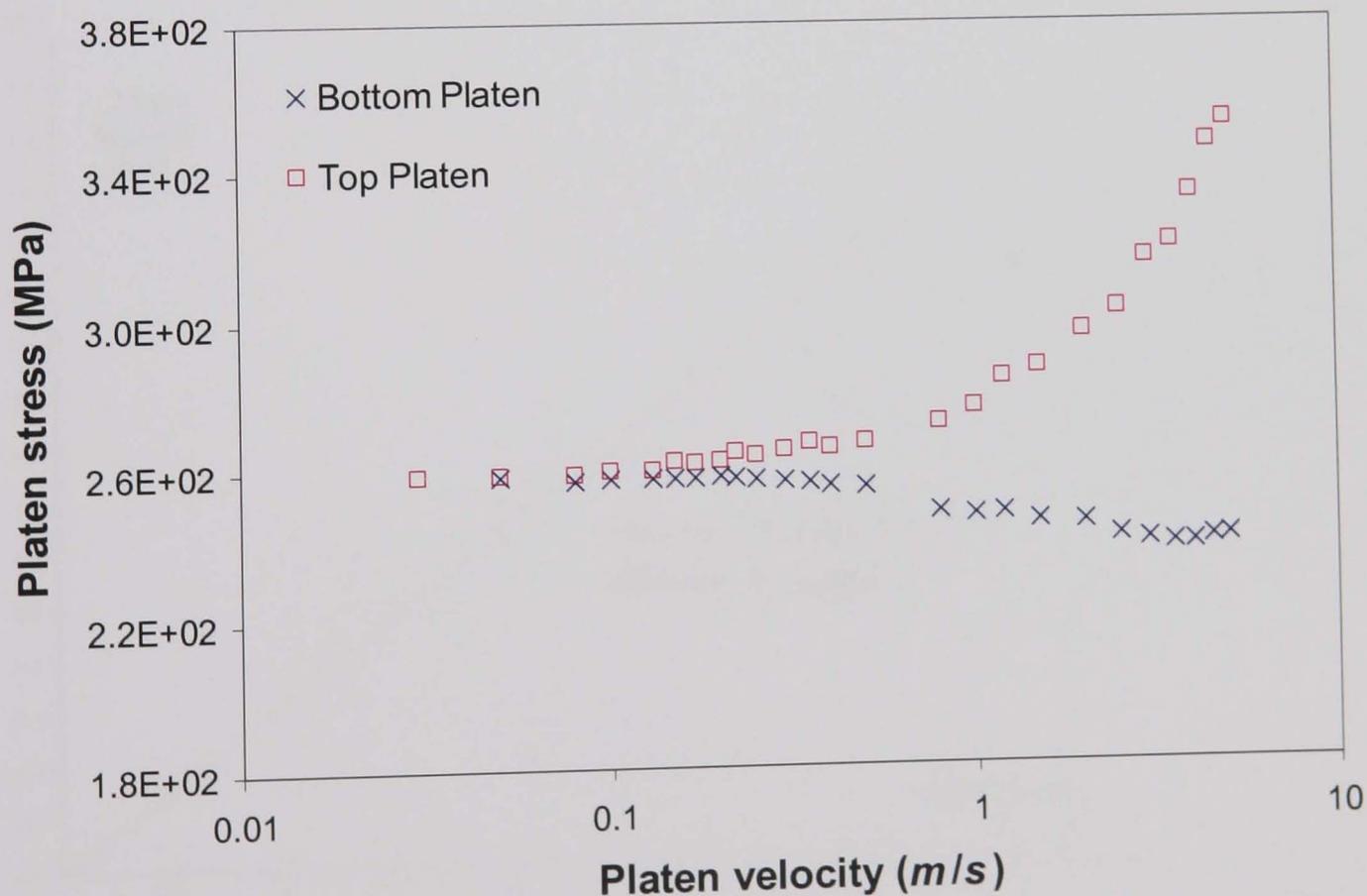
Figure 5.6: Reaction stresses on loading platens at different loading rates.
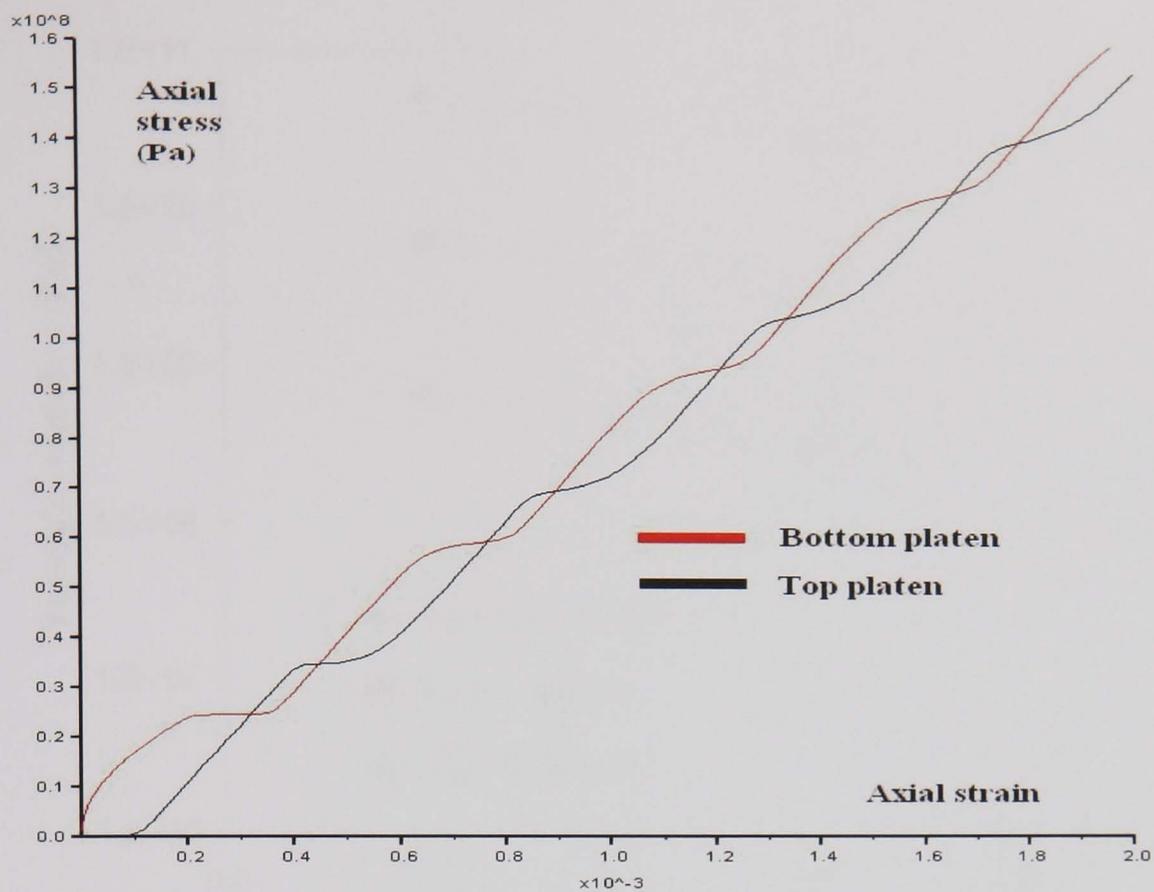
Figure 5.7: Reaction stresses on loading platens at loading rate of 1.2 m/s.
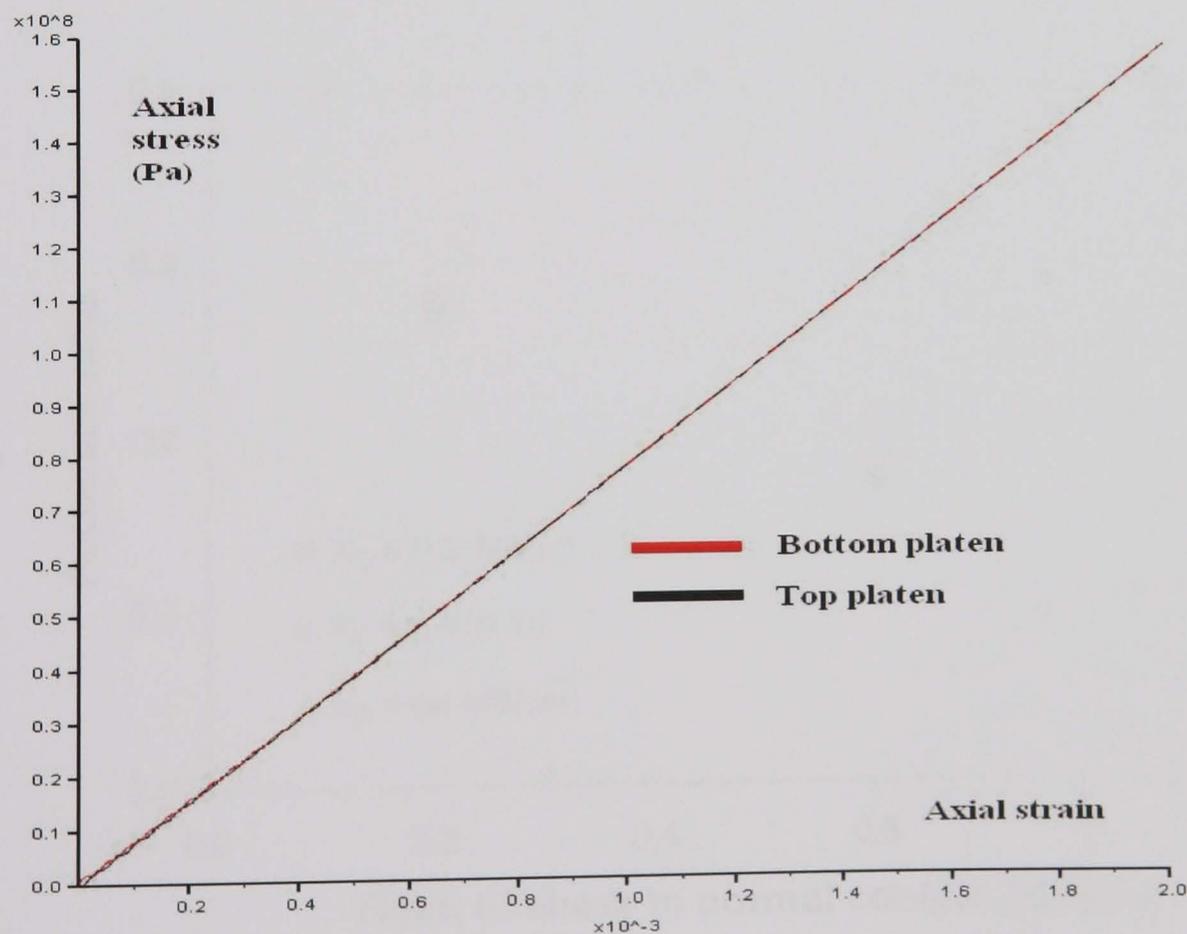
Figure 5.8: Reaction stresses on loading platens at loading rate of 0.1 m/s.
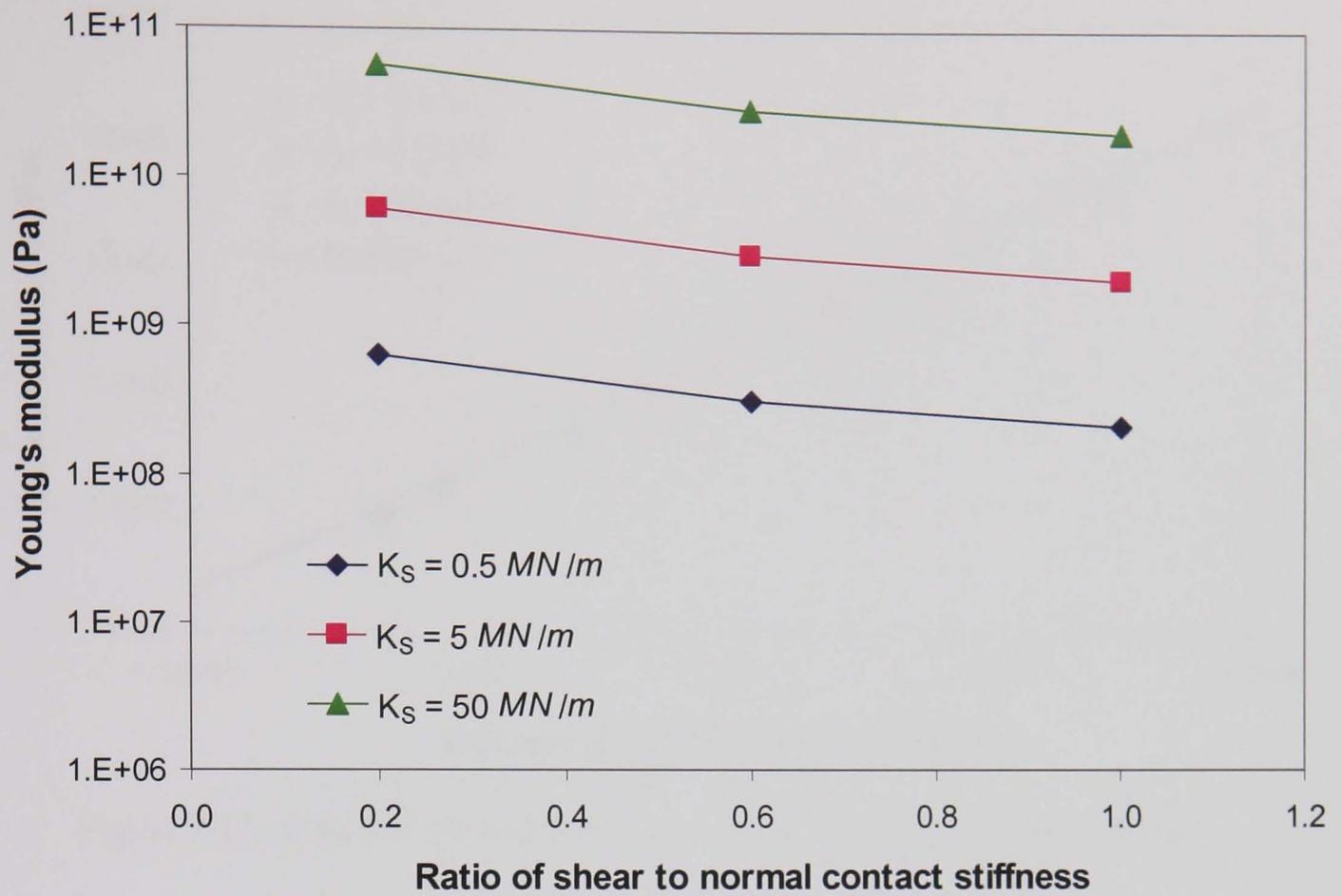
Figure 5.9: Effect of shear and normal contact stiffnesses on Young's modulus.
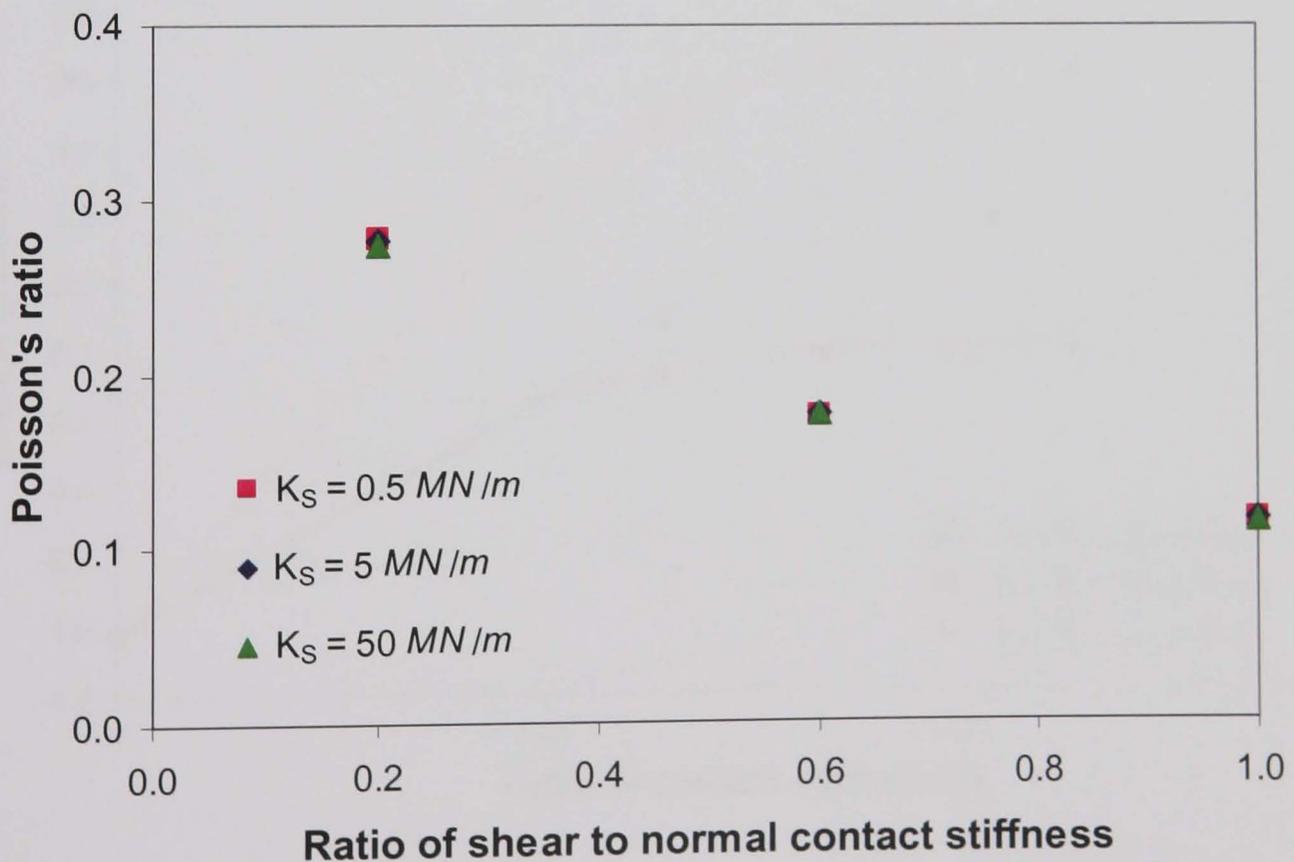
Figure 5.10: Effect of shear and normal contact stiffnesses on Poisson's ratio.
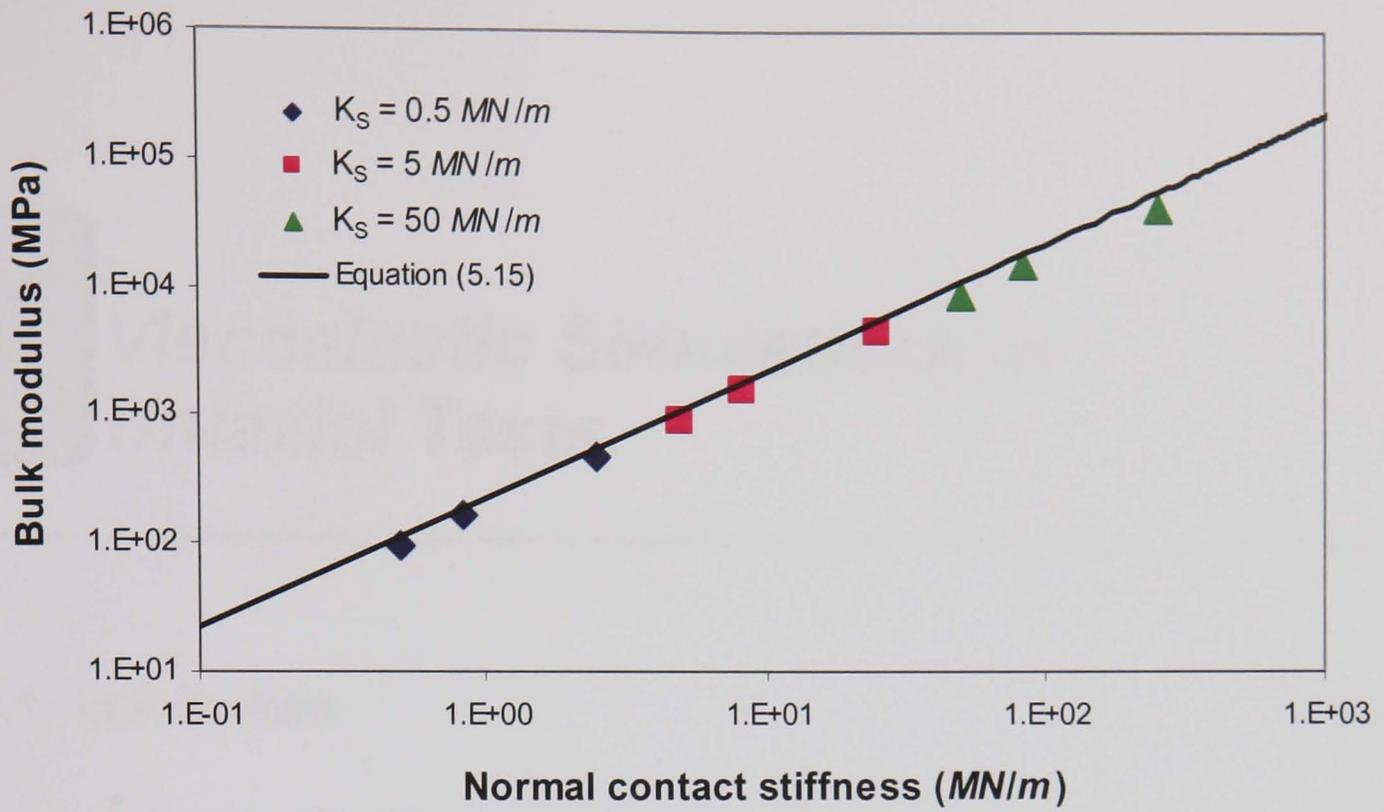
Figure 5.11: Effect of normal and shear contact stiffness on bulk modulus
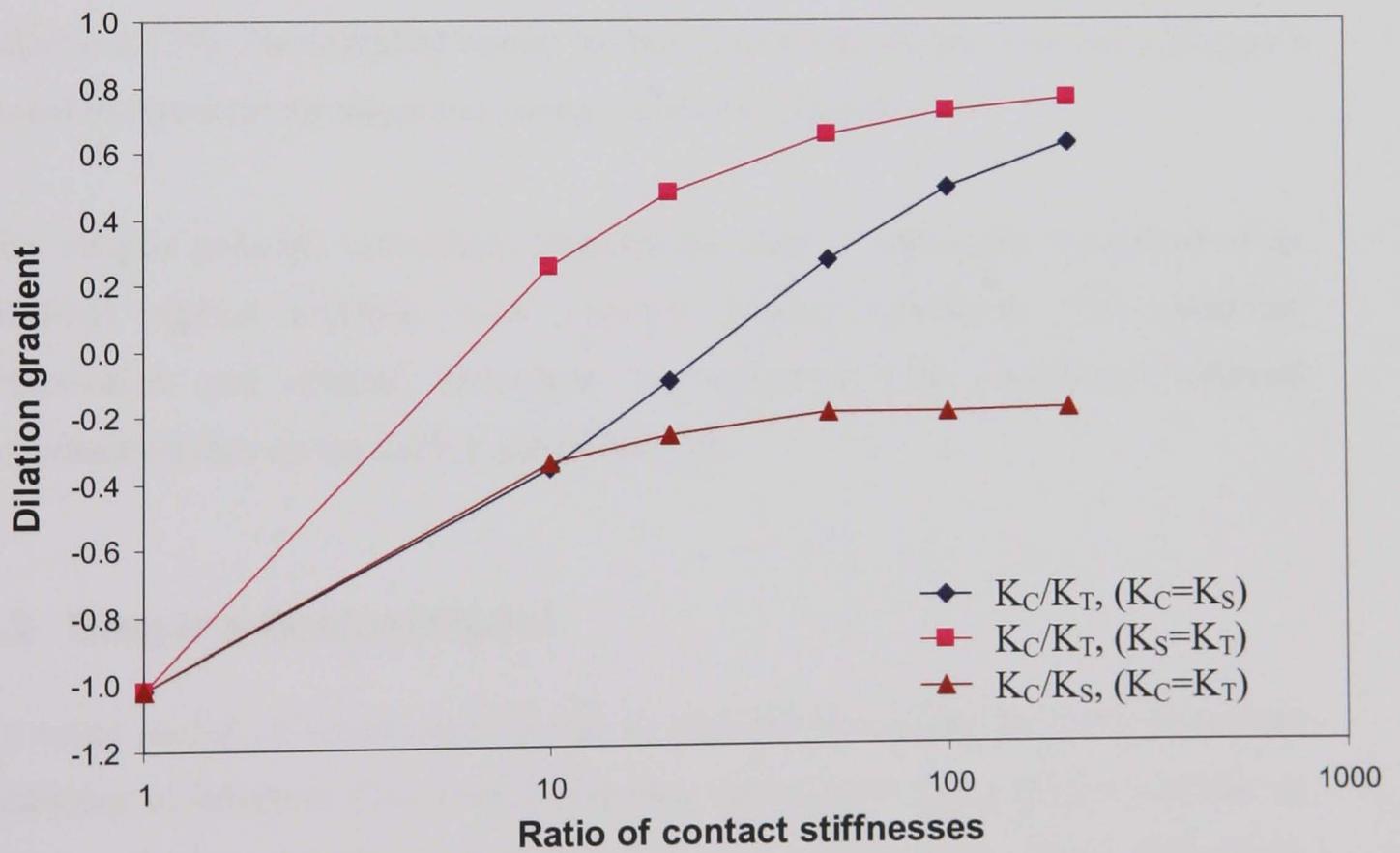
Figure 5.12: Dilation gradients versus ratio of contact stiffnesses.

6 Viscoelastic Simulations of Uniaxial Tests

6.1 Introduction

It was noted earlier that the behaviour of the idealised asphalt mixture is likely to be dominated by the bitumen and complex aggregate interlock effects are minimised in this type of mixture. It is well documented that asphaltic materials are both loading rate and temperature dependent exhibiting elastic, delayed elastic and viscous behaviour [39]. The simplest option to introduce these effects is to use a Burger's model to represent the shear and normal contact stiffnesses.

This chapter presents viscoelastic simulations used to model the behaviour of an idealised asphalt mixture under uniaixal loading conditions. The predicted deformation and dilation behaviour is compared with previously obtained experimental data on the same material [40, 65].

6.2 Burger's Contact Model

As noted earlier, a viscoelastic model is required to capture the time dependent behaviour of bitumen. The most appropriate option is to use a Burger's model to represent the contact stiffnesses. A Burger's model (for the shear contact stiffness) is shown in Figure 6.1. It can be seen that this model comprises a spring (K_1^s) and dashpot (C_1^s) in parallel (delayed elastic component) connected in series to a spring (K_0^s, elastic component) and a dashpot (C_∞^s, viscous component). It can readily be shown that the time dependent shear stiffness of the Burger's model is given by:

$$k_s = \left[\frac{1}{K_0^s} + \frac{t}{C_\infty^s} + \frac{1}{K_1^s}\left(1 - e^{-t/\tau^s}\right) \right]^{-1} \qquad (6.1)$$

where t is the loading time and $\tau^s = C_1^s/K_1^s$ is the relaxation time. It can be seen from Equation 6.1 that the contact stiffness will reduce as a function of loading time. In reality, the time dependent bond properties will be significantly more complicated. However, this simple approach is a necessary step before introducing additional complexities that require purpose written contact stiffness algorithms (user-defined subroutine in PFC3D).

The Burger's contact model is significantly more complex than its elastic counterpart requiring much more computation time. To increase the computation speed, a sample $7.3mm$ in diameter and $29.2mm$ in height, comprising 1,000 particles was used in the simulation. It should be noted that the sample was prepared using numerical sample preparation procedure described in Chapter 4. The model parameters are given in Table 6.1 and were chosen arbitrarily so that the shape of the predicted axial strain curve was similar to measured data for a similar material. The normal contact parameters were chosen to be a factor of 10 larger than the shear contact parameters so that the ratio of the initial (elastic) radial strain to the initial (elastic) axial strain (i.e. Poisson's ratio) would be similar to the results for the elastic case presented in Chapter 5. A very high contact bond strength is applied to all contacts to prevent the bond breakage. It should be noted that a Burger's contact model will automatically be created at any new contact formed during the simulation. A constant stress (creep) of $400kPa$ was applied to the loading platen and maintained by the PFC3D servo control mechanism (described in Section 3.3.6) over a period of time.

Figure 6.2 shows the predicted axial strain plotted as a function of loading time. It can be seen from this figure that, as expected for this type of contact model, the strain response is a function of loading time comprising elastic, delayed elastic and viscous components. The Burger's contact parameters (Table 6.1) can be readily adjusted to best fit the experimental data. It should be noted that for simplicity, the

bulk properties shown are based on sample size comprising of 1.000 particles. However, the results based on sample sizes comprising of 1,000 and 6,000 particles are shown in Section 6.4.9 where the comparison with experimental results is reported.

The particle contact forces in compression, tension and shear are updated regularly during the simulation. Figure 6.3 shows an example of contact force distribution in a 1,000 particles sample. The red lines represent compressive forces and the black lines represent tensile forces. The thickness of the lines connecting the spheres corresponds to the magnitude of contact force generated. It can be seen from this figure that the compressive forces (distributed in vertical direction) are formed due to the axial compressive loading, whilst the tensile forces (distributed in lateral direction) are formed at contacts in tension which resisted by a very high bond strength.

6.3 Computation Time Optimisation

It was noted earlier that the DEM simulation using viscoelastic contacts is a time consuming process. This section describes the methods of reducing the computation time in DEM simulation.

It was thought that the computation time is likely to be dominated by the magnitude of timestep in the simulation. To reduce the computation time, the magnitude of the timestep was increased artificially by 8% in one second of loading time during the simulation. Figure 6.4 shows a plot of the incremental timestep magnitude during the simulation. It can be seen from this figure that the magnitude of timestep increases by the factor of two (from 3×10^{-7} to 6×10^{-7}) in a 12-second simulation. However, this approach was not able to significantly reduce the computation and an alternative approach was required.

It was noted in Chapter 3 that the magnitude of timestep in PFC3D is determined by $t_{crit} = \sqrt{M/K}$ [3]. This means that using a higher value of particle mass (*M*) will result in a larger magnitude of timestep in the simulation, hence reducing the

computation time. Six viscoelastic simulations were performed on an identical sample as used in Section 6.1 with the exception that each sample was generated with different particle density ranging from 2.63×10^3 to 2.63×10^8 kg/m^3. The effects of particle density on bulk properties of the sample were investigated.

Figure 6.5 shows the plot of axial strain as a function of time for simulations on the samples with different particle densities. It can be seen from this figure that after an initial period the simulations are all very similar in shape. The initial differences caused by different loading times to reach the target stress cased by the large inertia associated with the high mass particles which results in a slower acceleration of the loading platen.

The variation of radial and axial strain for simulations on the samples with different particle densities is shown in Figure 6.6. It can be seen from this figure that there was no difference in response between the samples. This can be explained by the fact that the magnitude of the particle density should not have any effect on the deformation mechanism in a sample under constant stress creep loading. The unbalanced forces for all simulations are shown in Figure 6.7. It was found that the unbalanced forces are higher in the simulation with a higher particle density. However, the unbalanced force is still reasonably low (i.e. less than 1×10^{-4} N) and can be considered negligible compared with the magnitude of contact forces between particles.

Figure 6.8 shows the computation time required for a 20-second creep simulation on the samples with particle density ranging from 2.63×10^3 to 2.63×10^7 kg/m^3. It was found that the computation time for a simulation on a sample with a particle density of 2.63×10^7 kg/m^3 is reduced by the factor of 300 compared with a simulation on a sample with a particle density of 2.63×10^3 kg/m^3. Consequently, in order to reduce the computation time, the sample generated with a particle density of 2.63×10^7 kg/m^3 will be used in all simulations in this thesis. It should be noted that the gravity was set to be zero in all simulations.

6.4 Effect of Bond Breakage

It was noted above by previous researchers that asphalt dilates under uniaxial and triaxial loading. The previous elastic simulations have shown that the dilation of an asphalt mixture is greatly influenced by the ratio of compressive to tensile contact stiffness. However, the effect of bond breakage on dilation is unknown. This section performs a uniaxial viscolastic simulation to investigate the effect of bond breakage on dilation.

A series of simulations were performed on an identical sample as that used in Section 6.2, with the exception that a fraction of contact bonds (range from 5 to 25%) were removed for each sample prior to loading. A constant stress of 400*kPa* was applied. Figure 6.9 shows a plot of radial versus axial strains for these simulations. It can be seen from this figure that the slopes of radial to axial strains increase from 0.3 to 1.0 as the percentages of bonds removed increase from 5% to 25%, which indicates that the volumetric dilation is greater in the simulations with higher percentage of bonds removed. This is because a lower number of bonds in the sample cause lower constraint in the particle system, hence giving greater volumetric dilation. Consequently, it was thought that dilation could be modelled by breaking bonds progressively (simulate micro-cracking in a real sample) during the simulation.

It was noted earlier that the contact bond breaks when the tensile force exceeds the bond strength. The tensile contact force distribution in the simulation above (fully bonded) is plotted in Figure 6.10. It can be seen from this figure that the tensile contact forces within the particles are distributed between 0.1N and 1.9N with an average value of 0.53N. A random contact bond strength distribution with a mean of 1.45N and a standard deviation of 0.03 (as shown in Figure 6.11) was chosen arbitrarily for a simulation containing 1,500 particles. The sample was again loaded with a constant stress of 400*kPa*.

The resulting axial strain plotted as a function of time is shown in Figure 6.12. It can be seen from this figure that the axial strain curve looks similar to the curve where no bonds have been removed until an axial strain of approximately 5% where a

dramatic increment in strain was observed indicating failure of the sample. The percentage of bonds broken with respect to axial strain is plotted in Figure 6.13. It was found that approximately 6% of contact bonds were broken progressively over the first 5% axial strain and thereafter failure occurred. Figures 6.14 and 6.15 show the locations of broken bonds in the sample at 5% axial strain and at failure. It can be observed from Figure 6.15 that at failure, most of the broken bonds occurred at the top region of the sample which indicates localisation. The variation of radial and axial strain is plotted in Figure 6.16. It was found that the ratio of radial to axial strain remained at 0.4 at up to 5% axial strain, which indicates no dilation. This ratio increased dramatically at failure, which does not indicate dilation. Consequently, it was concluded that this approach alone can not be used to simulate dilation.

6.5 Simulation with Default Burger's Contact Model

Results from Chapter 5 showed that dilation in an elastic sample is dominated by the ratio of the contact stiffness in compression to the tension contact stiffness. This section investigates the effect of ratio of compressive to tensile normal contact stiffness using the Burger's contact model applied to all contacts in compression, shear and tension.

A sample containing 1,000 particles was generated according to previously developed sample preparation procedures. A high contact bond strength was applied to all contacts to prevent bond breakage. Five viscoelastic simulations were performed by applying a constant vertical compressive stress of *400kPa* to the sample. In all simulations, the contact stiffnesses in compression and shear were taken to be equal (value given in Table 6.2) whilst the tensile contact stiffnesses (elastic, viscoelastic, viscoplastic components) have been reduced so that the ratio of compressive (and shear) to tensile contact stiffness (K_C / K_T) ranges from 1 to 100. It should be noted that the compressive and tensile contact stiffnesses are time dependent and reduce simultaneously with time, hence the ratio of (K_C / K_T) is always constant throughout the simulation.

The graph of axial strain as a function of time is shown in Figure 6.17. It can be seen from this figure that, as expected for this type of contact model, the strain response is a function of loading time comprising elastic, delayed elastic and viscous components. A higher level of axial strain is found in the simulations with higher initial ratios of compressive to tensile contact stiffness (K_C / K_T) because of the lower absolute value of the tensile contact stiffnesses.

Figure 6.18 shows a plot of volumetric strain versus distortional strain for simulations with different ratios of compressive (and shear) to tensile contact stiffnesses (K_C / K_T). It can be seen from this figure that the general trend is for a higher level of dilation from simulations with higher ratios of (K_C / K_T). For example, the dilation gradient is 0.3 in the simulation with ratio of (K_C / K_T) equal to 10, whilst the dilation gradient is 1.0 in the simulation with ratio of (K_C / K_T) equal to 100. This is because in the simulation with higher ratio of (K_C / K_T), the particles are allowed to roll past each other hence giving in higher level of dilation (as in the elastic case discussed in the previous chapter). The dilation gradient is negative (contracting) in the simulation where the tensile and compressive contact stiffnesses are taken to be equal $(K_C / K_T = 1)$ because the particles are forced to overlap instead of being allowed to roll past each other.

Consequently, the Burger's model featured in PFC3D is able to model dilation in an asphalt mixture by introducing a higher ratio of compressive to tensile contact stiffness. However, in reality, the compressive stiffness does not reduce as a function of time under compression. As noted earlier, a viscoelastic model (Burger's model) is required to capture the time dependent behaviour of bitumen. For this type of model, the contact stiffness will reduce as a function of loading time. Whilst this is a reasonable approximation for the shear and normal tensile contact stiffnesses where particles are essentially moving away from each other, the normal compressive contact stiffness should increase as particles move towards each other tending towards the contact stiffness resulting from direct contact between two particles. As an approximation to this, elastic behaviour has been assumed for the compressive normal contact stiffness whereas viscoelastic behaviour has been assumed for the tensile normal contact stiffness and the shear contact stiffness. The default Burger's

contact model in PFC3D was modified using C++ language based on these assumptions to simulate the correct contact mechanism in the asphalt mixture.

6.6 Simulation with Modified Burger's Contact Model

This section performs a uniaxial simulation based on a modified Burger's contact model as mentioned above. A sample containing 1,000 particles was generated according to previously developed sample preparation procedures. A very high contact bond strength is applied to all contacts to prevent the bond breakage. The values of contact stiffnesses used in the simulations are given in Table 6.3. A uniaxial creep test simulation is performed by applying a constant vertical compressive stress of 400*kPa* to the sample. The axial strain plotted against loading time is shown in Figure 6.19. It can be seen from this figure that the axial strain response exhibits the deformation behaviour of a Burger's model.

Figure 6.20 shows a plot of the simulated volumetric strain versus distortional strain. It can be seen from this figure that early in the test at distortional strain levels less than approximately 0.3% the volumetric strain is negative indicating compaction of the material. The volumetric strain then increases approximately in proportion to the distortional strain as the material dilates, ie:

$$\dot{H} = s\left|\dot{E}\right|$$

(6.2)

where ($\dot{H}$) is the volumetric strain rate, ($\dot{E}$) is the distortional strain rate. The parameter s can be interpreted as the steady-state dilation gradient which can be directly compared to the dilation gradient introduced earlier in the elastic simulations.

Since an elastic compressive contact stiffness and a viscoelastic shear and tensile contact stiffness have been used, the ratio of compressive to tensile contact stiffness will increase during the simulation as described by:

$$\frac{K_C}{K_T} = \frac{E_C}{\left[\dfrac{1}{K_0^T} + \dfrac{t}{C_\infty^T} + \dfrac{1}{K_1^T}\left(1 - e^{-t/\tau}\right)\right]^{-1}} \qquad (6.3)$$

where K_C is the compressive contact stiffness, K_T is the tensile contact stiffness and E_C is the elastic stiffness for contacts under compression.

Since the ratio of compressive to tensile contact stiffness will increase during the simulation, by analogy to the results from the elastic simulation, it is likely that the dilation gradient will also change during the simulation. This can be seen from a careful inspection of the data shown in Figure 6.20 where the slope is not constant and is shown in Figure 6.21 where the dilation gradient is plotted as a function of the ratio of compressive to tensile normal contact stiffness calculated from Equation 6.3. It can clearly be seen from this figure that, as with the elastic case, the dilation gradient tends to increase as the ratio of compressive to tensile normal contact stiffness increases during the simulation.

In conclusion, it is possible to model the dilation behaviour of asphalt by assuming elastic behaviour for contacts under compression and viscoelastic behaviour for contacts under shear and tension.

6.7 Effect of Sample Density on Dilation

The previous section showed that the dilation gradient is a function of ratio of compressive to tensile contact stiffness. However, it is well understood in soil mechanics that soil dilation will reach a critical state, at which shear deformation (or distortional deformation) can continue in the absence of a volume change [93]. Bolton [12] stated that if the soil were denser than critical then it would tend to dilate when disturbed, so that the void ratio at a dense state can increase to a preordained void ratio at a critical state, in which the normal effective stress is fixed. This section investigates the effect of sample density on dilation.

A uniaxial creep simulation was performed on a sample containing 1,000 particles. A constant stress loading of 400kPa was applied over a long period of time of approximately 3000 seconds. It was expected that the dilation gradient will increase in proportion to the ratio of compressive to tensile contact stiffness as a function of time during the simulation. Figure 6.22 shows a plot of volumetric strain versus distortional strain. It can be seen from this figure that at a distortional strain of approximately 8% the dilation gradient is at a maximum of 0.8, thereafter it reduces. The dilation gradient then decreases gradually as the simulation continues to a larger distortional strain.

The change of dilation gradient corresponding to sample density in the simulation was investigated and plotted in Figure 6.23. It can be seen from this figure that during the simulation, the dilation gradient increases to a maximum value of approximately 0.8, whilst the sample density reduces from 0.64 to 0.62. This agrees with Bolton [12] where he stated that the initially dense soil sample dilates due to the reduction in density. Thereafter, the dilation gradient reduces to 0.6 simultaneously with the reduction in sample density from 0.62 to 0.58. This is because the packing characteristic of the sample has changed from dense to a looser packing state, giving a lower level of dilation.

Consequently, it can be concluded that the dilation gradient reaches a maximum value of 0.8 at approximately 8% distortional strain.

6.8 Effect of Contact Stiffnesses on Dilation

It was noted in Section 6.6 that the dilation gradient of an asphalt mixture should increase with the ratio of compressive to tensile contact stiffness as a function of time. However, the previous section has shown that the effect of sample "loosening" (reduction in sample density) limits the maximum amount of dilation at very high ratios of compressive to tensile contact stiffness.

This section develops a method to investigate the effect of contact stiffness ratio (compression, shear and tension) on dilation. A series of uniaxial simulations were

performed to investigate the effect of normal contact stiffness ratio on dilation. The sample preparation procedure was the same as that for the uniaxial simulation in the previous section. It should be noted that all simulations were carried on to a maximum distortional level of 4% to ensure that the simulated samples were in a dense packing state. The contact stiffnesses in compression and shear were taken to be equal to the value in Table 6.4, whilst an artificial factor $[F_T]$ has been introduced to vary the initial tensile contact stiffnesses (elastic, viscoelastic, viscoplastic components) so that the initial ratio of compressive (and shear) to tensile contact stiffnesses range from 1 to 100. The main reason for introducing the artificial factor $[F_T]$ into the tensile contact stiffness is to simulate the dilation at a very high ratio of compressive to tensile contact stiffness. For instance, introducing a factor $[F_T]$ of 1/100 results in an initial ratio of compressive (and shear) to tensile contact stiffness of 100 (see Table 6.4).

Figure 6.24 shows the relationship between volumetric strain and distortional strain for simulations with different factor $[F_T]$ under a constant compressive stress of 400kPa. It was found that the dilation gradient is higher in the simulation with a lower factor $[F_T]$. This is because in simulation with a lower factor $[F_T]$, the initial ratio of compressive to tensile contact stiffness is higher, therefore the particles are not allowed to overlap but forced to roll past each other and hence giving greater dilation. However, it is necessary to quantify the dilation gradient with the ratio of compressive to tensile normal contact stiffness.

The dilation gradients at specific distortional strains were obtained by careful inspection of the data shown in Figure 6.24. The ratio of (K_C/ K_T) is then calculated based on Equation 6.3 by substituting the values of the parameters in Table 6.4 and the loading times at specific distortional strains. The relationship between the dilation gradient and the ratio of compressive to tensile normal contact stiffness (K_C/ K_T) is plotted in Figure 6.25. It can clearly be seen from this figure that, the dilation gradient tends to increase approximately in proportion to the ratio of compressive to tensile normal contact stiffness. This behaviour is expected since during the simulation, the tensile contact stiffness reduces as a function of time whilst the compressive contact stiffness remains constant.

6.9 Effect of Deviator Stress

Previous researchers [40, 65] have found that the dilation gradient (ratio of volumetric strain to distortional strain) of an asphalt mixture under uniaxial and triaxial loading is independent of strain rate, stress or temperature. To investigate the effect of deviator stress on dilation, five uniaxial simulations were performed at stress levels ranging from $400kPa$ to $1000kPa$ on an identical sample containing 1,000 particles.

The axial strain responses as a function of loading time are shown in Figure 6.26. It can be seen from this figure that, as expected, the axial strain is larger in the simulation with the higher deviator stress. Figure 6.27 shows a plot of the corresponding volumetric strains versus distortional strains. The dilation gradients at distortional strains of 0.015 to 0.02 were measured and found to be the same in all simulations independent of deviator stress level. This indicates that the dilation gradient of an asphalt mixture in a uniaxial test is independent of the deviator stress. It can also be seen from Figure 6.27 that in simulations with higher deviator stress levels, the initial compaction phase at the beginning of the test is greater. However, no experimental data is available to justify the magnitude of the strain response under different deviator stresses.

6.10 Effect of Bitumen Film Geometry Factor

Results from previous studies [22, 49] have shown that the stiffness of a thin film of bitumen depends on the geometry (aspect ratio) of the film. For example, a thicker film was found to be less stiff compared to a thinner film. This section investigates the importance of this "geometric factor" on the predicted behaviour of sand asphalt mixtures.

Assuming that a thin film between two sand particles can be characterised as a disc of thickness $2T$ and diameter d, the aspect ratio is given by d / T. Assuming that bitumen is incompressible, the volume of bitumen is constant giving:

$$d^2 \times 2T = \text{constant}$$

$$d \propto \frac{1}{\sqrt{T}} \tag{6.4}$$

Therefore, the aspect ratio is given by:

$$A \propto \frac{1}{T^{3/2}} \tag{6.5}$$

Therefore, provided the distance between particles is known during the simulation, the aspect ratio of the bitumen films between particles can be updated using the following equation:

$$A_{t+\Delta t} = A_t \left[\frac{T}{T + \Delta U/2} \right]^{3/2} \tag{6.6}$$

where $A_{t+\Delta t}$ is the aspect ratio at time $t + \Delta t$, A_t is the aspect ratio at time t and ΔU is the change in normal displacement. It should be noted that an initial aspect ratio of approximately 10 was used in Equation (6.6) which was determined using a bitumen film thickness calculated using the procedure described in Shell Bitumen Handbook [90]. During the simulation, Equation (6.6) is used to update the "effective" aspect ratio at each contact. The "effective" thin film stiffening factor (T_F) as a function of aspect ratio is then determined from Figure 6.28 and used as a factor in reducing the tensile contact stiffness parameters (K_0, C_∞, K_1 and C_1) in Burger's contact model. Therefore, the contact stiffness in tension reduces as the aspect ratio decreases, i.e. as particles move further apart.

Two viscoelastic uniaxial simulations (one simulation incorporating this factor) were performed to investigate the effect of the geometry factor on the deformation of the sample. Figure 6.29 shows the predicted volumetric and distortional strain of the sample under a constant stress of $400kPa$. It can be seen from this figure that for a given distortional strain, the volumetric strain in the simulation including the geometry factor is higher than in the simulation excluding the geometry factor. This

is because the aspect ratio of bitumen films in tension decreases during the simulation causing a reduction in stiffness resulting in higher levels of volumetric strain. It should be noted that the geometric factor is not included in previous simulations and will be included in all further simulations presented in this thesis.

6.11 Comparison with Experimental Results

The objective of this section is to investigate the deformation and dilation of sand asphalt under simulated uniaxial tests. Two samples containing 1,000 and 6,000 particles were used. A high contact bond strength was applied to all contacts to prevent bond breakage. The model parameters are detailed in Table 6.5 and were calibrated to give sensible levels of axial strain and a similar shape creep curve compared to previously gathered experimental data [65]. Previous researchers [24, 69] have shown that the stiffnesses of pure bitumen in tension and in shear are expected to be related by the factor of 3 in the linear region of behaviour (refer to section 2.5). Hence, the value of shear contact stiffness in Table 6.5 is taken to be one third of the value of normal tensile contact stiffness.

Figure 6.30 shows the predicted axial strain plotted as a function of loading time for an axial stress of 400kPa. The measured curve is also shown in Figure 6.30 from where it can be seen that the predicted and measured curves are similar in magnitude and shape demonstrating the applicability of this approach.

Previous research has shown that at least 4,500 particles are required for the bulk elastic material properties (eg Young's Modulus) calculated from a DEM simulation to be within 2% of the values calculated using a much larger number of particles (see Collop *et al.* [27] for further details). To investigate whether this effect is similar in a viscoelastic simulation, results from a sample containing 6,000 particles were used for comparison with those from the sample containing 1,000 particles. Also shown in Figure 6.30 is the plot of predicted axial strain as a function of time for the sample containing 6,000 particles. It can be seen from this figure that at a particular loading time, the axial strain calculated from the sample containing 1,000 particles is higher than the axial strain calculated from the sample containing 6,000

particles. For example, at a loading time of 100 seconds the sample containing 1,000 particles results in an over-prediction of approximately 12% compared to sample containing 6,000 particles which is consistent with previous results from the elastic simulations [27]. It should be noted that for practical reasons (computation time), results presented in this thesis are based on samples containing 1,000 particles which will result in an over-prediction of the axial strain.

Figure 6.31 shows a plot of the simulated volumetric strain versus distortional strain. It can be seen from this figure that early in the test at distortional strain levels less than approximately 0.3% the volumetric strain is negative indicating compaction of the material. The volumetric strain then increases approximately in proportion to the distortional strain as the material dilates. For the case shown in Figure 6.31 the dilation gradient is approximately 0.8 (ie $s = 0.8$). Experimental data for the same idealised mixture tested at 20°C taken from Deshpande [40] is shown in Figure 6.31 for comparison. It can be seen by comparing the measured with the predicted data that, although the general shapes of the curves are similar, the measured dilation gradient is slightly higher and the simulation tends to over-predict the initial compaction phase at the beginning of the test. The under-prediction of the dilation gradient is likely to be because the particles in the numerical sample are perfectly spherical whilst in reality the sand particles are more angular, resulting in greater dilation. From the data shown in Figure 6.21 it can be concluded that the maximum dilation gradient for perfectly spherical particles under uniaxial stress conditions is approximately 0.8. To increase the dilation gradient further, more complex particle shapes are required. Also shown in Figure 6.31 is the result from a simulation undertaken using a sample containing 6,000 particles. It can be seen from this figure that the result from the simulation undertaken using 1,000 particles tends to slightly over-predict the volumetric strain at a given level of distortional strain although it should be noted that the effect is smaller than for the axial strain (see Figure 6.30).

6.12 Conclusions

The following conclusions can be drawn from this chapter.

- DEM has been used to simulate the behaviour of idealised asphalt mixture under uniaxial compressive loading.

- A computation time optimisation was performed resulting in a higher particle density being used.

- The dilation gradient was found to increase with bond breakage in the sample due to lower constraint in the particle system. However, failure of the sample was observed in simulation with progressive bond breakage.

- A viscoelastic Burger's model was introduced to give time-dependent shear and normal tensile contact stiffnesses, whilst the normal compressive contact stiffness was assumed to be elastic.

- The dilation gradient under uniaxial conditions was found to increase with time as the ratio of compressive to tensile contact stiffness increases.

- The maximum dilation gradient was found to be 0.8 at 8% distortional strain.

- The dilation gradient was found to be independent of the deviator stress level.

- The effect of changing bitumen film geometry during the simulation on contact stiffnesses has been investigated.

- The simulation results have been compared with experimental data and demonstrated the ability of this type of approach.

Tables:

Table 6.1: Burger's contact model parameters.

Shear Contact		Normal Contact	
Property	Value	Property	Value
K_o^s (MN/m)	0.1	K_o^n (MN/m)	1.0
C_∞^s (MNs/m)	0.5	C_∞^n (MNs/m)	5.0
K_1^s (MN/m)	0.1	K_1^n (MN/m)	1.0
C_1^s (MNs/m)	0.5	C_1^n (MNs/m)	5.0

Table 6.2: Burger's contact model parameters for simulation with default Burger's contact model.

Shear Contact		Tension Contact		Compression contact	
Property	Value	Property	Value	Property	Value
K_o^s (MN/m)	0.1	K_o^t (MN/m)	variable	K_o^c (MN/m)	1.0
C_∞^s (MNs/m)	1.0	C_∞^t (MNs/m)	variable	C_∞^c (MNs/m)	10.0
K_1^s (MN/m)	0.1	K_1^t (MN/m)	variable	K_1^c (MN/m)	1.0
C_1^s (MNs/m)	0.5	C_1^t (MNs/m)	variable	C_1^c (MNs/m)	5.0

Table 6.3: Burger's contact model parameters for simulation with modified Burger's contact model.

Shear Contact		Tension Contact		Compression contact	
Property	Value	Property	Value	Property	Value
K_o^s (MN/m)	0.60	K_o^n (MN/m)	0.60	E_o^n (MN/m)	0.60
C_∞^s (MNs/m)	4.50	C_∞^n (MNs/m)	4.50		
K_1^s (MN/m)	0.45	K_1^n (MN/m)	0.45		
C_1^s (MNs/m)	3.50	C_1^n (MNs/m)	3.50		

Table 6.4: Burger's contact model parameters with factor $[F_T]$.

Shear Contact		Tension Contact		Compression contact	
Property	Value	Property	Value	Property	Value
K_o^s (MN/m)	0.60	K_o^n (MN/m)	$[F_T] \times 0.60$	E_o^n (MN/m)	0.60
C_∞^s (MNs/m)	4.50	C_∞^n (MNs/m)	$[F_T] \times 4.50$		
K_1^s (MN/m)	0.45	K_1^n (MN/m)	$[F_T] \times 0.45$		
C_1^s (MNs/m)	3.50	C_1^n (MNs/m)	$[F_T] \times 3.50$		

Table 6.5: Burger's contact parameters for uniaxial viscoelastic simulation.

Shear Contact		Tension Contact		Compression contact	
Property	Value	Property	Value	Property	Value
K_o^s (MN/m)	0.12	K_o^n (MN/m)	0.36	E_o^n (MN/m)	0.70
C_∞^s (MNs/m)	0.80	C_∞^n (MNs/m)	2.40		
K_1^s (MN/m)	0.03	K_1^n (MN/m)	0.09		
C_1^s (MNs/m)	0.80	C_1^n (MNs/m)	2.40		

Figures:

Figure 6.1 : Burger's viscoelastic model.
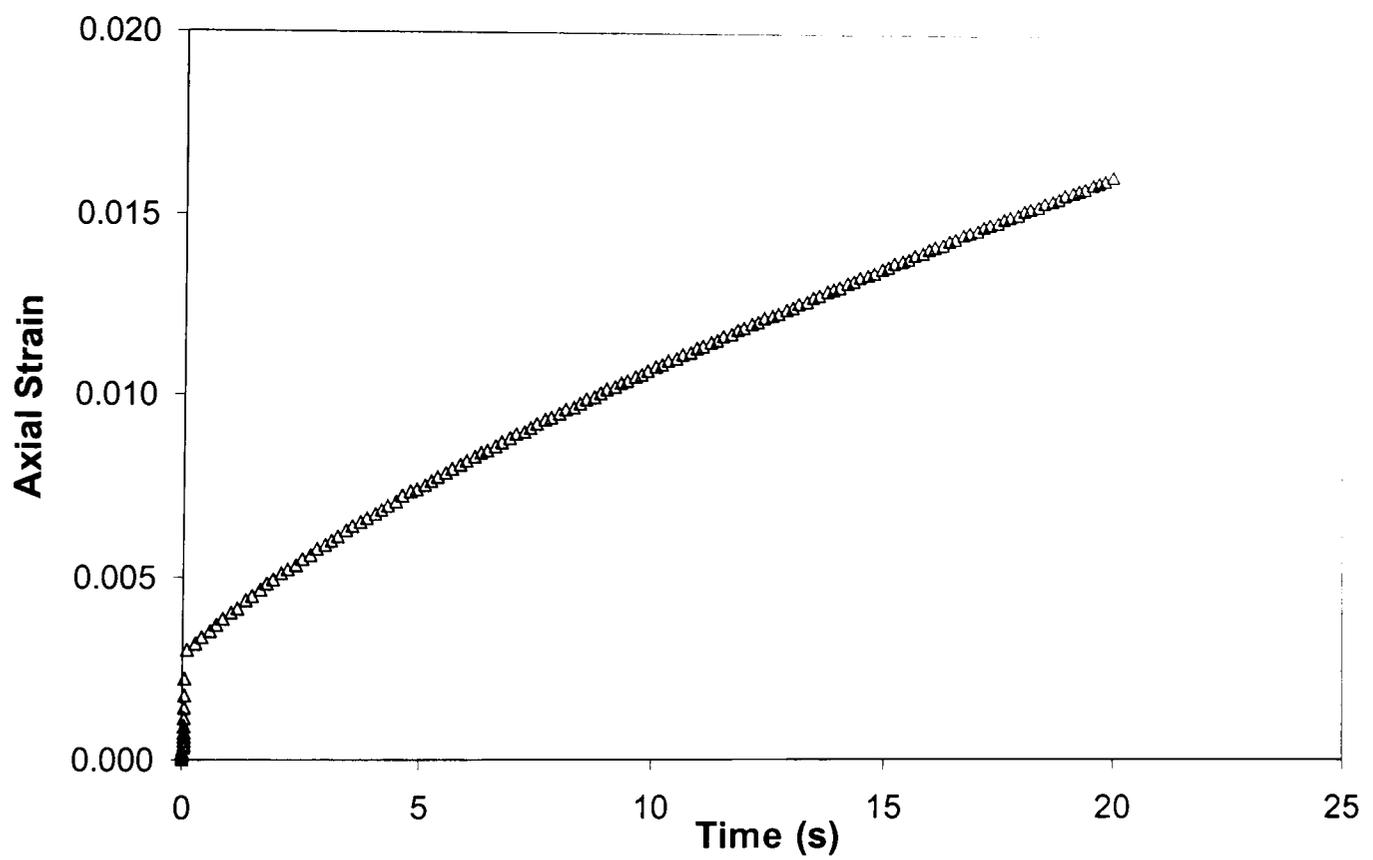
Figure 6.2: Axial strain versus time in preliminary simulation.
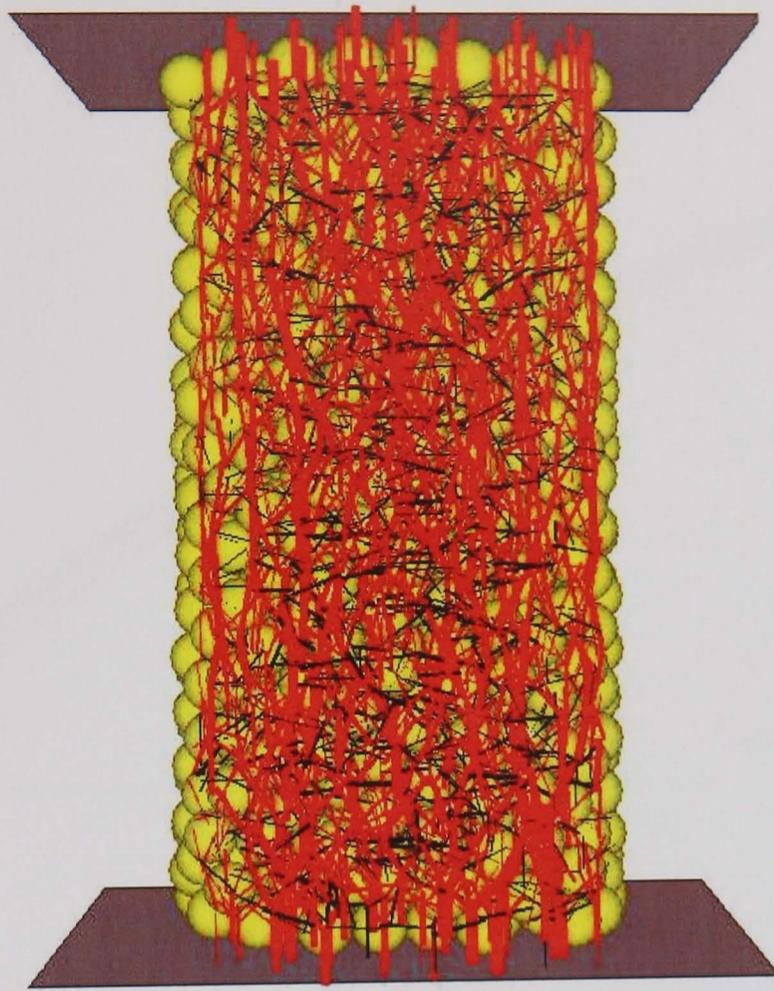
Figure 6.3: Compressive (red) and tensile (black) contact forces distribution in 1,000
particles sample.
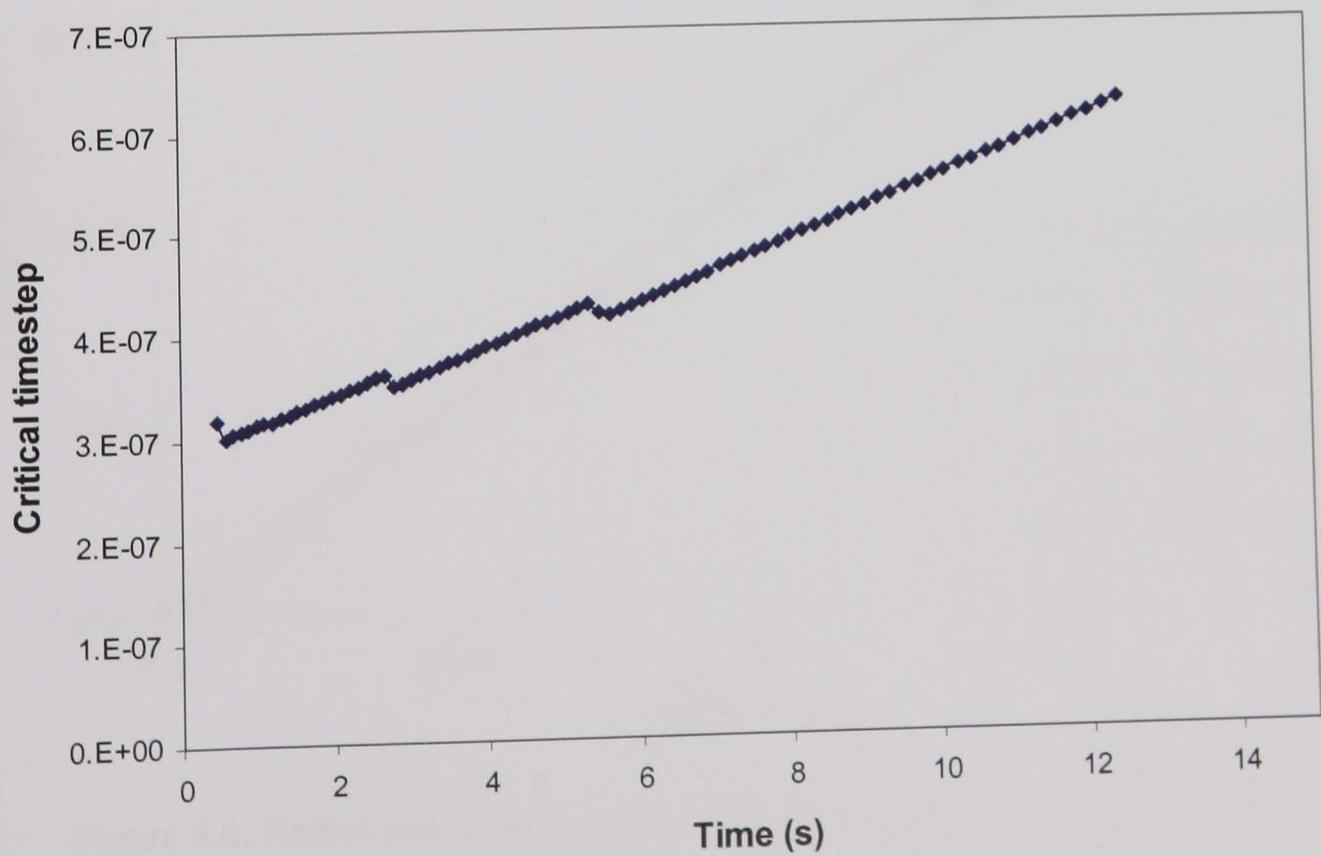
Figure 6.4: Increment of critical timestep
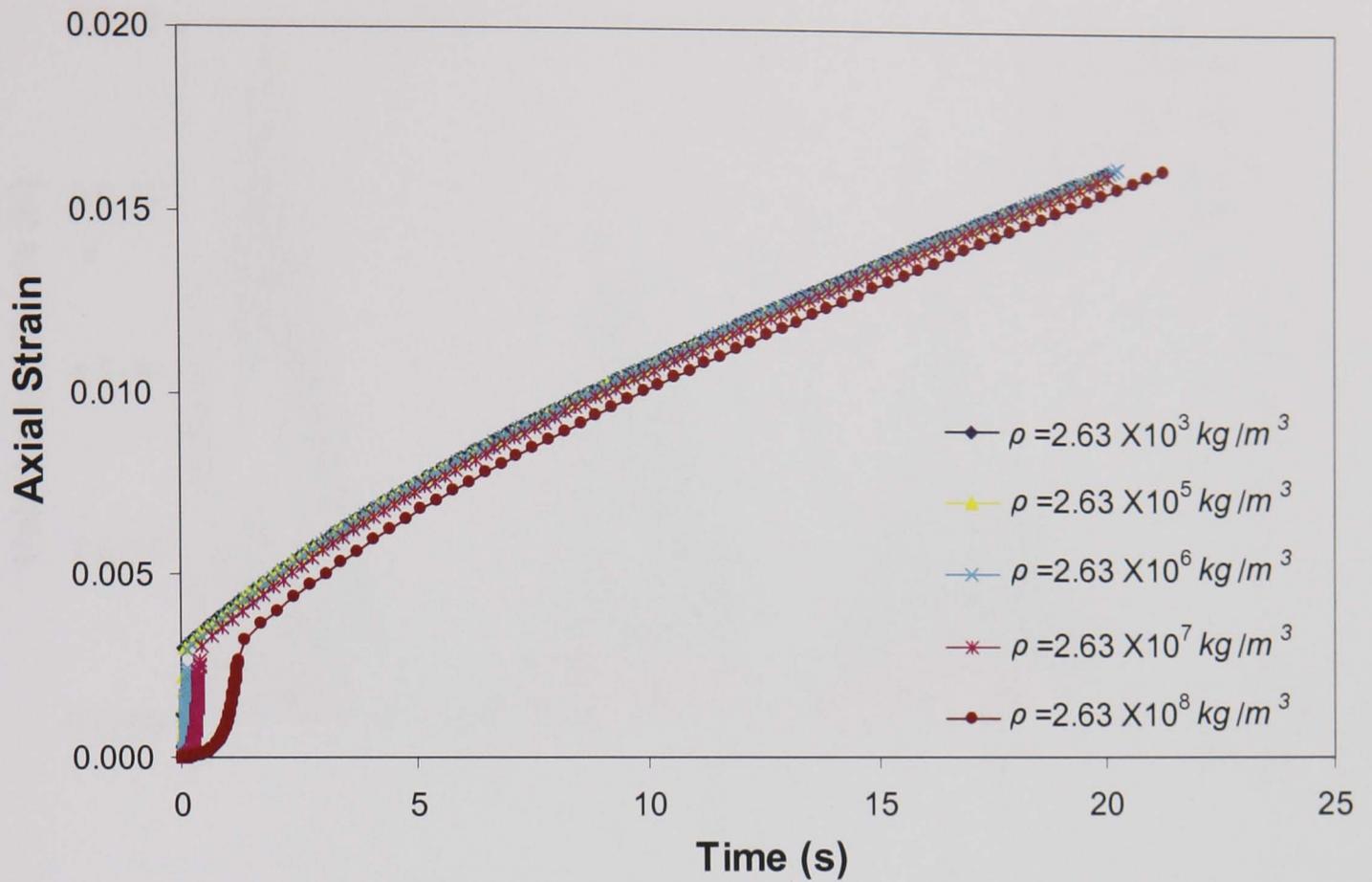
Figure 6.5: Axial strain versus time for simulations on samples with
different particle densities.
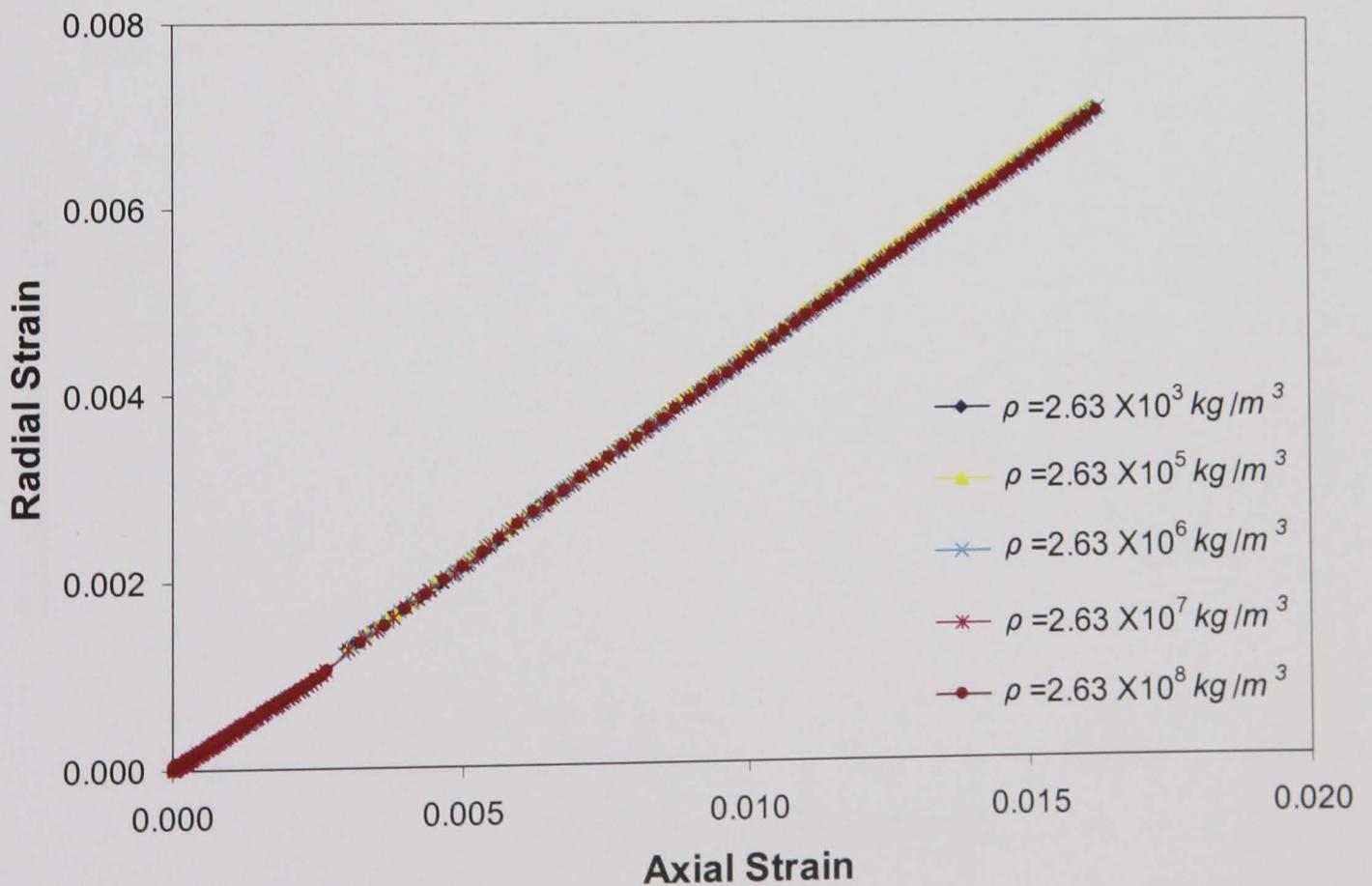
Figure 6.6: Radial and axial strain for simulations on samples with different
particle densities.
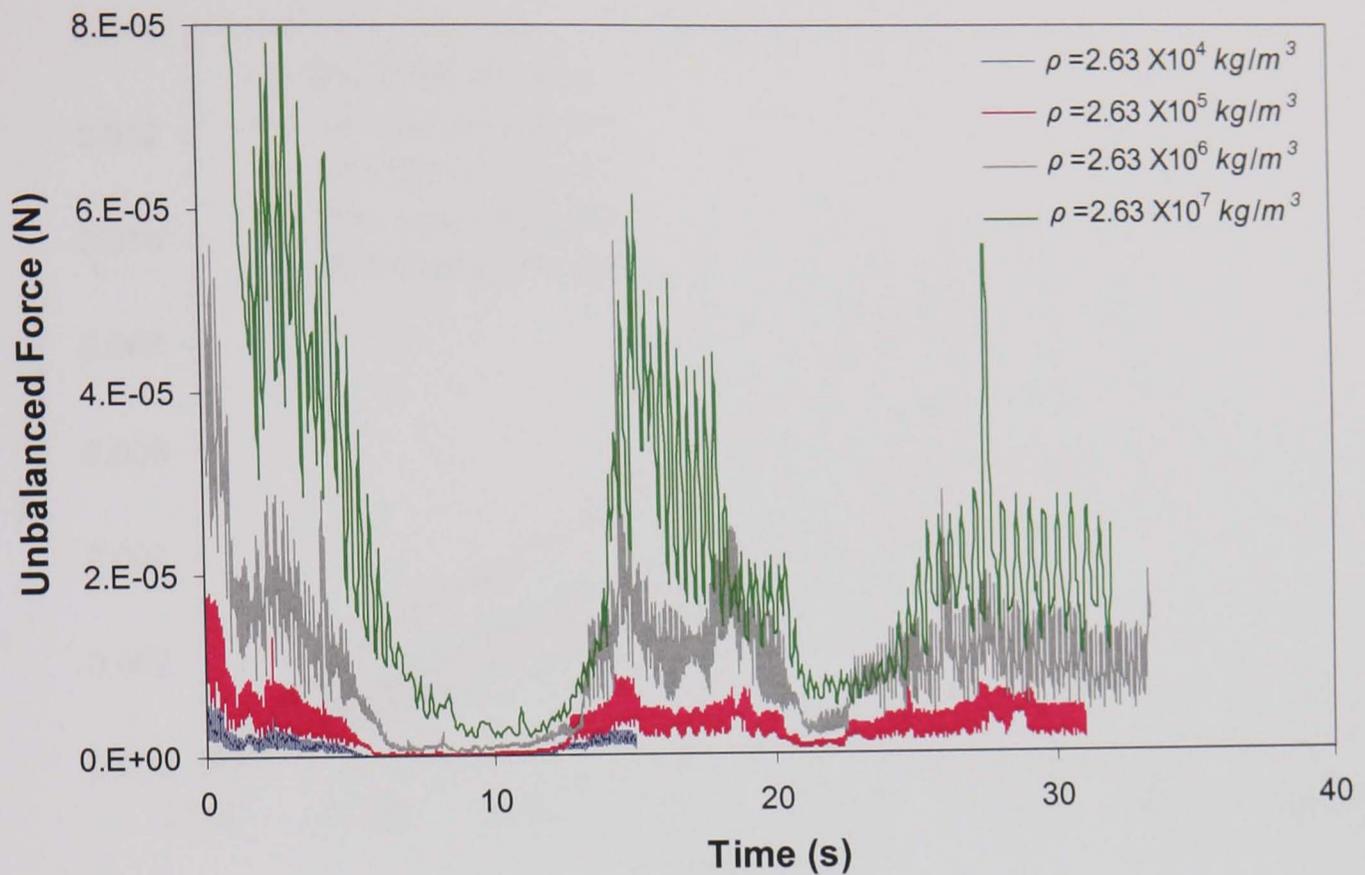
Figure 6.7: Unbalanced forces for simulations on samples with different particle densities.
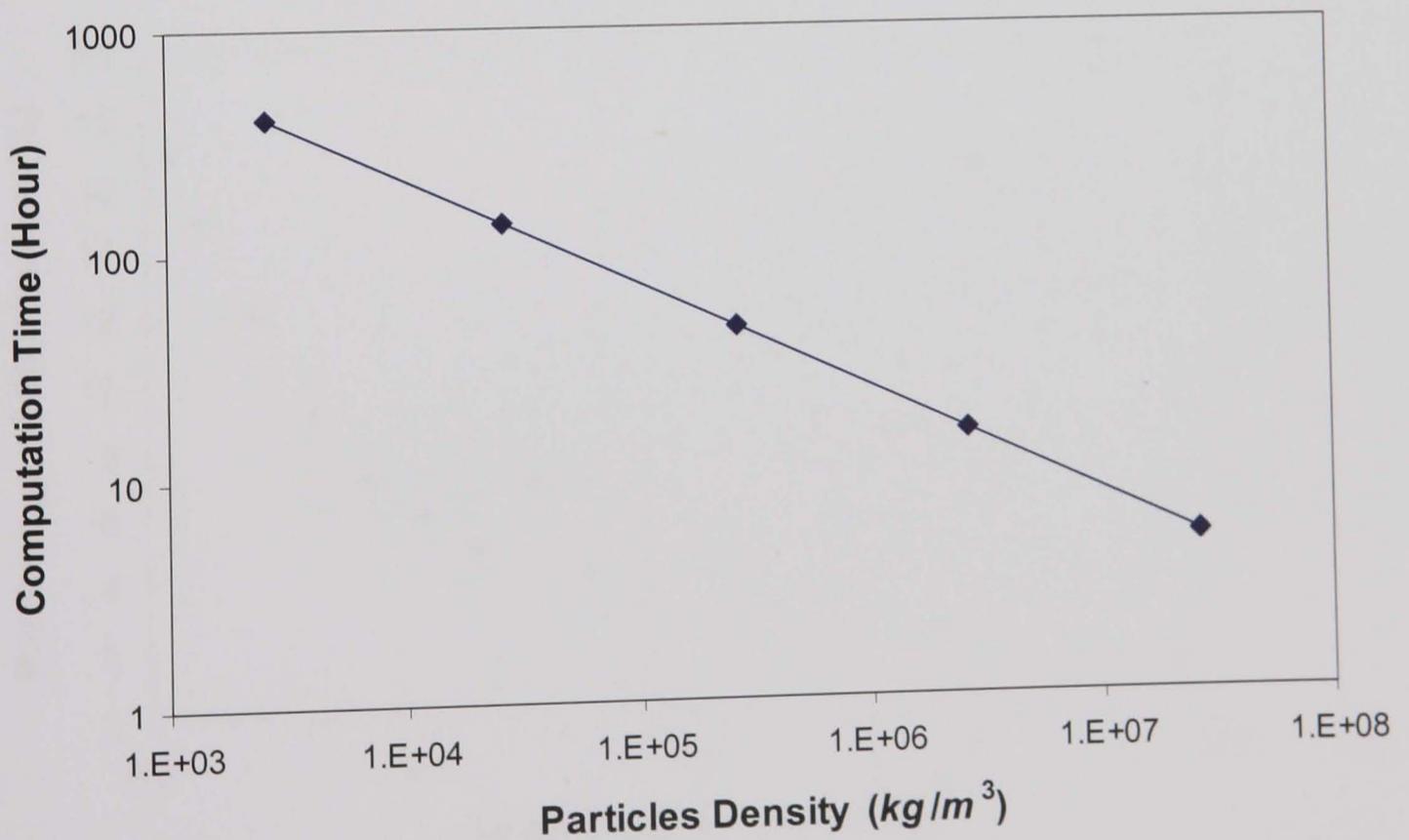
Figure 6.8: Computation time for simulations on samples with different particle densities.
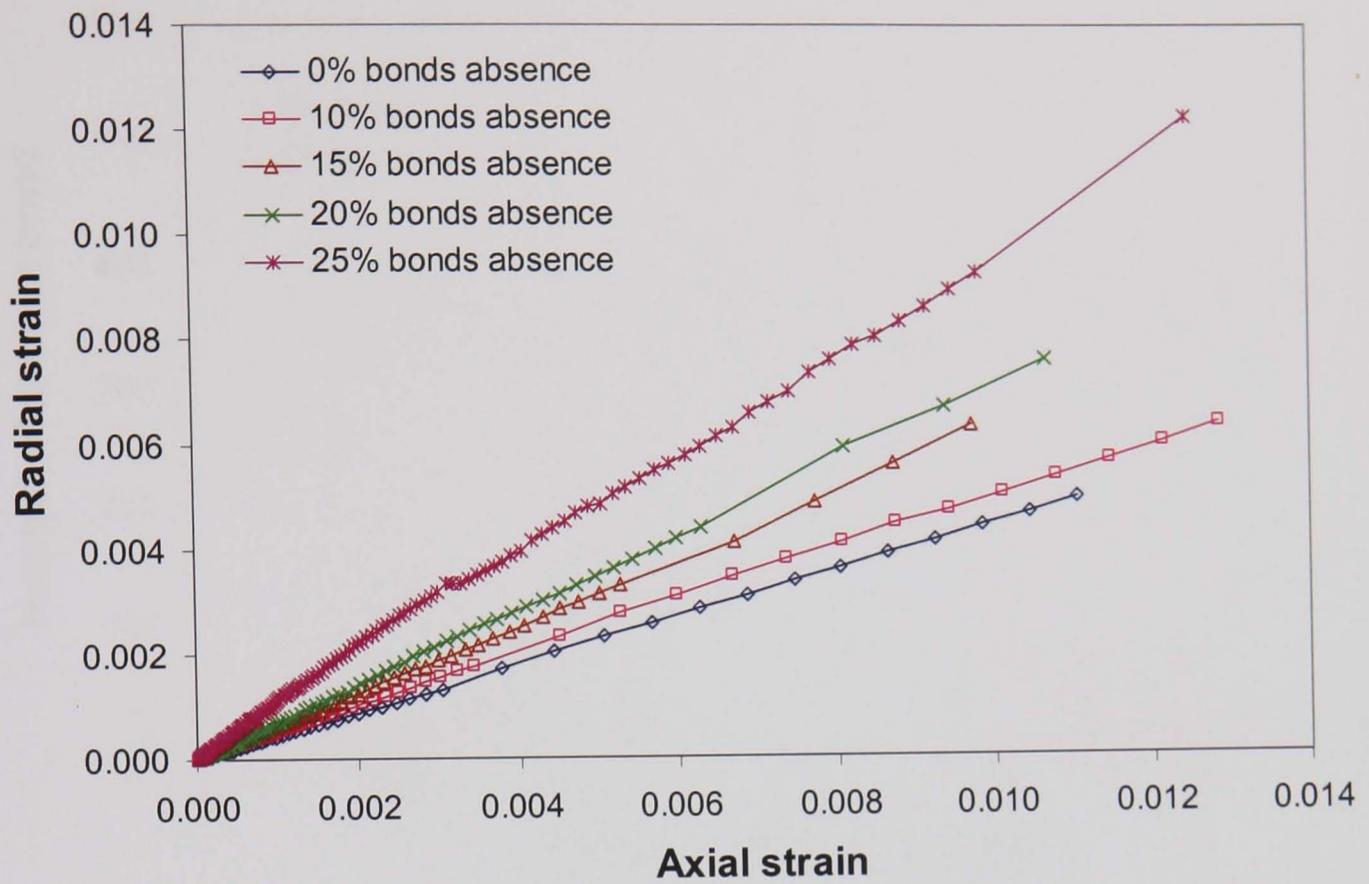
Figure 6.9: Radial versus axial strain for simulations at different percentages of bonds absence.
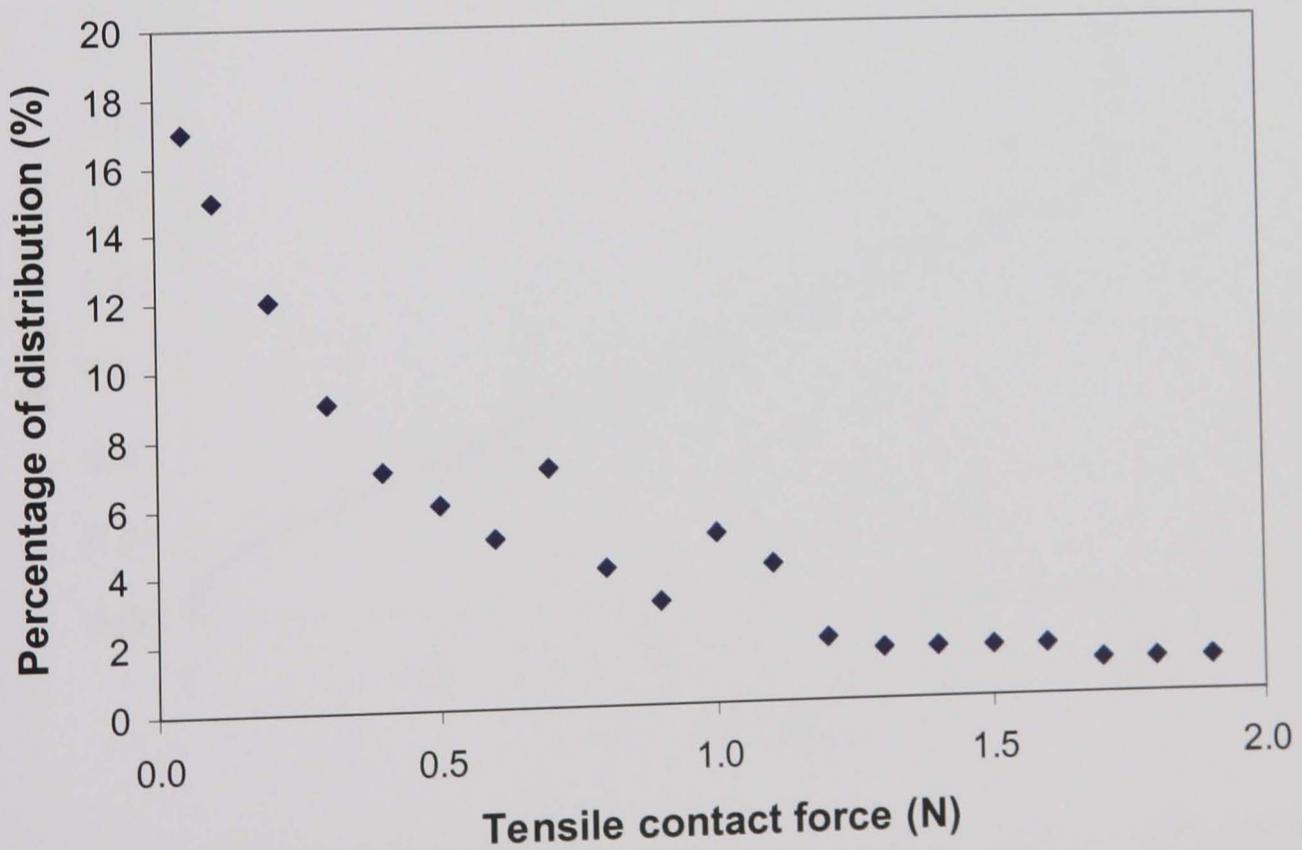
Figure 6.10: Distribution of tensile contact forces in the sample.
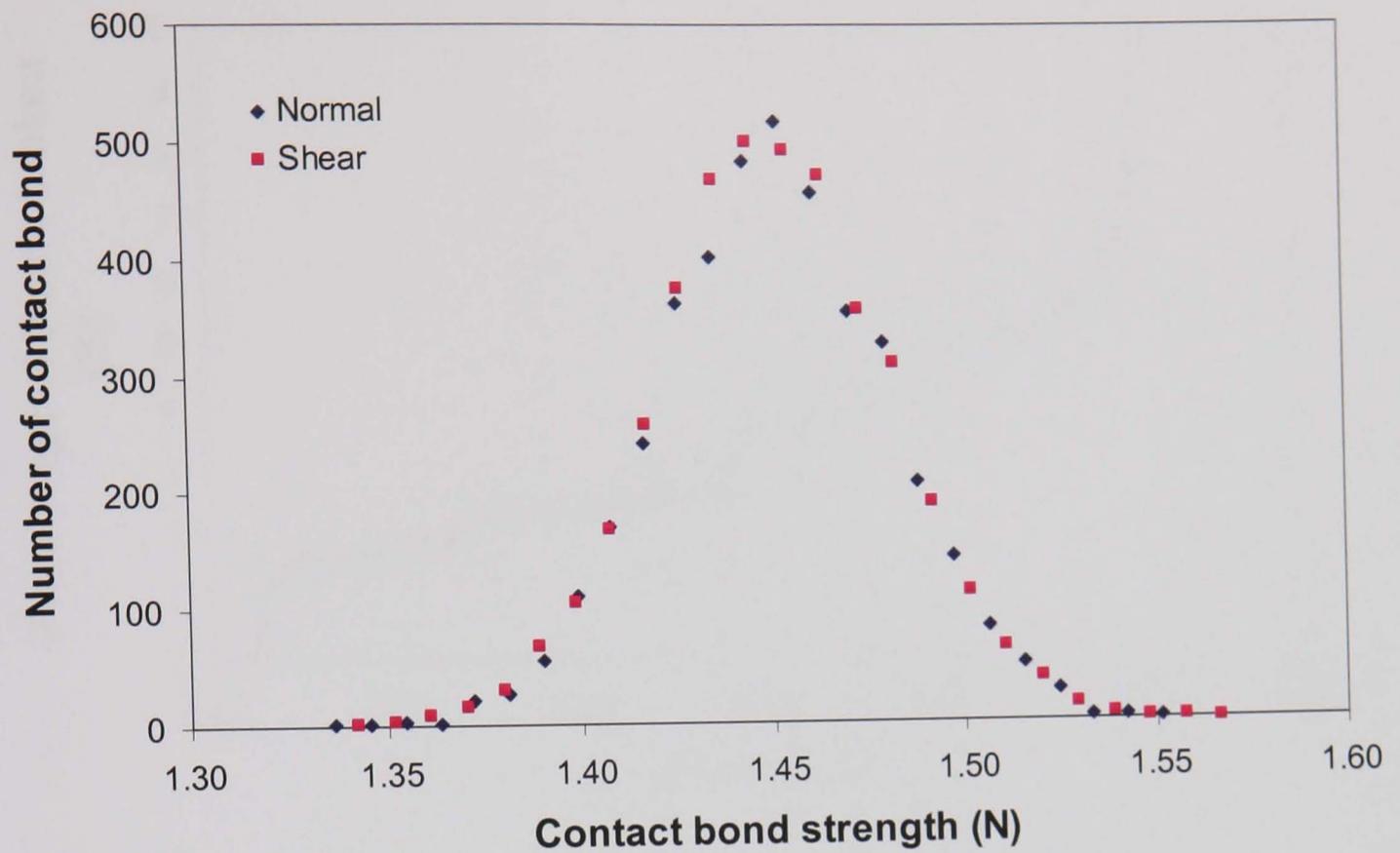
Figure 6.11: Distribution of contact bond strengths at mean of 1.45*N* and standard deviation of 0.03.
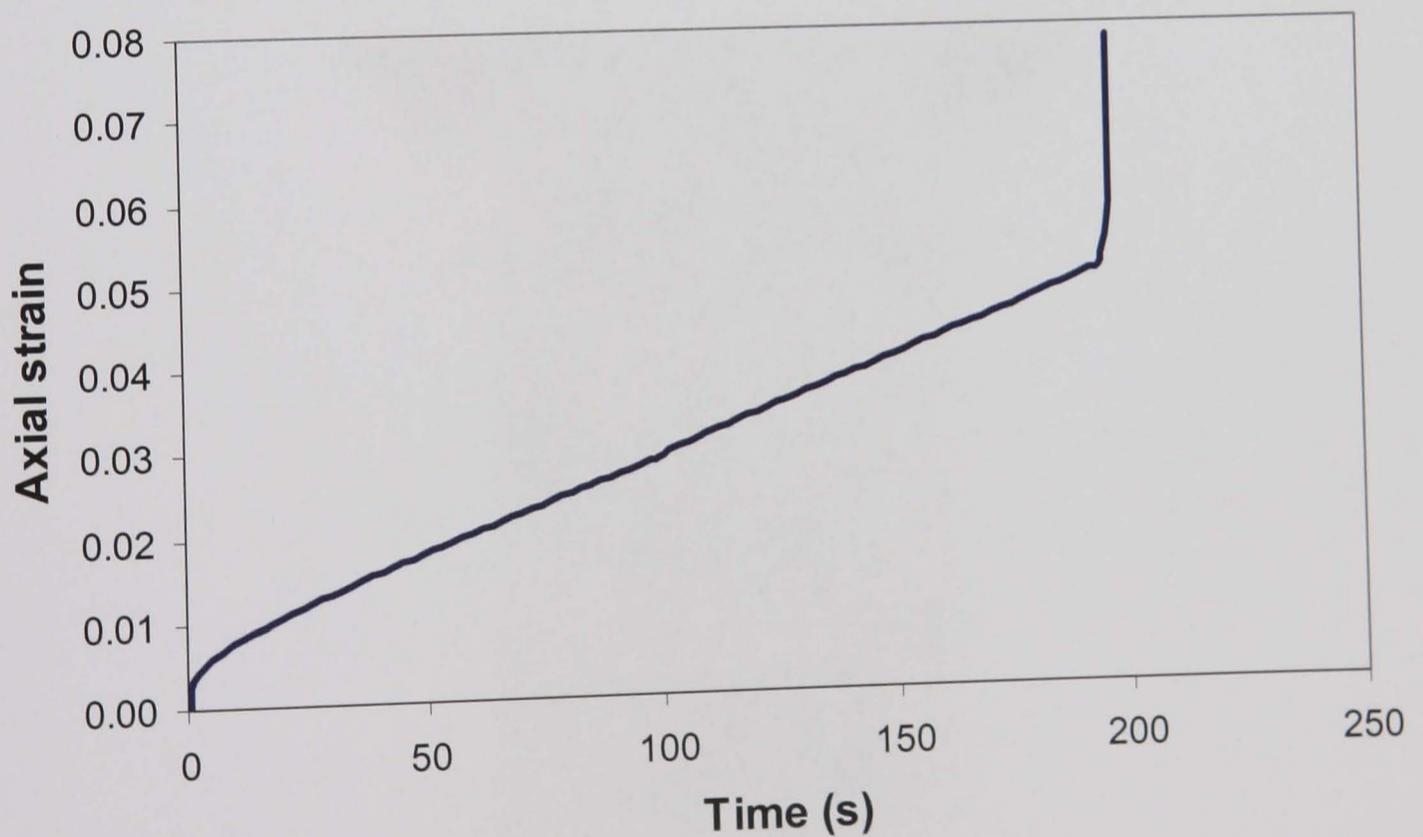
Figure 6.12: Axial strain as a function of loading time before and after catastrophic failure.
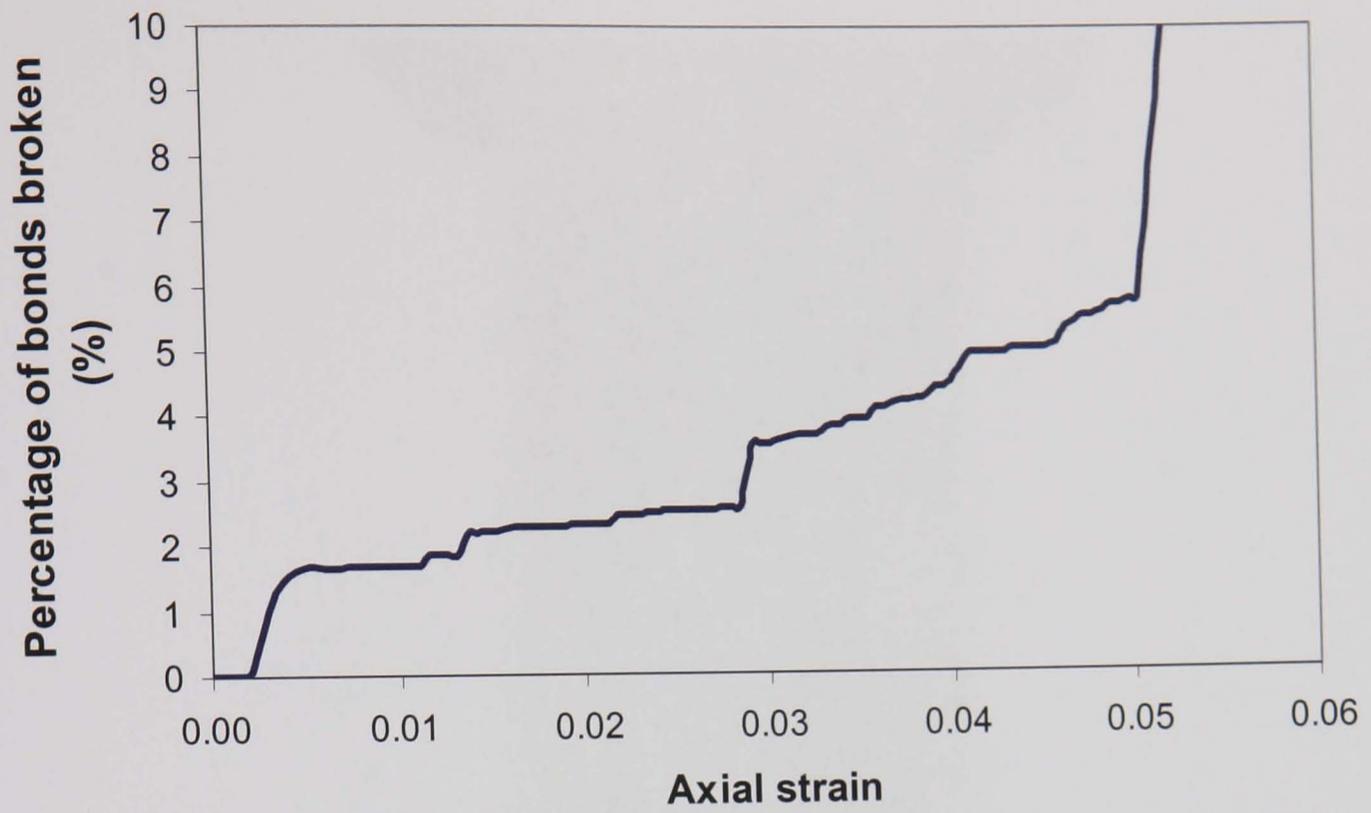
Figure 6.13: Percentage of bond broken versus axial strain.
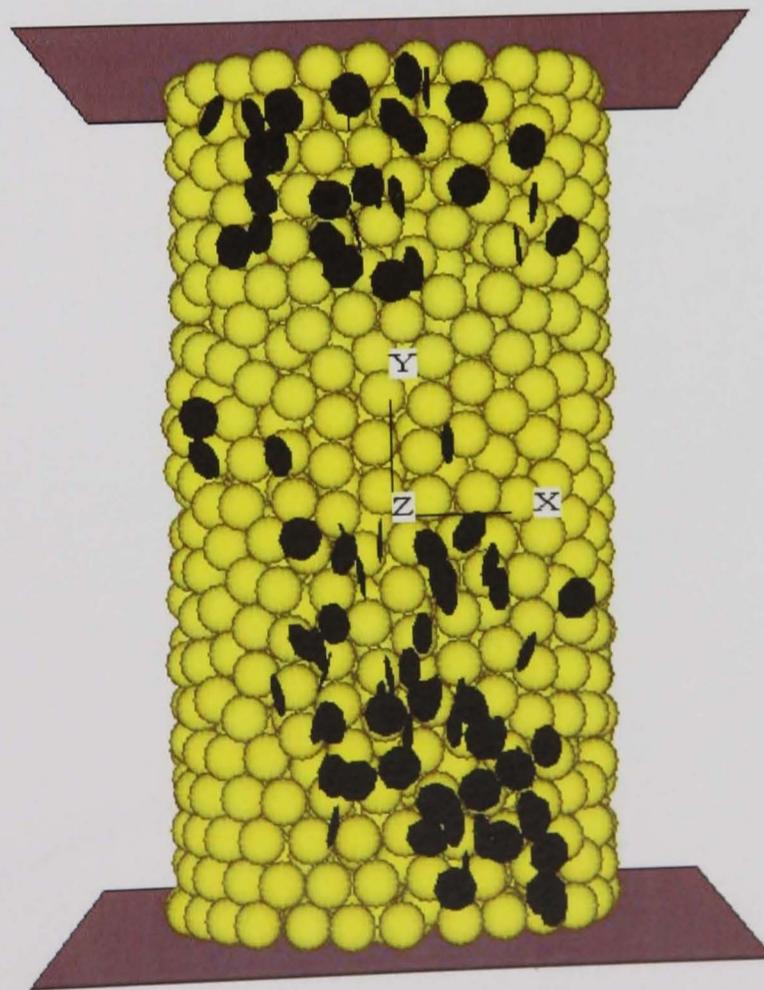
Figure 6.14: Distribution of broken bonds at 5% axial strain.
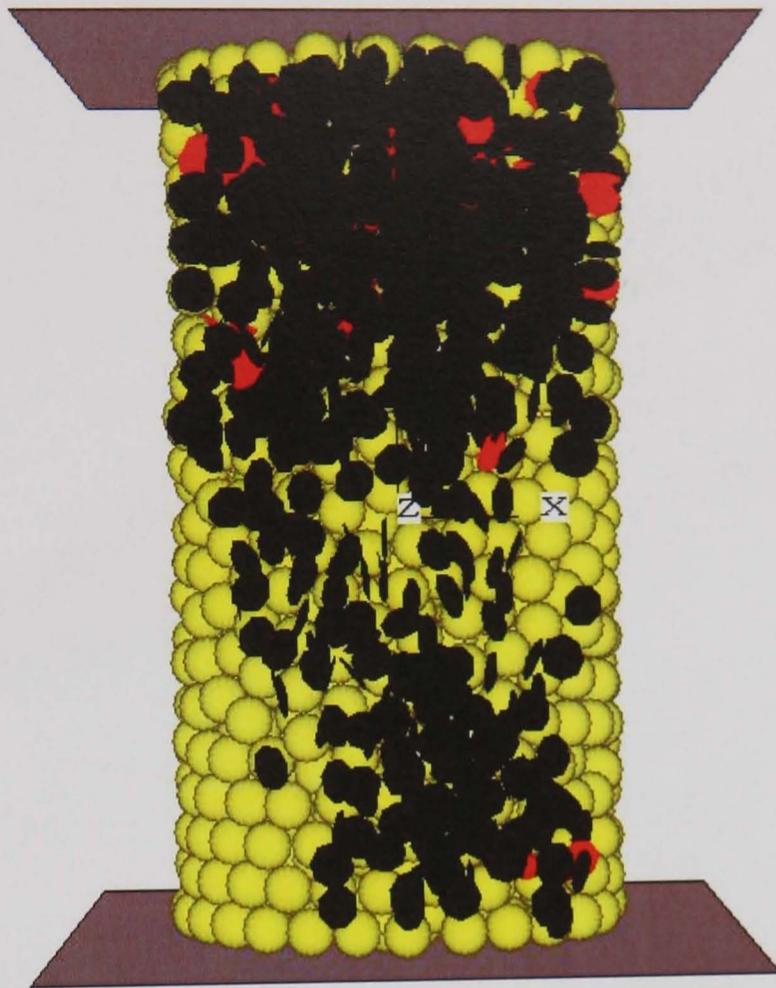
Figure 6.15: Distribution of broken bonds at catastrophic failure.
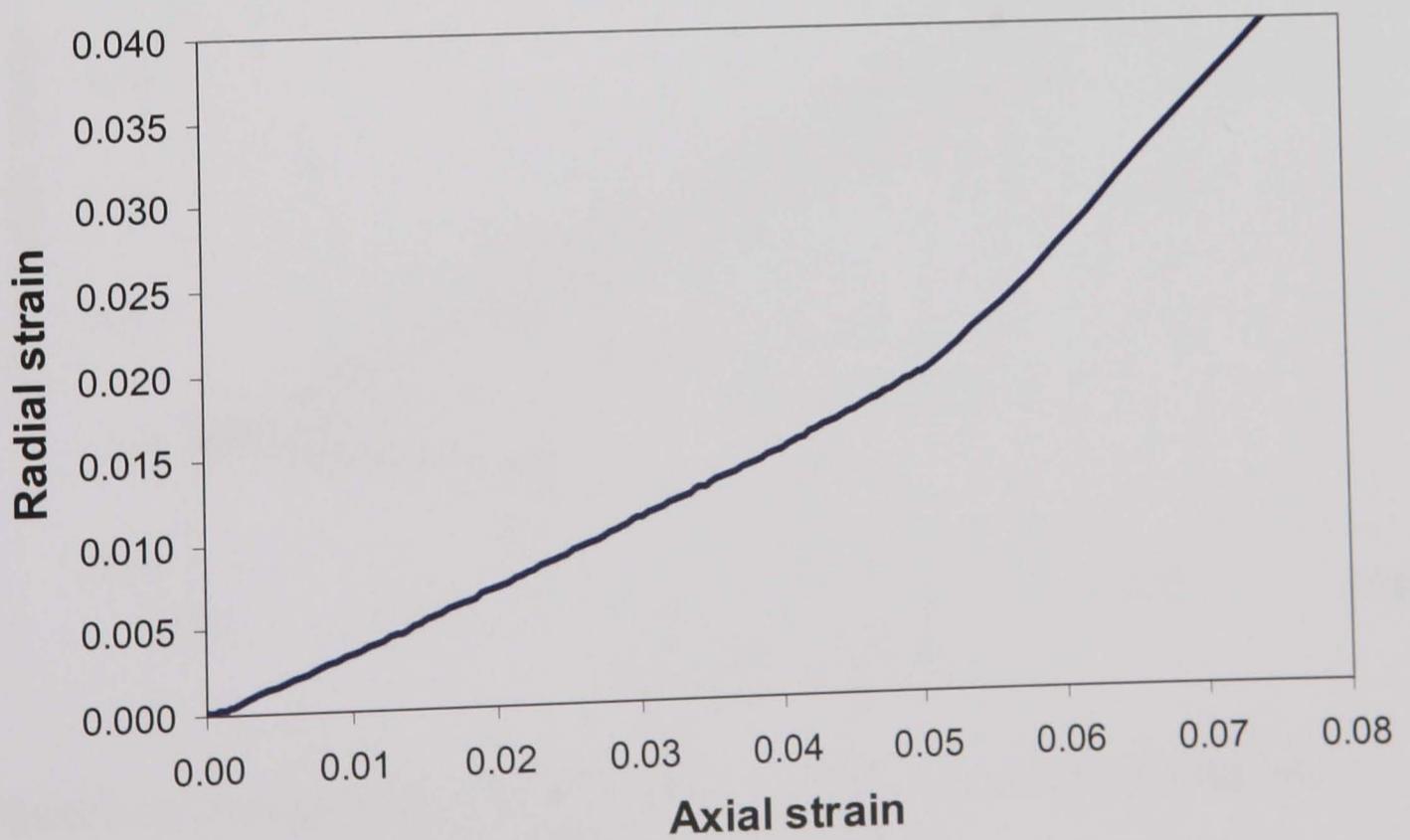
Figure 6.16: Radial versus axial strain before and after catastrophic failure.
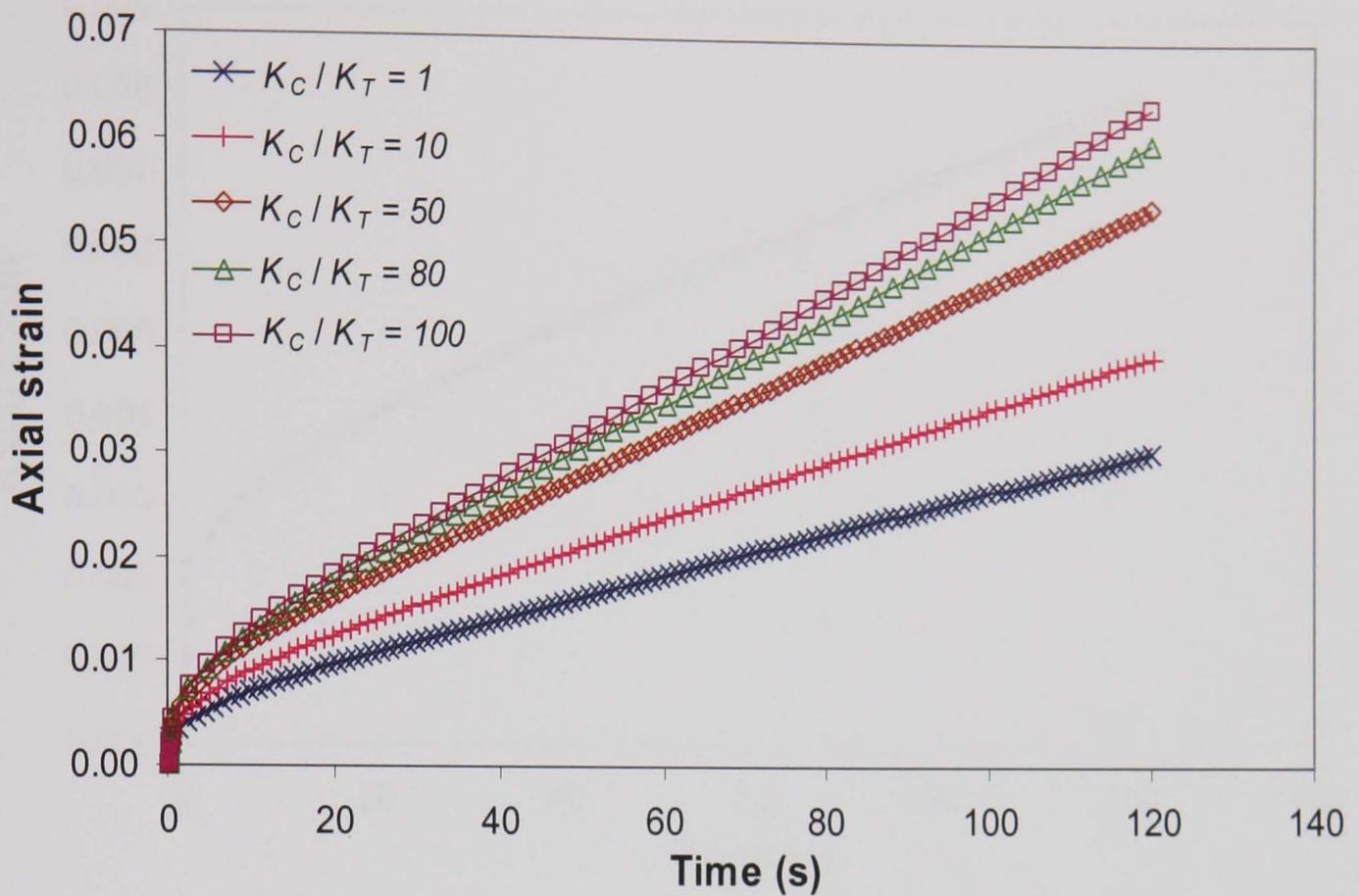
Figure 6.17: Axial strain versus loading time in simulations at different ratios of (K_C / K_T) with default Burger's contact model.
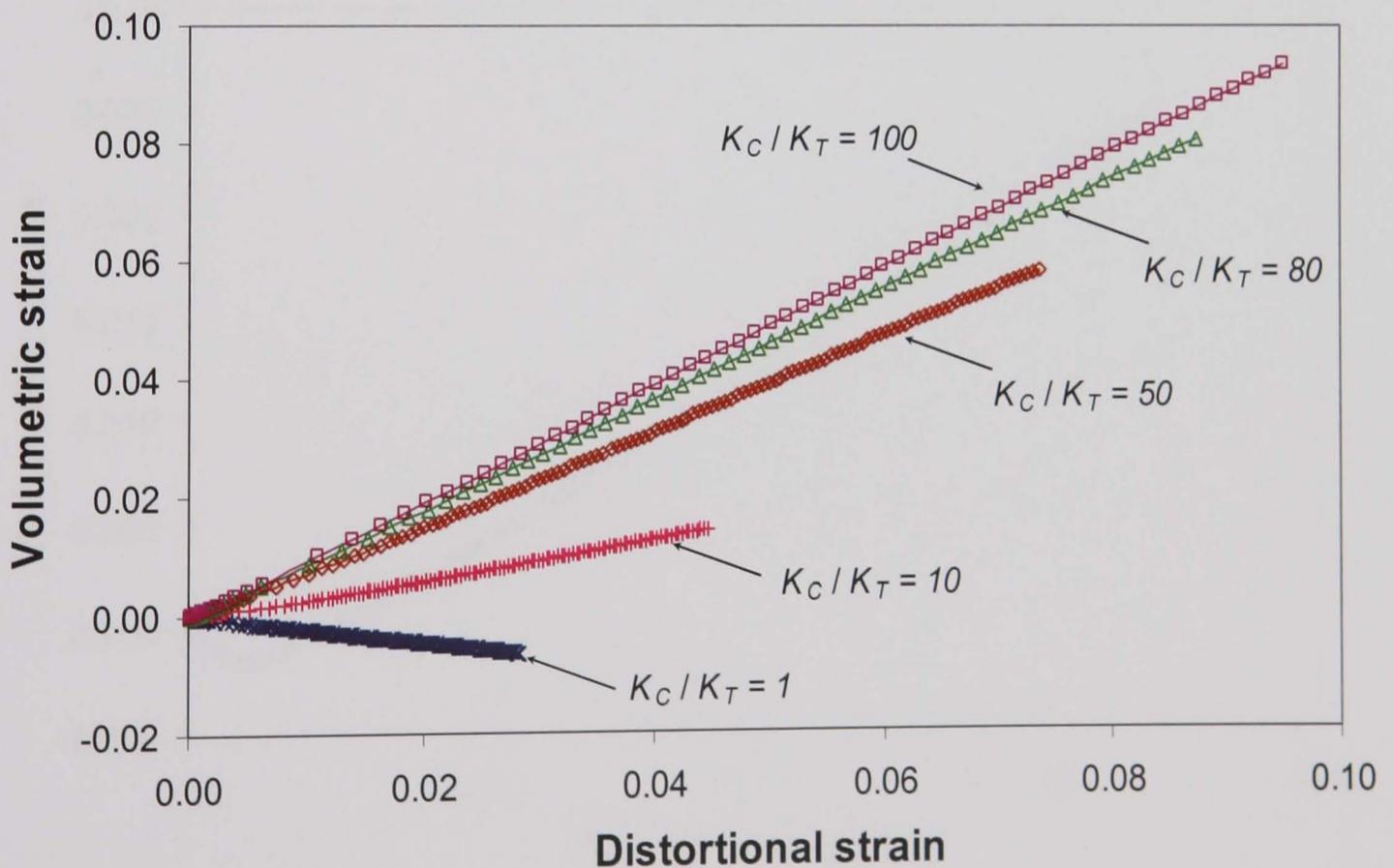
Figure 6.18: Volumetric and distortional strain in simulations at different ratios of (K_C / K_T) with default Burger's contact model.
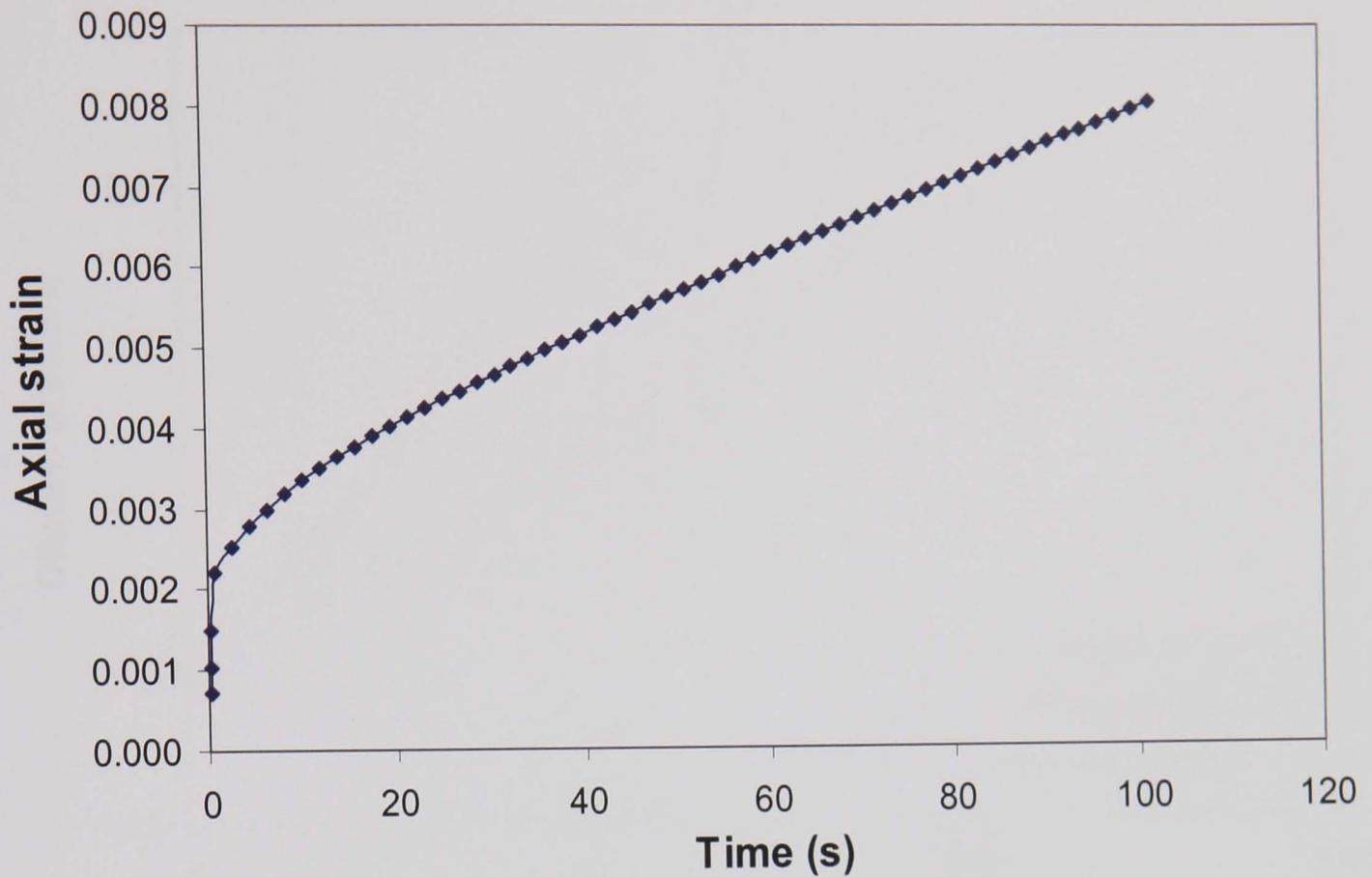
Figure 6.19: Axial strain versus loading time in simulation with modified Burger's contact model.
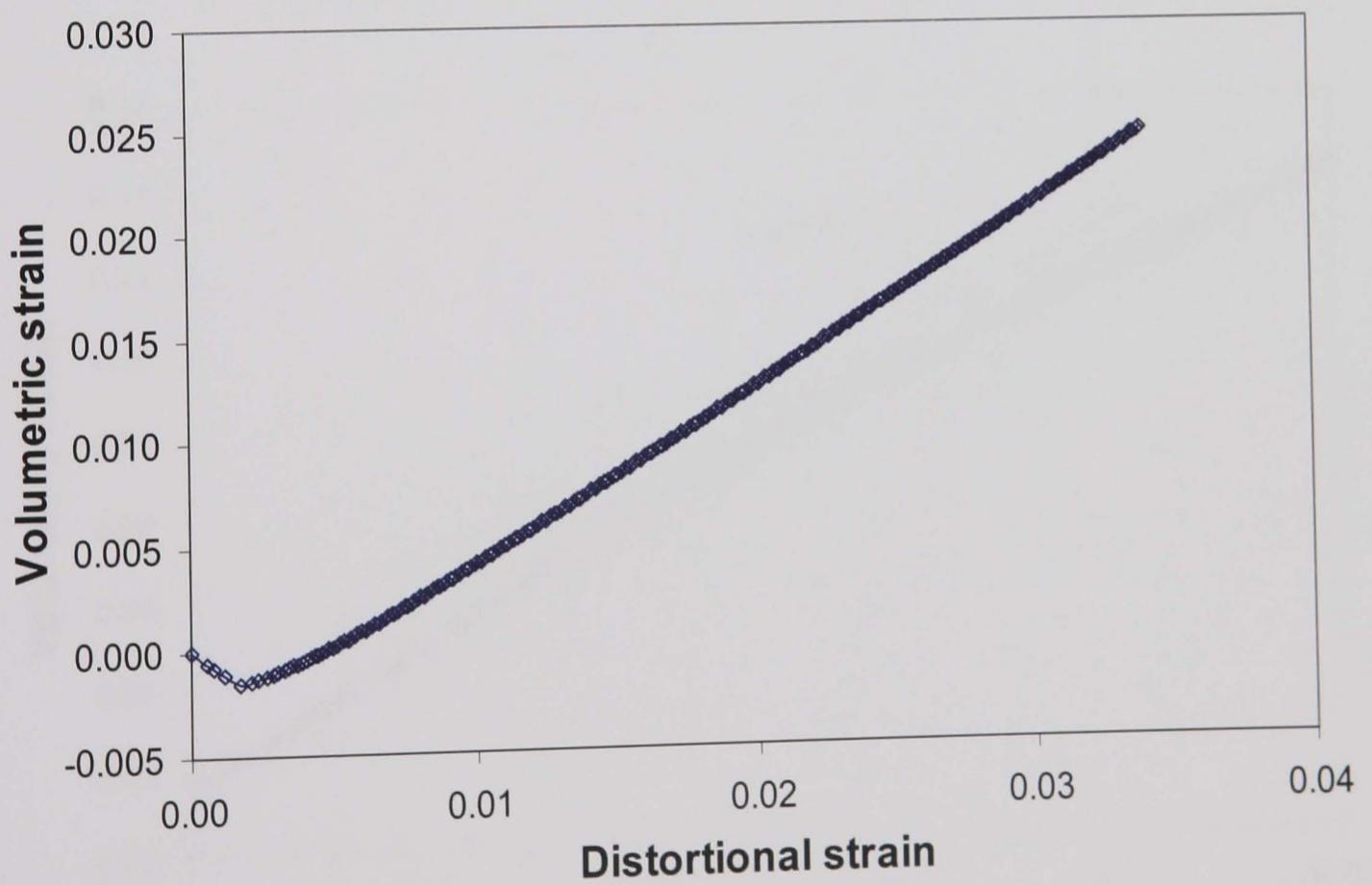
Figure 6.20: Volumetric strain versus distortional strain in simulation with modified Burger's contact model.
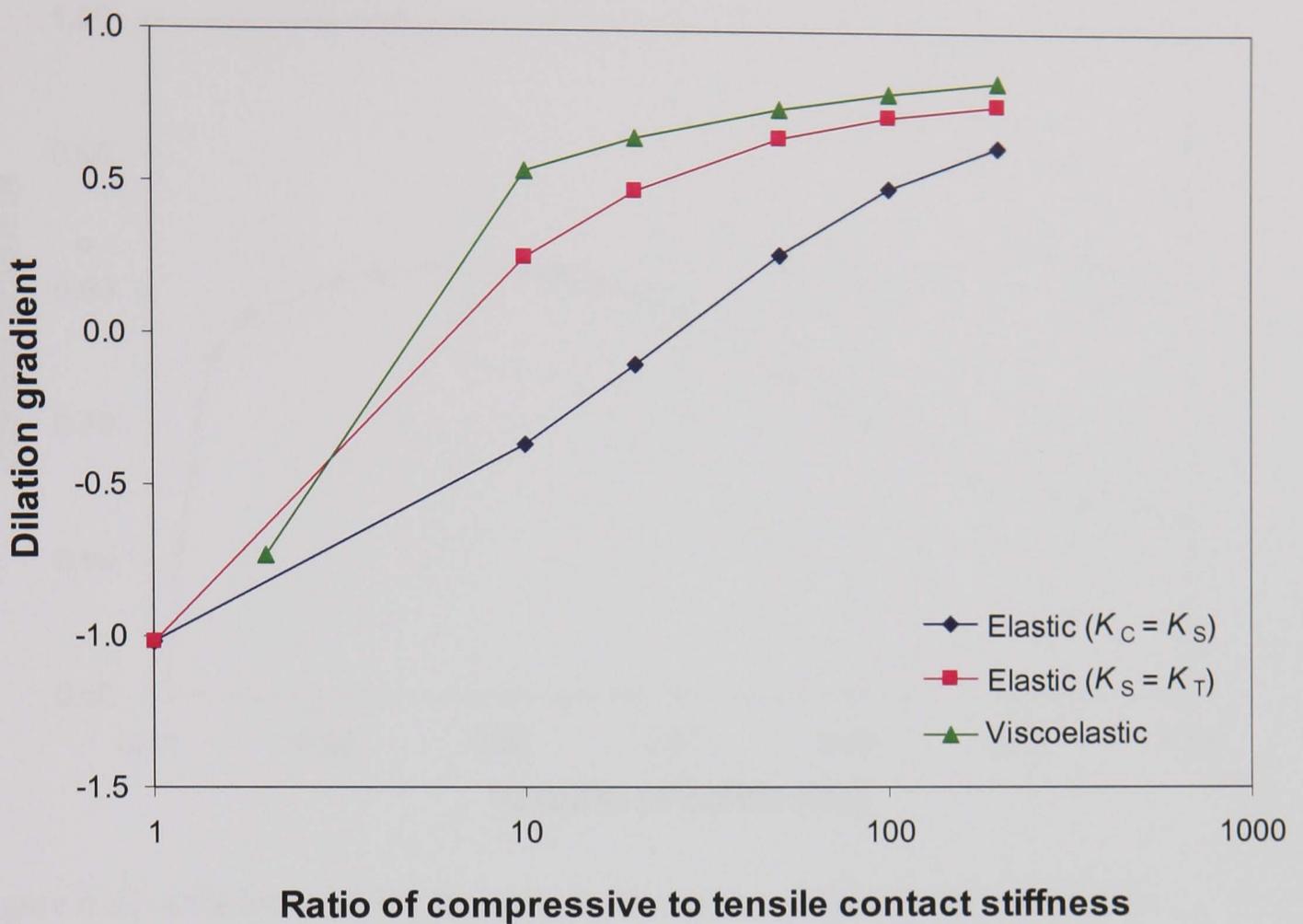
Figure 6.21: Effect of the ratio of contact stiffnesses on dilation gradients.
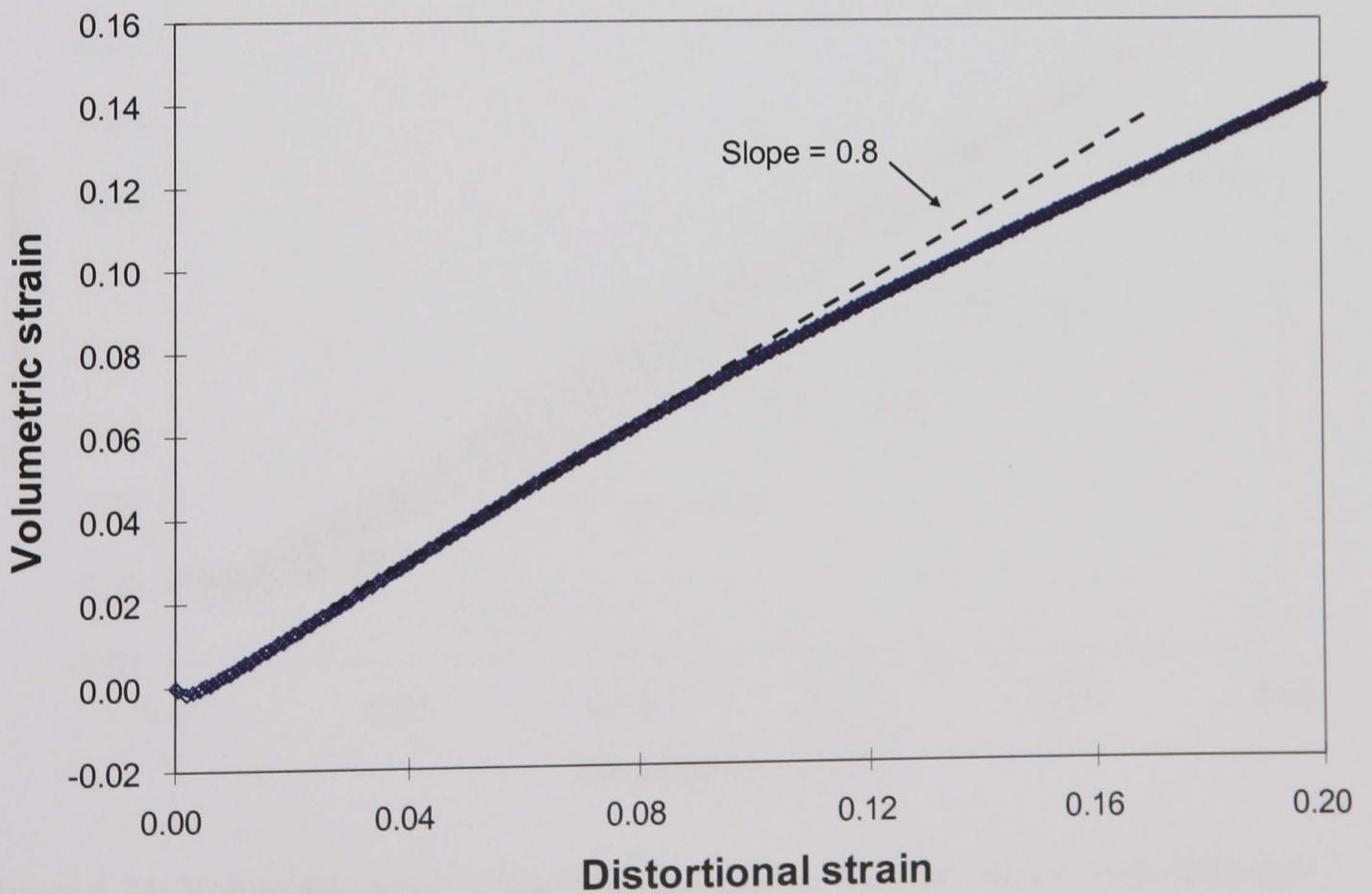
Figure 6.22: Volumetric strain versus distortional strain in uniaxial creep simulation.
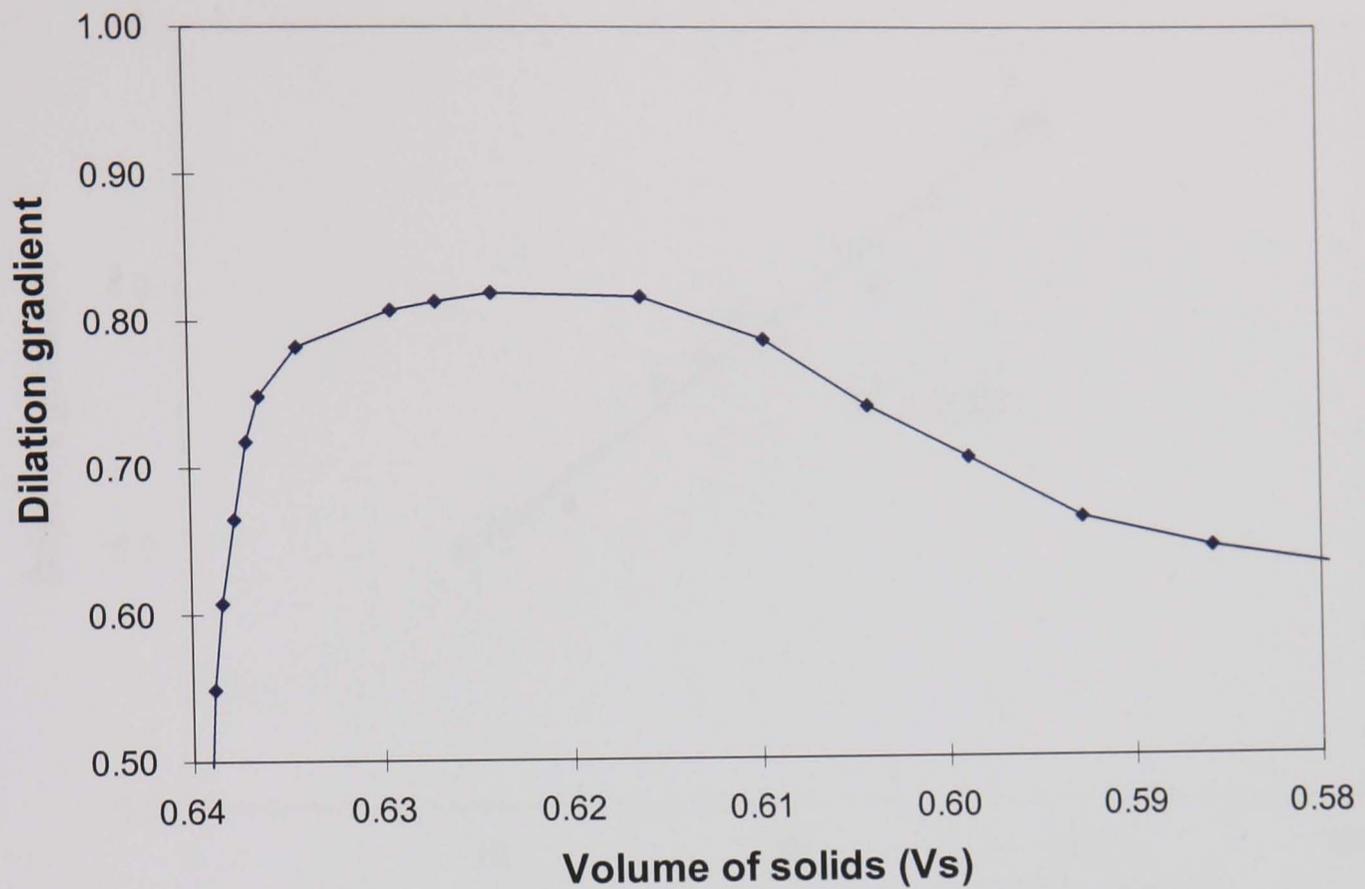
Figure 6.23: Dilation gradient and sample density in uniaxial creep simulation reaching critical state.
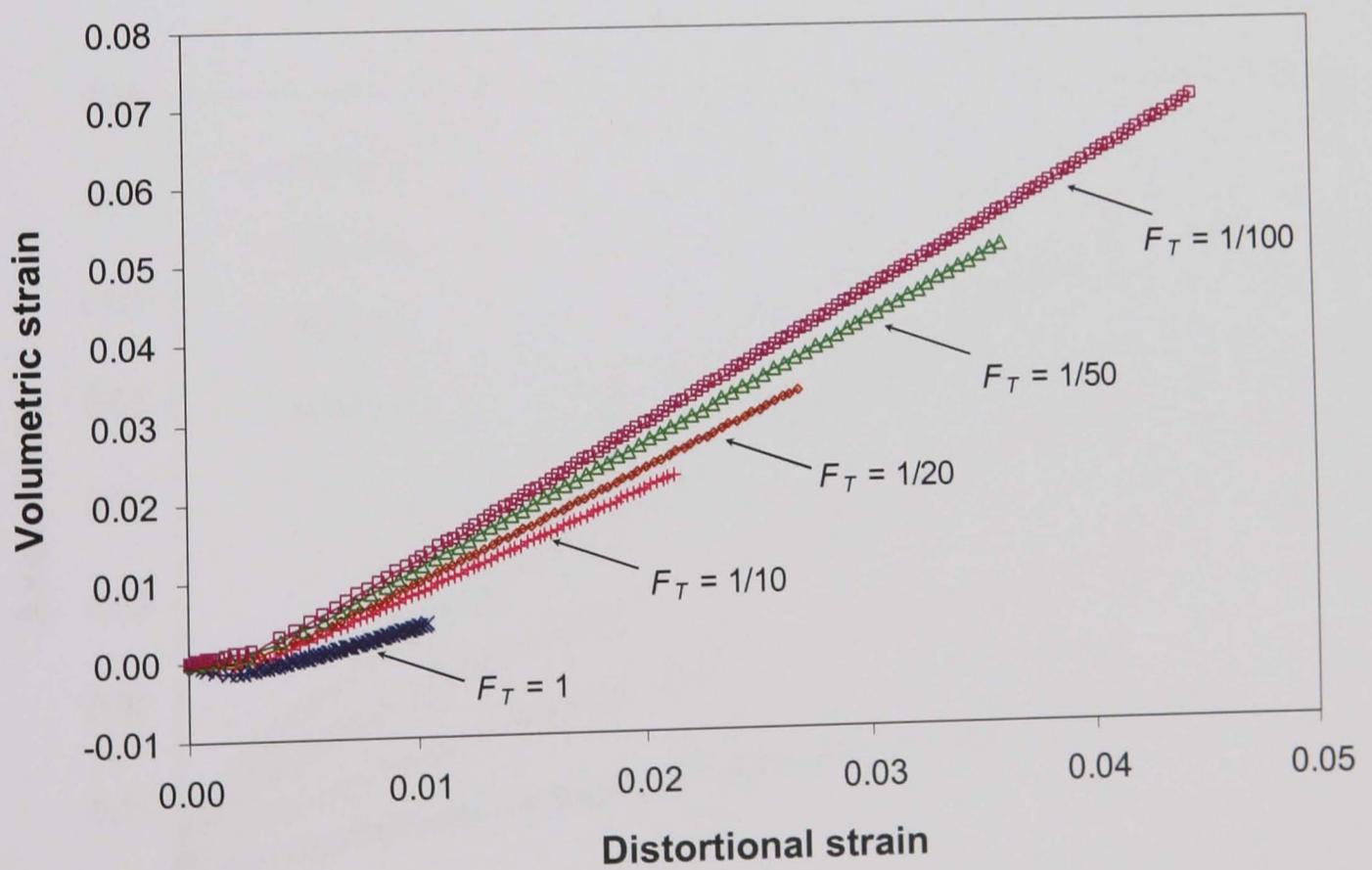
Figure 6.24: Volumetric strain versus distortional strain in simulations with different factors [F_T].
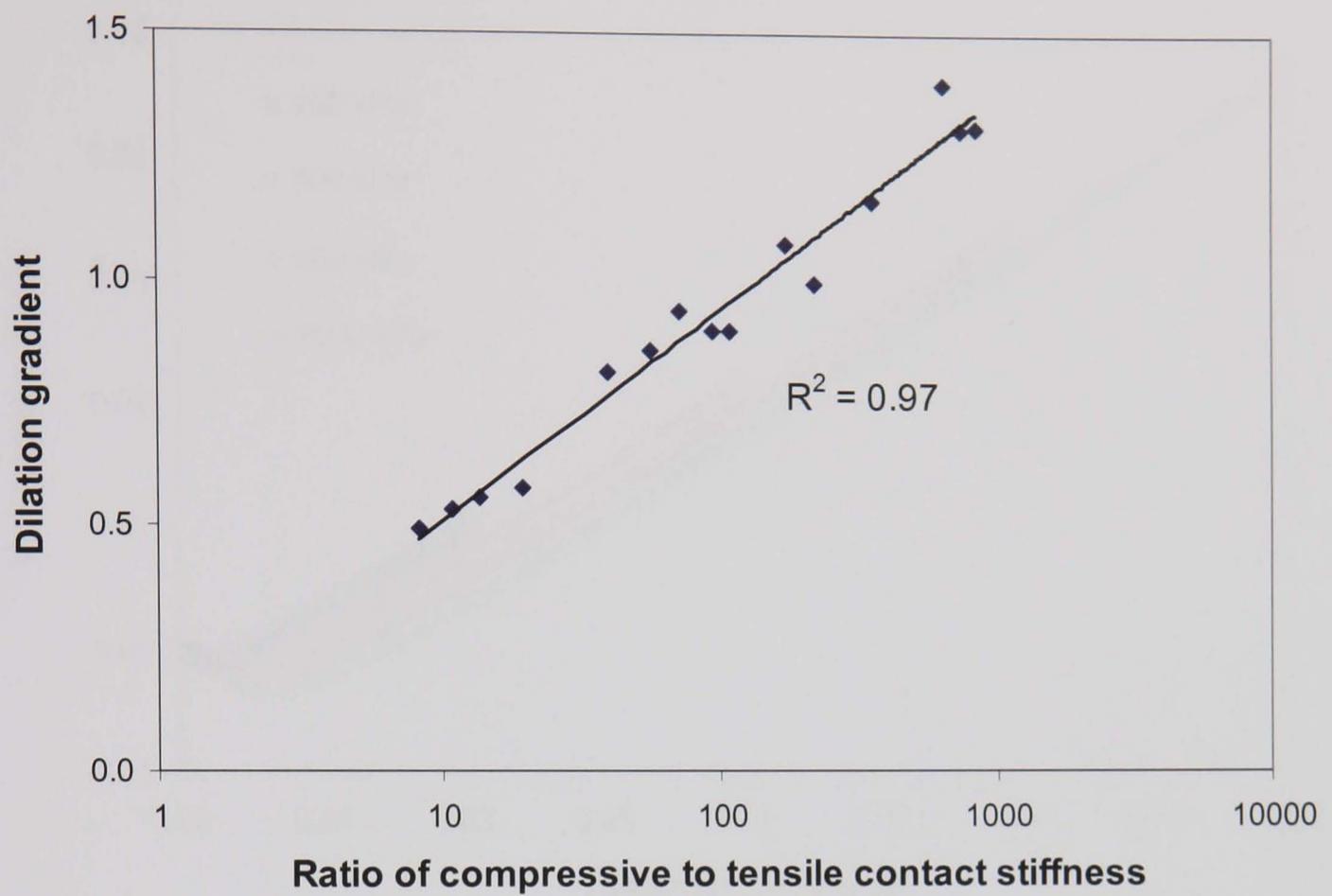
Figure 6.25: Relationship of dilation gradient and the ratio of compressive to tensile contact stiffness.
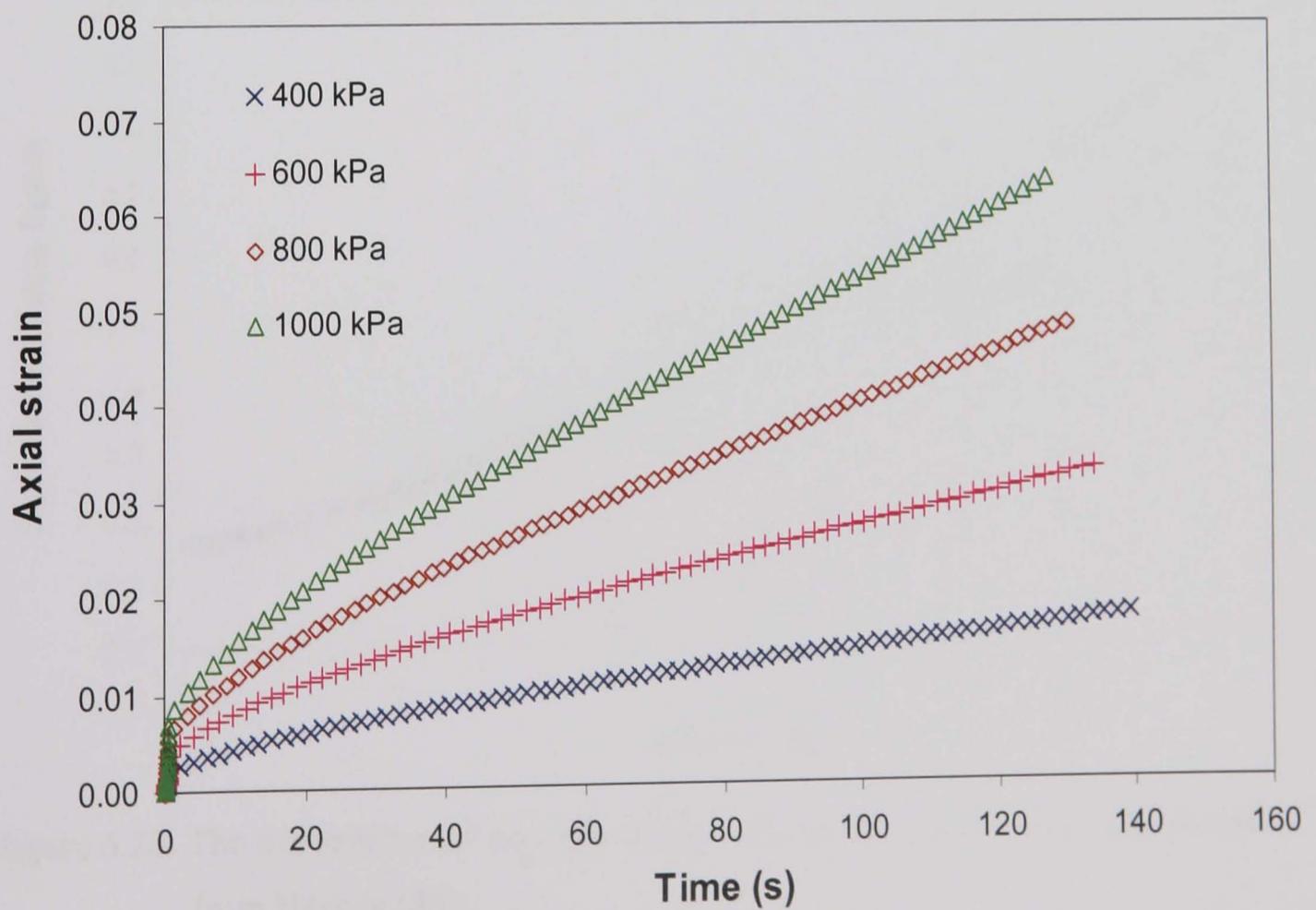
Figure 6.26: Axial strain as a function of time at different deviator stresses.
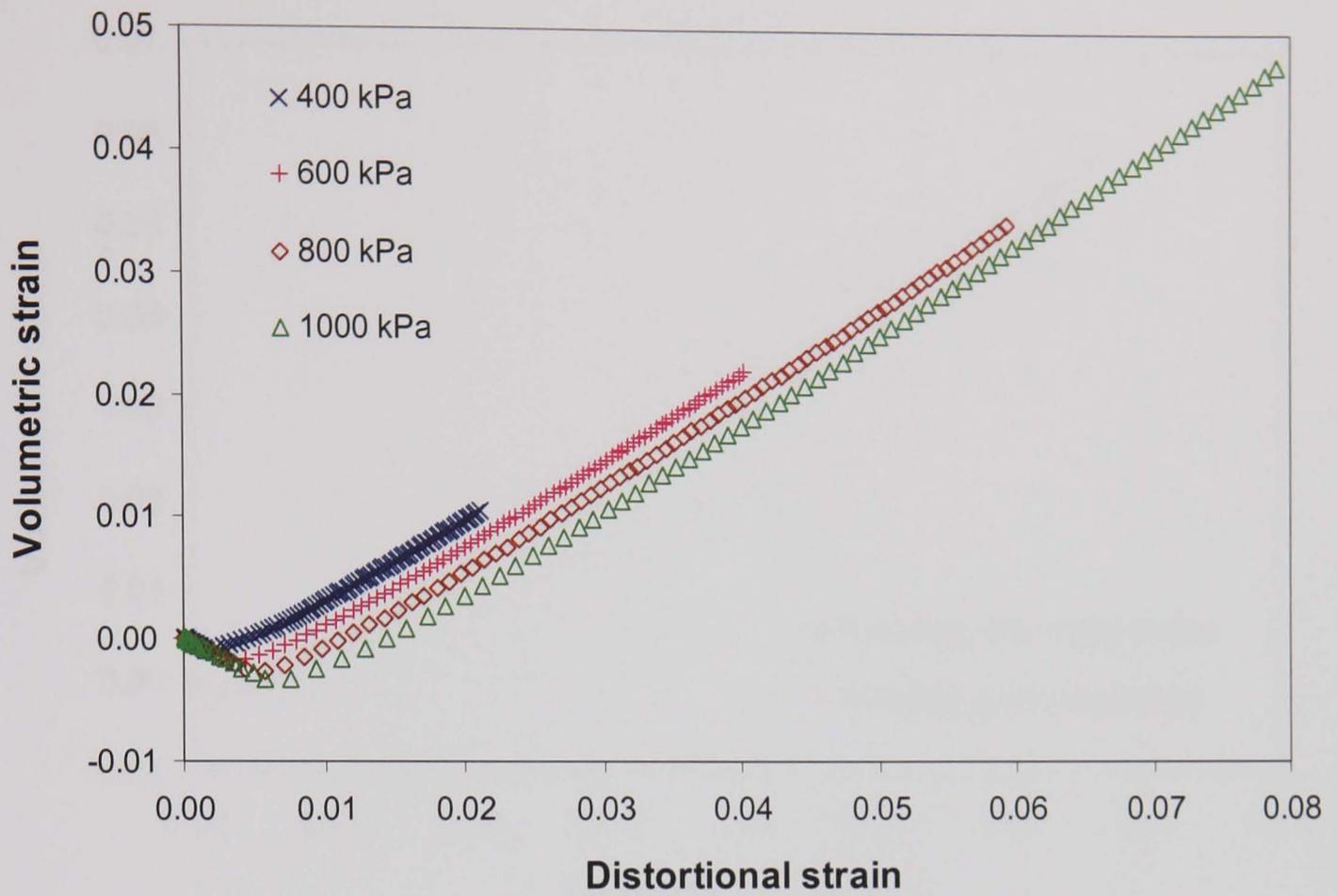
Figure 6.27: Volumetric strain versus distortional strain at different deviator stresses.
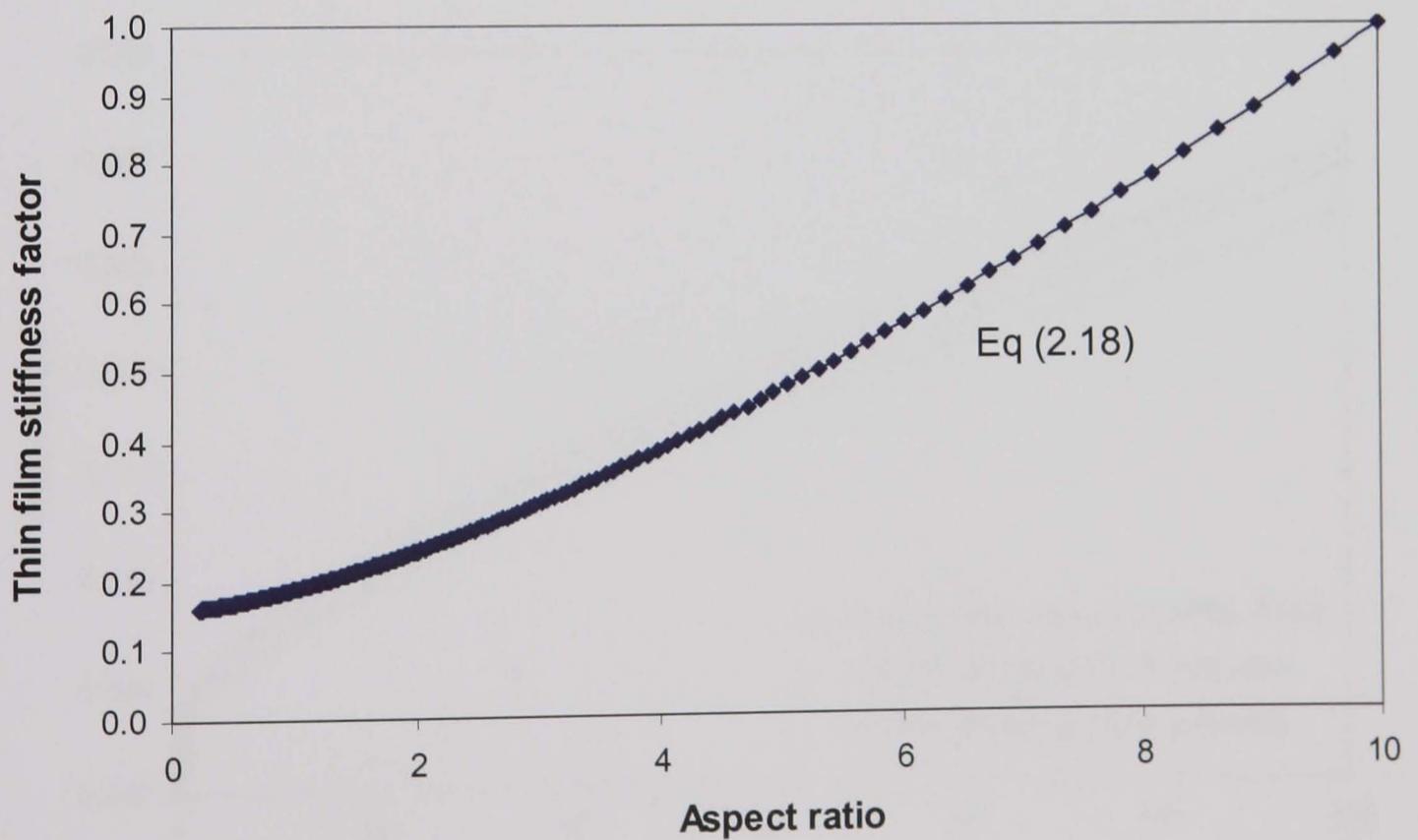
Figure 6.28: The dependence of thin film stiffness factor on aspect ratio, reproduced

from Harvey [50].
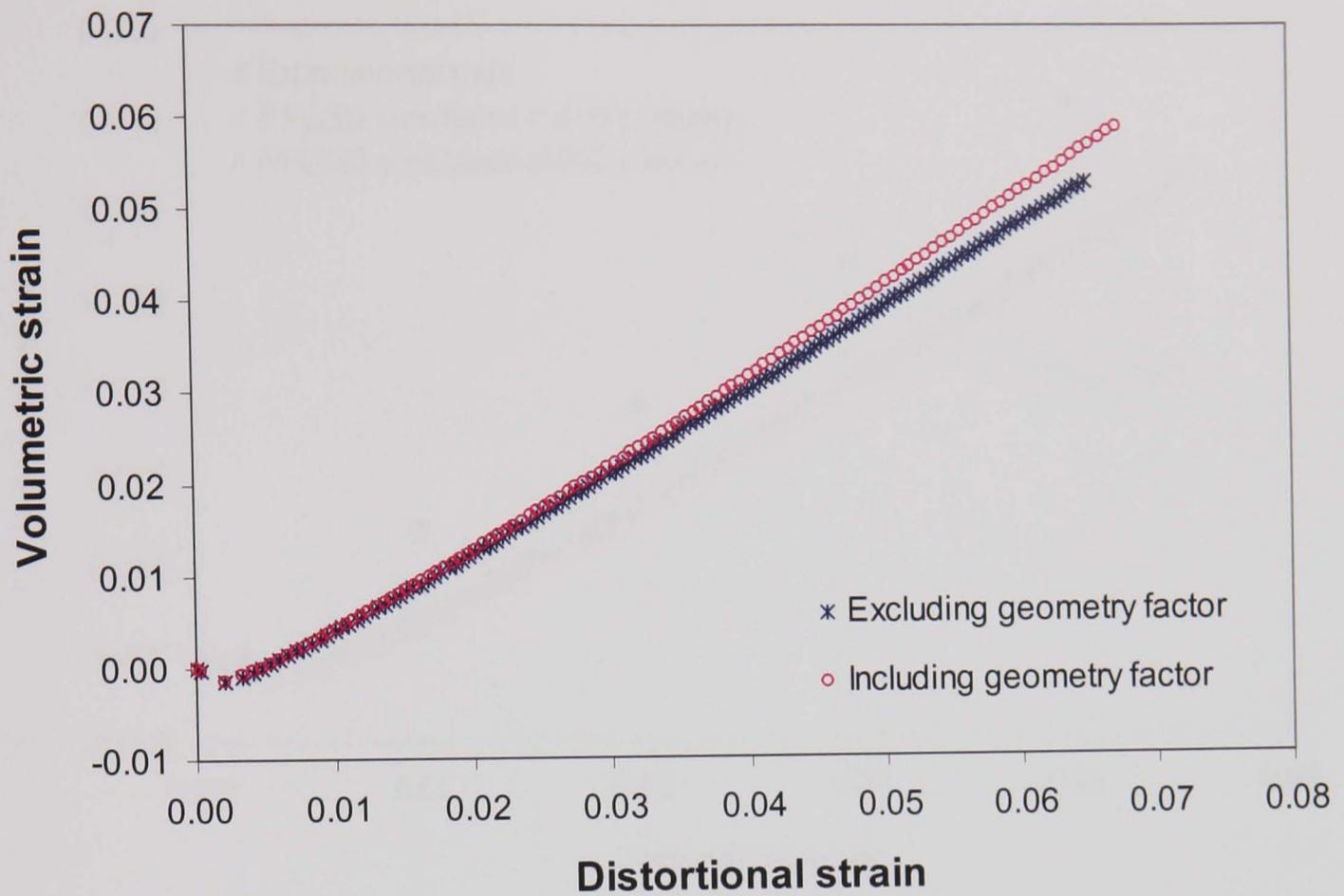
Figure 6.29: The effect of thin film geometry factor in the viscoelastic simulation.
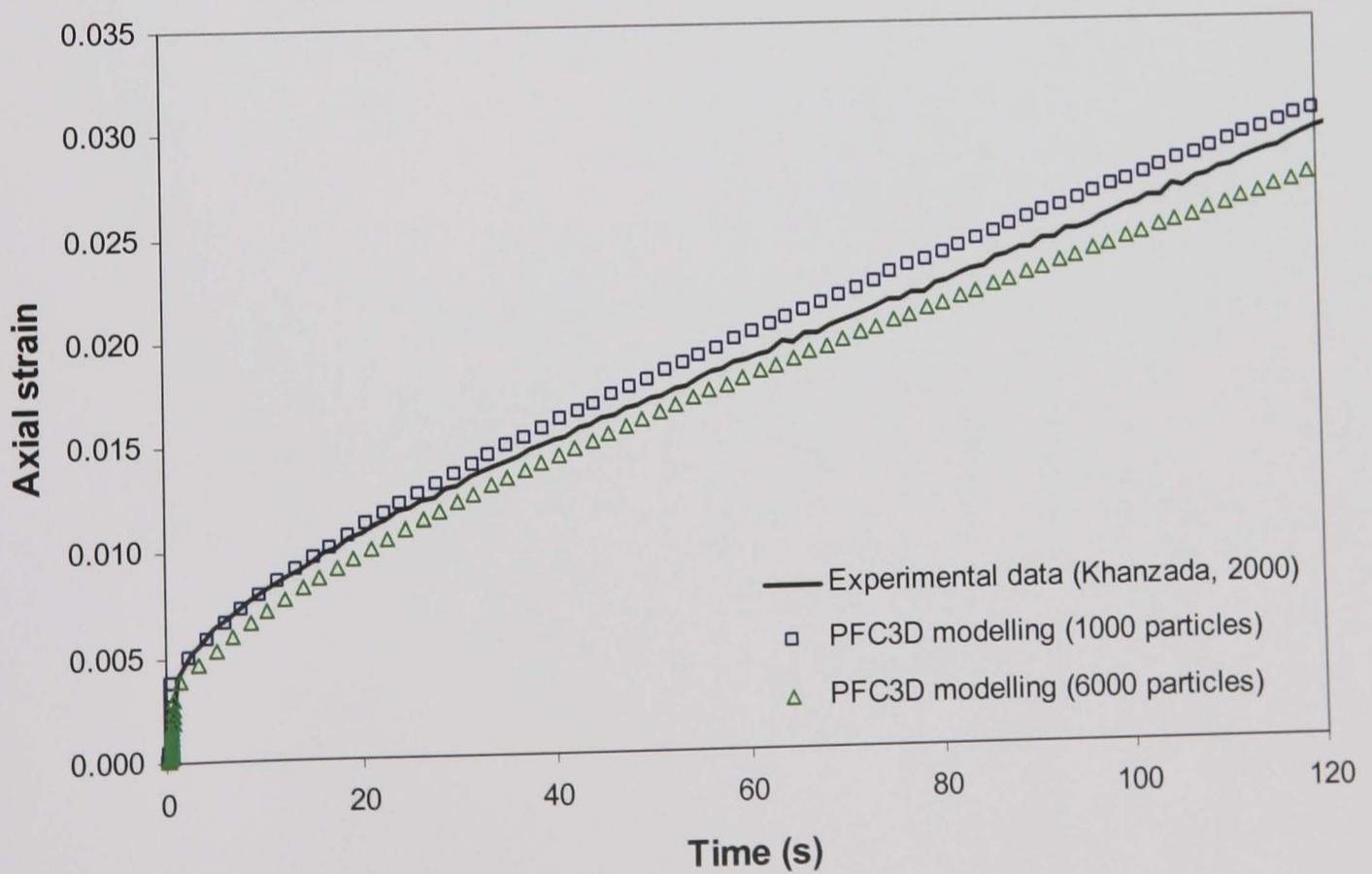
Figure 6.30: Predicted and measured axial strain for uniaxial creep test at $400kPa$ as a function of time.
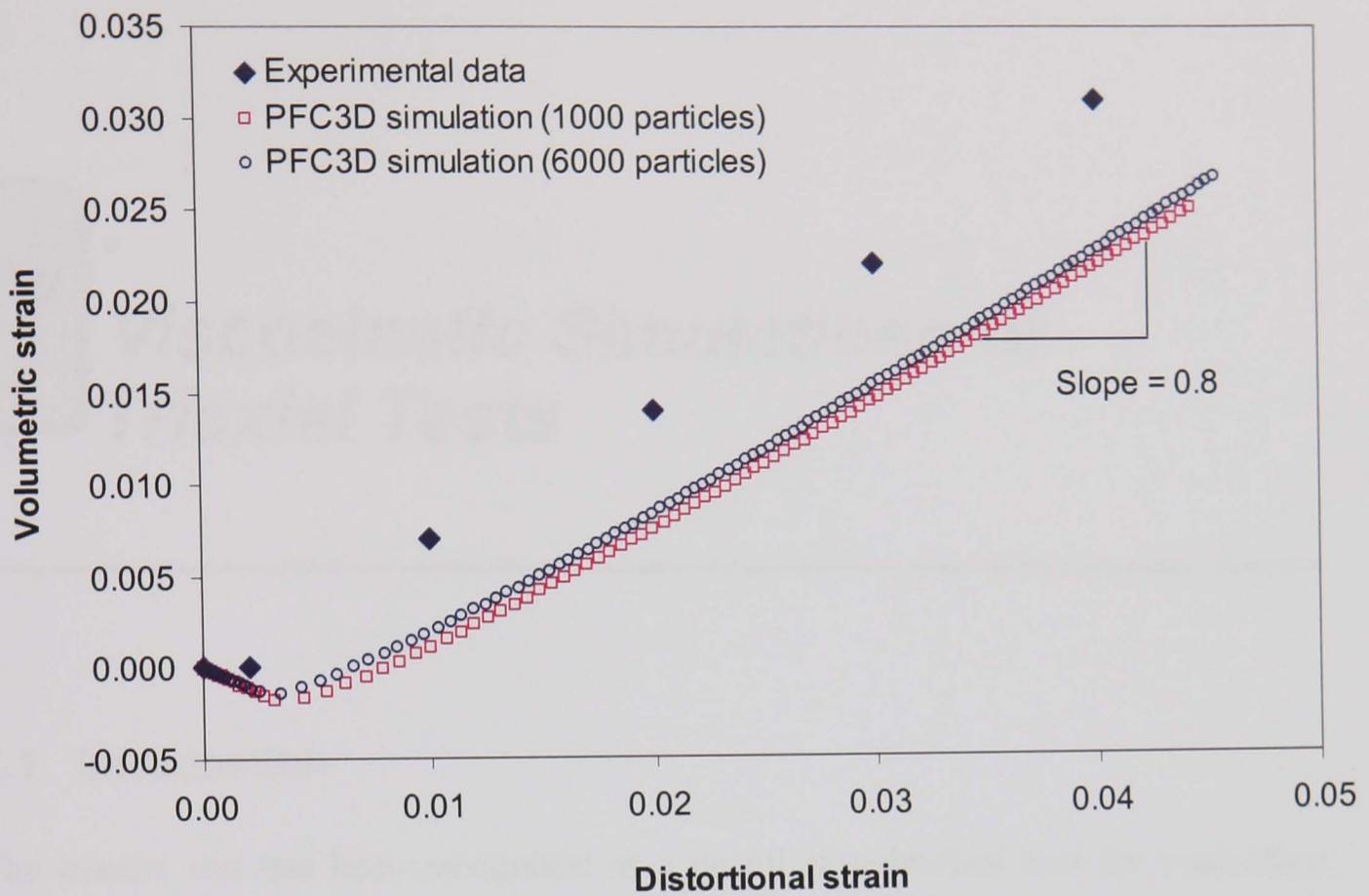
Figure 6.31: Predicted and measured volumetric strain and distortional strain for uniaxial test at $400kPa$.

7 Viscoelastic Simulations of Triaxial Tests

7.1 Introduction

The triaxial test has been recognised as a useful experimental tool for evaluating shearing resistance, stress-strain characteristics and strength properties of soils under various stress states. This test has been widely developed in soil mechanics. Brown and Cooper [16, 17] extensively studied the behaviour of asphalt mixtures through triaxial tests and showed that mixture behaviour was a function of the hydrostatic as well as deviatoric stresses. More recent applications of modelling of experimental results from triaxial tests to study the behaviour of asphalt mixtures can be found in [15, 70, 82].

The deformation behaviour of a pavement under a wheel load is highly dependent on the state of triaxial stresses in the asphalt layers. Thus, it is necessary to understand the behaviour of deformation and dilation of the asphalt under various stress states. This chapter describes the modelling of triaxial tests on asphalt mixtures using DEM.

7.2 Review of Triaxial Tests on Asphalt Mixtures

In a triaxial test, an axial load Q and a cell pressure P are related to the principal stresses (Figure 7.1) by:

$$\Sigma_{33} = Q/A + P$$

$$\Sigma_{11} = \sum {}_{22} = P \tag{7.1}$$

where A is the cross-sectional area of the specimen. Thus, the mean stress Σ_m and the deviator stress Σ are given by:

$$\Sigma_m = \Sigma_{kk}/3 = P + \frac{Q}{3A}$$

$$\Sigma = \Sigma_{33} - \Sigma_{11} = \frac{Q}{A}$$

$$\eta = \Sigma_m / \Sigma \tag{7.2}$$

The stress ratio, η is defined as the ratio of the mean stress to the deviator stress.

Deshpande and Cebon [41] conducted triaxial compression tests on idealised asphalt mixtures. They found that the deformation behaviour was dependent on the mean as well as deviatoric stresses. They concluded that for triaxial tests conducted on dense mixtures, the dilation gradient, s varied between 0.75 and 0.85 and was independent of the stress ratio, the deviatoric stress and the axial strain rate.

Figure 7.2 shows experimental data taken from Khanzada [65] where volumetric strain is plotted against distortional strain for deviator stresses of 400kPa and 1000kPa at stress ratios of 0.6 and 0.8. It can be seen from this figure that the dilation gradients from the tests with a stress ratio of 0.6 are slightly higher than the dilation gradients from the tests with a stress ratio of 0.8. It can also be seen from Figure 7.3 that at deviator stresses of 400kPa and 1000kPa, the same dilation gradient is observed at the same stress ratio. This indicates that the dilation gradient is only dependent on the stress ratio. More details on the experimental work can be found in Khanzada [65].

It should also be noted that a similar finding was found by Huang [57] in his experimental work on the triaxial compression testing of the sand asphalt mixtures at

temperature of 20°C. He found that for a given deviator stress of 620*kPa* (90*psi*), the volume change increased from 0.5% at a confining pressure of 138*kPa* (20*psi*) (Figure 7.3 (c)) to 6.5% at a confining pressure of 69*kPa* (10*psi*) (Figure 7.3 (b)) under the same loading time. This indicates that the volume change (dilation) is higher at a lower confining pressure. He also showed that at a given stress ratio of 0.53, the volume change at a deviator stress of 345*kPa* (50*psi*) (confining pressure 69*kPa*) is 1% and the volume change at a deviator stress of 689*kPa* (100*psi*) (confining pressure 138*kPa*) is 1.5%. This indicates that the volumetric dilation of the sand asphalt is only dependent on the stress ratio.

Sitharam [103] used DEM to model the effect of confining pressure on the constitutive behaviour of granular materials. Seven biaxial simulations at a constant axial strain rate of 2.5×10^{-4} mm/cycle with different lateral pressures ranging from 0.6*MPa* to 6*MPa* were performed on an identical sample. He stated that under low confining pressure (e.g. 0.6*MPa* and 0.8*MPa*), the assembly is not strongly held to resist the dilating tendency under the deviatoric stress. Hence the assembly is more susceptible to dilation. Consequently, he found that with an increase in the confining pressure there is an increase in the shear strength and a decrease in the dilation.

In summary, Deshpande and Cebon [41] stated that the dilation is independent of stress ratio. However, in contrast, the experimental studies performed by Khanzada [65] and Huang [57] showed that dilation is highly dependent on the stress ratio. Their findings are further supported by Sitharam [103] in numerical modelling. Therefore, it is necessary to perform the triaxial simulation using DEM to study the effect of stress ratio on dilation behaviour of sand asphalt.

7.3 Numerical Sample Preparation and Modelling Procedure

Since the objective of this chapter is to simulate simple laboratory tests using DEM, it is necessary to artificially generate a test specimen that replicates an idealised mixture. The numerical sample preparation procedure for triaxial simulations used in this chapter is the same as that used for the uniaxial simulations with the exception that the cylindrical boundary was not removed but was used to provide lateral

confinement to the sample. To decrease the computation time, a sample of 16.5*mm* in diameter and 33*mm* in height, containing 1,000 particles (1.88*mm* diameter) sample used in all simulations in this chapter. A high bond strength was applied to all contacts to prevent bond breakage.

As noted in the sample preparation procedure described in Chapter 4, the numerical sample is prepared to a low isotropic stress (less than 1*kPa*). In order to simulate the confining pressure, the numerical sample is then loaded isotropically using the numerical servo control (see Section 3.3.6) on the top, bottom and cylindrical boundaries to achieve the target confining stress. It should be noted that the boundary walls shear stiffness and friction coefficient were set to be zero. Figure 7.4 shows the contact force distribution in a numerical sample containing 1,000 particles under a confining stress of 100*kPa*. It can be seen from this figure that the distribution of contact forces is isotropic, which simulates the uniform confining pressure applied on the triaxial specimen in the laboratory prior to loading.

In should be noted that in a triaxial experiment, the confining pressure must be maintained at a constant value during testing. To simulate this condition, the servo control mechanism in PFC3D is applied on the lateral (cylindrical) boundary to maintain a constant confining stress to the sample. Figure 7.5 shows the magnitude of stresses on top, bottom and lateral boundaries in a triaxial simulation at a confining pressure of 100*kPa* and stress ratio of 0.6. At the beginning of the test, the top, bottom and lateral boundaries are subjected to the confining stress of 100*kPa*. During the test, an axial load was applied on the sample to an axial stress of approximately 500*kPa* (deviator stress 400*kPa*). It is shown in Figure 7.5 that during the loading period, the stress distribution on the top and bottom are equal throughout. The lateral stress is maintained at 100*kPa* during the simulation.

7.4 Effect of Stress Ratio

As mentioned earlier, previous researchers [57, 65, 103] have shown that the dilation gradient of the sand asphalt is a function of the ratio of mean stress to deviator stress in a triaxial test. The objective of this section is to investigate the effect of stress

ratio on the dilation behaviour of sand asphalt by using DEM simulations. It should be noted that the modified Burger's contact model is used for all triaxial simulations. Elastic behaviour has been assumed for the compressive normal contact stiffness whereas viscoelastic behaviour has been assumed for the tensile normal contact stiffness and the shear contact stiffness.

A series of triaxial simulations was performed to investigate the effect of stress ratio and deviator stress on the predicted dilation gradient of the sand asphalt mixture. A sample containing 1,000 particles was used. A high contact bond strength was applied to all contacts to prevent bond breakage. The contact parameters are given in Table 7.1. Figure 7.6 shows the predicted axial creep strains plotted as a function of time for a deviator stress of 400*kPa* and stress ratios of 0.33, 0.6 and 0.8. It can be seen from this figure that the axial strain response is a function of loading time comprising of elastic, viscoelastic and viscoplastic components. The axial strain in the uniaxial simulation (stress ratio of 0.33) is higher than that axial strain in triaxial simulations with stress ratios of 0.6 and 0.8. This indicates that the axial strain is lower in the simulation with a higher confining stress on the sample. Similar behaviour was observed by Sitharam [103] from biaxial DEM modelling with different confining pressures, where he found an increase in the failure stress with an increase in the confining pressure. This indicates that the sample bulk modulus is higher with an increase in the confining pressure, hence a lower axial strain. Also plotted in Figure 7.6 is an experimental result obtained for a similar idealised asphalt mixture tested at the same deviator stress and stress ratio of 0.6 taken from Khanzada [65]. It can be seen that agreement is reasonable although the DEM tends to over-predict the steady-state dilation gradient although it should be noted that, as discussed earlier, the effect of using 1,000 particles will be to over-predict the axial strain response.

Three triaxial simulations were performed at a deviator stress of 400*kPa* with stress ratios of 0.33 (uniaxial), 0.6 and 0.8. Figure 7.7 shows the predicted volumetric strain plotted against the distortional strain. It can be seen from this figure that early in the test, the volumetric strain is negative (initial compaction of material) after which it increases approximately in proportion to the distortional strain as the material dilates. It can also be seen from Figure 7.7 that, as the stress ratio is

increased, the dilation gradient reduces. The dilation gradients between distortional strains levels of 5.5% and 6% for simulation with different stress ratios were calculated and plotted in Figure 7.8. It can be seen from this figure that the dilation gradient decreases from 0.8 at a stress ratio of 0.33 (uniaxial conditions) to 0.6 at stress ratio of 0.8. This indicates that the dilation gradient is lower at higher stress ratios, which is in agreement with the experimental data shown in Figure 7.2 (where the dilation gradients are taken at the same distortional strain levels).

Figure 7.9 shows a plot of average number of contacts (coordination number) versus axial strain for simulations with different stress ratios. It can be seen from this figure that the coordination number is higher for higher stress ratios (e.g. a stress ratio of 0.8). This indicates that with an increase in confining pressure, the particles pack more closely, hence resulting a higher coordination number. It was found that an increase in coordination number (under high confining pressure) in a bonded sample decreases the dilatancy of material due to the higher constraints on the particles. Consequently, the dilation gradient is lower in simulations with a higher stress ratio. Similar results were found by Sitharam [103] where he stated that with an increase in the coordination number, the assembly at high confining pressures can sustain significant interparticle forces since there is no dilatancy in the system.

The DEM simulation results in this section clearly indicate that the stress ratio has a significant effect on the dilation of the sand asphalt mixture. However, the model was not able to predict the correct level of dilation gradient as measured by previous researchers [40, 65]. As mentioned earlier in section 6.11, more complex particle shape is required to simulate the correct level of dilation gradient.

7.5 Effect of Deviator Stress

The experimental result shown in Figure 7.2 [65] indicates that the dilation gradient of the sand asphalt is independent of deviator stress but only dependent on the stress ratio. The objective of this section is to simulate the dilation gradient of the sand asphalt subjected to different deviator stresses at the same stress ratio.

A series of triaxial simulations was performed with deviator stresses ranging from 100*kPa* to 800*kPa*. The confining stress varied so that the stress ratio remained at 0.6 (chosen arbitrarily) in all cases. Figure 7.10 shows the predicted volumetric strain plotted against the deviator strain. It can be seen from this figure that approximately the same dilation gradients are observed for different deviator stresses indicating that the dilation gradient is only dependent on the stress ratio, which agrees with previous research [57, 65]. In the simulation with the higher deviator stress (e.g. 800*kPa*), the confining pressure is higher under the same stress ratio of 0.6, therefore the material dilates at the same rate of volumetric strain to distortional strain compared to the simulations with lower deviator stresses at the same stress ratio. Hence the dilation gradient is only dependent on the stress ratio regardless of the magnitude of deviator stress and confining pressure.

It can also be seen from Figure 7.10 that for simulations with a higher deviator stress (higher confining pressure), the initial compaction phase (negative in volumetric strain) is larger. This is because a higher confining pressure results in greater compaction of the sample at the beginning of the test. However, the material then dilates with a same dilation gradient in all simulations.

In conclusion, the study based on DEM simulation results in this section has emphasised that the dilation gradient is only dependent on the stress ratio.

7.6 Conclusions

The following conclusions can be drawn from this chapter.

- A modelling procedure has been developed to simulate the condition of triaxial loading.

- The dilation gradients were found to be dependent only of stress ratio. The dilation gradient was found to increase as the stress ratio decreases.

- A higher coordination number was found in the sample subjected to a higher confining pressure.

- The dilation gradients were found to be independent of deviator stress under the same stress ratio.

- The comparison between the predicted and measured results has shown that the model is able to predict the effect of stress ratio on dilation.

- Future work will concentrate on correctly modelling the dilation gradients in order to achieve even better agreement between DEM and experimental data.

Tables

Table 7.1: Burger's contact parameters for triaxial viscoelastic simulation

Shear Contact		Tension Contact		Compression contact	
Property	Value	Property	Value	Property	Value
K_o^s (MN/m)	0.12	K_o^n (MN/m)	0.36	E_o^n (MN/m)	0.70
C_∞^s (MNs/m)	0.80	C_∞^n (MNs/m)	2.40		
K_1^s (MN/m)	0.03	K_1^n (MN/m)	0.09		
C_1^s (MNs/m)	0.80	C_1^n (MNs/m)	2.40		

Figures

Figure 7.1: Schematic showing the triaxial co-ordinate system
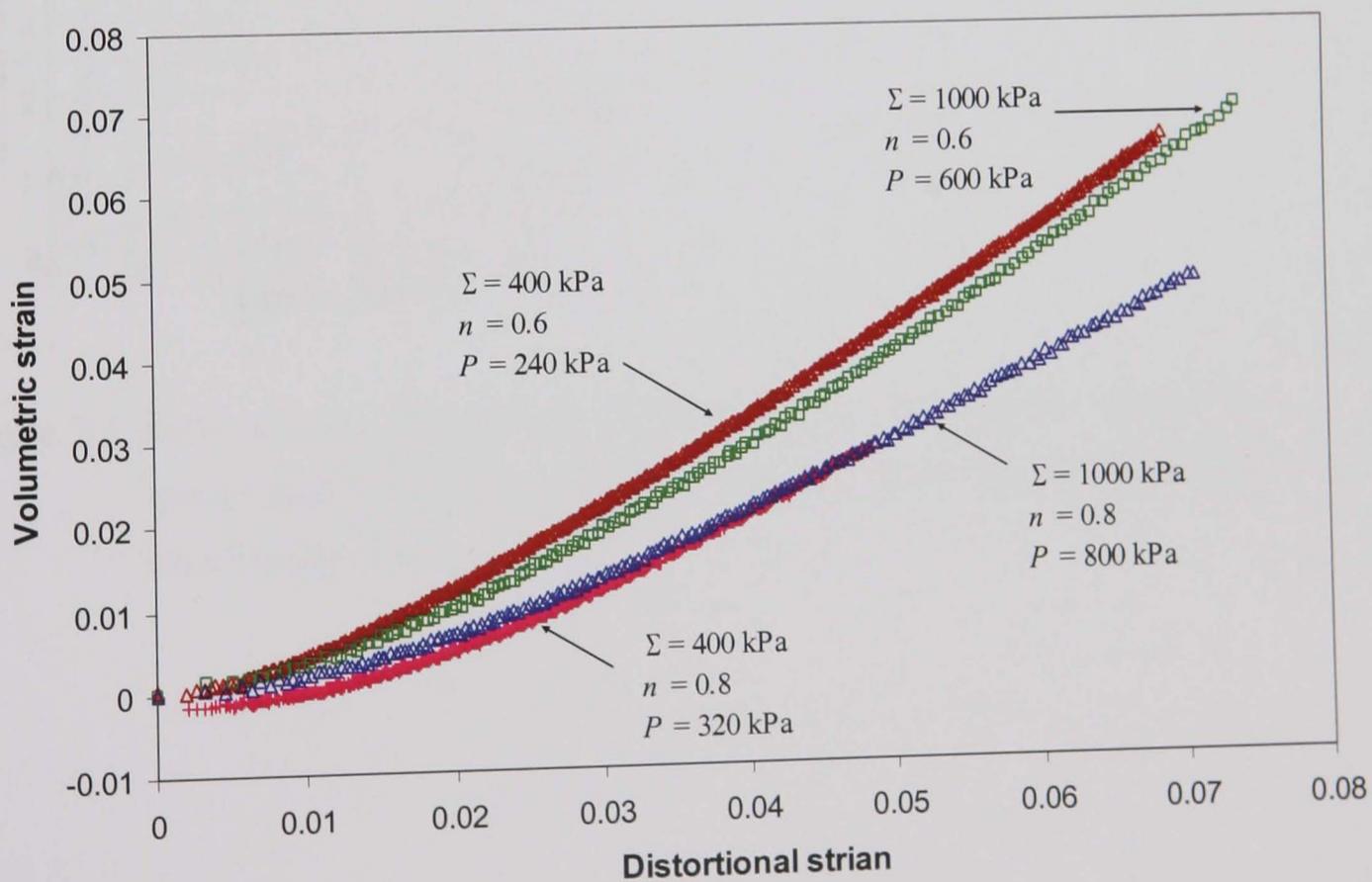
Figure 7.2: Measured volumetric strain and distortional strain at different deviator stresses Σ and stress ratios η (reproduced from Khanzada [65])
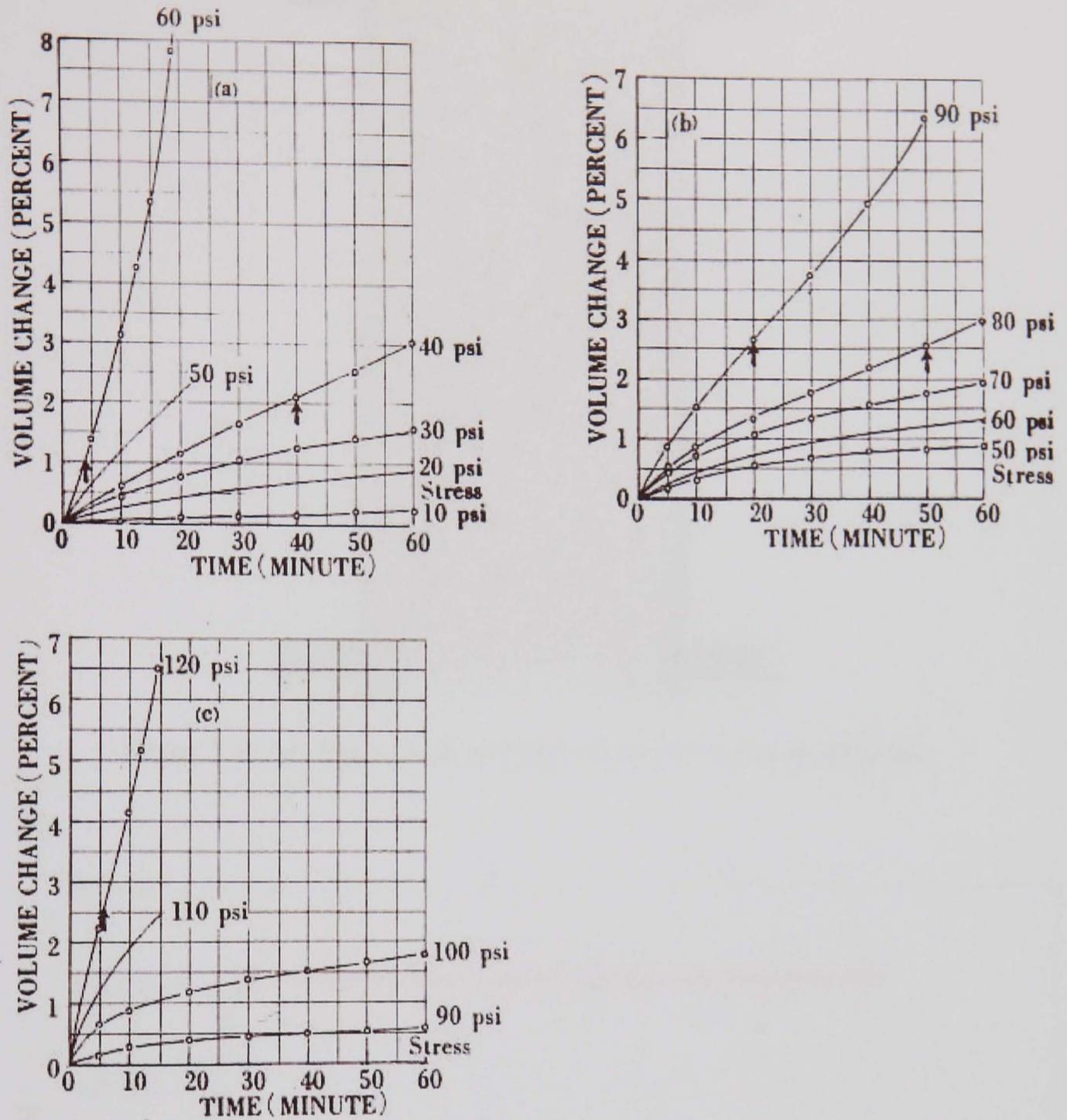
Figure 7.3: Stress-volume change-time relationship of a sand-asphalt mixture: (a) unconfined, (b) 10*psi* confining pressure, (c) 20*psi* confining pressure, after Huang [57].
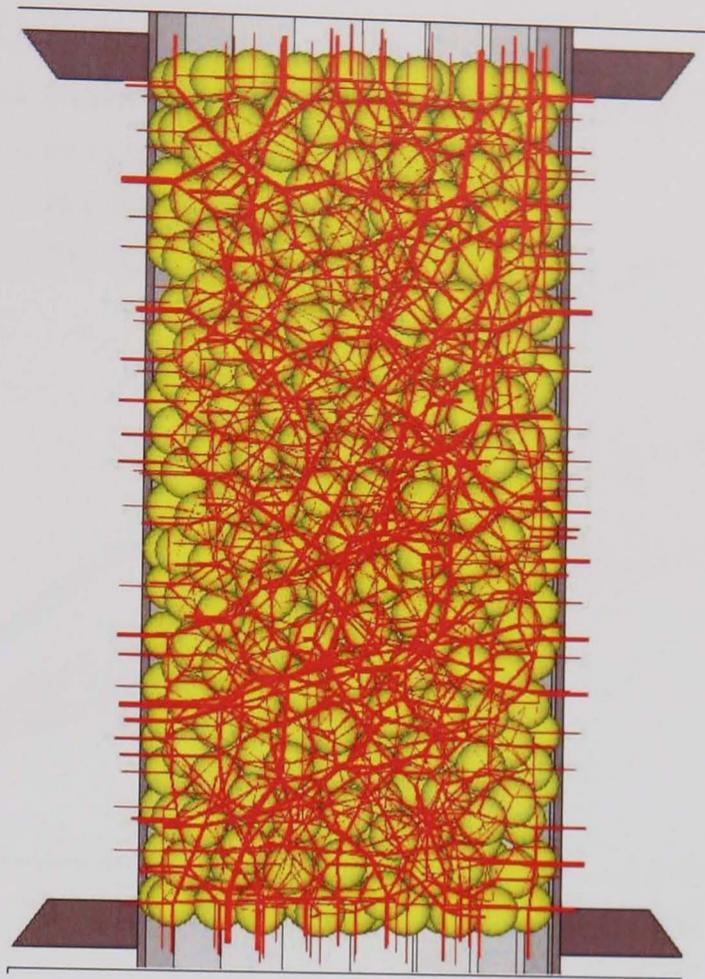
Figure 7.4: Isotropic stress distribution under confining pressure.
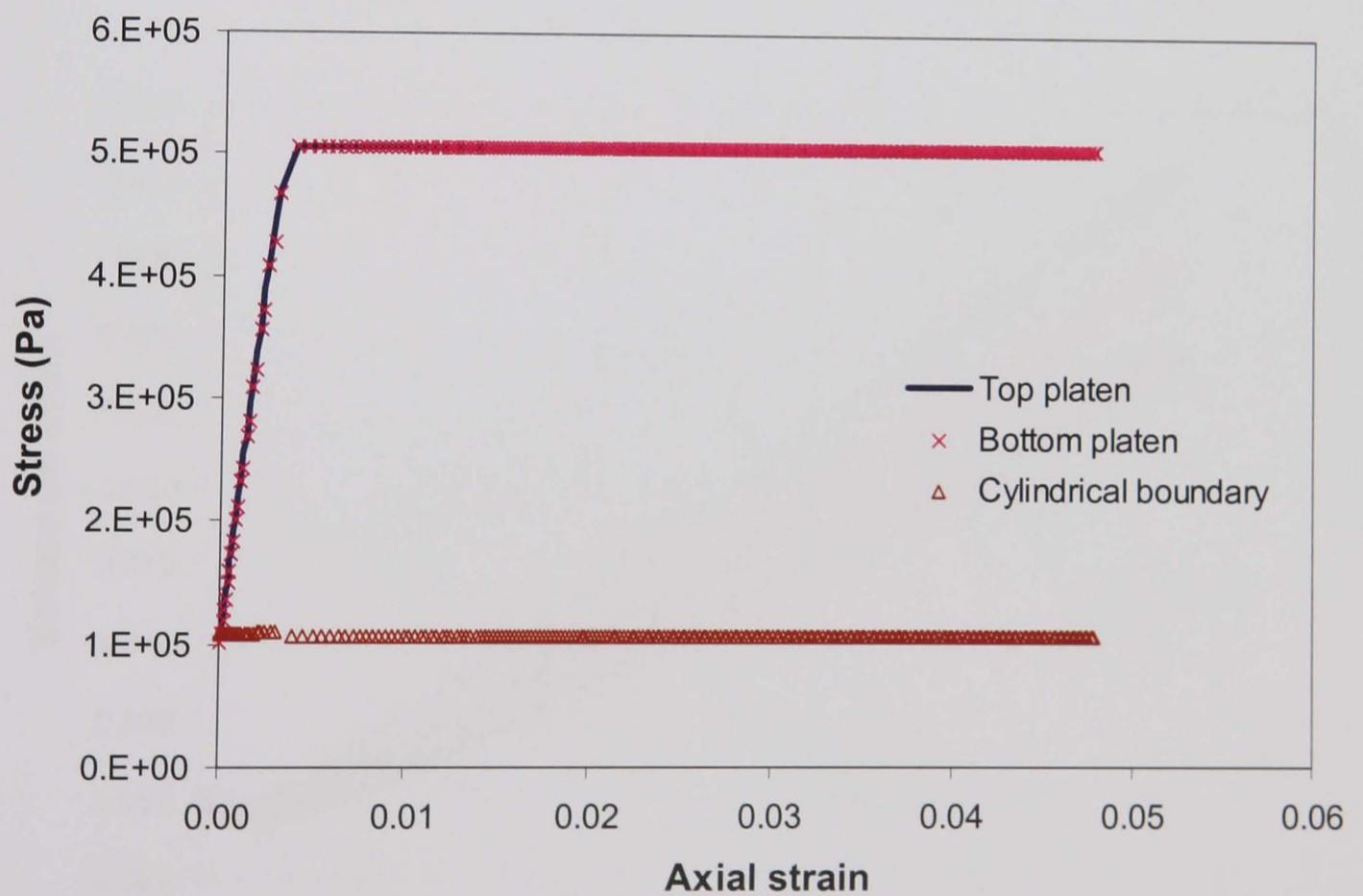
Figure 7.5: The stresses on top, bottom and lateral (cylindrical) boundaries during simulation.
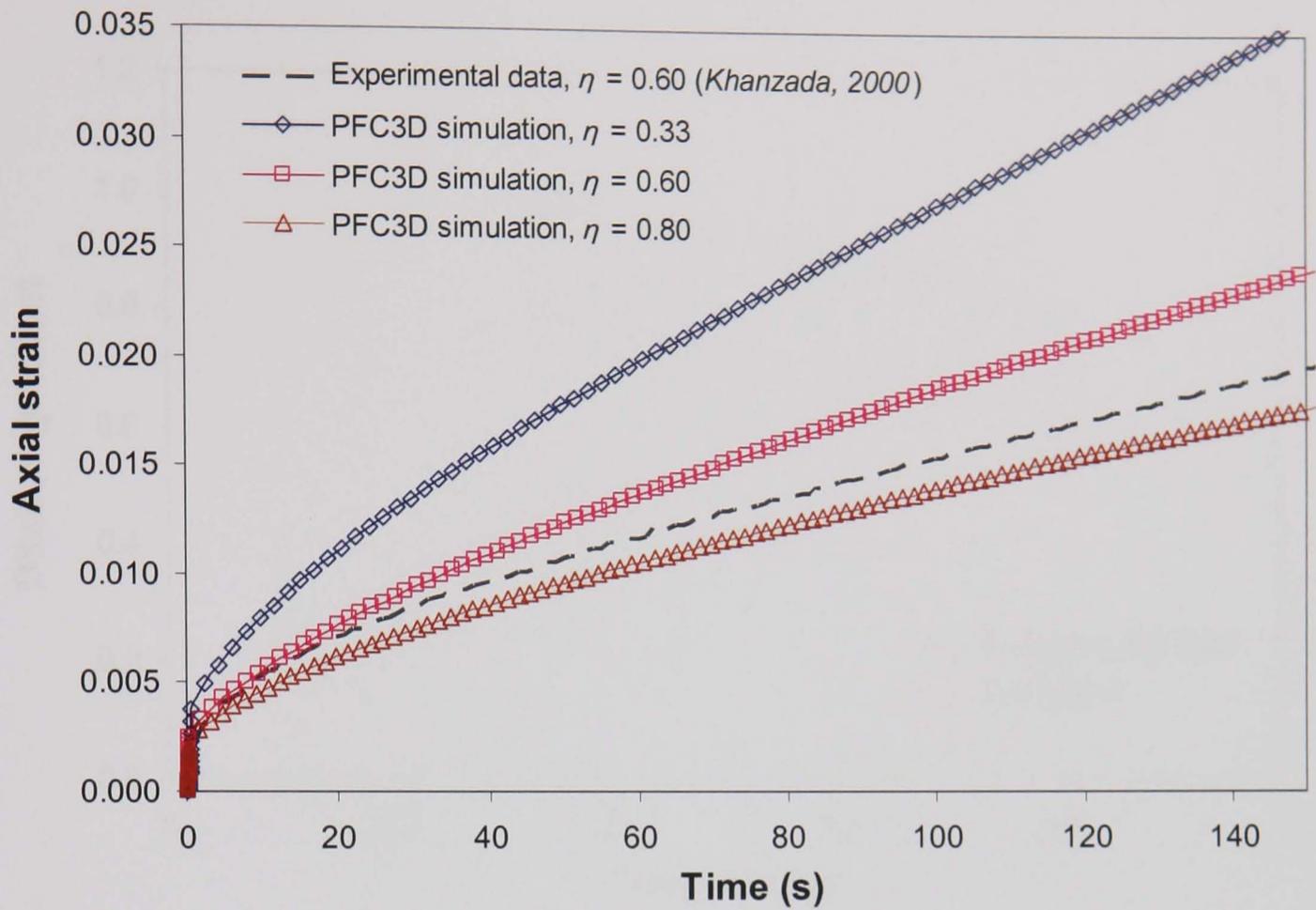
Figure 7.6: Effect of stress ratio on axial strain as a function of loading time at deviator stress of $400kPa$.
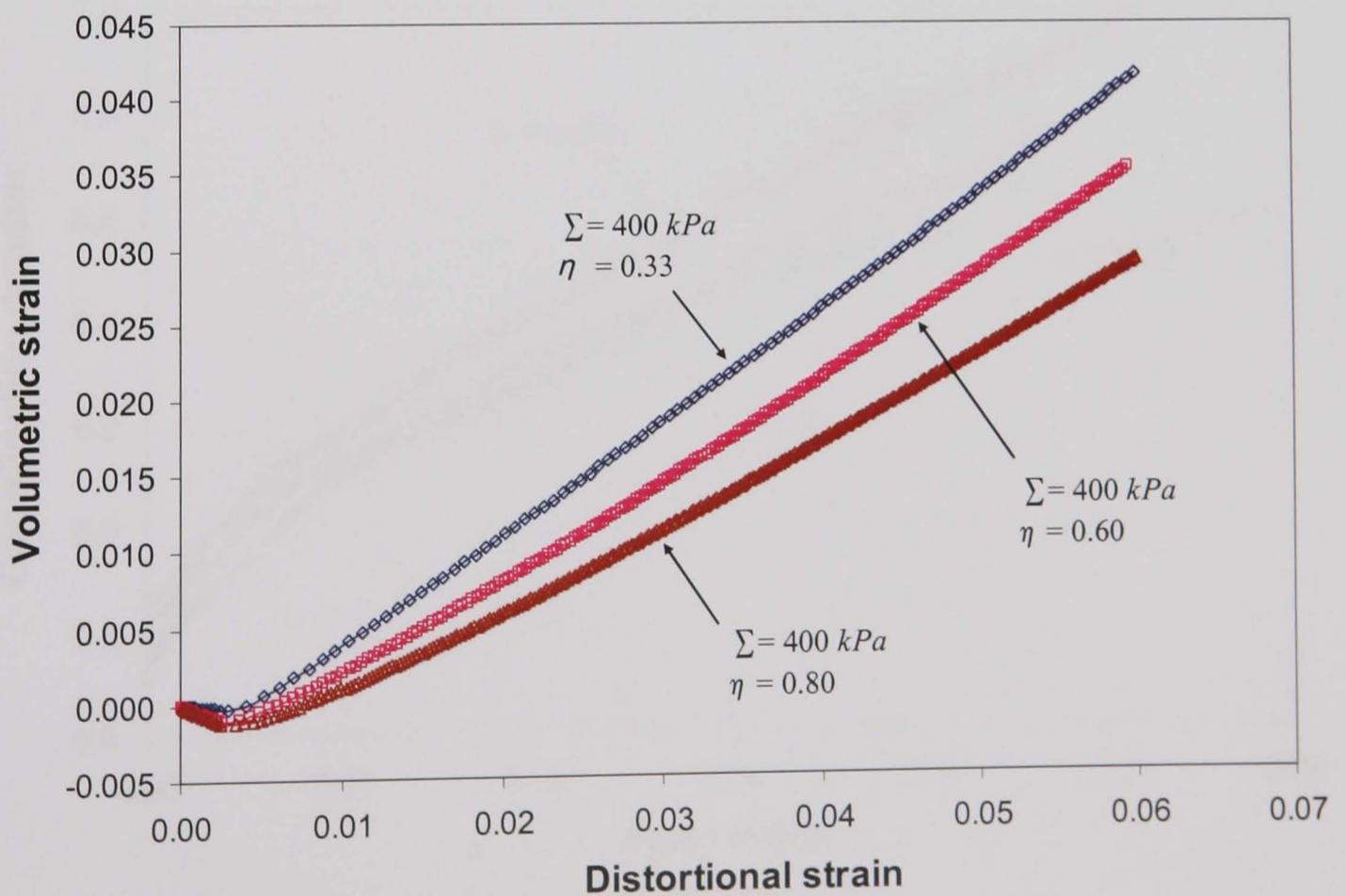
Figure 7.7: Effect of stress ratio on dilation gradient at deviator stress of $400kPa$.
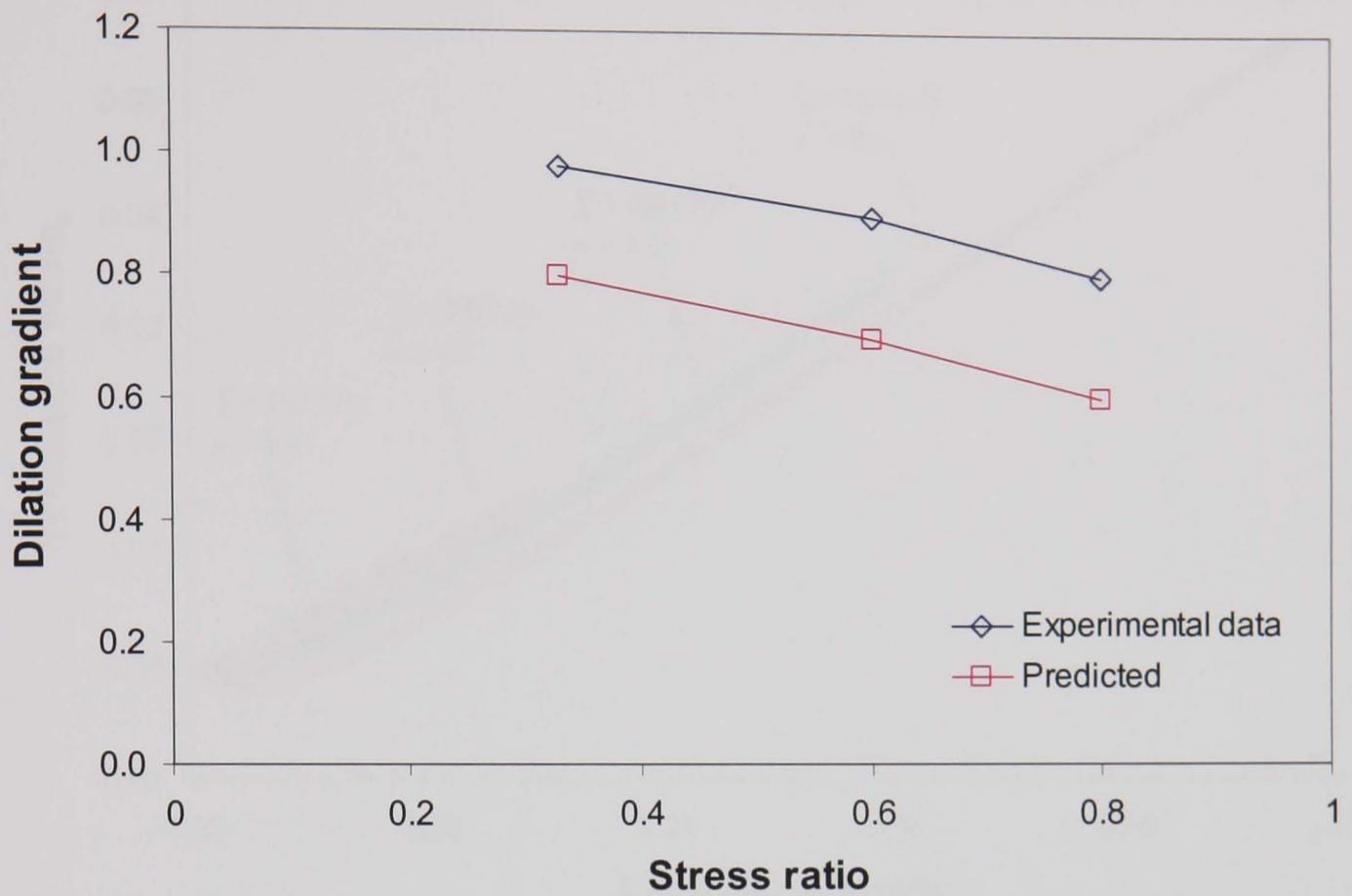
Figure 7.8: The measured and predicted "steady state" dilation gradients at stress ratios of 0.33, 0.6 and 0.8 for a deviator stress of $400kPa$.
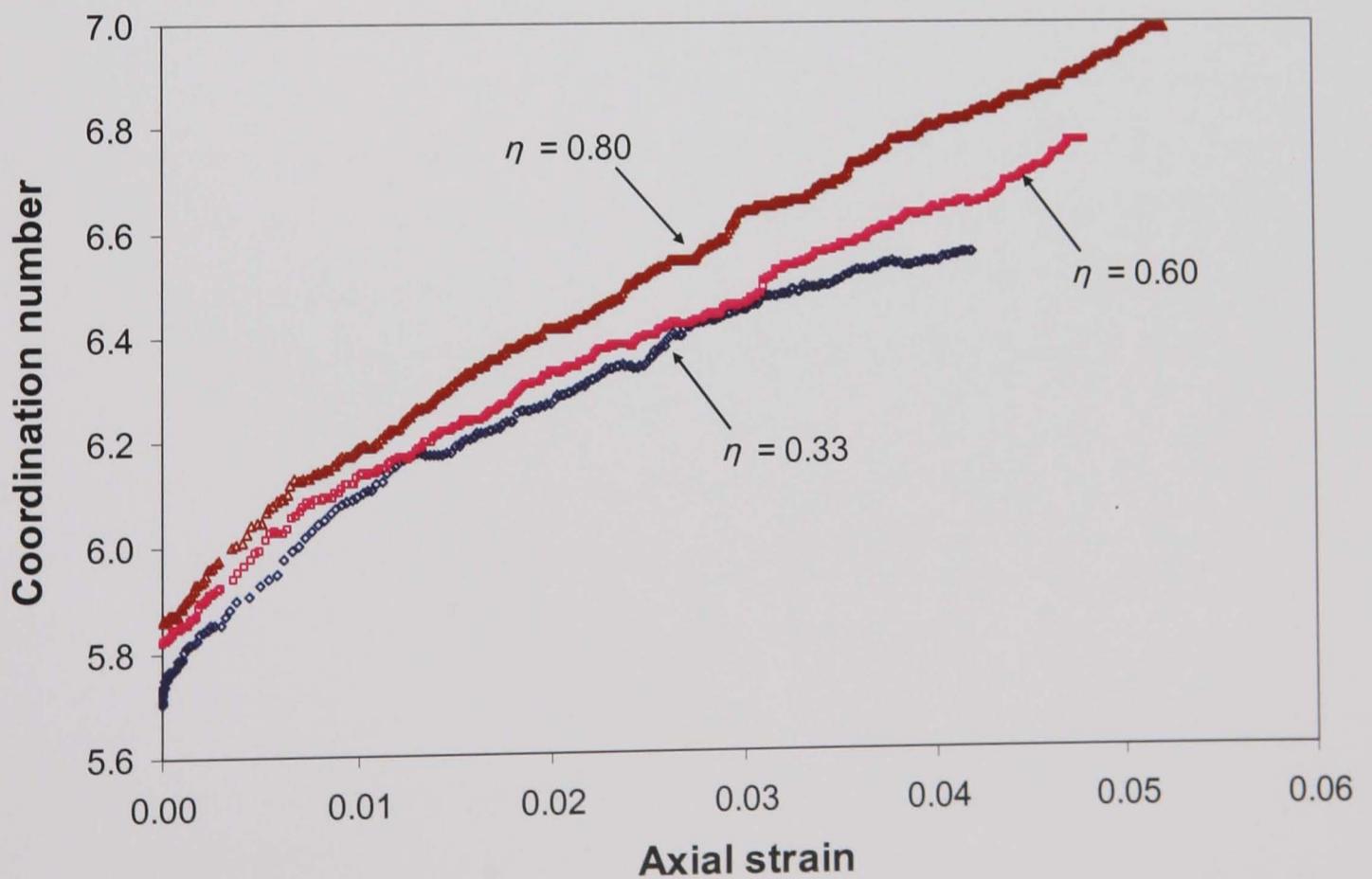
Figure 7.9: Effect of stress ratio on coordination number.
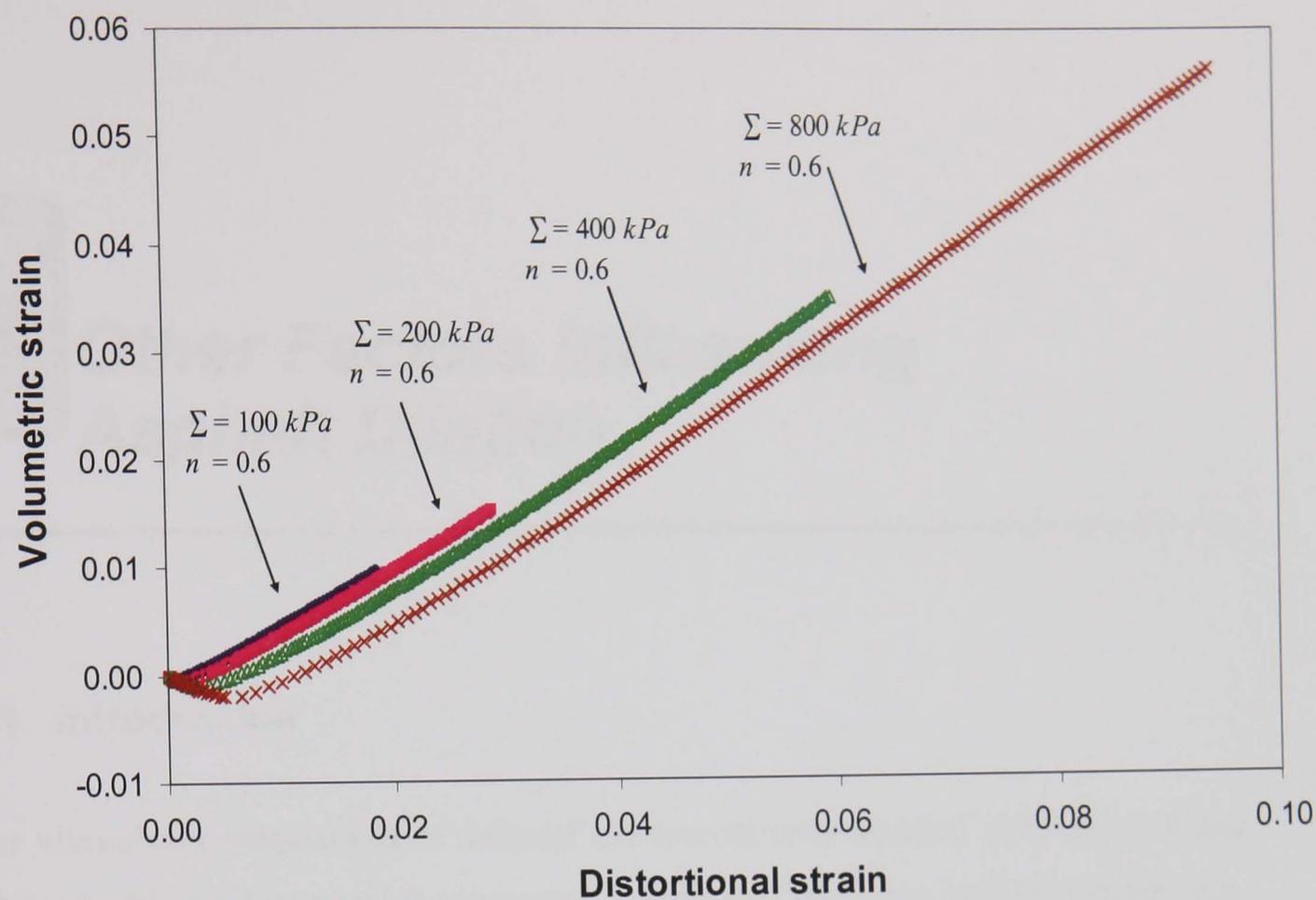
Figure 7.10: Effect of deviator stress on dilation gradient at stress ratio of 0.6.

8 Other Factors Influencing Asphalt Dilation

8.1 Introduction

The viscoelastic simulations of uniaxial and triaxial tests reported in Chapters 6 and 7 have highlighted some of the important factors that influence asphalt dilation (e.g. contact stiffnesses and stress ratio). However, the simulated dilation gradients were slightly under-predicted compared to the experimental data.

In reality, it is likely that a fraction of the total contacts in an asphalt mixture are directly between two aggregate particles resulting in frictional behaviour. Therefore, a proportion of the viscoelastic bonds should be replaced by frictional bonds. The magnitude of the friction coefficient is also likely to be important. Furthermore, the numerical samples comprise perfectly spherical particles which, although a reasonable assumption is unrealistic as the sand particles are more angular.

The main objective of this chapter is to investigate the effects of these factors on asphalt dilation and to try and replicate the measured level of dilation in the sand asphalt.

8.2 Influence of Bond Absence and Interparticle Friction on Asphalt Dilation

It is well known in soil mechanics that the deformation behaviour of a sand sample is significantly influenced by the interparticle friction [68, 80, 99]. Ni [80]

performed shear box simulations using PFC3D and found that at 16.7% shear strain, the volumetric dilation for a sample with an interparticle friction angle $(\varnothing_\mu)$ of 45° was approximately 12 times larger than that for a sample with $\varnothing_\mu = 5°$. Consequently, he concluded that interparticle friction had a significant effect on the overall volumetric dilation of the sample. For asphalt mixtures, Huschek [58] stated that internal friction due to the aggregate contacts is one of the components that contributes to the deformation resistance of asphalt. However, the friction component was not introduced in the previous viscoelastic simulations. Therefore, the aim of this section is to investigate the influence of bond absence and interparticle friction on the asphalt dilation.

In the previous viscoelastic simulations, the shear stiffnesses at all contacts in a numerical sample were assumed to be viscoelastic. As noted above, this approximation is simplistic and direct contact between two aggregates should be represented by the slip model featured in PFC3D, which is defined by a friction coefficient at the contact (μ). In PFC3D, this model is active when there is no contact bond specified. The contact is checked for slip conditions by calculating the maximum allowable shear contact force described by $F_{\max}^s = \mu \left| F_i^n \right|$.

Three series of uniaxial simulations were performed on samples containing 1,000 particles generated according to the sample preparation procedure described in Chapter 4. The contact parameters are stated in Table 8.1. Very high contact bond strength was used to prevent bond breakage. The first series of the simulations assumed that 20% of total contacts in the sample are frictional with friction coefficients of 0, 0.5 and 1. Figure 8.1 shows a plot of volumetric strain versus distortional strain under a uniaxial compressive stress of 400*kPa* for the three friction coefficients. It can be seen from this figure that the volumetric strain is predicted to be greater as the friction coefficient is increased. The second series of the simulations was the same as the first series with the exception that 50% of the contact bonds were replaced by frictional contacts in the numerical sample. The results of volumetric plotted against distortional strain for simulations with different friction coefficients are shown in Figure 8.2. It can be seen by comparing the results with Figure 8.1 that, as before, the volumetric strain is predicted to be greater as the

friction coefficient is increased with greater differences between the curves. The third series of the simulations was performed on an unbound sample where all shear contact stiffnesses are represented by frictional behaviour. It should be noted that in this simulation, a very low confining pressure of $1kPa$ was applied as lateral confinement. However, the stress ratio was very low (approximately 0.336) which is considered comparable to a uniaxial stress with a stress ratio of 0.33. Figure 8.3 shows the plot of volumetric against distortional strains for simulations with friction coefficients of 0.5 and 1. It can be seen from this figure that, as before, the predicted volumetric strain is greater as the friction coefficient is increased.

It was noted earlier in Section 6.7 that the maximum dilation gradient occurred at distortional levels of 6 to 8%. Therefore, to analyse the results from three series of simulations, the dilation gradients between the distortional levels of 6 to 8% were taken and plotted in Figure 8.4. It can be seen from this figure that for simulations with the friction coefficient equal to zero, the dilation gradient increases as the percentage of bonds replaced increases. For example, the dilation gradient increases from 0.8 to approximately 0.85 (6% increase) when the percentage of bonds replaced increases from 0% to 50%. Similar trends were observed from simulations with interparticle friction coefficients of 0.5 and 1.0 in Figure 8.4. This is because fewer contact bonds in a sample reduces the constraints (coordination number) allowing more freedom for them to roll over each other resulting in a higher level of dilation.

Figure 8.4 shows that in simulations on a sample with 20% of bonds replaced. The dilation gradient increases from 0.82 to 1.05 when the friction coefficient increases from 0 to 1.0. This clearly indicates that higher interparticle friction results in greater dilation. Similar behaviour is observed in the simulations with 50% of bonds removed. Skinner [104] stated that when the interparticle friction is increased, more particles roll rather than slide, in order to keep the energy balance the same. Therefore, higher interparticle friction increases the ability for particle rolling, hence resulting in greater volumetric dilation. For the simulations with the unbound sample, it can be seen from Figure 8.4 that the dilation gradient increases from approximately 1.05 to 1.15 when the friction coefficient increases from 0.5 to 1.0. The magnitudes of the dilation gradients are within a reasonable range for unbound

simulations where researchers have found a linear dependence of the volumetric strain on the shear strain, with values of dilation gradient ranging from 0.7 to 1.8 [8, 126].

Consequently, it can be concluded from this section that a greater level of asphalt dilation can be modelled by reducing the number of contact bonds (higher percentage of bonds absent) and increasing the interparticle friction at the frictional contacts.

8.3 Comparison with Experimental Results

The viscoelastic simulations presented in Chapters 6 and 7 under predicted the dilation gradient for the idealised asphalt mixture. It was shown above that a greater level of dilation can be obtained if frictional behaviour is included. The main objective of this section is to simulate the dilation of the idealised asphalt mixture and compare with the experimental results.

As noted earlier, a higher level of asphalt dilation can be simulated by replacing a proportion of the bonds with friction at the contacts. It can be seen from Figure 8.4 that in simulations with 20% of bonds removed, the dilation gradients lie in between 0.95 and 1.05 for friction coefficients between 0.5 and 1.0. Therefore, it can be concluded that a dilation gradient of approximately 1 can be modelled by using a friction coefficient of 0.7 (corresponding to an interparticle friction angle of 35°) in the contacts where the bonds have been removed.

A series of uniaxial and triaxial simulations were performed on samples containing 6,000 particles. The sample preparation procedures for uniaxial and triaxial samples are described in Chapter 4 and Section 7.3. The contact parameters are given in Table 8.1. As noted above, 20% of bonds in the sample were removed prior to testing and a friction coefficient of 0.7 was introduced to those contacts. Figure 8.5 shows the variation of volumetric and distortional strains under a deviator stress of 400kPa and stress ratios of 0.33 (uniaxial), 0.6 and 0.8. It can be seen from this figure that as expected, the volumetric strain is negative indicating initial

compaction at the beginning of the test. The volumetric strain then increases proportionally with the distortional strain. As noted above, the experimental results [40, 65] obtained for a similar idealised asphalt mixture tested at 20°C and the same stress level are also shown in Figure 8.5. It can be seen from this figure that the predicted and measured curves are similar in magnitude and shape demonstrating that the correct level of asphalt dilation can be modelled successfully.

Consequently, it can be concluded that in order to model the correct level of asphalt dilation using a single size sphere sample, it is necessary to remove 20% of the total bonds in the sample and introduce a friction coefficient of 0.7 to the contacts where bonds are absent to simulate the shear behaviour of aggregate to aggregate contact.

8.4 Influence of Particle Shape on Dilation

In soil mechanics, numerous researchers [61, 81, 88, 94, 113] have performed DEM simulations to investigate the effect of particle shape on the deformation behaviour of soil samples concluding that it has significant influence on volumetric dilation. Rothenburg and Bathurst [94] performed DEM simulations on assemblies of elliptical particles. They investigated the stress-strain behaviour during biaxial compression and found that at the same level of shear strain, the volumetric strain is greater in simulations with elliptical particles with larger eccentricity. Ting et al. [113] found similar results. Ni [80] performed DEM simulations of a biaxial test on soil. In his soil sample, each soil particle was modelled as two spheres bonded together with a high strength bond so that each pair of spheres behaves as a single rigid particle. He found that at an axial strain of 15%, the volumetric strain in the sample with spheres was 2% which increased to 10% in the simulation with more angular particles.

Consequently, researchers have shown that in soil mechanics, a greater volumetric dilation can be observed in the sample with more angular particles. However, no literature was found on simulations of bonded materials showing the effect of particle shape. The main objective in this section is to investigate the effect of particle shape on the asphalt dilation using DEM simulations.

8.4.1 Modelling Procedure

This subsection develops a procedure to prepare a sample using non-spherical particles in order to simulate the effect of particle shape on the dilation of asphalt mixture. A non-spherical particle is represented by the clump feature in PFC3D. A clump behaves as a rigid body where the particles comprising the clump remain at a fixed distance from each other. Contact forces are not generated within a clump and contacts within a clump are skipped during the calculation thus reducing the computation time. More details on clumps can be found in [3].

In order to prepare a numerical sample containing clumps, a sample comprising of spheres was first generated according to the sample preparation procedure as described in Chapter 4, with the exception that the lateral wall remained. After the sample settled with an equilibrium condition, the spheres in the sample were eliminated and replaced by the clumps. In this dissertation, a simple clump containing two spheres is used, where the ratio of the diameter of the small to large sphere was 2/3. The small sphere is bonded to the large sphere with the centroid of small sphere located on the surface of the large sphere, overlapping as shown in Figure 8.6. The clumps generated were randomly orientated. The sample generated with clumps was then allowed to settle to equilibrium.

To ensure that the sample generated is as dense as possible, a compacting stress of *20MPa* (chosen arbitrarily) was applied axially (the lateral wall was fixed), which simulates specimen compaction in the preparation of a real asphalt mixture. It should be noted that the sample must be prepared at low stress prior to loading. To simulate this, the top and bottom platen were released with a very low platen velocity so that the isotropic stress reduces to *1kPa*. Finally, the numerical sample was trimmed by removing the balls outside a certain range to ensure that the ratio of the sample's height to width is 2:1, the lateral wall was removed for the uniaxial tests. Consequently, the sample generated with clumps was then at a dense random packing state (typical density 0.68) under a low stress and ready for testing. The numerical sample comprising of 1,000 clumps prior to testing is illustrated in Figure 8.7.

8.4.2 Dilation with Bonds Removed

As discussed earlier in Section 8.2, the percentage of bonds removed has a significant influence on the dilation of the asphalt mixture using a sample containing spherical particles. It was also noted earlier that particle shape has a large influence on volumetric dilation. This section investigates the effect of bond removed on dilation of an asphalt sample containing non-spherical particles (clumps).

A series of uniaxial simulations was performed on a sample containing 1,000 clumps. The sample preparation procedure for clumps is described in the previous section and the contact parameters are given in Table 8.1. A constant compressive stress of 400*kPa* was applied. Figure 8.8 shows the variation in volumetric and distortional strains for simulations where 0%, 20%, 50% and 100% of the bonds have been removed. An interparticle friction coefficient of 0.5 was used at these contacts. It should be noted that in the simulation with the unbound sample, a very low lateral confining stress (1*kPa*) was applied to ensure that the sample is subjected to an approximately uniaxial stress with a stress ratio of approximately 0.336. It can be seen from Figure 8.8 that the general trend is for the dilation gradient to increase as the percentage of bonds removed increases. To quantify this effect, the dilation gradients calculated at distortional strain levels between 6 and 8% are plotted in Figure 8.9.

Figure 8.9 shows that the dilation gradient increases as the percentage of bonds removed increases from 0.75 in the simulation with the fully bonded sample (0% bonds absent) to 1.3 in the unbound sample (100% of bonds removed). Also shown in Figure 8.9 are the simulation results taken from the samples with spheres (taken from Figure 8.4) for comparison. It can be seen from this figure that in the simulation with a fully bonded sample, the dilation gradient is 0.75 in the sample with clumps, which is smaller compared to the dilation gradient in the sample with spheres (at the same friction coefficient). However, in simulations with 20% of bonds removed, the dilation gradient of the sample with clumps is close to that of the sample with spheres and in the simulation with 50% of bonds removed, the dilation gradient in the sample with clumps is 1.15, which is higher than the dilation gradient in the sample with spheres. The simulation results on unbound samples

showed a significant difference in dilation gradients between the two types of samples.

It was noted earlier that for the fully bonded sample, the dilation gradient of the sample with clumps was found to be lower than that of the sample with spheres. To explain this, the coordination numbers in both types of samples was investigated. Figure 8.10 shows the coordination number for both types of sample. It can be seen that for the sample with clumps, the coordination number is higher (approximately 25%) than for the sample with spheres. This is because the clump has a larger surface area compared to the sphere which results in a greater number of contacts with neighbouring particles. As explained earlier, a higher coordination number causes greater constraints for particles, hence results in lower levels of dilation.

In the simulation with 20% bonds removed, the dilation gradient of the sample with clumps is approximately 0.92. However, the difference is small compared with the dilation gradient in the sample containing spheres. A bigger difference in dilation gradients on both samples was observed from the simulations with 50% bonds removed and a significant difference in dilation gradients was observed in simulations for the unbound samples.

8.5 Conclusions

The following conclusions can be drawn from this chapter:

- Friction was introduced to simulate the shear contact behaviour at aggregate to aggregate contacts.

- The dilation increases as the percentage of bonds replaced by frictional contact is increased.

- The dilation gradient was found to increase with the coefficient of friction at the contacts where bonds were removed.

- Experimental results were successfully modelled by removing 20% of the bonds and using a friction coefficient of 0.7.

- A sample preparation procedure was developed to prepare a numerical sample comprising of non-spherical particles (clumps).

- Greater levels of dilation were found in samples with clumps under loading, providing the number of contact bonds is low.

- The dilation of asphalt seems to be controlled by the number of contact bonds and the shape of particles in the sample.

Tables:

Table 8.1: Burger's contact parameters for viscoelastic simulation.

Shear Contact		Tension Contact		Compression contact	
Property	Value	Property	Value	Property	Value
K_o^s (MN/m)	0.12	K_o^n (MN/m)	0.36	E_o^n (MN/m)	0.70
C_∞^s (MNs/m)	0.80	C_∞^n (MNs/m)	2.40		
K_1^s (MN/m)	0.03	K_1^n (MN/m)	0.09		
C_1^s (MNs/m)	0.80	C_1^n (MNs/m)	2.40		

Figures:

Figure 8.1: Effect of friction coefficient on volumetric and distortional strains for simulations with 20% of bonds replaced.
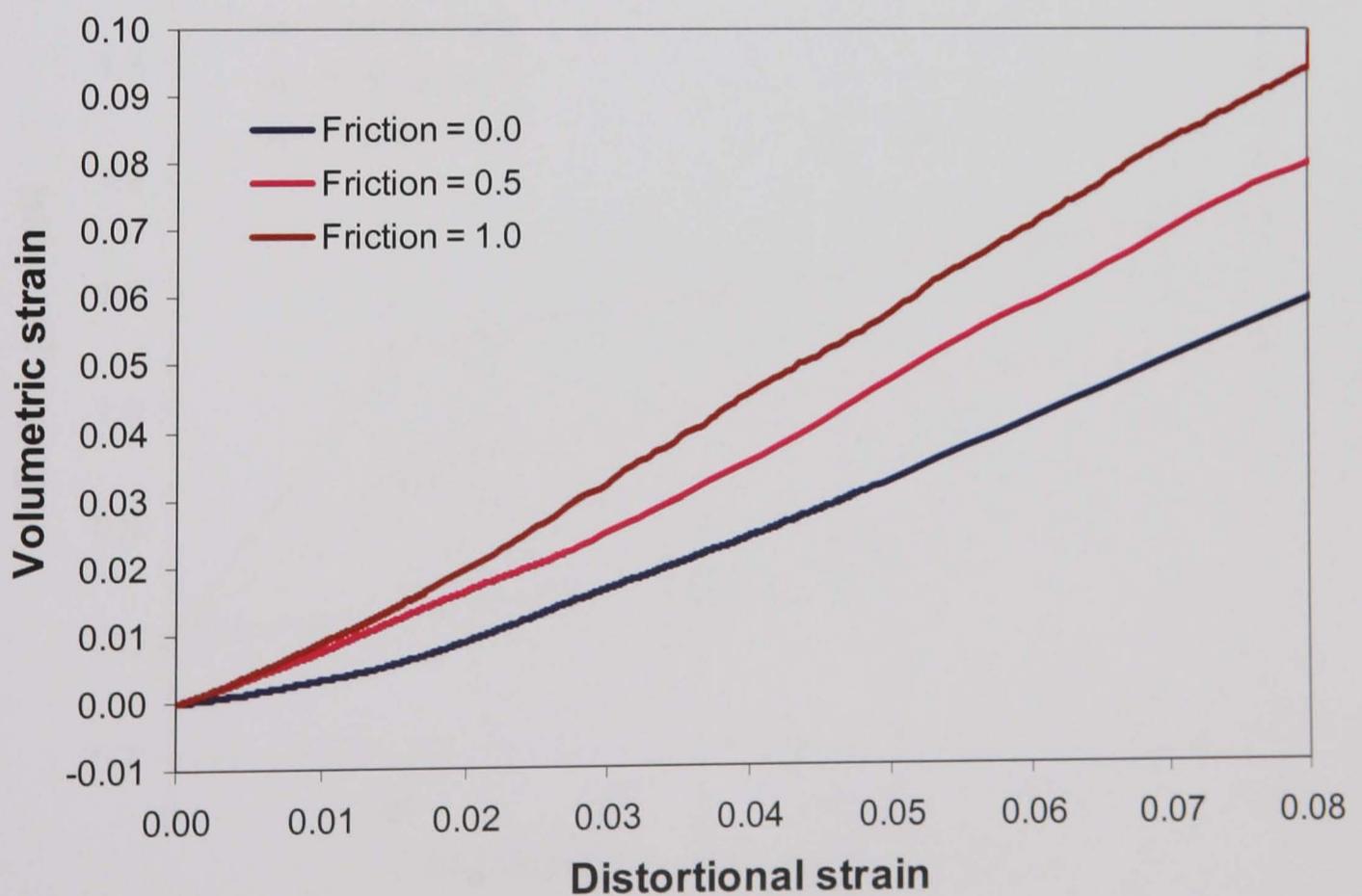
Figure 8.2: Effect of friction coefficient on volumetric and distortional strains for simulations with 50% of bonds replaced.
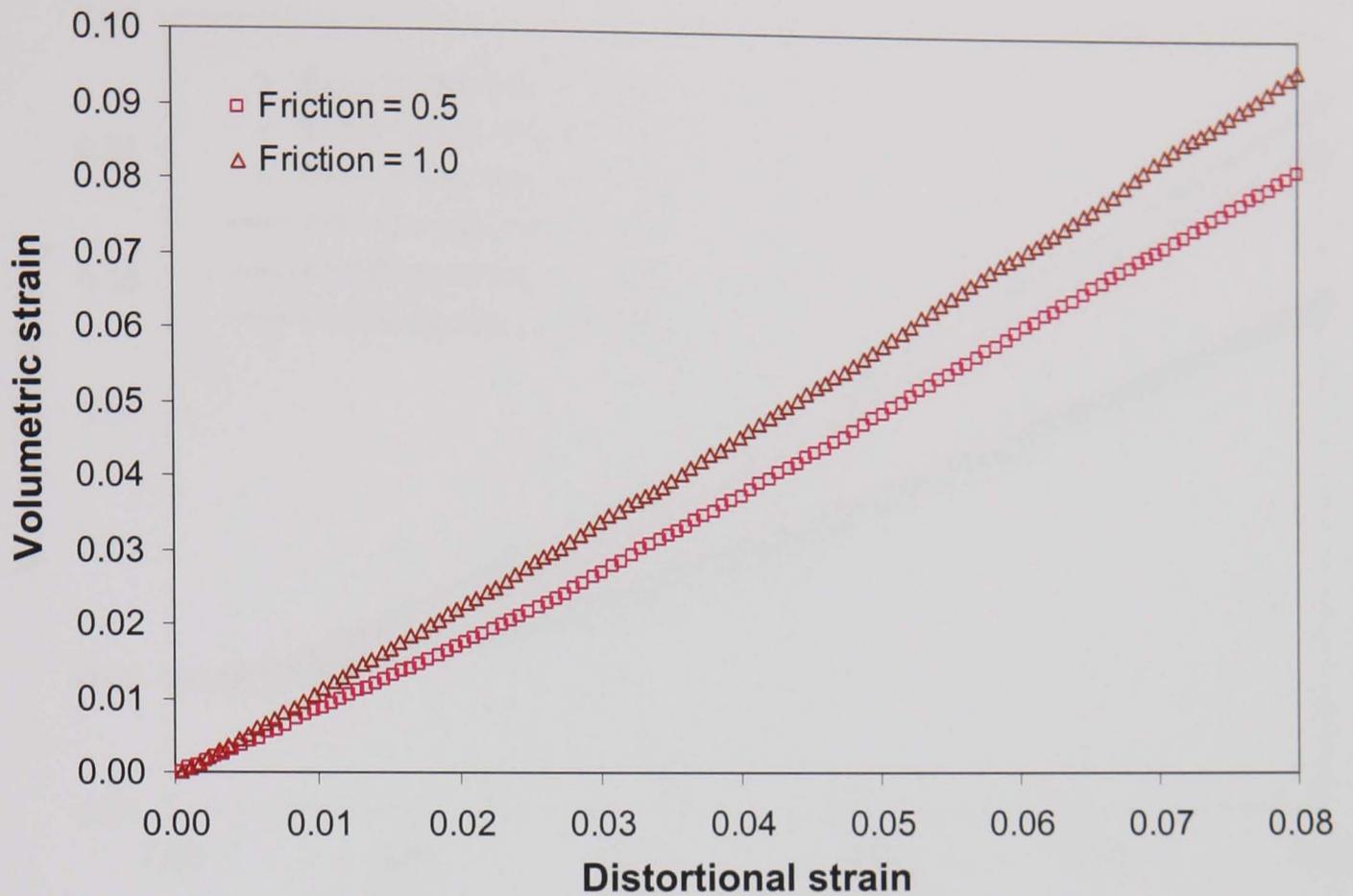
Figure 8.3: Effect of friction coefficient on volumetric and distortional strains for simulations with unbound sample.
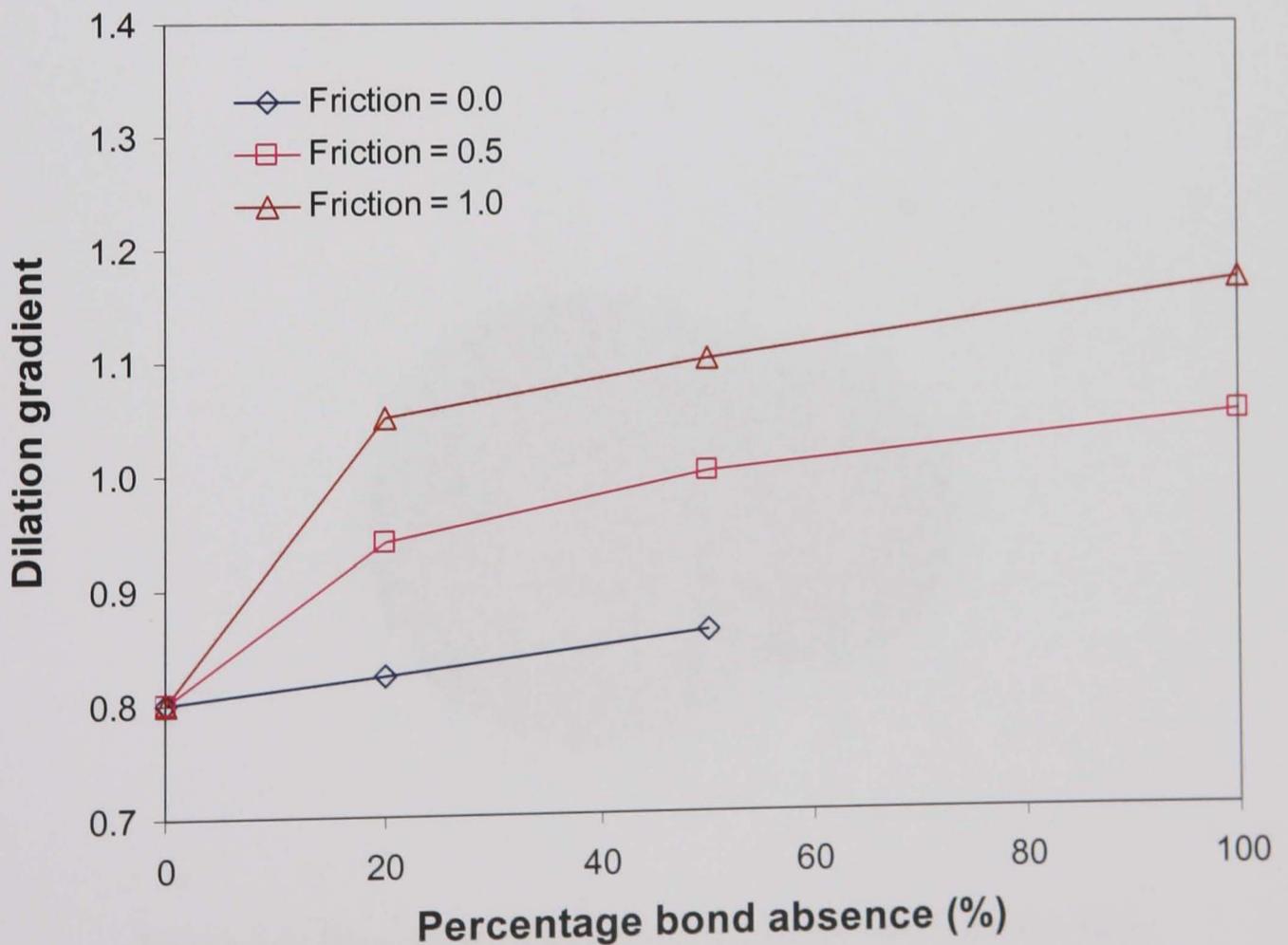
Figure 8.4: Effect of percentage of bonds replaced and friction coefficient on dilation gradients.
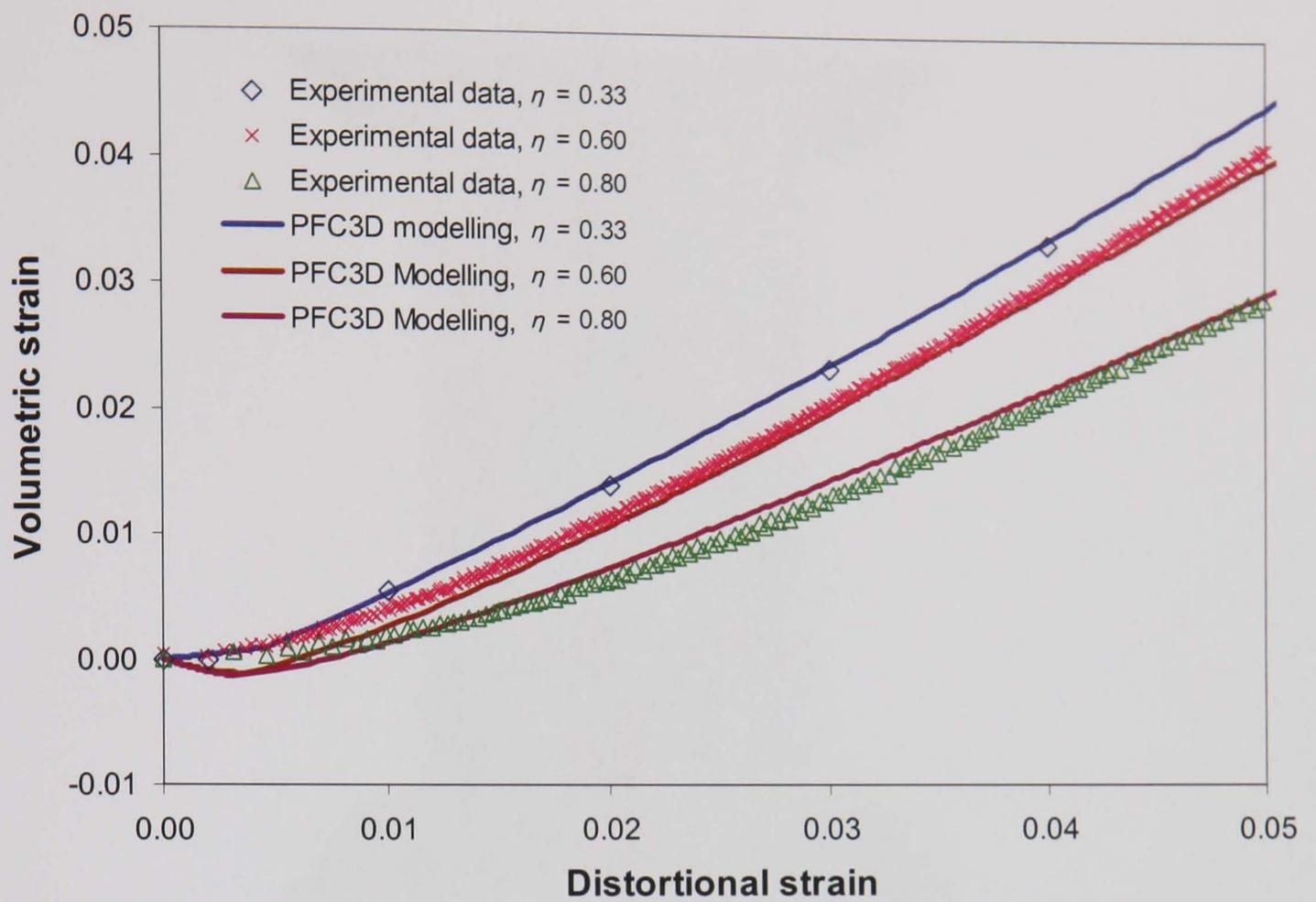
Figure 8.5: The predicted and measured volumetric and distortional strains in simulations with friction coefficient of 0.7 and 20% of bonds replaced.
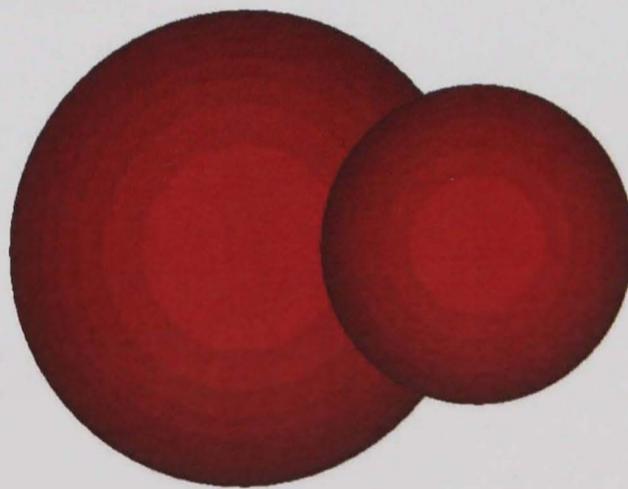
Figure 8.6: Illustration of a clump constructed from two particles.

Figure 8.7: A numerical sample comprising 1,000 clumps prior to loading.
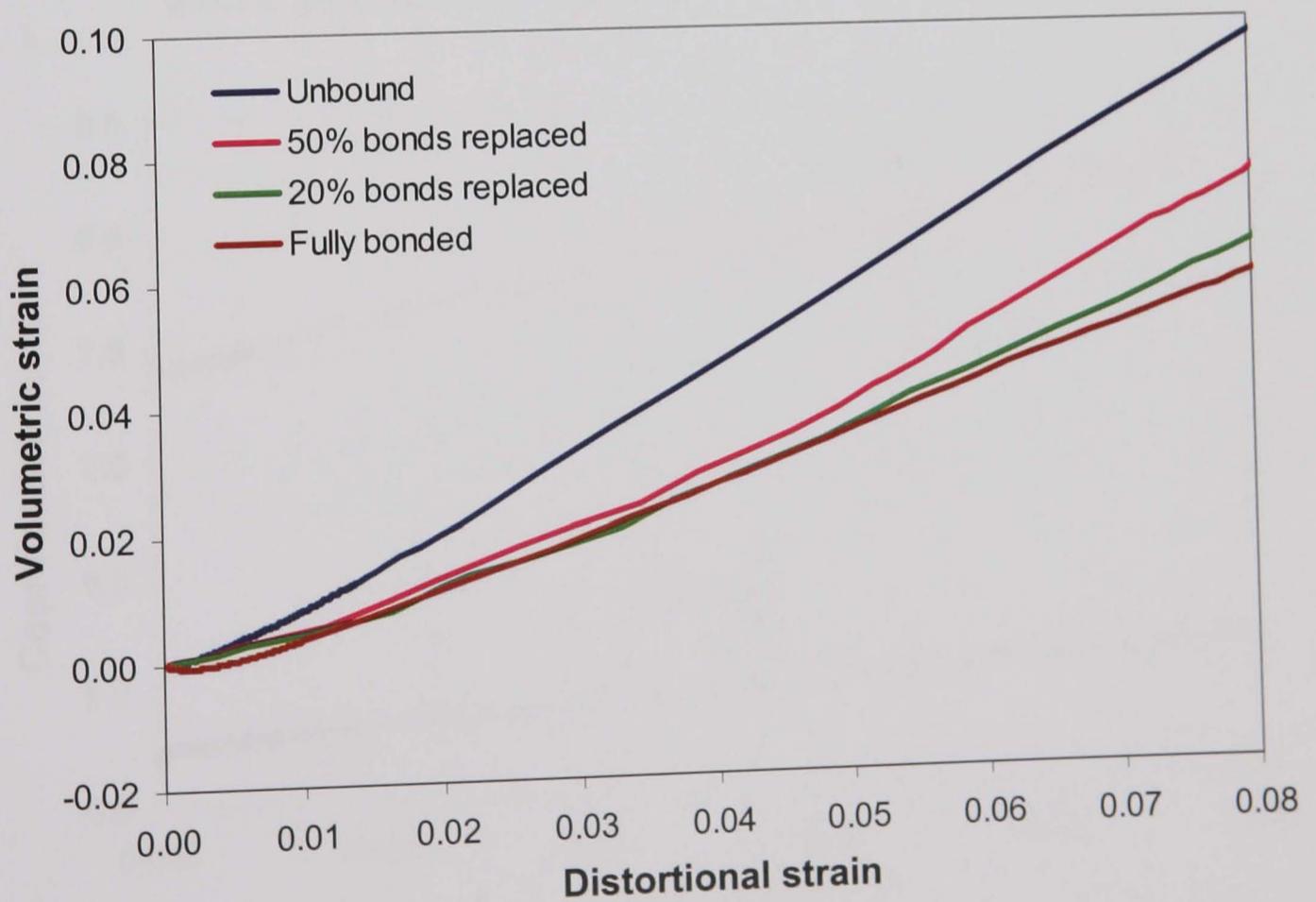
Figure 8.8: Volumetric strain against distortional strain in simulations with different percentages of bonds replaced and friction coefficient of 0.5.
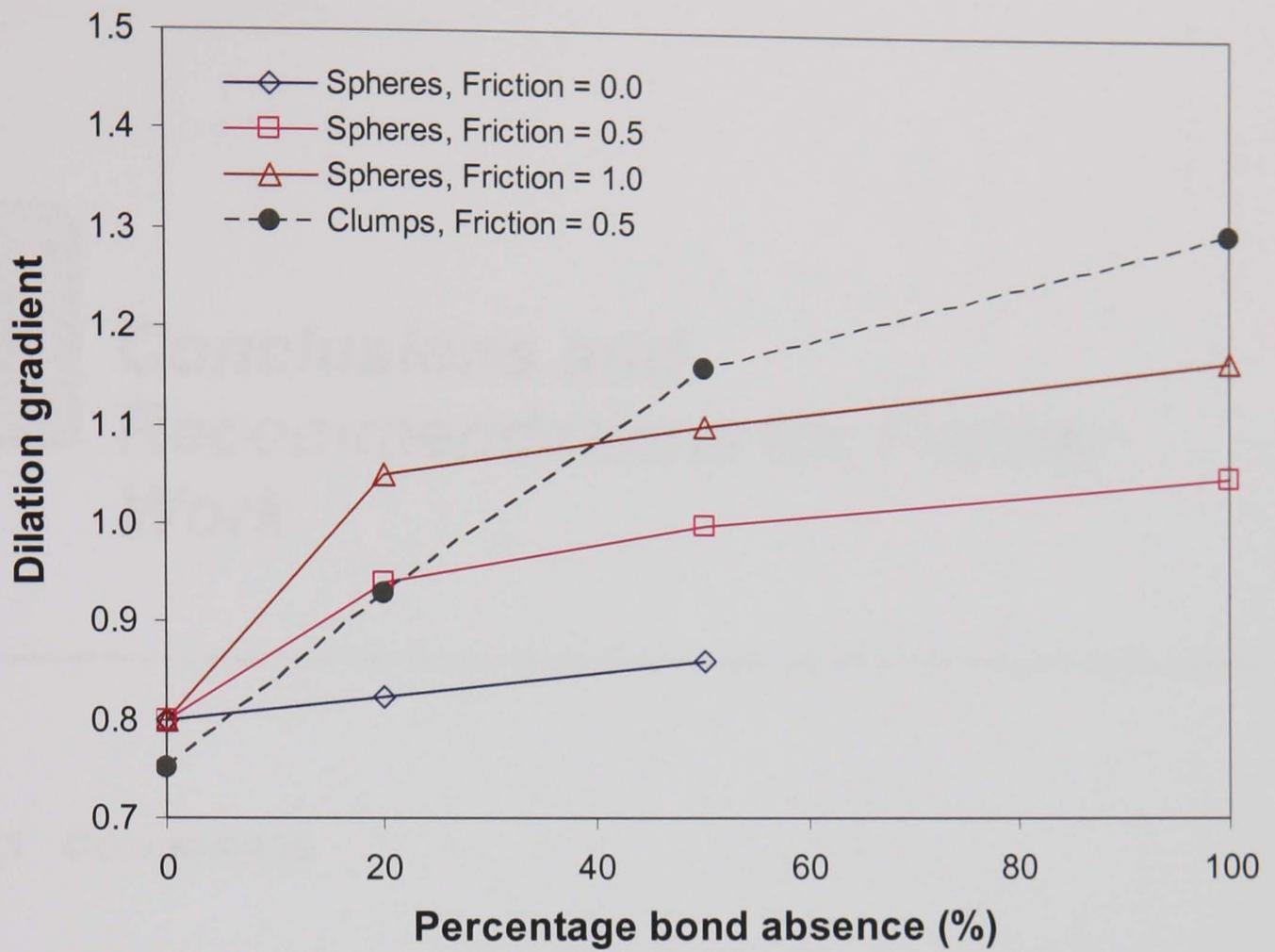
Figure 8.9: Effect of percentage of bonds replaced and friction coefficient on dilation gradients with clumps.
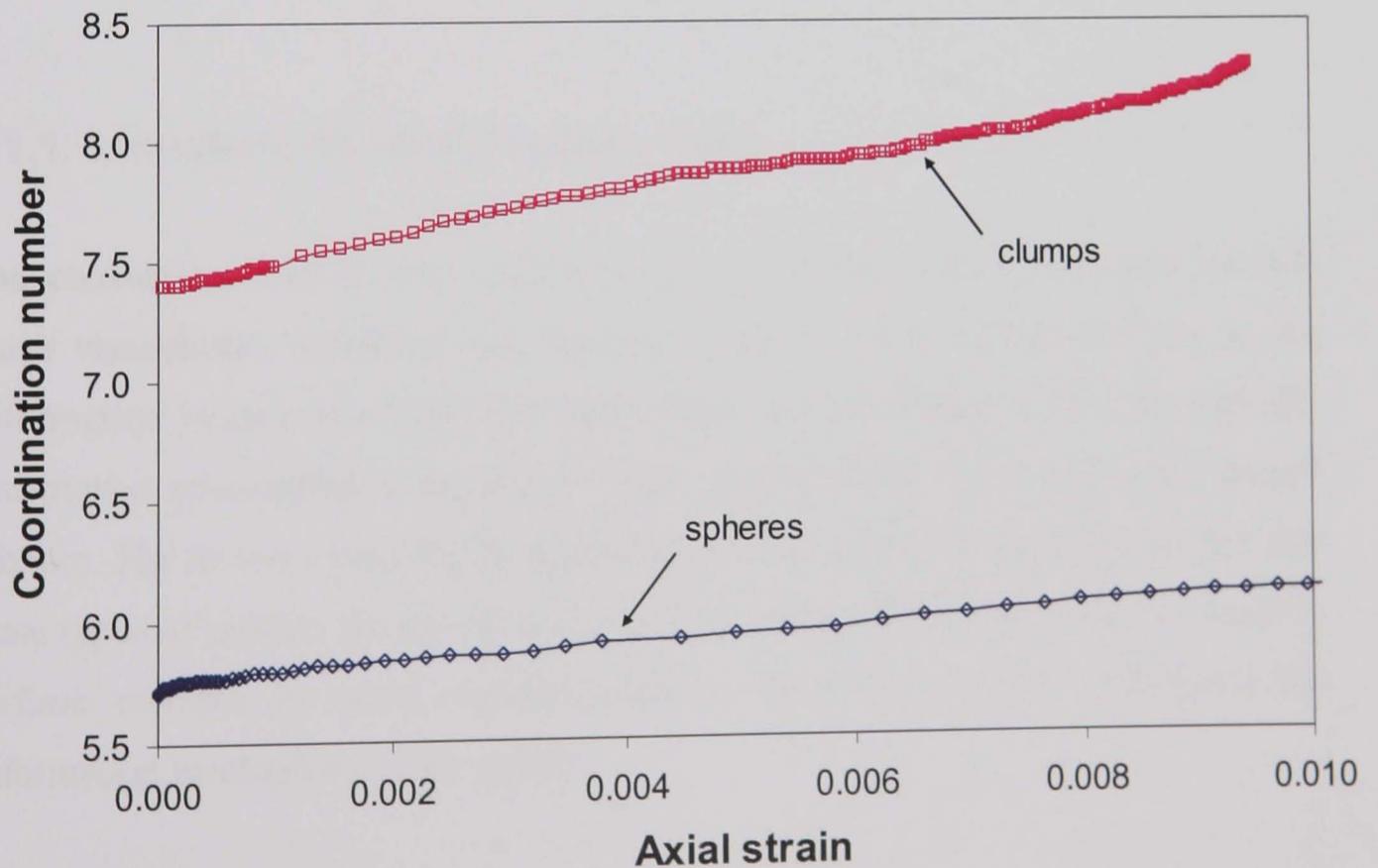
Figure 8.10: Coordination number of the sample with spheres and with clumps under loading.

9 Conclusions and Recommendations for Further Work

9.1 Conclusions

A three dimensional computer program (PFC3D) has been used to investigate the mechanical behaviour of an idealised asphalt mixture under uniaxial and triaxial loading. This chapter summarises the main conclusions from this thesis and provides recommendations for future research in this area.

9.1.1 Literature Review (Chapter Two)

The constitutive relationships proposed for describing asphalt behaviour include linear viscoelastic, nonlinear and elasto-visco-plastic. The literature review on the deformation behaviour of bitumen and asphalt showed that an elasto-visco-plastic constitutive relationship is capable of fully describing the behaviour of an asphalt mixture. The review of micromechanical models for asphalt mixtures has shown that these types of models are poorly developed at present. Therefore there is a need to perform research by using micromechanical modelling to better understand the deformation mechanism of the asphalt.

9.1.2 Introduction to Discrete Element Modelling (Chapter Three)

Recent developments in computer technology have allowed the simulation of asphalt behaviour as heterogeneous material using DEM. It was found that PFC3D has been applied in a wide range of applications by many researchers, therefore it was chosen as the DEM programming code for this thesis. Some of the features in PFC3D including the contact model, contact bond and servo control mechanism were reviewed and the Burger's contact model was chosen to simulate the time dependent behaviour of asphalt material in the DEM simulations using PFC3D.

9.1.3 Numerical Sample Preparation (Chapter Four)

A procedure for preparing a numerical sample that replicates a laboratory test specimen was developed in this chapter. A dense randomly packed sample was prepared with a volume fraction of solids equal to 64%. A procedure has been developed to prepare the numerical sample to an equilibrium state with a low isotropic stress. Normal and shear contact bonds were used at each contact to simulate asphalt as a bonded material. A method was developed to measure the radial strain by tracking the displacement of particles on the circumference of the sample. The axial strain was measured using the relative displacement of the loading platens during the simulation.

9.1.4 Elastic Simulations (Chapter Five)

The elastic response of an idealised asphalt mixture was modelled in this chapter. It was found that a sample containing at least 4,500 particles is required for Young's modulus and Poisson's ratio to be within 2% of the values calculated using a much larger number of particles. Poisson's ratio was found to be dependent on only the ratio of shear contact stiffness to the normal contact stiffness and the bulk modulus was found to be linearly dependent on the normal contact stiffness and independent of the shear contact stiffness. A mean field approach was used to develop a theoretical model that predicted this behaviour. To simulate asphalt dilation, non-equal tensile and compressive normal contact stiffnesses were used. The level of

dilation was found to be dominated by the ratio of normal compressive to normal tensile contact stiffnesses. Most importantly, it was found that the dilation gradient increases proportionally to this ratio.

9.1.5 Viscoelastic Simulations of Uniaxial Tests (Chapter Six)

The Burger's contact model was found to be reasonably good at simulating the deformation behaviour of idealised asphalt mixture. To reduce the computation time, a higher particle density was used. The normal compressive contact stiffness was assumed to be elastic to represent aggregate to aggregate contact, whilst the shear and normal tensile contact stiffnesses were assumed to be viscoelastic. From the uniaxial simulations, the dilation gradient was found to increase proportionally to the ratio of compressive to tensile contact stiffness as a function of time. It was found that the maximum dilation gradient of the asphalt sample occurred at between 6 and 8% distortional strain with a value of 0.8. The simulation results also showed that dilation gradient is independent of the deviator stress. The model is calibrated well and the predicted axial strain gives good agreement with the experimental data whilst the dilation gradient was under-predicted.

9.1.6 Viscoelastic Simulations of Triaxial Tests (Chapter Seven)

From simulations of triaxial tests, the dilation gradient was found to be dependent only on stress ratio and increases as the stress ratio decreases. However, the dilation gradient was found to be independent of deviator stresses at a given stress ratio. Also, a higher coordination number was found in the sample subjected to a higher confining pressure. Consequently, a comparison between the predicted and measured results was made and the model has shown the ability to predict the effect of stress ratio on dilation. However, the dilation gradients were still under-predicted.

9.1.7 Geometric Factors Influencing Asphalt Dilation (Chapter Eight)

The level of dilation was found to be dominated by the proportion of frictional contacts in the sample. Furthermore, the dilation gradient was found to increase as the coefficient of friction at these contacts is increased. Based on these findings, the dilation gradients from the experimental results were successfully modelled by introducing a friction coefficient of 0.7 at contacts replacing 20% of the bonds in the sample. To simulate the effect of particle shape, a procedure was developed to prepare a sample comprising non-spherical particles (clumps). The simulations on the sample with clumps demonstrated that the dilation gradient is greatly influenced by the percentage of frictional contacts. Greater dilation was found in the sample with clumps under loading, providing the number of absent bonds is high. Consequently, it was found that the dilation of the asphalt mixture seems to be controlled by the number of contact bonds and the shape of particles in the sample.

9.2 Recommendations for Further Work

9.2.1 Limitations of the Numerical Simulations

Numerical modelling relies on mathematical models based on certain assumptions to approximate reality. A good understanding of the physics of the problem is required so that a suitable numerical method can be chosen to represent the behaviour and physical structure of the problem being modelled. However for mathematical simplicity, the assumptions always result in lack of precision in describing the real behaviour of a problem. In a DEM simulation, a particle is modelled as a non deformable sphere. This assumption is reasonable at low stresses. However, this assumption is not true at high stresses, where particle deformation may occur. Consequently, it is important to realise that the numerical simulations only play a role in understanding the reality.

9.2.2 Modelling of Asphalt Dilation

The simulations carried out in this study assumed that the sample consists of single sized particles. However, this approximation is aimed at reducing the complexity in the simulations and it cannot represent a real size distribution of the aggregates in an asphalt mixture. The particle size distribution was not taken into consideration. Consequently, future research could be aimed at investigating the effect of particle size distribution on the dilation of asphalt mixture.

It should be noted that the simulations carried out in this study focussed on the deformation behaviour of asphalt in steady-state creep. The effect of fracture and damage was not considered, which will occur in the tertiary region of creep deformation. It is important to establish an understanding of fracture and damage mechanics of asphalt to model this behaviour by using numerical simulation. Future work should be focussed on research into this area.

Numerous researchers have performed experiments to investigate the effect of temperature on asphalt dilation. Further work can be performed by modelling the effect of temperature on the dilation of asphalt, maybe by establishing a relationship between the temperature effects and viscoelastic contact stiffnesses in the Burger's model.

9.2.3 Particle Shape

The simulations carried out in this study only touched on one type of particle shape. It should be noted that real sand particles are much more complicated and cannot be easily represented by a clump constructed from two spheres. It is possible to bond more particles together to form a more realistic shaped particle. Particle shape dramatically affects particle rotation and overall sample strength. Further work can be focussed on modelling dilation of asphalt by using different particle shapes.

Experimental data for uniaxial and triaxial tests on realistic mixtures are widely available. Further work can be performed by simulating the deformation behaviour of realistic mixtures such as DBM and HRA by using much more complicated

shaped particles with different angularity and grading. However, it might still impractical to model due to the limitation in computing power.

The clumps in PFC3D assumed no breakage in the shaped particle. However in reality, particle crushing could occur under high levels of loading stress. Future research could be aimed at considering the strength and crushing effects of the aggregate particles in the modelling.

9.2.4 Modelling of Wheel Tracking Test

Experimental data from wheel tracking tests is widely available from previous researchers. In order to create a better understanding of the deformation behaviour of asphalt mixtures, further works can be carried out by modelling the wheel tracking test. To reduce the computation time, modelling can be performed on a small strip of asphalt slab in the transverse direction where the wheel travels. The passing wheel load on a small strip of asphalt slab in a laboratory experiment can be represented by the repeated axial load from a wall on the small strip of asphalt slab in numerical modelling. Rut depths can be measured at several points at transverse distance and compared with the rut profile captured with a Mechanical Profilemeter from the experimented data.

More experimental works can be conducted to provide a better understanding of behaviour of thin film bitumen. A simple laboratory test can be performed by using two semi-spherical steel balls to represent the aggregates, bonded by a layer of thin film bitumen. The relationships of stiffnesses in compression, tension and shear can be established by performing the tests with these three loading actions. This also leads to defining the magnitude of parameters in Burger's contact model.

Recent development of X-ray tomography allows scanning into the internal structure of asphalt mixtures in three dimensions. The changes of internal structure of the asphalt mixtures at different stages when subjected to loading can be observed. The directions and magnitudes of particle rotations in an asphalt mixture can be compared and validated with DEM modelling.

References:

1. *"Particle Flow Code in Three Dimensions, FISH"*, Minnesota: Itasca Consulting Group Inc. 2003.

2. *"Particle Flow Code in Three Dimensions, Optional Features"*, Minnesota: Itasca Consulting Group Inc. 2003.

3. *"Particle Flow Code in Three Dimensions, Theory and Background."* Minnesota: Itasca Consulting Group Inc. 2003.

4. *"Particle Flow Code in Three Dimensions, User's Guide"*, Minnesota: Itasca Consulting Group Inc. 2003.

5. Abdulshafi, A. and K. Majidzadeh, *"Combo Viscoelastic-Plastic Modelling and Rutting of Asphaltic Mixtures"*. Asphalt Mixtures and Performance, Transportation Research Records, **968** p. 19-31, 1984.

6. Adam, D.J. and A.J. Matheson, *"Computation of Dense Random Packing of Hard Spheres"*. The J. of Chemical Physics, **56**(5) p. 1989-1994, 1972.

7. Baker, R.F. *"Pavement Design Using Rheologic Concepts"*. in *Proc. Int. Conf. on the Structural Design of Asphalt Pavements*. 1962.

8. Bashir, Y.M. and J.D. Goddard, *"A Novel Simulation Method for the Quasi-Static Mechanics of Granular Assemblages"*. Journal of Rheology, **35** p. 5, 1991.

9. Bathe, K.J. and E.L. Wilson, *"Numerical Methods in Finite Element Analysis"*: Englewood Cliffs: Prentice-Hall. 1976.

10. Bernal, J.D. and J. Mason, *"Co-ordination of Randomly Packed Spheres"*. Nature, **188** p. 910-911, 1960.

11. Bezrukov, A., D. Stoyan, and M. Bargiel, *"Spatial Statistics for SImulated Packings of Spheres"*. Image Anal. Stereol., **20** p. 203-206, 2001.

12. Bolton, M., *"A Guide to Soil Mechanics"*. 1979.

13. Bower, A.F., et al., *"Indentation of a Power Law Creeping Solid"*. Proc. of the Royal Society of London, **A441** p. 97-124, 1993.

14. Brown, A.B. and J.W. Sparks, *"Viscoelastic Properties of a Penetration Grade Paving Asphalt at Winter Temperature"*. Proc. Association of Asphalt Paving Technologists, **27** p. 35-51, 1958.

15. Brown, E.R. and K.Y. Foo, *"Comparison of Unconfined and Confined Creep Tests For Hot Mix Asphalt"*. J. of Materials in Civil Engineering, 6(2) p. 307-326, 1994.

16. Brown, S.F. and K.E. Cooper, *"A Fundamental Study of the Stress-Strain Characteristics of a Bituminous Material"*. Proc. Association of Asphalt Paving Technologists, **49** p. 476, 1980.

17. Brown, S.F. and K.E. Cooper, *"The Mechanical Properties of Bituminous Materials for Road Bases and Basecourses"*. Proc. Association of Asphalt Paving Technologists, **53** p. 415, 1984.

18. Brown, S.F. and Co-workers, *"Bituminous Pavements: Materials, Design and Evaluation"*. Residential Course Lecture Notes: School of Civil Engineering, University of Nottingham. 2002.

19. Buseck, H. and H. Hurtgen. *"A Design Procedure Based on Experimental Results"*. in *Proc. 6th Int. Conf. on the Struc. Design of Asphalt Pavement*. 1987.

20. Buttlar, W.G. and Z. You, *"Discrete Element Modelling of Asphalt Concrete: A Microfabric Approach"*. Transportation Research Record, **1757** p. 111-118, 2001.

21. Chang, G.K. and N.J. Meegoda. *"Simulation of the Behaviour of Asphalt Concrete Using Discrete Element Method"*. in *2nd Intl. Conf. On Discrete Element Methods*. M.I.T. 1993.

22. Cheung, C.Y., "Mechanical Behaviour of Bitumens and Bituminous Mixes", Ph.D Thesis, Department of Engineering, University of Cambridge, 1995.

23. Cheung, C.Y. and D. Cebon, *"Deformation Mechanisms of Pure Bitumen"*. J. of Materials in Civil Engineering, 9(3) p. 117-129, 1997.

24. Cheung, C.Y. and D. Cebon, *"Experiment Study of Pure Bitumen in Tension, Compression and Shear"*. Journal of Rheology, 41(1) p. 45-73, 1997.

25. Cheung, C.Y. and D. Cebon, *"Thin Film Deformation Behaviour of Power-law Creeping Materials"*. ASCE Journal of Engineering Mechanics, 123(11) p. 1138-1152, 1997.

26. Collop, A.C. and S. Khanzada. *"Permanent Deformation Behaviour of Idealised Bituminous Mixtures"*. in *Proc. 3rd European Symp. on Performance and Durability of Bituminous Materials and Hydraulic Stabilised Composites*. 1999.

27. Collop, A.C., G.R. McDowell, and Y. Lee. *"Modelling the Behaviour of an Idealised Asphalt Mixture Using The Distinct Element Method"*. in *Presented in TRB83rd Annual Meeting*. 2003.

28. Collop, A.C., G.R. McDowell, and Y. Lee, *"Use of the Distinct Element Method to Model the Deformation Behaviour of an Idealised Asphalt Mixture"*. Paper submitted to Int. J. of Pavement Engineering, 2003.

29. Collop, A.C., et al., *"Development and Finite Element Implementation of a Stress Dependent Elasto-visco-plastic Constitutive Model with Damage for Asphalt"*. Transportation Research Record, (In Press).

30. Cross, M.M., *"Rheology of Non-Newtonian Fluids: A New Flow Equation for Pseudo-plastic System"*. J. of Colloid Science, 20 p. 417-437, 1965.

31. Cundall, P.A. *"A Computer Model for Simulating Progressive, Large-scale Movement in Blocky Rock System"*. in *Proc. Symp. Int. Soc. Rock Mech. Nancy*. 1971.

32. Cundall, P.A., ed. *"Computer Simulation of Dense Sphere Assemblies"*. Micromechanics of granular materials, ed. M. Satake and J.T. Jenkins. Elsevier Science Publishers B.V.: Amsterdam. pp. 113-123. 1988.

33. Cundall, P.A., "*Formulation of a Three-Dimensional Distinct Element Model - Part1. A Scheme to Detect and Represent Contacts in a System Composed of Many Polyhedral Blocks*". Int. J. Rock Mech.,Min. Sci. & Geomech. Abstr., **25**(3) p. 107-116, 1988.

34. Cundall, P.A., A. Drescher, and O.D.L. Strack, eds. "*Numerical Experiment on Granular Assemblies; Measurements and Observations*". Deformation and Failure of Granular Materials, ed. P.A. Vermeer and H.J. Luger. A.A. Balkema: Rotterdam. pp. 355-370. 1982.

35. Cundall, P.A. and R. Hart, "*Numerical Modelling of Discontinua*". J. Engr. Comp., **9** p. 101-113, 1992.

36. Cundall, P.A. and O.D.L. Strack. "*The Development of Constitutive Laws for Soil Using the Distinct Element Method*". in *Third International Conference on Numerical Methods in Geomechanics*. Aachen. 1979.

37. Cundall, P.A. and O.D.L. Strack, "*A Discrete Element Model for Granular Assemblies*". Géotechnique, **29**(1) p. 47-65, 1979.

38. De Josselin de Jong, G. and A. Verruijt, "*Etude photo-elastique d'un empilement de disques*". Cahiers du Groupe Francais de Rheologie, **2**(1) p. 73-86, 1969.

39. Desai, C. "*Mechanistic Pavement Analysis and Design using Unified Material and Computer Model*". in *Proc. 3rd Int. Symp. on 3D Finite Elements for pavement Analysis, Design and Research*. Amsterdam, The Netherlands. 2002.

40. Deshpande, V.S., "Steady-State Deformation Behaviour of Bituminous Mixes", Ph.D. Thesis, Engineering Department, University of Cambridge, 1997.

41. Deshpande, V.S. and D. Cebon, "*Steady-state Constitutive Relationship for Idealised Asphalt Mixes*". Mechanics of Materials, **31** p. 271-287, 1999.

42. Dolezalova, M., P. Czene, and F. Havel, eds. *"Micromechanical Modeling of Stress Path Effects Using PFC2D Code"*. Numerical Modeling in Micromechanics via Particle Methods, ed. H. Konietzky. A.A. Balkema: The Netherlands. 173-181. 2003.

43. Drescher, A., J.R. Kim, and D.E. Newcomb, *"Permanent Deformation in Asphalt Concrete"*. J. of Materials in Civil Engineering, **5**(1) p. 112-127, 1993.

44. Eisenmann, J. and A. Hilmer. *"Influence of Wheel Load and Inflation Pressure on the Rutting Effect at Theoretical Investigations"*. in *Proc. 6th Int. Conf. on the Structural Design of Asphalt Pavements*. Ann Arbor, Michigan, USA. 1987.

45. Eisenmann, J., U. Lempe, and G. Leykauf. *"Methods for the Structural Design of Asphalt Pavement"*. in *4th Int. Conf. on the Structural Design of Asphalt Pavements*. University of Michigan. 1977.

46. Fitzgerald, J.E. and J. Vakili, *"Nonlinear Characterization of Sand-asphalt Concrete by Means of Permanent-memory Norms"*. Experimental Mechanics, **13** p. 504-510, 1973.

47. Gaskins, F.H., et al., *"The Rheology of Asphalt: Flow Characteristics of Asphalt"*. Transaction of the Society of Rheology, 4(435) p. 265-278, 1960.

48. Hart, R., P.A. Cundall, and J. Lemos, *"Formulation of a Three-Dimensional Distinct Element Model - Part2. Mechanical Calculation for Motion and Interaction of a System Composed of Many Polyhedral Blocks"*. Int. J. Rock Mech.,Min. Sci. & Geomech. Abstr., **25**(3) p. 117-125, 1988.

49. Harvey, J.A.F., "Bitumen Film in Tension", Ph.D Thesis, Department of Engineering, University of Cambridge, 2000.

50. Harvey, J.A.F., *"Failure Mechanism in Viscoelastic Films"*, J. of Materials Science, **38**, p. 1021-1032, 2003.

51.   Hazzard, J.F., R.P. Young, and S.C. Maxwell, *"Micromechanical Modelling in Cracking and Failure of Brittle Rocks"*. J. Geophysical Research, **105**(B7) p. 16683-16697, 2000.

52.   Heukelom, W. and A.J.G. Klomp, *"Road Design and Dynamic Loading"*. Proc. Association of Asphalt Paving Technologists, **33** p. 92-125, 1964.

53.   Hicks, R.G. and C.L. Monismith. *"Prediction of Resilient Response of Pavements Containing Granular Layers using non-linear Elastic Theory"*. in *Proc. 3rd Int. Conf. on the Struct. Design of Asphalt Pavements*. 1972.

54.   Hills, J.F., *"The Creep of Asphalt Mixes"*. J. of. Institute of Petroleum, **59**(570) p. 247-262, 1973.

55.   Hofstra, A. and A.J.G. Klomp. *"Permanent Deformation of Flexible Pavements under Simulated Road Traffic Conditions"*. in *Proc. 3rd Int. Conf. on the Structural Design of Asphalt Pavements*. London. 1972.

56.   Hofstra, A. and C.P. Valkering. *"The Modulus of Asphalt Layers at High Temperatures: Comparison of Laboratory Measurements under Simulated Traffic Conditions with Theory"*. in *Proc. 3rd Int. Conf. on the Struc. Design of Asphalt Pavement*. 1972.

57.   Huang, Y.H., *"Deformation and Volume Change Characteristics of a Sand Asphalt Mixture Under Constant Direct Triaxial Compressive Stresses"*. Highway Research Record, **178** p. 60, 1967.

58.   Huschek, S., *"The Deformation Behaviour of Asphaltic Concrete Under Triaxial Compression"*. Proc. Association of Asphalt Paving Technologists, **54** p. 407, 1985.

59.   Ishibashi, I. and Y.C. Chen, eds. *"Dynamic Shear Moduli and Their Relationship To Fabric of Granular Materials"*. Micromechanics of granular materials, ed. M. Satake and J.T. Jenkins. Elsevier Science Publishers B.V.: Amsterdam. 95-102. 1988.

60. Jenkins, J.T. and O.D.L. Strack, "*Mean Field Inelastic Behaviour of Random Arrays of Identical Spheres*". Mechanics of Materials, **16** p. 25-33, 1993.

61. Jensen, R.P., et al., "*DEM Simulation of Granular Media - Structure interface: Effects of Surface Roughness and Particle Shape*". Int. J. for Numerical and Analytical Methods in Geomechanics, **23** p. 531-547, 1999.

62. Johnson, K.L., "*Contact Mechanics*": Cambridge University Press. 1985.

63. Jongepier, R. and B. Kuilman, "*Characteristics of the Rheology of Bitumens*". Proc. Association of Asphalt Paving Technologists, **38** p. 98-112, 1969.

64. Judycki, J., "*Nonlinear Viscoelastic Behaviour of Conventional and Modified Asphaltic Concrete Under Creep*". Materials and Structures, **25** p. 95-101, 1992.

65. Khanzada, S., "Permanent Deformation in BItuminous Mixtures", Ph.D Thesis, Department of Civil Engineering, University of Nottingham, 2000.

66. Konietzky, H., L. te Kamp, and G. Bertrand, eds. "*Modeling of Cyclic Fatigue Under Tension with P.F.C.*" Numerical Modeling in Micromechanics via Particle Methods, ed. H. Konietzky. A.A. Balkema: The Netherlands. 101-105. 2003.

67. Lai, J.S. and D. Anderson, "*Irrecoverable and recoverable Nonlinear Viscoelastic Properties of Asphalt Concrete*". Highway Research Record, **468** p. 73-88, 1973.

68. Lee, K.L. and H.B. Seed, "*Drained Strength Characteristics of Sands*". J. of The Soil Mechanics and Foundation Division, ASCE, **93**(SM6) p. 117-141, 1967.

69. Lethersich, W., "*The Mechanical Behaviour of Bitumen*". J. of the Society of Chemical Industry, Transactions and Communications, **61** p. 101-108, 1942.

70. Low, B.H., S.A. Tan, and T.F. Fwa, "*Analysis of Marshall Test Behaviour With Triaxial Test Determined Material Properties*". J. of Testing and Evaluation, **21**(3) p. 192, 1993.

71. Martin, H.S., et al. "*Microstructural Simulation of Asphalt Materials: Modelling and Experimental Verification*". in *15th ASCE Engineering Mechanics Conference*. New York. 2002.

72. McDowell, G.R. and O. Harireche, "*Discrete Element Modelling of Soil Particle Fracture*". Géotechnique, 52(2) p. 131-135, 2002.

73. McDowell, G.R. and O. Harireche, "*Discrete Element Modelling of Yielding and Normal Compression of Sand*". Géotechnique, 52(4) p. 299-304, 2002.

74. Meegoda, N.J. and G.K. Chang. "*Modeling of Viscoelastic Behaviour of Hot Mix Asphalt (HMA) Using Discrete Element Method*". in *Proc. 3rd ASCE Materials Engineering Conference*. San Diego. 1994.

75. Moavenzadeh, F. and J. Soussou, "*Viscoelastic Constitutive Equation for Sand Asphalt Mixtures*". Highway Research Record, 256 p. 36-52, 1968.

76. Moavenzadeh, F. and R.R. Stander, "*Effect of Aging on Flow Properties of Asphalt*". Highway Research Record, 178 p. 1-29, 1967.

77. Monismith, C.L., R.L. Alexander, and K.E. Secor, "*Rheologic Behaviour of Asphalt Concrete*". Proc. Association of Asphalt Paving Technologists, 35 p. 400-450, 1966.

78. Monismith, C.L. and K.E. Secor. "*Viscoelastic Behaviour of Asphalt Concrete Pavements*". in *Proc. 1st Int. Conf. on the Structural Design of Asphalt Pavements*. 1962.

79. Nadai, A., "*Theory of Flow and Fracture of solids*". Vol. 2: McGraw-Hill. 1963.

80. Ni, Q., "Effect of Particle Properties and Boundary Conditions on Soil Shear Behaviour: 3-D Numerical Simulations", Ph.D. Thesis, Faculty of Engineering and Applied Science, University of Southampton, 2003.

81. Ni, Q., et al., "*Effect of Particle Properties on Soil Behaviour: 3-D Numerical Modelling of Shearbox Tests*". ASCE Geotechnical Special Publication, 96 p. 58-70, 2000.

82. Ossa, E.A., V.S. Deshpande, and D. Cebon, "*A Phenomenological Model for the Monotonic and Cyclic Behaviour of Pure Bitumen*", in *Paper submitted to J. of Material in Civil Engineering*. 2003.

83. Pagen, C.A., "*Dynamic Structural Properties of Asphalt Pavement Mixtures*". Proc. 3rd Int. Conf. on the Structural Design of Asphalt Pavements, 1 p. 290-316, 1972.

84. Pagen, C.A., "*Rheological Response of Bituminous Concrete*". Highway Research Record, **67** p. 1-26, 1965.

85. Papazian, H.S. "*The Response of Linear Viscoelastic Materials in the Frequency Domain*". in *Proc. Int. Conf. on the Structural Design of Asphalt Pavements*. 1962.

86. Perl, M., J. Uzan, and A. Sides, "*Visco-Elasto-Plastic Constitutive Law for a Bituminous Mixtures under Repeated Loading*". Asphalt Materials, Mixtures, Construction, Moisture Effects and Sulfur, Transportation Research Record, **911** p. 20-27, 1983.

87. Peutz, M.G.F., H.P.M. van Kempen, and A. Jones, "*Layered Systems under Normal Surface Loads*". Highway Research Record, **228** p. 34-45, 1968.

88. Powrie, W., et al., "*Effect of Particle Properties on Soil Behaviour: 3-D Numerical Modelling of Shearbox Tests*", ASCE Geotechnical Special Publication, 96, pp58-70, 2000.

89. Powrie, W., et al., "*Numerical Modelling of Plane Strain Tests on Sands Using a Particulate Approach*". Géotechnique, **55**(4) p. 297-306, 2005.

90. Read, J.M. and D. Whiteoak, "*The Shell Bitumen Handbook, 5th Edition*". Thomas Telford Publishing, 2003.

91. Reynolds, O., "*On the Dilatancy of Media Composed of Rigid Particles in Contact*". Phil. Mag., **20** p. 469-481, 1885.

92.   Roque, R. and B.E. Ruth. "*Materials Characterisation and Response of Flexible Pavement at Low Temperatures*". in *Proc. 2nd Int. Conf. on the Struc. Design of Asphalt Pavement*. 1967.

93.   Roscoe, K.H., "*The Influence of Strains in Soil Mechanics*". Géotechnique, **20**(2) p. 129-170, 1970.

94.   Rothenburg, L. and R.J. Bathurst, "*Micromechanical Features of Granular Assemblies with Planar Elliptical Particles*". Géotechnique, **42**(1) p. 79-95, 1992.

95.   Rothenburg, L., et al. "*Micromechanical Modelling of Asphalt Concrete in Connection with Pavement Rutting Problems*". in *7th International Conference on Asphalt Pavements*. 1992.

96.   Rowe, P.W., "*The Stress-Dilatancy Relation for Static Equilibrium of an Assembly of Particles in Contact*". Proc. Royal Society London A, **269** p. 500-529, 1962.

97.   Saal, R.N.J. and W.A. Labout, "*Rheologycal Properties of Asphaltic Bitumens*". J. of Applied Chemistry, **44** p. 149-165, 1940.

98.   Scarpas, A., et al. "*Finite Element Simulation of Damage Development in Asphalt Concrete Pavements*". in *Proc. 8th Int. Conf. on Asphalt Pavement*. Seattle. 1997.

99.   Schanz, T. and P.A. Vermeer, "*Angles of Friction and Dilatancy of Sand*". Géotechnique, **46**(1) p. 145-151, 1996.

100.   Scott, G.D., "*Packing of Spheres*". Nature, **188** p. 908-909, 1960.

101.   Sides, A., J. Uzan, and M. Perl, "*A Comprehensive Viscoelastic-plastic Charaterization of Sand-asphalt Compressive and Tensile Cyclic Loading*". J. of Testing and Evaluation, **13**(1) p. 49-59, 1985.

102.   Sisko, A.W., "*Determination and Treatment of Asphalt Viscosity Data*". Highway Research Record, **67** p. 27-37, 1965.

103. Sitharam, T.G., "*Micromechanical Modelling of Granular Materials: Effect of Confining Pressure on Mechanical Behaviour*". Mechanics of Materials. **31** p. 653-665, 1999.

104. Skinner, A.E., "*A Note on The Influence of Interparticle Friction of The Shearing Strength of a Random Assembly of Spherical Particles*". Géotechnique, **19**(1) p. 150-157, 1969.

105. Sohn, H.Y. and C. Moreland, "*The Effect of Particles Size Distribution on Packing Density*". The Canadian J. of Chemical Engineering, **64** p. 162-167, 1968.

106. Sousa, J.B. and S.L. Weissman, "*Modelling Pavement Deformation of Asphalt-aggregate Mixes*". Asphalt Paving Technology, **63** p. 224-257, 1994.

107. Sousa, J.B., et al. "*A Non-Linear Elastic Viscous with Damage Model to Predict Permanent Deformation of Asphalt Concrete Mixes*". in *Presented at 72nd Annual TRB Meeting*. Washington DC. 1993.

108. Starodubsky, S., I. Belchman, and M. Livneh, "*Stress-strain Relationship for Asphalt Concrete in Compression*". RILEM, Materials and Structures, **27** p. 474-482, 1990.

109. Thornton, C., M.T. Ciomocos, and K.K. Yin, eds. "*Fracture of Particulate Solids*". Powders and Grains, ed. R.P. Behringer and J.T. Jenkins. Balkema: Rotterdam. 131-134. 1997.

110. Thornton, C. and K.K. Yin, "*Impact of Elastic Spheres With and Without Adhesion*". Powder Technology, **65** p. 153-166, 1991.

111. Thornton, C., K.K. Yin, and M.J. Adams, "*Numerical Simulation of the Impact Fracture and Fragmentation of Agglomerates*". J. Phys. D: Appl. Phys., **29** p. 424-435, 1996.

112. Thrower, E.N., "*A Parametric Study of Fatigue Prediction Model for Bituminous Road Pavements*", in *TRRL Laboratory Report No. 892*. 1979.

113.   Ting, J.M., et al., "*An Ellipse-Based Discrete Element Model for Granular Materials*". Int. J. for Numerical and Analytical Methods in Geomechanics. **17** p. 603-623, 1993.

114.   Ulliditz, P., et al. "*Verification of Analytical-empirical Method of Pavement Evaluation Based on FWD Testing*". in *Proc. 6th Int. Conf. on the Structural Design of Asphalt Pavements*. 1987.

115.   Uzan, J., "*Asphalt Concrete Characterisation for Pavement Performance Prediction*". J. Asphalt Paving Technology, **65** p. 573-607, 1996.

116.   Uzan, J., A. Sides, and M. Perl, "*Viscoelastoplastic Model for Predicting Performance of Asphalt Mixtures*". Pavement System Analysis, Transportation Research Record, **1043** p. 78-89, 1985.

117.   van der Loo, P.J., "*The Creep Test: A Key Tool in Asphalt Mix Design and In The Prediction of Pavement Rutting*". Proc. Association of Asphalt Paving Technologists, **47** p. 523-557, 1978.

118.   Van der Poel, C., "*A General System Describing the Visco-elastic Properties of Bitumens and its Relation to Routine Test Data*". J. of Applied Chemistry, **4** p. 221-236, 1954.

119.   Van der Poel, C. "*Representation of Rheological Properties of Bitumen Over a Wide Range of Temperatures and Loading Times*". in *Proc. 2nd Int. Congress on Rheology*. 1954.

120.   Van der Poel, C., "*Time and Temperatures Effects on the Deformation of Asphaltic Bitumens and Bitumen-Mineral Mixtures*". J. Society of Petroleum Engineers, p. 47-53, 1955.

121.   Wanne, T., ed. "*PFC3D Simulation Procedure for Compressive Strength Testing of Anisotropic Hard Rock*". Numerical Modeling in Micromechanics via Particle Methods, ed. H. Konietzky. A.A. Balkema: The Netherlands. 241-249. 2003.

122.   Ward, I.M., *"Mechanical Properties of Solid Polymers"*: Wiley Interscience. 1971.

123.   Welborn, J.Y., E.R. Oglio, and J.A. Zenewitz, *"A Study of Viscocity Graded Asphalt Cements"*. Proc. Association of Asphalt Paving Technologists, **35** p. 19-60, 1966.

124.   Zheng, L., "Temperature-dependent Visco-elastic-plastic Analysis of Pavement Deformation in Bituminuos Pavements", Ph.D. Thesis, South Bank University, 1994.

125.   Zhou, J. and Y. Chi, eds. *"Shear-band of Sand Simulated by Particle Flow Code"*. Numerical Modeling in Micromechanics via Particle Methods, ed. H. Konietzky. A.A. Balkema: The Netherlands. 205-210. 2003.

126.   Zhuang, X., A.K. Didwania, and J.D. Goddard, *"Simulation of the Quasi-Static Mechanics and Scalar Transport Properties of Ideal Granular Assemblages"*. J. of Computational Physics, **121** p. 331, 1995.